FEEDBACK FROM ACTIVE GALACTIC NUCLEI: A STUDY OF ITS IMPACT AND NUMERICAL IMPLEMENTATIONS

by

James Howard Wurster

A thesis submitted to the faculty of
Saint Mary's University,
Halifax, Nova Scotia, Canada
in partial fulfillment of the requirements for the degree of

Doctor of Philosophy in Astronomy

Approved: Dr. Robert J. Thacker, Advisor

Approved: Dr. Luigi Gallo, Reader

Approved: Dr. David Clarke, Reader

Approved: Dr. Michael Balogh, External Examiner

Department of Astronomy and Physics
Saint Mary's University
August 2013

ABSTRACT

FEEDBACK FROM ACTIVE GALACTIC NUCLEI: A STUDY OF ITS IMPACT AND NUMERICAL IMPLEMENTATIONS

by James Howard Wurster

August 2013

Feedback from active galactic nuclei is now widely regarded as playing a fundamental role in modern theories of galaxy formation. Recent research has highlighted that not only may AGN feedback suppress star formation by heating, it may also promote star formation by producing rapidly cooling shocks. From both a theoretical and numerical perspective, modelling the physical processes responsible is highly challenging, as 13 orders of magnitude in both spatial and temporal scales are involved.

In the literature, there are several different numerical approaches to modelling AGN feedback in galactic and cosmological contexts. The various models make different physical assumptions and are simulated using different numerical codes starting from different initial conditions. Thus, a direct comparison of the results is not possible. We present a study of six distinct approaches to modelling AGN feedback within gravitohydrodynamic simulations of major mergers of Milky Way-sized galaxies. To constrain differences to only be between AGN feedback models, all simulations are run using the HYDRA code, including its associated star formation algorithm, and start from the same initial conditions. We focus on five key aspects of the AGN feedback algorithms: the black hole accretion rate, energy feedback rate and method, particle accretion algorithm, black hole advection algorithm and black hole merger algorithm. Our results yield a wide variation in the accretion behaviours of the models, which reinforces the fact that there remains much to be learnt about the evolution of galactic nuclei.

Using an augmented version of ZEUS-3D, we model an AGN in a system loosely resembling the Local Group. When the AGN is active, shocks are formed in the gas, and stars are born in these shocks. We track the stellar distributions over half a Hubble time to determine if triggered star formation in shocks can account for the observed stellar growth in a galaxy's outer regions. At all times, the stellar distribution can be fit with a Sérsic profile, and the stars continually migrate to larger radii.

ACKNOWLEDGMENTS

Throughout my studies at Saint Mary's University, there have been many people who have provided unwavering support, for which I am very grateful. I would first like to National Sciences and Engineering Research Council (NSERC) of Canada and Saint Mary's University for their financial support. I would next like to thank the administrative staff for all of their help, especially in alleviating the burden of mountains of paperwork. The faculty has always encouraged and fostered the unending quest for knowledge, and has done so in such a powerful way that it was never an unwanted quest. This was enhanced by the great social atmosphere within the department, with faculty and graduate students frequently socialising with one another. I would like to explicitly thank the faculty members who were part of my comprehensive and defence committees for their time and for their suggestions on my research and this thesis in particular.

Next, I would like to thank my family for their support. I would also like to thank my friends and colleagues for stimulating (and sometimes not so stimulating) conversations and distractions; these conversations often provided useful insights into various concepts, and helped to maintain a healthy baseline of sanity.

Most importantly, I would like to thank my supervisor, Dr Rob Thacker for all of his patience, guidance and support. Words cannot do justice for the gratitude and thanks that I feel. Working and socialising with Dr Thacker has been a tremendous experience that I will never forget, and this thesis would not have been possible without him.

Thank you to everyone who has made this thesis possible.

Contents

List of Tables

List of Figures

Chapter 1

Introduction

1.1 Λ-CDM cosmology

Cold dark matter with a cosmological constant, known as 'Λ-CDM', is now widely viewed as the standard cosmological model. The cosmological constant, Λ, is required to match the apparent large scale acceleration of the Universe (e.g. Barrow & Saich 1993). Dark matter is an equally important part of the theory that is required to account for gravitational effects observed in many astrophysical phenomena, such as gravitational lensing (e.g. Subramanian et al. 1987) or rotation curves of galaxies (e.g. van Albada et al. 1985) that cannot be explained on the basis of the observed matter content (essentially viewed as baryonic matter detectable via electromagnetic radiation). In a cosmological context, dark matter must be non-baryonic (e.g. White et al. 1993), and the specification that it be cold relates to it travelling at non-relativistic speeds when it decoupled from the photon fluid early in the development of structure in the Universe. Among other properties, cold dark matter cannot be cooled by radiating photons, and it only interacts with other matter through gravitational forces. Today, the relic cosmic microwave background provides a concise census of the relative fractions mass and energy in our Universe. From the results of Planck, the Universe is comprised of 4.8% baryons, 25.9% dark matter, and 69.1% dark energy (Planck Collaboration et al. 2013).

The early Universe was rapidly expanding and homogeneous, except for weak density fluctuations. These density fluctuations were amplified by gravity and ultimately grew into the structures we observe today (e.g. Edwards & Heath 1976). While the formation and linear evolution of density fluctuations can be calculated analytically, numerical simulations, such at the Millennium Simulation (Springel et al.

2005c), are required to follow the non-linear collapse of the density fluctuations and the subsequent formation of structures like galaxies and clusters of galaxies. In the Λ-CDM model, the build-up of structure is a hierarchical process: density fluctuations collapse to form dark matter haloes, and then these haloes merge to form larger dark matter haloes. The merger process is continual, and ultimately forms the large scale structure observed today. This large scale structure predicted by the Λ-CDM model is in excellent agreement with the observed large-scale structure of the Universe (e.g. Spergel et al. 2003).

1.2 Galaxy mergers within Λ-CDM cosmology

Baryonic matter is usually embedded within dark matter halos. Unlike dark matter, baryonic matter is subject to a number of different physical forces. Beyond the ubiquitous gravitational force, it is also subject to hydrodynamic and radiative forces that can show markedly different behaviours depending upon the precise temperature and density of the baryons. Nearly 40 years ago, the importance of these processes within a wider halo environment was first analysed for a uniform cloud model. The baryons cool, condense and form structures within the haloes, and the rate at which the baryonic structures form is approximately dependent on how quickly the gas can cool (Rees & Ostriker 1977; White & Rees 1978). For the large haloes, the gas cooling period is required to be long, but it is short for small haloes. Assuming that the luminosity is proportional to the mass of these baryonic structures (galaxies), then the above paradigm gives a prediction for the galaxy luminosity function - the number density of galaxies per luminosity interval. This predicts many small, faint galaxies, but only a few large, luminous galaxies; see the red line in Fig. 1.1, which shows a sketched galaxy luminosity function.

There are a few different curves to describe the galaxy luminosity function; one such curve is given Schecter function (Schechter 1976). Although the shape is predefined, the normalisation of the curve is obtained from redshift data (Loveday et al. 1992) or directly from number counts (Huang et al. 1997). By determining

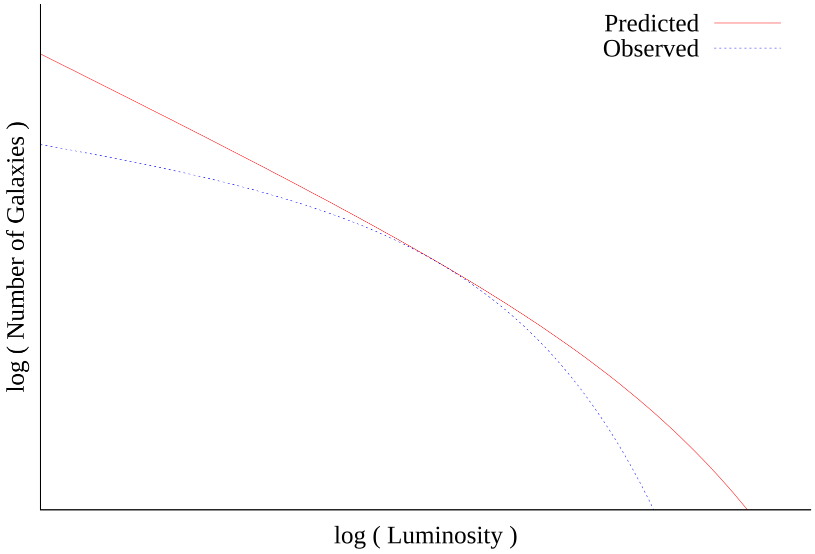

Figure 1.1: A sketch of the observed and predicted galaxy luminosity function.

the normalisation, the total number of galaxies at any given luminosity interval can be calculated. The function can be calculated for specific regions or bands, to yield specific information about those regions or bands.

In the hierarchical structure formation model, which is a product of the distribution of density fluctuations being progressively concentrated on small scales, tidal forces and dynamical friction dissipate the orbital energies of dark matter subhaloes to cause them to spiral towards more massive hosts and become stripped into the larger halo environment. Across a wide range of scales, the dark halo structure is similar (White & Rees 1978), and many smaller sub-halos will occupy a larger one. On galaxy cluster scales, this is seen as galaxies interacting with the brightest cluster galaxy and some of them becoming stripped into the intracluster medium or transformed from spiral to elliptical (e.g. Bekki & Couch 2011). Overall, the hierarchical picture is strongly corroborated by observational evidence indicating that interacting galaxies are common today, and are even more common at higher redshifts (e.g. Taffoni et al. 2003).

In tidal stripping, a satellite galaxy gets close to its host galaxy and the tidal forces of the host strip off outer layers of the satellite. The stripped-off layers are likely to be accreted on to the host (e.g. Read et al. 2006). In some cases, the satellite can be totally disrupted, creating a tidal stream of debris, as seems to be happening to the Milky Way's Sagittarius dwarf galaxy (Belokurov et al. 2006). Another possibility is that the satellite galaxy merges with its host (i.e. a minor merger, where the ratio of the host's mass to the satellite's mass is 3:1 or larger). Although minor mergers likely leave the disk of the host intact (e.g. Bournaud et al. 2005), it is possible that the merger can excite an instability in the host to drive gas into the galaxy's centre (e.g. Hernquist 1989; Hernquist & Mihos 1995), or trigger star formation in the host (Lambas et al. 2003).

Minor mergers are frequent, but the host galaxy does not experience significant growth from each event. It is possible that minor mergers may be important for the growth of massive galaxies due to their frequency, but recent simulations showed that major mergers (mergers between two galaxies with similar mass) dominate the construction of massive galaxies (Maller et al. 2006). In the major merger scenario for galaxies (Toomre & Toomre 1972; Toomre 1977), two similarly sized large galaxies merge to form a spheroidal galaxy. This process destroys the discs, and the violent relaxation process (Lynden-Bell 1967) leads to randomised orbits of the stars. Numerical simulations show that the progenitor galaxies must be gas rich ($> 25\%$; Robertson et al. 2006a) in order to obtain results that match the observed central densities of the spheroids (Hernquist et al. 1993).

1.2.1 Growth of supermassive black holes

A supermassive black hole (SMBH; $M_{\rm SMBH} = 10^6$–10^9 M$_\odot$) is expected to reside at the centre of every galaxy with a stellar spheroid (e.g. Kormendy & Richstone 1995; Ferrarese & Merritt 2000). These black holes likely started as 'seed' black holes, born either through the collapse of Population III stars (e.g. Madau & Rees 2001; Schneider et al. 2002; Islam et al. 2003), or the direct collapse of matter in high-redshift, low angular momentum haloes (e.g. Loeb & Rasio 1994; Bromm & Loeb 2003; Begelman et al. 2006). Each formation mechanism would yield different initial masses ($M_{\rm seed} = 10^2$–10^3 $\rm M_\odot$ for the collapse of stars, and $M_{\rm seed} \sim 10^5$ $\rm M_\odot$ for the direct collapse of matter), but both would grow into SMBHs via accretion of gas and stars, and through mergers with other black holes.

There are several methods to calculate the accretion rate of gas on to a black hole. The simplest prescription assumes that a non-moving, non-rotating black hole is in the centre of a non-rotating polytropic gas which has uniform density at infinity, ρ_∞ (Hoyle & Lyttleton 1939; Bondi & Hoyle 1944). The temperature-limited accretion rate is then given by

$$\dot{M}_{\rm t\text{-}l} = \frac{4\pi\lambda G^2 M_{BH}^2 \rho_\infty}{c_\infty^3}, \tag{1.1}$$

where $M_{\rm BH}$ is the mass of the black hole, c_∞ is the sound speed at infinity, and λ is a dimensionless parameter that depends on the value of the adiabatic index. If, however, the black hole were moving through the gas, then the gas would be deflected as it passed by the black hole. The gas would be focused into a wake behind the black hole, and then accrete on to it with the velocity-limited rate

$$\dot{M}_{\rm v\text{-}l} = \frac{2\pi\alpha G^2 M_{BH}^2 \rho_\infty}{v^3}, \tag{1.2}$$

where v is the relative velocity of the black hole and the distant (undisturbed) parts of the cloud, and α is a dimensionless parameter. Given an adiabatic index of $\gamma = \frac{3}{2}$, Bondi (1952) interpolated these two rates to obtain the Bondi accretion rate[1],

$$\dot{M}_{Bondi} = \frac{2\pi G^2 M_{BH}^2 \rho_\infty}{(c_\infty^2 + v^2)^{3/2}}. \tag{1.3}$$

Numerical simulations by Shima et al. (1985) found that this equation needed an additional factor of two so that it would match the Hoyle-Lyttleton accretion rate (equation 1.1) as the sound speed became insignificant.

---

[1] a.k.a. the Bondi-Hoyle-Lyttleton accretion rate

It is normally assumed that the maximum possible accretion rate is the Eddington accretion rate, which assumes that the gas around the black hole is spherically symmetric and in hydrostatic equilibrium. Then the luminosity of the black hole is given by

$$L_{\mathrm{Edd}} \equiv \frac{4\pi G M_{\mathrm{BH}} m_{\mathrm{p}} c}{\sigma_{\mathrm{T}}}, \tag{1.4}$$

where m_{p} is the proton mass, and σ_{T} is the Thomson cross section. Through the simple argument of $\dot{E} = \dot{M}c^2$, the maximum rate of gas accretion is

$$\dot{M}_{\mathrm{Edd}} \equiv \frac{4\pi G M_{\mathrm{BH}} m_{\mathrm{p}}}{\epsilon_{\mathrm{r}} \sigma_{\mathrm{T}} c}, \tag{1.5}$$

where ϵ_{r} is the radiative efficiency (i.e. the mass-to-energy conversion efficiency, which is set by the amount of energy that can be extracted from the innermost stable circular orbit around a black hole; e,g, Springel et al. 2005b), which is typically set to $\epsilon_{\mathrm{r}} = 0.1$ (Shakura & Sunyaev 1973). Although it is possible to accrete gas at super-Eddington accretion rates (e.g. Kurosawa et al. 2009), most systems are accreting at the Eddington rate or lower (e.g. Ho 2008).

Rather than radial motion as assumed above, the gas around the SMBH would likely have some angular momentum. As it sheds its angular momentum, the gas will settle on to a circular orbit around the SMBH, forming an accretion disc (c.f. Hobbs et al. 2011). However, the process by which the angular momentum is shed and the method by which the gas is transported to these smaller scales remains uncertain (e.g. Goodman 2003; Hopkins & Quataert 2010). On large scales, it is likely that turbulence plays a role in shedding the angular momentum, while jets play a role on the small scale. Once the gas has settled on to the accretion disc, it will lose angular momentum through collisions and travel through the disc, where it will ultimately be accreted on to the black hole (e.g. King 2010). The two types of accretion discs most commonly modelled are geometrically thin, radiatively efficient (Shakura & Sunyaev 1973) and geometrically thick, radiatively inefficient (e.g. Narayan & Yi 1994; Narayan et al. 1998).

As matter is accreted on to the black hole, some of it is converted to energy that is returned to the surrounding environment. If we consider a typical galaxy bulge, its binding energy is $E_{\rm gal} \approx M_{\rm gal}\sigma^2$, where $M_{\rm gal}$ is the galaxy's mass and σ is its velocity dispersion. Assuming that the black hole grows via accretion, and that 10% (Shakura & Sunyaev 1973) of the accreted mass is converted into energy, then the available energy from the black hole is $E_{\rm BH} = 0.1 M_{BH} c^2$. With typical values of $\sigma < 400$ km s^{-1} and $M_{\rm BH} \approx 1.4 \times 10^{-3} M_{\rm gal}$ (e.g. Merritt & Ferrarese 2001), then $E_{\rm BH}/E_{\rm gal} > 80$. Thus, if even a small fraction of this energy is transferred to the gas, it will have a profound impact on the host galaxy and its evolution (Fabian 2012).

1.3 Downsizing

There were problems with the predictive powers of the early CDM model. First, the predicted luminosity function overstated both the number of faint and luminous galaxies; compare the red and blue curves sketched in Fig. 1.1. Second, if hierarchical growth continued as predicted, then the most massive galaxies would be forming today; if we naively assume that mass and luminosity are proportionally related, then this also means that the most luminous galaxies exist today. However, the most luminous and the most active galaxies exist at redshifts of $z \sim 2$ (e.g. Shaver et al. 1996; Madau et al. 1996). Moreover, supermassive black holes of $M_{\rm BH} \sim 10^9 {\rm M}_\odot$ were already in place by this epoch (e.g. Hopkins et al. 2008), and this was the epoch of greatest star formation (e.g. Behroozi et al. 2013). For successively less luminous and less active galaxies, the peak spatial density occurs at successively lower redshifts (e.g. Ueda et al. 2003). Also, the accretion rate onto these massive black holes slows, but the lower mass black holes continue to accrete and grow to successively higher masses (e.g. Hopkins et al. 2008).

In massive galaxies, with masses of $M \sim 10^{12} {\rm M}_\odot$, galaxy merger (Hopkins et al. 2008) and star formation efficiencies (Behroozi et al. 2013)) are the most efficient around $z \sim 2$. Thus, the most massive galaxies at this epoch were the most active. The lower merger and star formation efficiencies in the lower mass galaxies hindered the accretion onto the black hole, thus the activity in the lower mass galaxies is considerably lower than in the high mass galaxies.

Observations show that the most luminous galaxies formed their stars earlier than the early models predicted, thus the early model was missing a mechanism that could account for the decrease in black hole accretion and precipitous decrease of star formation from $z \sim 2$ to today. This reduction in number of luminous and active galaxies from $z \sim 2$ to today has been termed 'downsizing' by Cowie et al. (1996).

The luminosity of a galaxy can be reduced by suppressing star formation; with no new stars forming, the galaxy as a whole will get fainter with age. Thus, it is anticipated that there is some mechanism to suppress the star formation. For the faint end of the galaxy luminosity function, stellar feedback (e.g. stellar winds and supernovae) can heat the gas to prevent or delay further star formation, systematically ensuing lower mass haloes are less bright. This feedback mechanism was not included in the early CDM model, but was soon added to account for the flattening (e.g. see Benson et al. 2003). However, stellar feedback is not powerful enough to affect the high-luminosity end, nor can it account for downsizing (e.g. Silk & Mamon 2012).

As discussed at the end of §1.2.1, there is considerable energy available from gas accreting on to black holes, especially in active galactic nuclei where the accretion rate on to the SMBH is high. It is now generally accepted that some of the accreted matter is converted into energy, which is then returned to its environment (e.g. Fabian 2012). Although the precise contribution is still debated, AGN feedback energy is widely viewed as the cause for downsizing and the cause for the decreased number density of high-luminosity galaxies (Fabian 2012), although observational verification remains a challenge.

1.4 Active galactic nuclei

To trigger an AGN episode, a large amount of cold gas must efficiently be funnelled into the central regions and on to the black hole. The two broad AGN triggering mechanisms are secular (internal) and external (e.g. Alexander & Hickox

2012). In secular methods, an instability grows in the isolated galaxy (e.g. a galactic bar), and drives gas on to the black hole. Although this will trigger some AGN activity, the flow is unlikely to be strong enough to trigger a major AGN episode (Hopkins et al. 2008); however, there is growing evidence that secular evolution may be the dominant trigger between $z \sim 2$ and today (Orban de Xivry et al. 2011; Kocevski et al. 2012). Major mergers with ratios of 3:1 or less (Dasyra et al. 2006; Woods et al. 2006), however, can excite strong inflows that quickly and efficiently deliver a large quantity of gas to the core region (Hernquist 1989; Barnes & Hernquist 1991; Barnes & Hernquist 1996). It is during this time of bright AGN activity that the SMBH acquires most of its mass (Soltan 1982). This phase of bright AGN activity typically lasts for a Salpeter (1964) time of $\sim 10^{7.5}$ yr.

AGN have been observed at many wavelengths, including infrared (e.g. Lacy et al. 2004; Daddi et al. 2007; Hickox et al. 2007), optical (e.g. Steidel et al. 2002; Alexander et al. 2008; Yan et al. 2011), ultraviolet (e.g. Vasudevan & Fabian 2007) and X-ray (e.g. Bauer et al. 2004; Tozzi et al. 2006; Gilli et al. 2007). X-rays are the most effective wavelength to detect AGN since they are not easily obscured, and there are few, if any, bright X-ray sources in a galaxy (e.g. Alexander et al. 2011). Once observed, there are several features that give insights into the power of the black hole, such as large X-ray cavities in the hot gas around the AGN (e.g. Boehringer et al. 1993; McNamara et al. 2000; Gastaldello et al. 2009). Once the size of the cavity is known, then the amount of energy required to evacuate the cavity can be calculated using pdV heating (i.e. the volume of the cavity and the external pressure on it). Cavities typically have radii on the order of 10 kpc, and thus require an outburst of 10^{58}–10^{61} ergs of energy every few $\sim 10^{8}$ yr (Bîrzan et al. 2004; McNamara et al. 2005), or a time-averaged output of $\sim 10^{43}$–10^{45} ergs s^{-1} (Churazov et al. 2002), to keep them inflated. Typical AGN have luminosities of 10^{40}–10^{47} erg s^{-1} (Fabian 1999a); for comparison, the inactive nuclei of the Milky Way has a luminosity of 4×10^{39} erg s^{-1} (Nobukawa et al. 2011), and our Sun's luminosity is 3.8×10^{33} erg s^{-1}.

Further evidence of AGN feedback is provided in the relationships between the black hole mass and the stellar velocity dispersion ($M_{\rm BH}$–σ; e.g. Silk & Rees 1998; Ferrarese & Merritt 2000; Gebhardt et al. 2000; Tremaine et al. 2002; King 2003; Gültekin et al. 2009), and the black hole mass and the bulge mass ($M_{\rm BH}$–$M_{\rm b}$; Magorrian et al. 1998; McLure & Dunlop 2002; Marconi & Hunt 2003). Moreover, Hopkins et al. (2007) showed that these two relations are connected, forming a black hole fundamental plane, which is analogous to the elliptical galaxy fundamental plane (Dressler et al. 1987; Djorgovski & Davis 1987). This suggests that the black hole and the stellar spheroid in which it resides did not evolve independently. If evolution was co-dependent, then this implies a self-regulating system: Feedback from the black hole following a strong accretion event interacts with the surrounding gas, inhibiting further accretion events, and hence limiting black hole growth (e.g. Silk & Rees 1998; Fabian 1999b; Scannapieco & Oh 2004).

Luminous AGN are orders of magnitude more common at $z \sim$1–2 than they are today (e.g. Schmidt 1968; Hartwick & Schade 1990; Ueda et al. 2003). At present, approximately 5–10% of galaxies host luminous optical AGN activity (e.g. Veilleux & Osterbrock 1987; Kewley et al. 2001; Hao et al. 2005). The accretion rate of gas on to the SMBH in most of these galaxies, however, is highly sub-Eddington, indicating that the majority of the black hole mass was accumulated in the past; approximately 0.2% of the local (optical) AGN account for $\sim$ 50% of the total mass growth of the local SMBHs (Heckman et al. 2004). Moreover, high quality observational data indicates that $\sim$95–99% of the integrated mass growth occurred at $z > 0.1$ (e.g. Marconi et al. 2004; Shankar et al. 2004; Merloni & Heinz 2008; Aird et al. 2010). Thus, in order to better understand AGN and constrain the parameters that govern them, high-redshift AGN must be observed in detail, which can be a challenging task.

1.5 AGN feedback theory

The details of the feedback mechanism and how the energy couples to the black hole's environment is poorly understood. Possible mechanisms are line radiation pressure (e.g. Castor et al. 1975; Proga et al. 2000), radiation pressure on dust grains (e.g. Murray et al. 2005), Compton heating of infalling gas (e.g. Ciotti & Ostriker 2001) and photo-ionisation pressure (Buff & McCray 1974; Cowie et al. 1978). Although the details are unknown, the feedback mechanisms can broadly be divided into two modes: radiative and kinetic.

The radiative mode (or wind mode) relies on the accretion being radiatively efficient and near the Eddington limit. The energy released from the accretion process is returned to the environment as a wide opening angle, high-velocity (but sub-relativistic) wind. These winds typically operate near the black hole, and hence are likely the feedback mechanism responsible for the $M_{\rm BH}$–σ relationship. Due to galaxies being more gas-rich in the past, it is likely that this mechanism was most effective at $z \sim 2$–3 (Fabian 2012).

The other feedback mechanism is kinetic feedback. This typically occurs when the black hole is accreting at sub-Eddington rates after the radiative feedback has modified the black hole's environment. The kinetic feedback keeps the galaxy vacated of gas, or keeps the gas warm to prevent further accretion (Fabian 2012). Kinetic feedback also takes the dramatic form of jets, typically launched from the geometrically thick, radiatively inefficient accretion discs (e.g. Rees et al. 1982). The jets inflate the large cavities in the gas, where the energy is transferred in the form of pdV work (e.g. Bîrzan et al. 2004; Cavagnolo et al. 2010), rather than than through strong shocks; observations indicate that inflating cavities is a gentle process (Fabian 2012).

One primary result of feedback is that it may 'blow away' all the gas, leading to a 'red and dead' galaxy (e.g. Springel et al. 2005b), named so because star formation has stopped (i.e. via 'negative feedback'). However, it has also been suggested that AGN feedback actually triggers star formation (i.e. 'positive feedback'; e.g. Silk & Norman 2009; Ishibashi & Fabian 2012; Silk 2013). If an outflow from the AGN is travelling through a gas-rich region, then the shocked gas cools faster than the shock can propagate; this results in the shocked gas being swept up into a geometrically thin shell. If the shell is denser than the tidal density (which is a reasonable assumption), then the shell can fragment into star forming clumps (Zubovas et al. 2013). Observations show that high redshift galaxies are more compact than today's counterparts (Daddi et al. 2005; Trujillo et al. 2007; van Dokkum et al. 2008; Bezanson et al. 2009; van Dokkum et al. 2010; Patel et al. 2013). Since the central densities are similar, it has been suggested that this growth occurs at the outer radii (Bezanson et al. 2009; van Dokkum et al. 2010; Patel et al. 2013), which is consistent with stars forming in outflows that have reached the gas-rich outer regions of the host.

1.6 Numerical algorithms for studying galaxy formation

Astronomy is an observational science in the sense that we can merely *observe* astronomical objects. The characteristic evolution of most extragalactic objects (e.g. galaxies) occurs on timescales much greater than the age of human civilisation, thus it is impossible to observe the entire evolution of a single galaxy. Also, we cannot create experiments to observe the evolution from a specific set of initial conditions. Thus, observationally, we are restricted to observing many objects at many different stages of evolution to piece together our understanding of the class of objects. To gain a better understanding of the full evolutionary process, computer simulations with specified initial conditions are used. If the observational and computer resolutions are comparable, the a comparison would be possible.

Many astrophysical systems are dominated by gravitational and gaseous evolution. It is thus common to numerically solve coupled gravitohydrodynamical equations. This set of equations include the continuity equation,

$$\frac{\mathrm{D}\rho}{\mathrm{D}t} + \rho\boldsymbol{\nabla}\cdot\boldsymbol{v} = 0, \tag{1.6a}$$

the equation of motion,

$$\frac{\mathrm{D}\boldsymbol{v}}{\mathrm{D}t} = -\frac{1}{\rho}\boldsymbol{\nabla}P - \boldsymbol{\nabla}\phi, \tag{1.6b}$$

and the conservation of energy equation,

$$\frac{\mathrm{D}u}{\mathrm{D}t} = -\frac{P}{\rho}\boldsymbol{\nabla}\cdot\boldsymbol{v}, \tag{1.6c}$$

where ρ, $\boldsymbol{v}$, P and u are the density, velocity, pressure and specific energy. Rather than solving for the specific energy, we can solve for the internal energy density, e, where $u = e/\rho$. The $\frac{\mathrm{D}}{\mathrm{D}t}$ denotes the Lagrangian, or comoving, derivative,

$$\frac{\mathrm{D}\boldsymbol{v}}{\mathrm{D}t} \equiv \frac{\partial}{\partial t} + \boldsymbol{v}\cdot\boldsymbol{\nabla}. \tag{1.7}$$

These equations are closed with the Poisson equation,

$$\nabla^2\phi = 4\pi G\rho, \tag{1.8a}$$

where ϕ is the gravitational potential, and an equation of state

$$P \equiv P(\rho, u). \tag{1.8b}$$

There are several numerical codes that solve these equations, and they fall into two broad categories: particle based (i.e. smooth particle hydrodynamics; Lucy 1977; Gingold & Monaghan 1977) and grid codes. Within these two subgroups, there are several different approaches to solving the equations, thus in our description below, we will focus on the equations used in the two numerical codes used in this thesis. For smooth particle hydrodynamics (see §1.6.1), we will discuss the form of the equations used in the parallel version of HYDRA (Couchman et al. 1995; Thacker & Couchman 2006), and for the grid code (see §1.6.2), we will discuss the form used in ZEUS-3D (Clarke 1996; Clarke 2010). As a final note, HYDRA uses an Adaptive Particle-Particle, Particle-Mesh algorithm (Couchman 1991) to calculate gravitational forces, which will be briefly discussed in §1.6.1.1 for completeness.

1.6.1 Smooth particle hydrodynamics

Smooth particle hydrodynamics (SPH; for review, see Monaghan 1992) is a particle-based Lagrangian numerical method used to obtain approximate solutions from the equations of fluid dynamics. By treating a fluid as a set of particles, all calculations are performed without the need of a grid. This is advantageous since the calculations are occurring where the matter is, rather than over a preset area/volume of space. The first SPH codes were developed concurrently, but independently, for astrophysical purposes by Lucy (1977) and Gingold & Monaghan (1977). Since then, SPH has been developed extensively for use in computational astrophysics and other fields; notable modifications of the 'classical' SPH are smoothed particle magnetohydrodynamics (SPMHD; Price & Monaghan 2004) and SPH with a higher order dissipation switch to account for proper fluid mixing (SPHS; Read & Hayfield 2012).

The SPH method relies upon interpolating values from a set of points (i.e. particles) to a specific point. The integral interpolant, $A_{\mathrm{I}}(\boldsymbol{r})$, of any function $A(\boldsymbol{r})$ is given by

$$A_{\mathrm{I}}(\boldsymbol{r}) = \int A(\boldsymbol{r}')W(\boldsymbol{r}-\boldsymbol{r}', h)\mathrm{d}\boldsymbol{r}', \tag{1.9}$$

or more usefully by

$$A_{\mathrm{I}}(\boldsymbol{r}) = \int \frac{A(\boldsymbol{r}')}{\rho(\boldsymbol{r}')}W(\boldsymbol{r}-\boldsymbol{r}', h)\rho(\boldsymbol{r}')\mathrm{d}\boldsymbol{r}', \tag{1.10}$$

where $\mathrm{d}\boldsymbol{r}'$ is the differential volume element, W is an interpolating kernel, h is the smoothing length of a particle and $\rho(\boldsymbol{r}')d\boldsymbol{r}'$ is the mass element of a particle. For use in numerical simulations, the continuous integral must be converted to a discrete sum, viz.

$$A_{\mathrm{I}}(\boldsymbol{r}) = \sum_j m_j \frac{A_j}{\rho_j} W(\boldsymbol{r}-\boldsymbol{r}_j, h), \tag{1.11}$$

where the subscript j refers to quantities at position $\boldsymbol{r}_j$, and m_j is the mass of the j'th particle. The density at $\boldsymbol{r}_j$ is calculated using

$$\rho_j \equiv \rho(\boldsymbol{r}_j) = \sum_k m_k W(\boldsymbol{r}_j - \boldsymbol{r}_k, h_j), \tag{1.12}$$

where m_k is the mass of particle k.

The smoothing length, h, is the characteristic width of the kernel, which describes the contribution from each neighbour, depending on its distance from the particle. While h can be set as a fixed parameter, it is practical to give each particle its own time-dependent smoothing length. For a varying smoothing length, h_i is chosen such that particle i has approximately N neighbours (i.e. there are N particles within a sphere of radius $2h_i$ around particle i); in HYDRA, the number of neighbours is set such that $30 < N < 80$, with an average of $N \sim 50$ (Thacker et al. 2000). This inherently leads to a higher resolution in more dense regions, so computational time is not wasted in low density regions where evolution is slow. It is also useful to define a minimum and maximum possible smoothing length, with $h_{\min} \leq h_i \leq h_{\max}$. This prevents h_i from falling below a reasonable resolution of the simulation (i.e. a resolution limit set by the gravitational solver; see §1.6.1.1) or covering an unreasonable distance (as h_i increases in regions of really low density, the density at particle i approaches the self-density of the particle and not arbitrary low values; thus beyond a given $h_{\max}$, further resolution is not gained by searching for particles at even larger radii Theuns et al. 1998). Setting $h_{\min}$ to a fraction of the resolution of the gravity solver can lead to problems in very dense regions where the number of particles rises extensively, producing an N^2-like slowdown in computational time; it should be noted that several SPH codes do take steps to mitigate this problem.

When choosing a kernel, W, the kernel and its first derivative must be continuous functions that have the following properties:

$$\int_V W(\boldsymbol{r} - \boldsymbol{r}', h) \mathrm{d}\boldsymbol{r}' = 1, \tag{1.13}$$

and

$$\lim_{h\to 0} W(\boldsymbol{r}-\boldsymbol{r}', h) = \delta(\boldsymbol{r}-\boldsymbol{r}'). \tag{1.14}$$

One common kernel is a Gaussian kernel, where the contribution of particles falls off rapidly for $|\boldsymbol{r}-\boldsymbol{r}'| \geq h$. However, it is computationally more useful to have a kernel that goes to zero at some finite distance. Thus, the B_2 spline (Monaghan & Lattanzio 1985),

$$W(\boldsymbol{r}-\boldsymbol{r}_j, h) = \frac{W_{\mathrm{s}}(r/h)}{h^3}, \tag{1.15}$$

where $r = |\boldsymbol{r}-\boldsymbol{r}_j|$, is commonly used. If we define $x \equiv \frac{r}{h}$, then

$$W_{\mathrm{s}}(x) = \frac{1}{4\pi}\begin{cases} 4-6x^2+3x^3 & \text{if } 0 \leq x \leq 1 \\ (2-x)^3 & \text{if } 1 < x \leq 2 \\ 0 & \text{if } x > 2 \end{cases}, \tag{1.16}$$

The kernel's first derivative, which has been modified from the analytical result such that it will give a small repulsive force for close particles (to prevent artificial clustering), is given by (Thomas & Couchman 1992)

$$\nabla W_{\mathrm{s}}(x) = -\frac{1}{4\pi}\begin{cases} 4 & \text{if } 0 \leq x \leq \frac{2}{3} \\ 3x(4-3x) & \text{if } \frac{2}{3} < x \leq 1 \\ 3(2-x)^2 & \text{if } 1 < x \leq 2 \\ 0 & \text{if } x > 2 \end{cases}. \tag{1.17}$$

Thus, particles at distances greater than $2h$ do not contribute to the interpolation.

Since the kernel is chosen such that its first derivative is continuous, (1.10) can be differentiated to give,

$$\begin{aligned} \frac{\partial}{\partial \boldsymbol{r}} A_{\mathrm{I}}(\boldsymbol{r}) =& \frac{\partial}{\partial \boldsymbol{r}} \int \frac{A(\boldsymbol{r}')}{\rho(\boldsymbol{r}')} W(\boldsymbol{r}-\boldsymbol{r}', h)\rho(\boldsymbol{r}')\mathrm{d}\boldsymbol{r}' \\ =& \int \frac{A(\boldsymbol{r}')}{\rho(\boldsymbol{r}')} \frac{\partial W(\boldsymbol{r}-\boldsymbol{r}', h)}{\partial \boldsymbol{r}} \rho(\boldsymbol{r}')\mathrm{d}\boldsymbol{r}', \end{aligned}$$

which can be converted to a summation, viz.,

$$\boldsymbol{\nabla} A_{\mathrm{I}}(\boldsymbol{r}) = \sum_j m_j \frac{A_j}{\rho_j} \boldsymbol{\nabla} W(\boldsymbol{r} - \boldsymbol{r}_j, h), \tag{1.18}$$

where $\boldsymbol{\nabla} \equiv \frac{\partial}{\partial \boldsymbol{r}}$. An alternative derivation is presented in Appendix A. Thus, we have an exact derivative of an approximate function. However, this form of the derivative will not vanish if A is constant since the distribution will likely not be perfectly spherically symmetric. The derivative can be made to exactly vanish if we first rewrite $\boldsymbol{\nabla} A$ as

$$\boldsymbol{\nabla} A = \frac{1}{\rho} \boldsymbol{\nabla}(\rho A) - \frac{A}{\rho} \boldsymbol{\nabla} \rho. \tag{1.19}$$

Then, the derivative of A_{I} becomes

$$\boldsymbol{\nabla} A_{\mathrm{I}}(\boldsymbol{r}) = \frac{1}{\rho} \sum_j m_j (A_j - A_{\mathrm{I}}) \boldsymbol{\nabla} W(\boldsymbol{r} - \boldsymbol{r}_j, h), \tag{1.20}$$

which equals zero if A is constant.

Using (1.11), (1.12) and (1.20), interpolation functions can be made for the hydrodynamic equations, (1.6); from now on, we write the Lagrangian derivative in the more common total derivative form of $\frac{\mathrm{D}}{\mathrm{D}t} = \frac{\mathrm{d}}{\mathrm{d}t}$. The SPH interpolation of the continuity equation becomes

$$\frac{\mathrm{d}\rho_i}{\mathrm{d}t} = \rho_i \sum_j \frac{m_j}{\rho_j} \boldsymbol{v}_{ij} \cdot \boldsymbol{\nabla}_i W_{ij}, \tag{1.21}$$

where $\boldsymbol{v}_{ij} \equiv \boldsymbol{v}_i - \boldsymbol{v}_j$ and $W_{ij} \equiv W(\boldsymbol{r}_i - \boldsymbol{r}_j, h_i)$ for particle pair i and j.

For the equation of motion, (1.6b), it is better to follow the approach of (1.19) and rewrite the pressure term as

$$\frac{1}{\rho} \boldsymbol{\nabla} P = \boldsymbol{\nabla} \left(\frac{P}{\rho} \right) + \frac{P}{\rho^2} \boldsymbol{\nabla} \rho. \tag{1.22}$$

Using this form will allow for exact conservation of linear and angular momentum if h is constant or a symmetric function of i and j (Monaghan 2005). Then the equation of motion becomes (Monaghan 1992)

$$\frac{\mathrm{d}\boldsymbol{v}_i}{\mathrm{d}t} = -\sum_j m_j \left(\frac{P_j}{\rho_j^2} + \frac{P_i}{\rho_i^2} \right) \boldsymbol{\nabla}_i W_{ij}, \tag{1.23}$$

where we have intentionally dropped the gravitational acceleration term, $\boldsymbol{\nabla}\phi$, which will be discussed in §1.6.1.1.

As done in Thomas & Couchman (1992), it is possible to symmetrise (1.23), making use of kernel averaging,

$$W_{ij} \rightarrow \frac{1}{2} \left[W(\boldsymbol{r}_i - \boldsymbol{r}_j, h_i) + W(\boldsymbol{r}_i - \boldsymbol{r}_j, h_j) \right], \tag{1.24}$$

and the approximation

$$\boldsymbol{\nabla}_i W(\boldsymbol{r}_i - \boldsymbol{r}_j, h_i) \simeq -\boldsymbol{\nabla}_j W(\boldsymbol{r}_i - \boldsymbol{r}_j, h_j). \tag{1.25}$$

Then (1.23) becomes,

$$\begin{aligned} \frac{\mathrm{d}\boldsymbol{v}_i}{\mathrm{d}t} = & -\sum_{j,\ r_{ij}<2h_i} m_j \frac{P_i}{\rho_i^2} \boldsymbol{\nabla}_i W(\boldsymbol{r}_i - \boldsymbol{r}_j, h_i) \\ & + \sum_{j,\ r_{ij}<2h_j} m_j \frac{P_j}{\rho_j^2} \boldsymbol{\nabla}_j W(\boldsymbol{r}_i - \boldsymbol{r}_j, h_j). \end{aligned} \tag{1.26}$$

Finally, the conservation of energy equation can be written as

$$\frac{\mathrm{d}u_i}{\mathrm{d}t} = -\frac{P_i}{\rho_i^2} \sum_j m_j \boldsymbol{v}_{ij} \cdot \boldsymbol{\nabla}_i W_{ij}, \tag{1.27}$$

where $\boldsymbol{v}_{ij} \equiv \boldsymbol{v}_i - \boldsymbol{v}_j$ and $W_{ij} \equiv W(\boldsymbol{r}_i - \boldsymbol{r}_j, h_i)$ for particle pair i and j.

Even if starting from smooth initial conditions, shocks and contact discontinuities may be produced (Landau & Lifshitz 1959). However, the discretised SPH equations cannot correctly describe the shock since they keep entropy constant across the shock, but the Rankine-Hugoniot jump conditions show that entropy must increase. Thus, it is necessary to add at term that will allow for dissipation to produce entropy. This term is introduced as an artificial viscosity, which is analogous to real viscosities, but replacing the mean free path with the resolution length. One difficulty with introducing an artificial viscosity is that it must act only on shocks; ideal gas dynamics may be negatively impacted if the artificial viscosity acts on gas that is not in a shock (Springel 2010b).

Although viscous terms could be calculated by interpolation of the SPH equations, Monaghan & Gingold (1983) devised a viscosity by simple arguments about its form and relation to gas viscosity (Monaghan 2005). This viscosity, Π_{ij}, is then added to the pressure terms. The viscosity we will describe below is the one presented in Thacker et al. (2000), which is a variation of the one presented by Monaghan & Gingold (1983). Here, the viscosity is given by

$$\Pi_{ij} = \frac{-\alpha\mu_{ij}\bar{c}_{ij} + \beta\mu_{ij}^2}{\tilde{\rho}_{ij}} f_i, \tag{1.28}$$

where

$$\mu_{ij} = \begin{cases} \left(\bar{h}_{ij}\boldsymbol{v}_{ij} \cdot \boldsymbol{r}_{ij}\right) / \left(r_{ij}^2 + \nu^2\right) & \text{if } \boldsymbol{v}_{ij} \cdot \boldsymbol{r}_{ij} < 0 \\ 0 & \text{if } \boldsymbol{v}_{ij} \cdot \boldsymbol{r}_{ij} \geq 0 \end{cases}, \tag{1.29}$$

and

$$\tilde{\rho}_{ij} = \frac{\rho_i}{2}\left[1 + \left(\frac{h_i}{h_j}\right)^3\right], \tag{1.30}$$

where the bar represents the arithmetic averaging of the quantities for particles i and j, c_i is the sound speed of particle i, $\nu^2 = 0.01\bar{h}_{ij}^2$ is included to prevent numerical divergences, α and β are coefficients, and f_i will be discussed below. The variable $\tilde{\rho}_{ij}$ is used rather than $\bar{\rho}_{ij}$ for computational efficiency, and is based upon the approximation $\rho_j \simeq \rho_i h_i^3/h_j^3$.

In the presence of shear flows, the artificial viscosity may not vanish, leading to an undesirable shear viscosity. Balsara (1995) added a shear correcting term, f_i, to the viscosity, which has been modified by Steinmetz (1996):

$$f_i = \frac{|\langle \boldsymbol{\nabla} \cdot \boldsymbol{v} \rangle_i|}{|\langle \boldsymbol{\nabla} \cdot \boldsymbol{v} \rangle_i| + |\langle \boldsymbol{\nabla} \times \boldsymbol{v} \rangle_i| + 0.0001 c_i / h_i}. \tag{1.31}$$

For compressional flows, $f_i = 1$, and for shear flows, $f_i = 0$, leading to zero viscosity as desired.

Including the artificial viscosity, the final (symmetrised) equation of motion and energy equations become

$$\begin{aligned} \frac{\mathrm{d}\boldsymbol{v}_i}{\mathrm{d}t} = & -\sum_j m_j \left(\frac{P_i}{\rho_i^2} + \frac{\Pi_{ij}}{2} \right) \boldsymbol{\nabla}_i W(\boldsymbol{r}_i - \boldsymbol{r}_j, h_i) \\ & + \sum_j m_j \left(\frac{P_j}{\rho_j^2} + \frac{\Pi_{ji}}{2} \right) \boldsymbol{\nabla}_j W(\boldsymbol{r}_i - \boldsymbol{r}_j, h_j), \end{aligned} \tag{1.32}$$

and

$$\frac{\mathrm{d}u_i}{\mathrm{d}t} = \sum_j m_j \left(\frac{P_i}{\rho_i^2} + \frac{\Pi_{ij}}{2} \right) \boldsymbol{v}_{ij} \boldsymbol{\nabla}_i \cdot W(\boldsymbol{r}_i - \boldsymbol{r}_j, h_i). \tag{1.33}$$

1.6.1.1 Gravitational solvers for SPH codes

Gravity plays an important role in most astrophysical problems, including star formation, galaxy formation and evolution, and large-scale structure formation. In these problems, gas also evolves under the influence of gravity (e.g. collapsing to form a star, or rotating in a viscous disc), thus gravitational forces must be computed in addition to the hydrodynamical forces described in §1.6.1. Since gravity is a long-range force, it is not reasonable to follow the SPH approach where the fluid calculations are locally computed; due to computational limitations, it is not practical to perform an N^2 calculation over all of the particles. Thus, codes that advect gas particles via the SPH algorithm typically also include a separate algorithm to deal with the gravitational interactions.

Two common gravitational solvers are the 'tree code' (Barnes & Hut 1986) and the Particle-Particle Particle-Mesh (P^{3}M) algorithm (Efstathiou & Eastwood 1981; thoroughly described in Hockney & Eastwood 1981); we will focus on the latter since

HYDRA uses an adaptive P^{3}M algorithm. In the P^{3}M method, the gravitational force is first split into short and long range forces, viz.

$$\boldsymbol{F}_{\mathrm{grav}} = \boldsymbol{F}_{\mathrm{short}} + \boldsymbol{F}_{\mathrm{long}}. \tag{1.34}$$

The short range forces are calculated via the Particle-Particle method, which simply calculates the force by summing over all particles within a given radius. The long range force uses the Particle-Mesh method, which first interpolates the (Lagrangian) particles on to an (Eulerian) grid. Next, this mass density grid is Fourier transformed and the resulting k-space field is multiplied by a Green's function which is calculated to minimise the errors associated with the mass assignment procedure. Following this convolution, the resulting potential grid is then differenced to obtain the force grid. Finally, the Particle-Mesh accelerations are found from the force grid and the mass assignment function used to create the mass density grid. The accuracy of the force calculation can be improved by further smoothing the mesh force, $\boldsymbol{F}_{\mathrm{long}}$, hence increasing the range over which the short range forces are calculated. The cost for this improved accuracy is a slowdown from the increased number of particle-particle interactions.

In dense regions, there will be many particles contributing to $\boldsymbol{F}_{\mathrm{short}}$, which increases the runtime of the calculation. To remove this inefficiency, a sub-grid can be placed over the dense region and the P^{3}M algorithm be repeated with its own fast Fourier transform and shaped force. The short range force is then calculated using fewer neighbours. This refinement can be done as frequently as required to optimise performance; this version of the P^{3}M code is known as the Adaptive Particle-Particle Particle-Mesh (AP^{3}M) algorithm (Couchman 1991). Tests performed by Couchman (1991) showed that the mean and rms errors between this method and the true force were on the order of 0.2%.

The gravity solver combined with the SPH algorithm fully describes self-gravitating gas. However, many astrophysical problems contain more components than just gas (e.g., galaxies contain stars, black holes and dark matter). Adding these other components is trivial for (e.g.) a combined SPH-AP^{3}M code such as Hydra; this is done by adding additional particle sets to represent these additional components. All particles are tagged by their type, so they can undergo the proper treatment. Gas particles are essentially fluids, so they must be given the full gravitohydrodynamic treatment; star, black hole and dark matter particles are treated as collisionless particles, thus are only advected by the gravity solver.

1.6.2 Grid codes

The hydrodynamic equations can be solved on a grid using either an Eulerian approach or a Lagrangian approach. In the former, the grid cells are fixed and all values associated with them evolve with the simulation; this is the approach used in Zeus-3D. In the Lagrangian approach, each cell is given an initial mass, and the grid boundaries evolve such that the mass of the cell is constant throughout the simulation.

Unlike SPH where all algorithms are variants of the equations presented in §1.6.1, there is no one specific algorithm used to solve the hydrodynamic equations on a grid. Godunov and higher order Godunov algorithms (e.g. Godunov 1959; van Leer 1977; Colella & Woodward 1984) have proved to be the most robust and efficient for ideal hydrodynamics. Other methods better suited for non-ideal hydrodynamics, such as Zeus-3D, use a staggered mesh, where scalars are zone-centred quantities and vector components are centred at the zone-interfaces; see Clarke (1996) for an extensive discussion on the Consistent Method of Characteristics used in Zeus-3D to transport the quantities.

Eulerian grid codes are adept at handling fluid interactions and strong density gradients, such as shocks, mixing, and avoid suppressing physical fluid instabilities (e.g. Agertz et al. 2007; Scannapieco et al. 2012); Eulerian treatment of these gradients is far superior to SPH treatments of similar problems. As mentioned in §1.6.1, SPH codes have an inherent characteristic of higher resolution in denser regions, which does not exist explicitly in Eulerian grid codes. One can naively run an Eulerian code with high resolution, but then much time is wasted on inactive areas that evolve on long time-scales. One option (available in Zeus-3D) is to use logarithmic spacing. While this is practical for a large suite of problems, it assumes *a priori* knowledge of which regions evolve on short time-scales. The other alternative is to implement an adaptive mesh, where sub-grids are placed on top of dense regions to increase the resolution locally. This happens dynamically, such that sub-grids are added and removed as the problem evolves and the dense regions move. Adaptive meshes have been implemented in the successor to Zeus-3D, AZEuS (Ramsey et al. 2012), but are not used in this work.

Lagrangian grid codes, where the grid itself moves, are typically fraught with practical difficulties but do resolve some issues that are common to other numerical codes. For example, the grid nature allows for shocks to be better resolved than in particle codes, and the moving mesh is Galilean invariant and sensitive to the presence of bulk velocities, unlike Eulerian codes. One astrophysical Lagrangian grid code is AREPO (Springel 2010a), where the mesh is defined as the Voronoi tessellation of a set of discrete points, which are allowed to move freely. The mesh continuously deforms and changes topology without mesh-tangling effects present in other Lagrangian grid codes.

1.7 Numerical simulations of AGN related phenomena

Solving numerical problems in astrophysics can be a daunting task, given the large range of scales involved. For example, consider all the scales involved in studying AGN feedback. The supermassive black hole itself has a radius on order 10^{6-8} km, while its accretion disc is ∼1000 times larger; this is the region from which feedback is expected to be launched. Kinetic energy is expected to be deposited on the galactic (10^{1-2} kpc) scale, which, in some cases, can affect the cluster (∼1 Mpc) scale. Hence we have a range of spatial scales covering up to 13 orders of magnitude. For AGN, the black hole's luminosity is expected to have short term variability on time spans of days to years, but is active for $\sim 10^{7-8}$ yr. Thus, long and short timescales must be considered to understand the full impact on the environment.

Further complications include the black hole's immediate environment of an accretion disk (with number densities of $n \sim 10^2$ cm^{-3}), a narrow line region (with electron density $n_\mathrm{e} \sim 10^{3-6}$ cm^{-3}) and a broad line region (with $n_\mathrm{e} \sim 10^8$ cm^{-3}). Once the feedback escapes from this region, it will interact with the interstellar medium (ISM), which has a range of number densities of 10^{2-6} cm^{-3}. If the feedback is powerful enough to impact the intracluster medium, then it will interact with gas with a particle density of 10^{-3} cm^{-3}. Thus, the problem of computational astrophysics is apparent: Small scale events have large scale implications, thus large domains must be highly resolved in time and space. For the range of scales related to AGN, this is not possible with the current computing power, even when using adaptive resolution.

The two common ways to circumvent these scale problems are to model only the small-scale around the black hole (where large-scale affects are undetermined), or to model the large scale (where the feedback originates on sub-resolution scales); both of these scales have been independently studied in the literature. The smallest simulations typically extend out to a few Schwarzschild radii, and use full general relativistic formalism to study the accretion flow or inner corona (e.g. Fragile & Meier 2009; Noble & Krolik 2009; Bucciantini & Del Zanna 2011; Shiokawa et al. 2012). Typical small-scale studies extend from a few Schwarzschild radii to few thousand astronomical units (or even a few pc) and are performed in a Newtonian framework (e.g. Proga et al. 2000; Kurosawa et al. 2009; Fukumura et al. 2010; Nixon et al. 2011; Barai et al. 2012). In these simulations, knowledge on $\sim$6 dex is still required, so some assumptions are still required. The large-scale simulations must make many assumptions about the accretion rate and feedback mechanism (which is occurring many orders of magnitude below the resolved scale of the simulation), but are able to study the feedback effects on galactic (e.g. Kawata & Gibson 2005; Springel et al. 2005b; Debuhr et al. 2011; Gaspari et al. 2012) or cosmological (e.g. Thacker et al. 2006; Sijacki et al. 2007; Okamoto et al. 2008; Booth & Schaye 2009; Dubois et al. 2012) scales. It is challenging to merge simulations of two different scales into a single study since the entire small-scale simulation would typically be on the order of the resolution of the large-scale simulation; however, Hopkins & Quataert (2010) have performed nested hydrodynamic simulations that do not include AGN feedback. Likewise, there is difficulty in comparing and combining large scale cosmological simulations with galactic scale simulations, where the former typically has softening lengths of a few kiloparsecs (e.g. Okamoto et al. 2008) and the latter a few dozen parsecs (e.g. Debuhr et al. 2011). This is especially problematic in studies of AGN feedback where the energy is being deposited (e.g.) on a scale similar to the simulation's softening length. Thus, not only is it necessary to understand how AGN feedback works on all scales, it is equally necessary to understand the implications of the resolution of the simulation.

In most simulations, there are many physical processes occurring on scales below the resolution of the simulation. Although unresolved, frequently these processes do need to be taken into account. Thus sub-grid models are introduced, where the effects of the sub-grid processes are estimated based upon a chosen theoretical prescription and the large scale properties resolved in the simulation. Both of these, as well as the extrapolation of the small scale effects to the resolved scale will affect the results. Since an underlying theory is involved in sub-grid models, the calculations and effects are not determined directly from first principles.

The smaller the scale of the simulation, the less sub-grid physics that is required. For example, the AGN feedback model of Proga (2007) considers only a sphere of radius 5.7 pc around the black hole, thus they can directly impart a wind on to the gas with only a few assumptions regarding the heating and cooling processes of the gas and obtain relatively detailed results. In Debuhr et al. (2011), however, the smallest resolved gas particle has a mass of $\sim 4 \times 10^4$ $M_\odot$, and the wind is imparted on all gas particles within a radius of 188 pc around the black hole, thus most of the detailed physics is unresolved and only general inferences can be made. Thus, it is clear that the smaller the total scale of the simulation, the less assumptions that are required for about sub-grid processes.

Although sub-grid processes may be well-understood from a physical perspective, it does not lessen the challenge of implementing them in a numerical code. Two sub-grid processes that are fundamental to this thesis are star formation and AGN feedback. Star formation can be simplistically thought of as the following processes: Gas begins to self-gravitate and condenses into stars; energy is released back into the ISM upon their death. The simple numerical prescription states that when an element of gas meets certain criteria, the gas is turned into stars and feedback energy is immediately returned to the surrounding gas. One method of numerical star formation for particle codes is the 'classical' approach (e.g. Katz 1992; Thacker & Couchman 2000; Brook et al. 2004; Stinson et al. 2006; Governato et al. 2007). Here, if a gas particle meets a set of given criteria, a portion of the gas is converted into stars; this is a bookkeeping process and does not affect how the particle behaves in the simulation. When a set fraction of the gas particle has been converted into stars, the gas particle is converted to a star particle and feedback energy is immediately released to the surrounding gas particles. The lack of delay between star particle formation and feedback energy release is not a significant issue because at typical SPH resolutions, each gas particle represents several molecular clouds, thus process is averaging over several molecular clouds and the evolution is representative at best. Another prescription is the multiphase model (e.g. Springel & Hernquist 2003; Springel et al. 2005b; Booth & Schaye 2009; Hopkins et al. 2009). Here, the star formation process is derived from a model of cold clouds (where stars form) embedded in a hot, pressure-confining phase. Above a given density threshold, the gas is thermally unstable to the onset of this two-phase medium. The mass fraction in each phase is determined by star formation and feedback, evaporation of the cold clouds through thermal conduction, and the growth of clouds through radiative cooling. The star formation rate is then calculated based upon a prescribed law and an equation of state.

The second sub-grid process is AGN feedback, which is the topic of this thesis, and will be discusses in the following section.

1.8 Specifics of AGN feedback prescriptions

AGN feedback has been implemented in many numerical simulations (see references in §1.7). In most cases, a sub-grid algorithm is required to determine the accretion rate on to the black hole, how much energy needs to be returned to the gas, and how the energy is returned to the gas. Since AGN feedback was first implemented in Kawata & Gibson (2005) and Springel et al. (2005b), many sub-grid models have been created, and each use different physical and numerical assumptions. This is inherently a product of the uncertainty involved in both the accretion process and how the black hole systems evolve.

Although physical arguments can be made to compare the algorithms, to date there has not been a numerical study of the various algorithms. Since the algorithms in the literature are implemented using different numerical codes and different initial conditions, it is not possible to directly compare these algorithms based upon the currently published results. This point is supported by Scannapieco et al. (2012), who performed a comparison of several SPH and adaptive mesh refinement (AMR) codes (without AGN feedback); the study concluded that, even starting from the same initial conditions, mass and spatial resolution, the different hydrodynamical approaches, gas cooling, star formation and stellar feedback algorithms of different numerical codes produce (sometimes drastically) different results.

Thus, to numerically compare the AGN feedback algorithms, all other numerical affects and differences must be minimised. This requires the comprehensive comparison be run using only one numerical code. In Chapter 2, we have taken four AGN feedback algorithms found in the literature, specifically those found in Springel et al. (2005b), Okamoto et al. (2008), Booth & Schaye (2009) and Debuhr et al. (2011), and implemented their AGN feedback algorithms in the AP^{3}M–SPH code HYDRA; we also created a fifth algorithm specifically for this study. The algorithms were then applied to a major merger simulation of two Milky Way-size galaxies, where all non-AGN-feedback initial conditions and algorithms were held constant. By doing this, the differences in each model are a direct result of the AGN feedback algorithm. We explicitly note that the purpose of this chapter is to compare and contrast the various algorithms, not to make any strong statements about the 'accuracy' of the given models. The results of this chapter are published in Wurster & Thacker (2013a).

As the analysis for Chapter 2 was in progress, a novel new accretion method was proposed by Power et al. (2011). This accretion method varied greatly from the methods previously studied in that the accretion rate was dependent solely on the location of gas particles relative to the black hole particle and not the physical properties of the gas near the black hole. This algorithm was originally tested in an ideal, small scale scenario, thus we were required to modify it so that it could be included in a merger simulation. In Chapter 3, we have modified the accretion algorithm of Power et al. (2011), and tested it in the same major merger simulations used in Chapter 2. We then present a parameter study based upon resolution and two free parameters that govern the accretion rate. The results of this chapter are published in Wurster & Thacker (2013b). We note that this chapter deviates from the paper in that we have removed information that also appears in Chapter 2; we make explicit notes of this in Chapter 3 and direct the reader to the relevant sections of Chapter 2. Moreover, in Chapter 3, we only make a brief comparison of this model to two models found in Chapter 2, thus in Appendix B we have replotted the important figures using data from the primary models in Chapter 2 and the fiducial model in Chapter 3.

The results of these AGN feedback simulations imply that negative feedback energy typically inhibits star formation. However, there may well be certain epochs when star formation is enhanced due to shock propagation, even if only slightly (e.g. Silk & Norman 2009; Ishibashi & Fabian 2012). Given the simulations in Chapters 2 and 3, it is not possible to discuss positive feedback triggering star formation. Specifically, in these simulations, it is not possible to determine if the increased star formation is a result of AGN feedback or from the merger itself. Thus, in Chapter 4, we study the impact of positive feedback directly using the Eulerian grid code ZEUS-3D. We set up a Milky Way-size system and include AGN feedback as a luminous source that pushes the gas out of the system; star formation is triggered in the shocks created by the luminous source. The goal here is to track the stars and stellar orbits. While this is a simple analytical task for an ffidealised system, we perform the study in a more realistic scenario, where the central source has a duty cycle, there are several dwarf satellite galaxies to perturb the gas and stars, and there is an external potential (an M31 analogue) to perturb the entire system. Thus, with these realistic perturbations in place, we will be able to properly study the stellar trajectories.

Chapter 2

A Comparative Study of AGN Feedback Algorithms

This chapter is published as Wurster & Thacker (2013a). Here, we present data for Model ONB until 1.25 Gyr, as opposed to 1.1 Gyr in the paper; this does not change our conclusions.

Abstract

Modelling AGN feedback in numerical simulations is both technically and theoretically challenging, with numerous approaches having been published in the literature. We present a study of five distinct approaches to modelling AGN feedback within gravitohydrodynamic simulations of major mergers of Milky Way-sized galaxies. To constrain differences to only be between AGN feedback models, all simulations start from the same initial conditions and use the same star formation algorithm. Most AGN feedback algorithms have five key aspects: the black hole accretion rate, energy feedback rate and method, particle accretion algorithm, black hole advection algorithm and black hole merger algorithm. All models follow different accretion histories, and in some cases, accretion rates differ by up to three orders of magnitude at any given time. We consider models with either thermal or kinetic feedback, with the associated energy deposited locally around the black hole. Each feedback algorithm modifies the region around the black hole to different extents, yielding gas densities and temperatures within $r \sim 200$ pc that differ by up to six orders of magnitude at any given time. The particle accretion algorithms usually maintain good agreement between the total mass accreted by $\dot{M}\mathrm{d}t$ and the total mass of gas particles removed from the simulation, although not all algorithms guarantee this to be true. The black hole advection algorithms dampen inappropriate dragging of the black holes by two-body interactions. Advecting the black hole a limited distance based upon local mass distributions has many desirable properties, such as avoiding large artificial jumps and allowing the possibility of the black hole remaining in a gas void. Lastly, two black holes instantly merge when given criteria are met, and we find a range of merger times for different criteria. This is important since the AGN feedback rate changes across the merger in a way that is dependent on the specific accretion algorithm used. Using the $M_{\rm BH}$–σ relation as a diagnostic of the remnants yields three models that lie within the one-sigma scatter of the observed relation and two that fall below the expected relation. The wide variation in accretion behaviours of the models reinforces the fact that there remains much to be learnt about the evolution of galactic nuclei.

Key words: black hole physics – galaxies: interactions – galaxies: active – methods: numerical

2.1 Introduction

In the hierarchical model of galaxy formation, the largest galaxies are assembled last. Naively, we would expect the highest star formation rates (SFRs) and the activity from Active Galactic Nuclei (AGNs) to occur in these most massive galaxies. However, observational evidence contradicts this, showing that in massive galaxies, the peak SFRs and peak AGN activity occurred at redshifts 1–2 (e.g. Shaver et al. 1996; Madau et al. 1996), and not today. This reduction in activity from $z \sim 2$ to today was termed 'downsizing' by Cowie et al. (1996). One favoured explanation of downsizing is that during mergers, gas from the merger fuels both star formation and AGN activity (e.g. Sanders et al. 1988; Scannapieco et al. 2005). The feedback from the increased AGN activity then blows away all the gas preventing further accretion and quenching star formation, leading to a red and dead galaxy (e.g. Springel et al. 2005b).

The observational motivation for this picture is the evidence that a supermassive black hole resides at the centre of all galaxies with stellar spheroids (e.g. Kormendy & Richstone 1995; Ferrarese & Merritt 2000), and that they did not evolve independently of one another. The two strongest correlations are the relationship between the black hole mass and the stellar velocity dispersion ($M_{\rm BH}$–σ; e.g. Silk & Rees 1998; Ferrarese & Merritt 2000; Gebhardt et al. 2000; Tremaine et al. 2002; King 2003; Gültekin et al. 2009), and the black hole mass and the bulge mass ($M_{\rm BH}$–$M_{\rm b}$; Magorrian et al. 1998; McLure & Dunlop 2002; Marconi & Hunt 2003). A likely implication of these relations is that the AGN feedback is self-regulated: Outflows from the black hole following a strong accretion event interact with the surrounding gas, inhibiting further accretion events, and hence limiting black hole growth (e.g. Silk & Rees 1998; Fabian 1999b; Scannapieco & Oh 2004). Large X-ray cavities in the hot gas halo around AGN (e.g. Boehringer et al. 1993; McNamara et al. 2000) suggest that some outflow events can be quite powerful; these cavities are likely formed by jets from the AGN (e.g. McNamara & Nulsen 2007). Although there is significant evidence supporting the AGN scenario for explaining downsizing, it is not yet understood precisely how feedback energy couples to the surrounding gas; possible mechanisms are line radiation pressure (e.g. Castor et al. 1975; Proga et al. 2000), radiation pressure on dust grains (e.g. Murray et al. 2005), Compton heating of infalling gas (e.g. Ciotti & Ostriker 2001) and photo-ionisation pressure (Buff & McCray 1974; Cowie et al. 1978).

AGN feedback has been implemented in many numerical simulations (e.g. Kawata & Gibson 2005; Di Matteo et al. 2005; Springel et al. 2005b; Thacker et al. 2006; Sijacki et al. 2007; Okamoto et al. 2008; Kurosawa et al. 2009; Booth & Schaye 2009; Debuhr et al. 2011; Dubois et al. 2012), but both theoretical understanding and numerical implementations are fraught with difficulties. First, the spatial scales involved in studying AGN and the related feedback span many orders of magnitude, and information on all of these scales is needed simultaneously to fully and properly understand AGN and their feedback. On the smallest scale is the Schwarzschild radius,

$$r_{\mathrm{S}} = \frac{2GM_{\mathrm{BH}}}{c^2}, \tag{2.1}$$

where M_{BH} is the mass of the black hole, G is Newton's gravitational constant and c is the speed of light; typical values range $r_{\mathrm{S}} \approx 3 \times 10^{6-8}$ km. On the next larger scale is the Bondi radius (Bondi 1952),

$$r_{\mathrm{Bondi}} = \frac{GM_{\mathrm{BH}}}{c_{\infty}^2}, \tag{2.2}$$

where c_{∞} is the sound speed of gas at infinity. The value of the Bondi radius is dependent on the black hole's environment and can range from a few parsecs to tens of parsecs (e.g. Kurosawa et al. 2009; Springel et al. 2005b). This radius, also known as the capture radius, divides a gas flow in to two regimes (Frank et al. 2002). Consider a spherically symmetric gas cloud centred on a black hole, where the gas is initially at rest at infinity. The only forces acting on the gas are the gravitational force from the central black hole and the pressure forces within the gas (assuming we neglect the self-gravity of the gas). Well-beyond the Bondi radius, the gas is comparatively uninfluenced by the black hole and flows subsonically. As the black hole is approached, the gas density begins to increase, and the gas flow inward eventually reaches a sonic point. At the sonic point, the gas plunges at a free-fall rate in to the black hole (Hobbs et al. 2012).

The last spatial scale of interest is that of an entire galaxy (or a galaxy cluster), which can span dozens of kiloparsecs (or a few megaparsecs). When considering all of these scales, comparing the size of a black hole to its massive host galaxy is similar to comparing a coin to the Earth (Fabian 2012).

To complement the range of spatial scales, studying AGN feedback also requires a large range of temporal scales. At short intervals, observations show the luminosity of the central engines of AGN varies on time-scales ranging from days to years (e.g. Webb & Malkan 2000 and references therein; Sarajedini et al. 2011); moreover, there are short term differences in variability amongst the different classes of AGN, making the variable luminosity challenging to understand and constrain. Large scale observations have detected large (~10 kpc radius) X-ray cavities in the gas around some AGN. To inflate these cavities, an outburst of 10^{58}–10^{61} ergs of energy would be required (Bîrzan et al. 2004; McNamara et al. 2005) every few $\sim 10^8$ yr, or a time-averaged output of $\sim 10^{43}$–10^{45} ergs s^{-1} (Churazov et al. 2002). Thus, the next inherent difficulty in modelling AGN becomes obvious: AGN luminosity varies on time-scales as short as days, yet they are expected to produce major outbursts every few $\sim 10^8$ yr.

Numerically, we can draw a few parallels between AGN feedback and stellar feedback. Both have been added to numerical simulations to improve realism, and the result was better agreement with observations. However, star formation and stellar feedback is a conceptually simpler problem than AGN feedback. In numerical simulations, if a packet of gas meets a given set of criteria, then stars are formed and feedback energy is returned; the star formation and feedback parameters can be reasonably well constrained using current observations, where there are detailed observations of outflows at many different stages of stellar evolution, such as T-Tauri stars (e.g. Cabrit et al. 1990; Hartigan et al. 1995), Wolf-Rayet stars (e.g. Crowther 2007), mass loss and stellar winds from evolved stars (e.g. Willson 2000) and supernovae (e.g. Reynolds 2008). AGN feedback is much harder to constrain since there are fewer candidates for detailed observation due to the peak of AGN activity being so far in the past. The nearest black hole candidate to study, Sagittarius A*, is currently in a quiescent phase; even during a recent flare to 4×10^{39} erg s^{-1} (Nobukawa et al. 2011), its luminosity remained below the typical AGN luminosity range of 10^{40}–10^{47} erg s^{-1} (Fabian 1999a). In addition to uncertainty in modelling AGN feedback, tremendous amounts of energy can be returned to the region around the back hole, creating steep gradients and presenting a challenge to numerical integration. Unlike numerical stellar feedback where there is difficulty in preventing unrealistically rapid cooling after the feedback event (e.g. Gerritsen & Icke 1997; Mori et al. 1997; Thacker

& Couchman 2000; Springel & Hernquist 2003), continual AGN feedback may create shocks or unrealistically disrupt the system.

When AGN feedback is included in numerical simulations, the approaches can vary widely, in both physics and numerical implementation. Also, the physics is often modelled using different numerical codes with different star formation algorithms and different initial conditions. Even starting from the same initial conditions, mass and spatial resolution, the different hydrodynamical approaches, gas cooling, star formation and stellar feedback algorithms of different numerical codes produce different results, as shown in the comparison by Scannapieco et al. (2012); this comparison did not include AGN feedback. Currently, a direct numerical comparison of the AGN feedback mechanisms does not appear to have been published nor can it be compiled from the assembled literature. Here, we run four of the algorithms found in the literature using the numerical code HYDRA. We also present a fifth simulation that is new to this study; this model is designed to take advantage of the 'best' features of the other models. All of our simulations start from the same initial conditions and use the same star formation algorithm; this approach is conservative, but well constrained. We explicitly state that the goal of this is to highlight the different behaviours of the different algorithms and not to critique the various approaches.

By using a pseudo-multiphase star formation model for all simulations, we unavoidably introduce some compromises in the AGN feedback models that rely upon a multiphase gas description; to compensate for this, we have introduced additional variables to represent hot and cold fractions of the gas. Although this star formation model is not precisely equivalent to those implemented in other simulations of AGN feedback, we consider using it a necessary compromise to ensure that the variations in our results are only from the AGN feedback algorithm.

The layout of this chapter is as follows. In Section 2.2 we discuss our simulations, focusing on how the initial conditions are constructed and the AGN feedback algorithms. In Section 2.3, we will discuss our results, focusing on the impact of the different AGN feedback algorithms. In Section 2.4, we discuss the final state of each simulation, and we conclude with a review in Section 2.5.

2.2 Numerical Simulations

To perform our simulations, we use the parallel version of Hydra (Couchman et al. 1995; Thacker & Couchman 2006), which uses an Adaptive Particle-Particle, Particle-Mesh algorithm (Couchman 1991) to calculate gravitational forces and the standard smooth particle hydrodynamics method (SPH; Gingold & Monaghan 1977; Lucy 1977) to calculate gas forces. It includes a star formation algorithm (see section 2.2.3), and has been modified to include black holes and AGN feedback (see section 2.2.4).

2.2.1 Galaxy models

To construct our model galaxy, we first use the GalactICs package (Kuijken & Dubinski 1995; Widrow & Dubinski 2005; Widrow et al. 2008) to create a Milky Way-sized galaxy that consists of a stellar bulge, stellar disc, and a dark matter halo; this is done through an iterative process to produce a self consistent system. The free parameters are chosen such that the component masses are similar to the component masses in Springel et al. (2005b), and are given in Table 2.1.

The stellar bulge density profile is given by

$$\tilde{\rho}_{\rm b}(r) = \rho_{\rm b}\left(\frac{r}{R_{\rm e}}\right)^{-p} {\rm e}^{-b(r/R_{\rm e})^{1/n}}, \tag{2.3}$$

which yields a Sérsic law for the projected density profile if $p = 1 - 0.6097/n + 0.05563/n^2$, where n is a free parameter. The constant $\rho_{\rm b}$ is defined using $\sigma_{\rm b} \equiv \left\{4\pi n b^{n(p-2)}\Gamma\left[n(2-p)\right] R_{\rm e}^2\rho_{\rm b}\right\}^{1/2}$, where $\sigma_{\rm b}^2$ is the depth of the gravitational potential

Component	Parameter	Value
Bulge	σ_{b}	292 km s^{-1}
	R_{e}	0.7 1kpc
	n	1.1
Disc	R_{d}	2.46 kpc
	z_{d}	0.49 kpc
	R_{trunc}	30 kpc
	z_{trunc}	1 kpc
	σ_{R0}	119 km s^{-1}
Dark Matter Halo	a_{h}	13.6 kpc
	r_{h}	275 kpc
	δr_{h}	25 kpc
	σ_{h}	330 km s^{-1}
	γ	0.81
metallicity	Z	0.05 $\mathrm{Z}_{\odot}$
mean molecular weight	μ	0.6

Table 2.1: The chosen parameters for our model galaxies. All parameters are defined in Section 2.2.1 of the text.

associated with the bulge and R_{e} is the radial scale parameter, which is a free parameter; the variable b is adjusted such that R_{e} encloses half the total projected light or mass.

The stellar disc has a truncated density profile that falls off approximately exponentially in R and follows sech^2 in z; the disc has radial and vertical scale heights R_{d} and z_{d} and truncation distances R_{trunc} and z_{trunc}. The radial velocity dispersion is given by $\sigma_{\mathrm{R}}^2(R) = \sigma_{\mathrm{R0}}^2 \mathrm{e}^{-R/R_\sigma}$, where σ_{R0} is the central velocity dispersion and $R_\sigma = R_{\mathrm{d}}$ for simplicity.

The dark matter halo profile follows a generalised NFW profile of

$$\tilde{\rho}_{\mathrm{h}} = \frac{2^{2-\gamma}\sigma_{\mathrm{h}}^2}{4\pi a_{\mathrm{h}}^2} \frac{1}{(r/a_{\mathrm{h}})^{\gamma}(1+r/a_{\mathrm{h}})^{3-\gamma}} C(r; r_{\mathrm{h}}, \delta r_{\mathrm{h}}), \tag{2.4}$$

where a_{h} is the halo scale length, r_{h} is the cutoff radius, γ is the central cusp strength and σ_{h} is a (line of sight) velocity scale that sets the mass of the halo. The truncation function, $C(r; r_{\mathrm{h}}, \delta r_{\mathrm{h}}) = \frac{1}{2}\mathrm{erfc}\left(\frac{r-r_{\mathrm{h}}}{\sqrt{2}\delta r_{\mathrm{h}}}\right)$, smoothly goes from one to zero at $r = r_{\mathrm{h}}$ over width δr_{h}.

We then modify this initial galaxy in three ways. First, we convert ten per cent of the total stellar mass into gas to create a gas disc; the gas disc is the same as the stellar disc except that it has been reflected in the $x = y$ plane (where the z-axis is the rotational axis of the disc) so that the star and gas particle are not coincidence. Although the gas scale height is initially larger than physically motivated, cooling allows the gas to collapse into a thin disc within a few 10 Myr; this produces a short transient evolution of the gas accompanied by a brief increase in the SFR. At resolutions higher than presented here, this vertical collapse produces a strong ring-shaped shock which propagates outwards. One method to prevent the shock is to relax the gas disc in a fixed potential and then implement the relaxed disc in the initial conditions; another solution is to reduce the initial scale height of the gas disc. Studies in Williamson & Thacker (2012) show that at our fiducial resolution the pressure wave dissipates comparatively quickly, and is largely insignificant at our lowest resolutions. Given also that we are interested in the relative differences between the feedback algorithms during the merger, which is clearly a much more dynamic event, we consider the above gas disc construction acceptable.

Second, we add a hot gas halo (hgh), which is chosen to follow the observationally motivated β-profile (e.g. Cavaliere & Fusco-Femiano 1976):

$$\rho_{\rm hgh}(r) = \rho_0 \left[1 + \left(\frac{r}{r_{\rm c}} \right)^2 \right]^{-\frac{3}{2}\beta}, \tag{2.5}$$

where ρ_0 is the central density, $r_{\rm c}$ is the core radius, and β is the outer slope parameter; we choose $r_{\rm c} = 1.75$ kpc and $\beta = 2/3$ as done in Moster et al. (2011). We set ρ_0 by choosing the mass of the hot gas halo within 40 kpc to be equal to two per cent of the total disc mass (Rasmussen et al. 2009); to conserve total halo mass generated by GalactICs, we reduce the mass of the dark matter halo by the total mass of the hot gas halo. By assuming isotropy and hydrostatic equilibrium, the temperature profile of the hot gas halo is given by (Kaufmann et al. 2007)

$$T_{\mathrm{hgh}}(r) = \frac{\mu m_{\mathrm{p}}}{k_{\mathrm{B}}} \frac{1}{\rho_{\mathrm{hgh}}(r)} \int_{r}^{\infty} \rho_{\mathrm{hgh}}(r) \frac{GM(r)}{r^2} \mathrm{d}r, \tag{2.6}$$

where μ is the mean molecular weight, m_{p} is the proton mass, k_{B} is the Boltzmann constants, and $M(r)$ is the total mass interior to r. The hot gas halo is given an initial angular momentum which scales with the circular velocity, $j_{\mathrm{hgh}}(R) \propto R v_{\mathrm{circ}}(R)$, where R is the distance from the spin axis of the galaxy (Moster et al. 2011).

The final modification to the galaxy is the addition of a black hole (sink) particle, which is placed at the centre of mass and given an internal mass of 10^5 $\mathrm{M}_{\odot}$. While this initial mass is more than ten times lower than expected from estimates of the mass of the Milky Ways central black hole ($M_{\mathrm{BH}} \sim (4.36 \pm 0.42) \times 10^6$ $\mathrm{M}_{\odot}$; Gillessen et al. 2009), it does match the initial black hole masses in Springel et al. (2005b) and Debuhr et al. (2011). Moreover, an initial mass lower than anticipated from the M_{BH}–σ relationship would be expected to grow quite quickly in a few Salpeter times because feedback at low masses is comparatively weak. At every step, we calculate a smoothing length for the black hole in order to calculate the gas properties around it, but the sink particle itself only experiences gravitational forces.

Each galaxy has a total mass of 9.60×10^{11} $\mathrm{M}_{\odot}$, 1 287 743 (168 351) particles for the fiducial (low) resolution simulations, and a Plummer softening length of $\epsilon_{\mathrm{Plummer}} = 120$ pc ($\epsilon_{\mathrm{Plummer}} = 300$ pc). The Plummer softening length is related to the S2 gravitational softening length, ϵ_{S2}, by $\epsilon_{\mathrm{Plummer}} = \epsilon_{\mathrm{S2}}/2.34$. See Table 2.2 for a breakdown of each galaxy. Lastly, we create a second, identical galaxy, and separate them by 70 kpc; we then place them on parabolic trajectories around one another, in close agreement with the trajectories from Springel et al. (2005b).

		Fiducial resolution		Low resolution	
	Total mass (10^{10} M$_\odot$)	Particle mass (10^5 M$_\odot$)	Number of particles	Particle mass (10^5 M$_\odot$)	Number of particles
Dark matter halo	89.92	11.75	765 000	89.92	100 000
Hot gas halo	0.60	0.36	165 343	2.77	21 619
Stellar bulge	1.34	2.37	56 649	18.10	7 407
Stellar disc	3.56	2.37	150 375	18.10	19 662
Gas disc	0.54	0.36	150 375	2.77	19 662
Black hole[a]	10^{-5}	1.00	1	1.00	1

Table 2.2: Component breakdown for each galaxy.

[a] Particle (dynamical) mass is 10^9 M$_\odot$ for Model DQM; internal mass of the black hole remains at 10^5 M$_\odot$.

2.2.2 Verification against other codes

Since many of the models in the literature are run using Gadget2 (Springel et al. 2001; Springel & Hernquist 2002), we ran the same adiabatic merger simulation with both Hydra and the publicly available version of Gadget2 to test the differences. Neither simulation included stellar or AGN feedback, thus we were essentially comparing the gravity and SPH solvers. The galaxies in each simulation followed the same trajectory, and synchronisation – as measured by the time to reach second periapsis – was within 0.2 per cent. Thus we can be confident that our results will be comparable with those currently found in the literature.

2.2.3 Star formation

The star formation algorithm implemented in Hydra is described and tested in Thacker & Couchman (2000); we will provide a brief summary here. This algorithm follows an approach to star formation that has now been studied extensively in the literature. Star formation is allowed to proceed in regions where:

1. The gas exceeds the density limit of $n_{\mathrm{H}} \sim 0.01$ cm^{-3},
2. The flow is convergent, $\nabla \cdot \mathbf{v} < 0$,
3. The gas temperature is less than 3×10^4 K,
4. The gas is partially self-gravitating: $\rho_{\mathrm{g}} > 0.4\rho_{\mathrm{DM}}$.

When a gas particle meets the above criteria, the Schmidt Law (e.g. Katz 1992; Kennicutt 1998) is used to determine the amount of gas that is 'converted' in to stars. When the cumulative converted mass of a gas particle reaches half of the particle's original mass, m_{g}, a star particle is spawned with mass $m_{\mathrm{g}}/2$ and the gas particle's mass is reduced to $m_{\mathrm{g}}/2$; when 80 per cent of the remaining gas mass is converted into stars, a second star particle is spawned with mass $m_{\mathrm{g}}/2$ and the gas particle is removed from the simulation. For computational efficiency, Hydra uses a Lagrangian form of the Schmidt Law, based upon the local density of the SPH particle,

$$\frac{\mathrm{d}M_*}{\mathrm{d}t} = C_{\mathrm{sfr}}\rho_{\mathrm{g}}^{1/2}M_{\mathrm{g}}, \tag{2.7}$$

where C_{sfr} is the star formation rate normalisation, ρ_{g} is the SPH density of the gas particle, and M_{g} is the mass of the gas in the particle that has not been converted in to stars. All other calculations in the code (e.g. density, smoothing length, etc...) assume that the entire particle is a gas particle of mass m_{g} or $m_{\mathrm{g}}/2$.

Whenever a star particle is created, feedback energy is immediately returned to the surrounding environment. Although our fiducial resolution models takes $\mathcal{O}(10^2)$ steps to evolve through the lifetime of an 8 $\mathrm{M}_{\odot}$ star, the lack of delay between star particle formation and feedback energy release is not a significant issue because at the resolution considered here we are still averaging over a number of giant molecular clouds per particle and the evolution is representative at best. For every 100 $\mathrm{M}_{\odot}$ of stars formed, there is one supernova event, which contributes 10^{51} ergs to the interstellar medium (Sommer-Larsen et al. 1999), and feeds back $5 \times 10^{15}e^*$ ergs g^{-1} of gas converted in stars, where e^* is a dimensionless parameter; we set $e^* = 0.4$ to match Navarro & White (1993).

As first showed by Katz (1992), feedback energy returned to the interstellar medium (ISM) is radiated away quickly in high density regions. A reduced density is used in the cooling algorithm to prevent this immediate loss, thus allowing the feedback to influence the surrounding environment; the reduced density decays back to its local SPH value with a half-life of $t_{1/2} = 5$ Myr. The parameters e^* and $t_{1/2}$ are chosen to match those set in Thacker & Couchman (2000) to reproduce the Milky Way's star formation rate in a simulation of an isolated Milky Way-like galaxy.

This star formation algorithm is conceptually similar to the methods used in Brook et al. (2004), Stinson et al. (2006) and Governato et al. (2007), however, it varies from the sub-resolution multiphase models found in Springel & Hernquist (2003), Springel et al. (2005b), Booth & Schaye (2009) and Hopkins et al. (2009). In multiphase models, the subgrid physics is derived from a model of cold clouds (where stars form) embedded in a hot, pressure-confining phase. Above a given density threshold, the gas is thermally unstable to the onset of this two-phase medium. The mass fraction in each phase is determined by star formation and feedback, evaporation of the cold clouds through thermal conduction, and the growth of clouds through radiative cooling. The star formation rate is then calculated based upon a prescribed law and an equation of state. An important difference between this method and our method is that in the multiphase method, gas can freely flow between phases, whereas in Hydra, once gas is 'converted' to stars, it is carried forward and not allowed to cool until the specified cooling period is reached (i.e. the 'flow' between 'phases' is in one direction only).

2.2.4 Black hole and AGN feedback algorithms

AGN feedback algorithms essentially have five key components:

1. The accretion rate on to the black hole,
2. The SPH particle accretion algorithm,
3. The energy feedback algorithm,
4. The black hole advection algorithm, and
5. The black hole merger algorithm.

Each component will briefly be discussed below, then we will discuss the models in section 2.2.5.

2.2.4.1 Accretion rates

A commonly used accretion rate is the Bondi accretion rate (Bondi 1952),

$$\dot{M}_{\rm Bondi} = \frac{2\pi G^2 M_{\rm BH}^2 \rho_\infty}{(c_\infty^2 + v^2)^{3/2}}, \tag{2.8}$$

where ρ_∞ and c_∞ are the gas density and sound speed at infinity, v is the relative velocity between the gas at infinity and the black hole, and $M_{\rm BH}$ is the mass of the black hole. In hydrostatic equilibrium, the maximum physical accretion rate is the Eddington accretion rate,

$$\dot{M}_{\rm Edd} \equiv \frac{4\pi G M_{\rm BH} m_{\rm p}}{\epsilon_{\rm r}\sigma_{\rm T} c}, \tag{2.9}$$

where $m_{\rm p}$ is the proton mass, $\sigma_{\rm T}$ is the Thomson cross section, and $\epsilon_{\rm r}$ is the radiative efficiency (i.e. the mass-to-energy conversion efficiency); we set $\epsilon_{\rm r} = 0.1$ (Shakura & Sunyaev 1973). Typically, numerical simulations limit their accretion rate to the Eddington accretion rate, and we follow this convention. If the assumption of spherical symmetry is ignored, super-Eddington accretion rates can be achieved, which are associated with collimated outflows. In small scale outflow simulations by Kurosawa et al. (2009), they find steady-state results where super-Eddington accretion occurs in the equatorial plane.

2.2.4.2 Black hole mass growth and particle accretion

In all cases, the 'internal' and 'dynamical' masses of the black hole is tracked. The internal mass, $M_{\rm BH}$, is the mass of the black hole, which is increased by $\dot{M}_{\rm BH}{\rm d}t$ at every iteration; this mass is used in all calculations concerning AGN feedback. The dynamical mass, $m_{\rm BH}$, is the mass of the sink particle, which is increased by the mass of a gas particle whenever one is accreted. The particle accretion algorithm should ideally maintain $M_{\rm BH} \sim m_{\rm BH}$ and directly address the loss of gas near the black hole due to accretion. In Model DQM (see §2.2.5.4), the dynamical mass is fixed for all time (except during a black hole merger), so the included particle accretion algorithm only simulates the loss of gas. When a particle is accreted on to the black hole, its mass and momentum are added to the black hole particle (except for Model DQM), and the gas particle is removed from all further computations; this accretion does not affect the internal mass of the black hole. There are three categories of particle accretion algorithms:

1. *Stochastic-Unconditional*: At all times, all nearby particles are tested to see if they will stochastically accrete.
2. *Stochastic-Conditional*: All nearby particles are tested to see if they stochastically accrete if given criteria of the $m_{\rm BH}$–$M_{\rm BH}$ relationship are satisfied.
3. *Continual-Conditional*: Nearby particles are continually accreted while given criteria of the $m_{\rm BH}$–$M_{\rm BH}$ relationship are satisfied.

2.2.4.3 Feedback

In all simulations, a portion of the accreted mass is returned as feedback energy, $E = \epsilon \dot{M}_{\rm BH} c^2 {\rm d}t$, where ϵ is a dimensionless efficiency parameter; the efficiency is typically set to the radiative efficiency, ϵ_r, or lower. This energy is returned to the nearby particles (except Model ONB; see §2.2.5.3) either by increasing their internal energy (thermal feedback models), or by increasing their momentum via $p = E/c$ (kinetic feedback models).

2.2.4.4 Black hole advection

Properly tracking the black hole particle is critical since accretion rates (hence feedback rates) depend on the local gas properties around the black hole. Ideally, a single black hole should stay at the bottom of the local potential well, but if gas or star particles have similar masses to the black hole particle, the black hole can be inappropriately dragged away from the bottom of the potential well by two-body forces. This will lead to the inaccurate calculation of gas properties, thus avoiding such behaviour is clearly desirable. Although other particles (i.e. star and gas particles) will also be dragged by two-body interactions, the distribution is more important than the position of any particular particle. Thus any undesirable effects of the two-body interactions will be averaged out when considering all of the nearby star or gas particles.

In all of the simulations, a black hole advection algorithm is implemented to minimise the inappropriate movement (i.e. to keep the black hole within a reasonable distance from the bottom of the potential well). Except in Model DQM (see §2.2.5.4), the black hole's position is artificially updated after the completion of the gravitational solver algorithm but before the calculation of the accretion rate.

2.2.4.5 Black hole mergers

The process by which black holes merge is still a matter of active research (e.g. Escala et al. 2004; Berentzen et al. 2009; Khan et al. 2011; Bode et al. 2012). Given that our simulations result in a combined halo and stellar system producing drag, it is reasonable to expect that the black holes would merge. Since any merger occurs on sub-resolution scales, models include a merger prescription to instantly merge the black holes when given criteria are met. When two black holes merge, one sink particle is removed and the remaining sink particle has the combined mass (both internal and dynamical) and momentum, and is repositioned to the centre of mass of the two progenitors.

Little is known about the exact merger process, and specifically its energetics. It is possible that, in a gas-rich environment as expected from these simulations, gravitational waves will be emitted during the merger. If the initial black hole system is not symmetric, then the resulting asyemmetric gravitational waves may cause a recoil in wich the black hole is kicked away from the bottom of the potential well (e.g. Blecha et al. 2011), ultimately affecting its accretion rate. The direct effect on the nearby gas of the gravitational waves and other phenomena caused by the merger is still a matter of active research, and is not included in these simulations.

2.2.4.6 Black hole's local environment

Around every black hole we define a radius of influence, r_{inf}. All gas particles within r_{inf} contribute to the accretion properties at the black hole, are eligible to receive feedback energy (except for Model ONB), and are eligible to be accreted on to the black hole particle. Gas particles outside of r_{inf} have no explicit impact on the black hole or the AGN feedback algorithms. We set $r_{\mathrm{inf}} = \max(2h_{\mathrm{BH}}, 2h_{\mathrm{min}})$, where a sphere with radius $2h_{\mathrm{BH}}$ around the black hole particle includes 60 gas particles, and h_{min} is the smallest resolved smoothing length in the SPH solver.

2.2.5 The Models

In sections 2.2.5.1 to 2.2.5.5, we describe the particular AGN feedback algorithms of our five primary models; a summary of each model can be found in Table 2.3. We ran four additional models, each of which is a slight variant of a primary model; these are described in section 2.2.5.6. Every model was run at both fiducial and low resolutions. For nomenclature, we name these models after the initials of the authors of the paper it originally appeared in. The variant models have the same name as their parent model, followed by a lower case character to signify the difference. A model name followed by a subscript ‘l’ explicitly refers to the low resolution version of the model; no subscript will refer to either the fiducial resolution version or to both versions, depending on context.

2.2.5.1 Model SDH

This model is based upon that found in Springel et al. (2005b) (herein SDH05). The accretion rate is given by a modified Bondi accretion rate,

$$\dot{M}_{\mathrm{B}} = \frac{4\pi\alpha G^2 M_{\mathrm{BH}}^2 \rho}{\left(c_{\mathrm{s}}^2 + v_{\mathrm{rel}}^2\right)^{3/2}}, \tag{2.10}$$

where c_{s} and ρ are the local sound speed and density of the gas, and v_{rel} is the relative velocity of the black hole to the nearby gas. The free parameter, α, is included to relate the numerically calculated gas density and sound speed to what one would expect in reality. Booth & Schaye (2009) argue that modest resolutions underestimate the density and overestimate the sound speed by orders of magnitude, thus justifying

	Model SDH	Model BS	Model ONB	Model DQM	Model WT
Accretion Rate	$\dot{M}_{\mathrm{B}}(\alpha = 100)$	$\dot{M}_{\mathrm{B}}(\alpha \equiv \alpha(n_{\mathrm{H}}))$	$\dot{M}_{\mathrm{drag}}$	$\dot{M}_{\mathrm{visc}}$	$\dot{M}_{\mathrm{B}}(\alpha = 100)$
Energy Feedback FB Distribution	$\dot{E} = 0.005\dot{M}_{BH}c^2$ kernel-weighted	$\dot{E} = 0.015\dot{M}_{\mathrm{BH}}c^2$ random packets of E_{crit}	$\dot{E} = 0.1L_{\mathrm{jet}}$ to 40 low-ρ particles	$\dot{p} = 10L/c$ isotropic	$\dot{E} = 0.005\dot{M}_{\mathrm{BH}}c^2$ isotropic
Particle Accretion	stochastic-unconditional	stochastic-conditional	continual-conditional	continual-conditional	continual-conditional
BH Advection	gas particle with $v_{\mathrm{rel}} < 0.25c_{\mathrm{s}}$ and smallest U	gas particle with with $v_{\mathrm{rel}} < 0.25c_{\mathrm{s}}$ and smallest U	Δl_{ONB} along stellar gradients	tracer mass	Δl_{WT} towards centre of mass
BH Merger	$d < h_{\mathrm{BH}}$ & $v_{\mathrm{rel}} < c_{\mathrm{s}}$	$d < h_{\mathrm{BH}}$ & $v_{\mathrm{rel}} < v_{circ}$	$d < \epsilon_{S2}$ & gravitationally bound	$d < h_{\mathrm{BH}}$	$d < h_{\mathrm{BH}}$ & $v_{\mathrm{rel}} < c_{\mathrm{s}}$

Table 2.3: A summary of our five primary models describing each key algorithm. More detail and definitions of the variables are given in subsections 2.2.5.1 to 2.2.5.5. Numerically, $h_{\mathrm{BH}} = \max(h_{\mathrm{BH}}, h_{\mathrm{min}})$, where a sphere with radius $2h_{\mathrm{BH}}$ around the black hole particle includes 60 gas particles, and h_{min} is the smallest resolved smoothing length in the SPH solver.

large values of α. As in SDH05, we set $\alpha = 100$. Finally, the accretion rate is Eddington-limited, thus $\dot{M}_{\rm BH} = \min\left(\dot{M}_{\rm B}, \dot{M}_{\rm Edd}\right)$.

A given fraction of the accreted mass is allowed to return to the surrounding environment as feedback energy. The rate of return is

$$\dot{E}_{\rm feed} = \epsilon_{\rm f}\epsilon_{\rm r}\dot{M}_{\rm BH}c^2, \tag{2.11}$$

where $\epsilon_{\rm r} = 0.1$ is the radiative efficiency, and $\epsilon_{\rm f} = 0.05$ is the fraction of energy that can couple with the gas. This energy is distributed amongst all the particles within $r_{\rm inf}$ with weights following the smoothing kernel.

is returned kernel-weighted to the gas particles within $r_{\rm inf}$.

To track the growth of the black hole particles, a stochastic-unconditional particle accretion algorithm is used. At every iteration, a probability, p_i, is calculated for each particle, i, within $r_{\rm inf}$. This probability is then compared to a random number, x_i, and if $p_i > x_i$, then the particle is accreted. In this algorithm, the probability is given by

$$p_i = w_i\dot{M}_{\rm BH}\rho^{-1}{\rm d}t, \tag{2.12}$$

where w_i is the kernel weight of gas particle i relative to the black hole, and x_i is uniformly distributed on the the interval (0,1).

To minimize inappropriate motions of the black hole particles, at every iteration the black hole is relocated to the nearby gas particle with the minimum potential energy provided that $v_{\rm rel} < 0.25c_{\rm s}$. If no gas particle meeting the velocity criteria exists within $r_{\rm inf}$, then the black hole is not advected. Once $m_{\rm BH} > 10m_{\rm g}$, the black hole advection is turned off and its movement is handled only by the gravitational solver.

Lastly, two black holes merge when they come within each other's smoothing lengths and have a relative velocity less than the local sound speed; SDH05 argue that the local sound speed represents a simple measure of the characteristic velocity scale of the galaxies, and hence provides a reasonable velocity scale at which the black holes are able to merge.

2.2.5.2 Model BS

This model is based upon that found in Booth & Schaye (2009) (herein BS09); this model has many similarities to Model SDH, but was originally implemented in a cosmological simulation. We caution that implementing their model in a higher-resolution simulation could lead to unwanted behaviours as a number of the model parameters were chosen for their specific resolution. This model uses the (modified) Bondi accretion rate given in (2.10). If the resolution is sufficient, BS09 argue that the justifications for $\alpha = 100$ given in section 2.2.5.1 break down in low-density regions. Thus, this model sets α to be a function of the local hydrogen density, $n_{\rm H}$:

$$\alpha = \begin{cases} 1 & \text{if } n_{\rm H} < n_{\rm H}^* \\ \left(\frac{n_{\rm H}}{n_{\rm H}^*}\right)^\beta & \text{otherwise} \end{cases}, \tag{2.13}$$

where $n_{\rm H}^*$ is the critical value required for the formation of a cold interstellar gas phase, and β is a free parameter; as in BS09, we set $n_{\rm H}^* = 0.1$ cm^{-3} and $\beta = 1$. Finally, the accretion rate is Eddington-limited, thus $\dot{M}_{\rm BH} = \min\left(\dot{M}_{\rm B}, \dot{M}_{\rm Edd}\right)$.

The rate of feedback is also given by (2.11), with $\epsilon_{\rm r} = 0.1$ and $\epsilon_{\rm f} = 0.15$, which is three times more efficient than Model SDH. The feedback energy is allowed to accumulate until $E > E_{\rm crit}$, at which point a random gas particle within $r_{\rm inf}$ receives $E_{\rm crit}$ energy; this is repeated until the accumulated energy drops below $E_{\rm crit}$. The critical energy is defined as

$$E_{\rm crit} = \frac{m_{\rm g} k_{\rm B} \Delta T}{(\gamma - 1)\, \mu m_{\rm H}}, \tag{2.14}$$

where $m_{\rm g}$ is the (initial) mass of a gas particle and ΔT is the temperature increase a particle experiences with every feedback event. Due to the higher resolution in our model ($m_{\rm gas,\ fiducial} = 3.6 \times 10^4$ M$_\odot$ compared to 8.64×10^7 M$_\odot$ h^{-1} in BS09; $\epsilon_{\rm fiducial} = 120$ pc compared to 2 kpc h^{-1} after $z = 2.91$ in BS09), we set $\Delta T = 5 \times 10^6$

K as opposed to $\Delta T = 10^8$ K used in BS09. Using the value in BS09 produces very large temperature gradients in the SPH solver that are difficult to integrate accurately.

Gas particles are accreted by a stochastic-conditional particle accretion algorithm. If $M_{\rm BH} < m_{\rm BH}$, then no particles will be accreted. Otherwise, every nearby particle, i, is given a probability,

$$p_i = w_i \left(M_{\rm BH} - m_{\rm BH}\right) \rho^{-1} \tag{2.15}$$

and, as in Model SDH, particle i is accreted if $p_i > x_i$.

The black hole advection is the same as in Model SDH. Lastly, two black holes merge when they come within each other's smoothing lengths and have a relative velocity less than the circular velocity at the radius of the most massive black hole's smoothing length. BS09 explicitly state that this merging criteria differs from SDH05 since the feedback returned may temporarily increase the local sound speed, and thus may not be a representative velocity scale.

2.2.5.3 Model ONB

This model is based upon the model found in Okamoto et al. (2008) (herein ONB08), which was originally implemented in a simulation with cosmological initial conditions. We also note that this model is distinctly different from our other models in that it is specifically designed to reproduce the radio mode of feedback. In this model, it is assumed that radiation from stars (e.g. through starbursts or winds) interacts with the rotating, clumpy ISM. This radiation irradiates one layer of gas at a time, extracting angular momentum from it. This permits an inflow of gas towards the galactic centre, and ultimately on to the black hole itself (Umemura et al. 1997; Umemura 2001; Kawakatu & Umemura 2002). Thus, an accretion rate of gas on to the black hole can be calculated by considering the stellar clouds in the region of star formation (RSF) near the black hole. Using these assumptions, ONB08 calculate the drag accretion to be

$$\dot{M}_{\rm drag} = \epsilon_{\rm drag} \frac{L_{\rm RSF}}{c^2} \left(1 - {\rm e}^{-\tau_{\rm RSF}}\right), \tag{2.16}$$

where $\epsilon_{\rm drag} = 1$ is the drag efficiency, $L_{\rm RSF}$ is the total bolometric luminosity of all the stars in the RSF, and $\tau_{\rm RSF}$ is the total optical depth of the RSF. The total luminosity is calculated by summing the age-dependent bolometric luminosities, which are obtained from a lookup table generated by PEGASE2 (Fioc & Rocca-Volmerange 1997). Next, the total optical depth of a gas cloud is given by $\tau_{\rm c} = \chi_{\rm d}\rho_{\rm c}r_{\rm c} \simeq \chi_{\rm d}m_{\rm c}/r_{\rm c}^2$ where $\rho_{\rm c}$, $m_{\rm c}$ and $r_{\rm c}$ are the density, mass and radius of the cloud, respectively. Assuming that all the clouds are identical and randomly distributed over the region of star formation, the total optical depth can be approximated by

$$\tau_{\rm RSF} = \frac{3\chi_{\rm d}}{4\pi} \frac{M_{\rm c}}{R_{\rm RSF}^2}, \tag{2.17}$$

where $\chi_{\rm d} = 50$ cm^2 g^{-1} is the mass extinction coefficient, $M_{\rm c}$ is the total mass of the clouds in the RSF, and $R_{\rm RSF}$ is the radius of the RSF; since HYDRA does not explicitly track a multiphase gas, we set $M_{\rm c}$ to be half of the total gas mass within the RSF. We initialise $R_{\rm RSF} = \max\left(R_{40}, 2h_{\rm min}\right)$, where a sphere with radius R_{40} centred on the black hole contains 40 gas particles. Then, we increase the sphere's radius by increments of $\Delta r = 0.01h_{\rm min}$, and pick the radius that maximises $\dot{M}_{\rm drag}$. Since there is no direct relationship between the number of star particles (controlling $L_{\rm RSF}$) and gas particles (controlling $\tau_{\rm RSF}$ through $M_{\rm c}$) within a given radius, a maximum accretion rate will ultimately be reached. Lastly, if the gas density within the sphere is less than $\rho_{\rm thresh} = 5 \times 10^{-25}$ g cm^{-3}, the accretion rate is set to zero.

In this model, it is explicitly assumed that the feedback heats the halo gas through the production of jets. The jet mechanism used here is that of Meier (2001), and generates power from the rotational energy of the accretion flow and from the black hole itself. The accretion flow is divided into two regimes: standard thin discs

(SD; optically thick, geometrically thin, radiatively efficient) and radiatively inefficient accretion flows (RIAF; optically thin, geometrically thick). Using the parameters in ONB08, the respective accretion-dependent luminosities are

$$
\begin{aligned}
L_{\rm jet}^{\rm SD} &\approx 8.1 \times 10^{-5} \dot{M}_{\rm BH} c^2 && \text{if } \dot{m} > \dot{m}_{\rm crit} && (2.18)\\
L_{\rm jet}^{\rm RIAF} &\approx 2.6 \times 10^{-1} \dot{M}_{\rm BH} c^2 && \text{if } \dot{m} \leq \dot{m}_{\rm crit}, && (2.19)
\end{aligned}
$$

where $\dot{m} \equiv \dot{M}_{\rm BH}/\dot{M}_{\rm Edd}$ and $\dot{m}_{\rm crit} \approx \alpha^2$ is the critical accretion rate that sets the division between the SD and RIAF regimes (e.g. Narayan et al. 1998). As in ONB08, we set $\alpha_{\rm SD} = \alpha_{\rm RIAF} \equiv \alpha = 0.1$, where $\alpha_{\rm SD}$ and $\alpha_{\rm RIAF}$ are the viscosity parameters for SD and RIAF's, respectively. The feedback rate is then given by $\dot{E}_{\rm feed} = \epsilon_{\rm r} L_{\rm jet}$, and the energy is distributed equally to the 40 nearest diffuse gas particles with $\rho < 0.1\rho_{\rm thresh}$.

To accrete particles, this model uses a continual-conditional particle accretion algorithm. When the internal black hole mass exceeds its dynamical mass, nearby gas particles are given a weighted probability for accretion,

$$p_i = \frac{M_{\rm BH} - m_{\rm BH}}{m_i N_{\rm RSF}}, \tag{2.20}$$

where $N_{\rm RSF}$ is the number of gas particles within the region of star formation, and m_i is the mass of the i'th gas particle. Particles are then stochastically accreted based upon their weight until the dynamical mass exceeds the internal mass.

To track the black hole, at every iteration, the local stellar density fields are computed and the black hole is moved along the steepest gradient by an amount

$$\Delta l_{\rm ONB} = \min(0.01\epsilon_{\rm S2}, 0.03\,|\boldsymbol{v}|\,{\rm d}t), \tag{2.21}$$

where $\epsilon_{\rm S2}$ is the gravitational softening length, $|\boldsymbol{v}|$ is the velocity of the black hole, and dt is the time-step; these coefficients are the same as in ONB08 and were determined empirically.

Lastly, two black holes are assumed to merge when they are within a softening length of one another and are gravitationally bound.

2.2.5.4 Model DQM

This model is based upon that found in Debuhr et al. (2011) (herein DQM11), and models accretion through the transportation of angular momentum, which is based upon multi-scale SPH simulations by Hopkins & Quataert (2010). The accretion rate is

$$\dot{M}_{\rm visc} = 3\pi\delta\Sigma\frac{c_{\rm s}^2}{\Omega}, \tag{2.22}$$

where δ is the dimensionless viscosity, Σ is the mean gas surface density, and $\Omega = \sqrt{GM/r_{\rm inf}^3}$ is the rotational angular velocity of the gas. DQM11 treat δ as a free parameter, and it characterises both the efficiency of angular momentum transport and the fraction of gas that is being converted into stars versus being accreted on to the black hole; as in DQM11, we set $\delta = 0.05$.

The feedback is returned as momentum using

$$\dot{p} = \tau\frac{L}{c}, \tag{2.23}$$

where τ is the infrared optical depth, and $L = \min\left(\epsilon_{\rm r}\dot{M}_{\rm visc}c^2, L_{\rm Edd}\right)$ is the Eddington-limited luminosity. This momentum outflow is used to approximate radiation pressure produced by absorption and scattering of the AGN's feedback; specifically, the ultraviolet radiation (emitted from the black hole) will deposit $\dot{p}_{\rm UV} = L/c$ on to the gas, while infrared radiation (re-emitted from dust) will deposit $\dot{p}_{\rm IR} = \tau L/c$ on to the gas. Thus, the total $\dot{p}$ can be approximated as $(1+\tau)L/c \simeq \tau L/c$ for $\tau \gtrsim 1$, which is valid near the peak of AGN activity when the black hole gains most of its mass. As in DQM11, we set $\tau = 10$. Lastly, the momentum is returned radially, such that every gas particle within $r_{\rm inf}$ receives an equal acceleration.

In this model, there is no explicit artificial black hole advection algorithm. Instead, a tracer mass is used to represent the black hole particle; that is, the dynamical mass of the black hole is initialised to $m_{\rm BH} = 10^9$ M$_\odot$ and held constant throughout the simulation. The black hole particle is now only advected by the gravitational solver; since the tracer mass in the fiducial resolution simulations is $\sim 10^3 m_{\rm DM}$ and $\sim 3 \times 10^4 m_{\rm g}$, it will not undergo artificial dragging by the surrounding particles. By initialising $m_{\rm BH} = 10^9$ M$_\odot$ rather than $m_{\rm BH} = M_{\rm BH}$, the mass of each galaxy is increased by 0.01 per cent. This means that Model DQM has slightly (but unavoidably) different initial conditions than the other models. The internal mass of the black hole is still initialised to 10^5 M$_\odot$, and this mass allowed to grow as calculated by the accretion rate given in (2.22).

Since the dynamical mass of the black hole is fixed, a continual-conditional particle accretion algorithm removes 'accreted' gas particles, but does not add their properties to the dynamical mass. Here, a random particle within $r_{\rm inf}$ is removed whenever there is a mismatch between the amount of gas accreted via (2.22) and the total mass of removed gas particles.

Lastly, black holes merge when they come within $r_{\rm inf}$ of each other, regardless of velocity. In this model, black hole mergers are the only mechanism to increase the dynamical mass of the black hole.

2.2.5.5 Model WT: This study

This model uses the modified Bondi accretion rate given in (2.10) for both its simplicity and for its wide use in the literature (e.g. SDH05; Robertson et al. 2006b; Croft et al. 2009; Johansson et al. 2009); as in Model SDH, we set $\alpha = 100$. The energy feedback rate is given by (2.11), and the feedback energy is equally distributed amongst all the gas particles within $r_{\rm inf}$. This provides an isotropic heating to the core rather than preferentially heating (or super-heating) the particles very near the black hole, which may be transient.

The black hole advection algorithm is a modified version of that presented in Model ONB. First, the black hole is displaced towards the centre of mass of the sphere with radius $r_{\rm inf}$ centred on the black hole rather than along stellar gradients.

This method still gives preference to the stellar distribution, but also considers the dark matter and gas distributions. Second, the distance the black hole is displaced has been modified to

$$\Delta l_{\mathrm{WT}} = \min(0.10 h_{\mathrm{BH}}, 0.30\,|\boldsymbol{v}|\,\mathrm{d}t, d_{\mathrm{CM}}), \tag{2.24}$$

where d_{CM} is the distance from the black hole to the centre of mass. We choose to use the black hole smoothing length rather than the softening length since all of the properties near the black hole are calculated using $2h_{\mathrm{BH}}$ as the characteristic length. As in (2.21), our coefficients are empirically chosen so that non-negligible displacement would be possible. Specifically, for the first option, $h_{\mathrm{BH}} < \epsilon_{\mathrm{S2}}$, so its coefficient needs to be increased. For the second option, our resolution is higher than in ONB08, thus we will have a smaller $\mathrm{d}t$, and again we need a larger coefficient. We choose this method rather than potential-well method of Models SDH and BS for the following reasons: If the AGN feedback creates a gas void around the black hole, then either there will be no artificial displacement (allowing for the possibility of unnatural motion) or the black hole will be coupled to a gas particle on the edge of the void. In this method, as in Model ONB, the black hole only moves towards a particle rather than being coupled to it.

As in Models ONB and DQM, we include a continual-conditional particle accretion algorithm: When $M_{\mathrm{BH}} > m_{\mathrm{BH}} + m_{\mathrm{g}}/2$, we accrete the gas particle that is nearest to the black hole. The term $m_{\mathrm{g}}/2$ forces the dynamical and internal mass to oscillate around one another, and choosing the nearest particle is to remove stochastic events in the simulation and better facilitate reproducability.

The black hole merger algorithm is the same as given in Model SDH. We choose this algorithm since it had a distance and a velocity criteria, and its velocity requirement is less stringent than in Models BS and ONB. The merger algorithms in Models BS and ONB were created for cosmological models, whose resolution is lower than our fiducial resolution runs, thus we argue that our implementation of their merger prescriptions are more stringent than they intended.

2.2.5.6 Additional models

We have tested four additional models, each of which is a slight variation of one the above models. These models are identical to their parent models described above, except for the variation listed below.

- *Model BSw*: This uses the black hole advection algorithm of Model WT; early tests of Model BS showed very erratic black hole motion that could possibly compromise the results.
- *Model ONBc*: This uses a very conservative search algorithm to calculate $\dot{M}_{\rm drag}$ (i.e. we initialise $R_{\rm RSF} = R_{40}$ and increase the sphere's radius by increments of Δr such that each new sphere contains one additional gas particle); this yields a very small $R_{\rm RSF}$ and a very low accretion rate.
- *Model WTh*: For a resolution test, this model uses $h_{\rm min} \rightarrow h_{\rm min}/2$; this should only impact calculations performed in very dense regions.
- *Model DQMe*: This model uses $r_{\rm inf} \equiv 4\epsilon_{\rm S2} = 1.17$ kpc (compared to $r_{\rm inf} \sim 73$ pc of Model DQM); in DQM11, they fix $r_{\rm inf} \equiv 4\epsilon_{\rm S2}$, although this value is $\sim$188 pc in their models.

2.3 Results

Each of our models was evolved through a merger event, similar to that of SDH05. Model ONB was evolved for 1.25 Gyr and the rest were evolved for 1.5 Gyr (including Model $\mathrm{ONB_l}$). By returning the feedback energy to the halo gas in Model ONB, a dense galactic core formed near the core merger epoch, which resulted in an extremely large wall-clock time per step for the fiducial resolution version.

Each model followed a similar qualitative history, which is shown for Model WT in Figs. 2.1 and 2.2 for the gas column density and gas temperature, respectively.

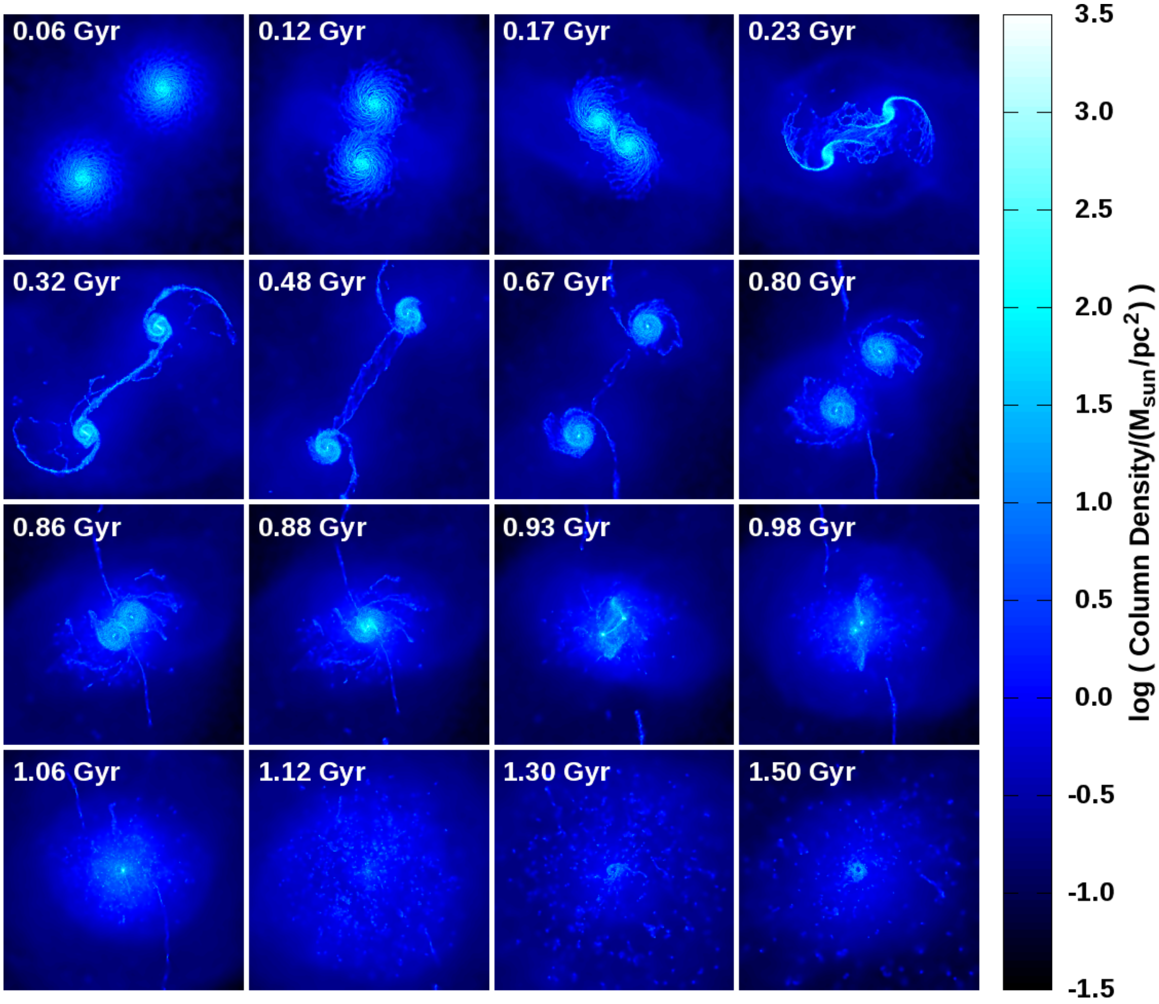

Figure 2.1: Evolution of gas column density for Model WT. Times from the onset of the simulation are listed in each frame; each frame measures 100 kpc per side, with an image resolution of 98 pc pixel^{-1}.

From this evolution, we see four significant epochs: first periapsis, apoapsis, second periapsis, and core merger. The times of these epochs are calculated using the black holes as proxies for the centres of the galaxies, thus the epochs essentially represent the local minimum and maximum separation of the two black holes. In all models, first periapsis occurs at 166 Myr and apoapsis occurs at 480 Myr; the latter is sustained for approximately 100 Myr. Second periapsis occurs approximately 11 Myr earlier for Model DQM than for the rest of the models. We have verified that this more

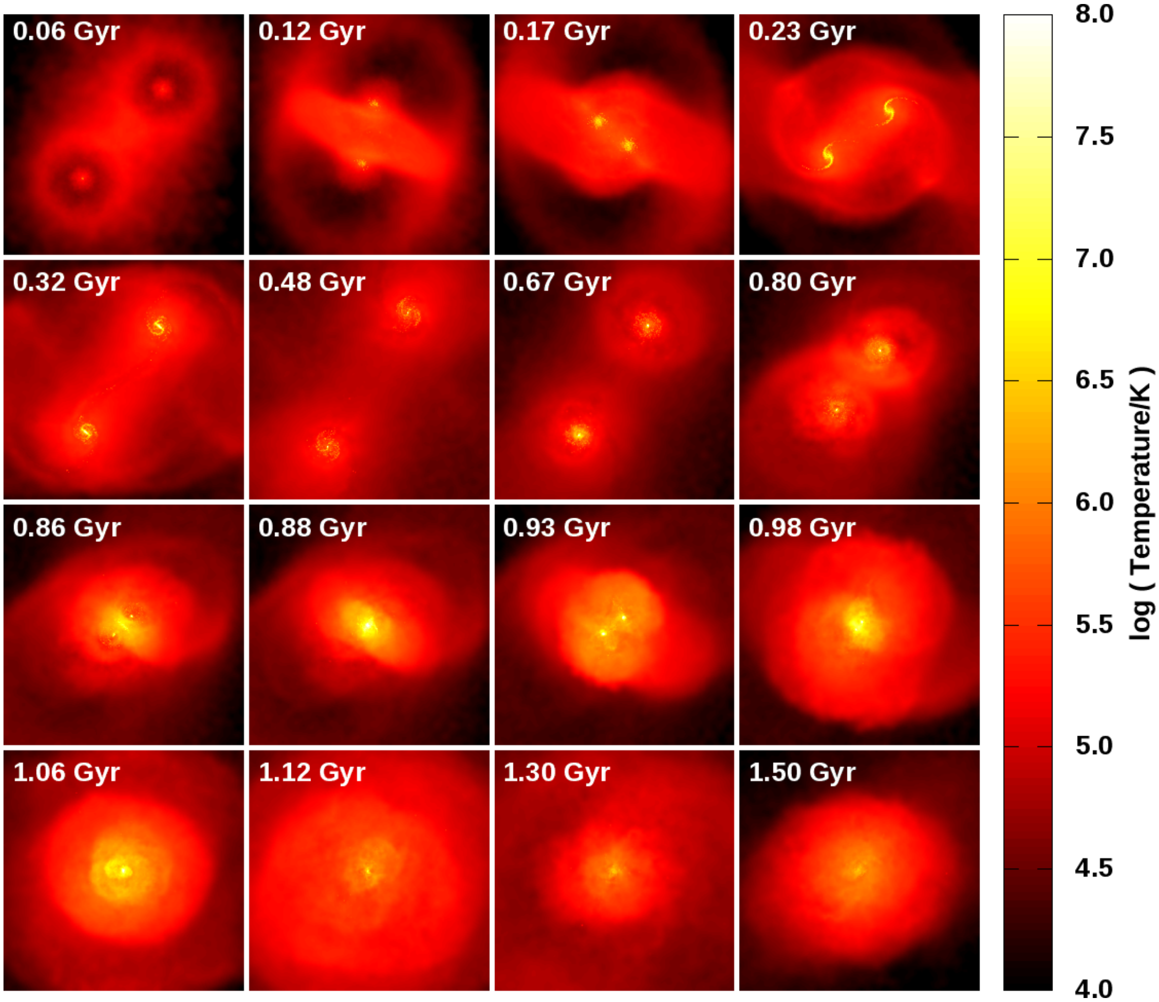

Figure 2.2: Evolution of gas temperature for Model WT. Times from the onset of the simulation are listed in each frame; each frame measures 100 kpc per side, with an image resolution of 98 pc pixel^{-1}. The top right panel at 0.23 Gyr has a large filling factor of supernova events, caused by tidal interactions at first periapsis. Although ubiquitously occurring through the galaxies, the global star formation rate is at a local minimum (see section 2.3.6).

	Dynamic Mass	Tracer Mass
First Periapsis/Gyr	0.166 (0.166)	0.166 (0.166)
Apoapsis/Gyr	0.480 (0.480)	0.480 (0.480)
Second Periapsis/Gyr	0.884 (0.870±0.001)	0.872 (0.861)
Core Merger/Gyr	0.988±0.007 (0.974±0.006)	0.970 (0.962)

Table 2.4: Important epochs from the onset of the simulation for the fiducial (low) resolution models. The Dynamic Mass models are Models SDH, BS, ONB and WT; the Tracer Mass model is Model DQM.

rapid evolution is due to the inclusion of a more massive sink particle representing the black hole. In two-body simulations, where each particle represents one galaxy and dynamical friction is avoided, the period of the particles representing galaxies in Model DQM is 3.4 Myr (0.23 per cent) shorter than the particles representing the galaxies without tracer masses. For the full system, we find that the maximum separation at apoapsis is very slightly smaller (1.1 per cent), likely due to slightly higher dynamical friction, leading to an earlier second periapsis. Lastly, the core merger takes approximately 10 Myr to complete, and the onset of this process spans a range of 15 Myr amongst the different models. See Table 2.4 for a list of when these epochs occur.

As might be expected, there are notable morphological differences between the models; this is readily apparent in Fig. 2.3, which displays the gas temperature, gas column density and stellar column density of the top right galaxy in each model at apoapsis. By apoapsis, a bar has developed in our non-tracer mass models (Models SDH, BS, ONB and WT), with bar strength depending on model. We have verified that the lack of bar formation in Model DQM is a result of the additional mass from the tracer mass and not from the kinetic feedback. This extra mass causes an increase in the rotational velocity curve of the galaxy. See Fig. 2.4 where we have plotted the (S2 softened) rotation curve for five variations on Model WT_1 just prior to the onset of bar formation; in this test suite, a tracer mass represents the black hole and has been varied between 10^6 and 10^9 $\mathrm{M}_\odot$. The rotation curves for $M_{\mathrm{tracer}} = 10^{6-8}$ $\mathrm{M}_\odot$ are similar, and the peak velocity is 2.5 per cent higher for $M_{\mathrm{tracer}} = 5 \times 10^8$ $\mathrm{M}_\odot$ and 4.0 per cent higher for $M_{\mathrm{tracer}} = 10^9$ $\mathrm{M}_\odot$. The higher rotational velocities for $M_{\mathrm{tracer}} = 10^9$ $\mathrm{M}_\odot$ stabilises the galaxy against bar formation.

To ensure that our initial black hole mass is reasonable, we ran Model WT_l with seed black hole masses of 10^5, 10^6 and 10^7 $\mathrm{M}_\odot$. All three models had final black hole masses within 1.5 per cent of one another, and all three remnants had M_{BH}–σ relations that agreed with the observed relation within the one-sigma standard deviation.

2.3.1 Black hole advection

The location of the black hole with respect to the galactic core plays a fundamental role in determining the gas properties used to calculate the accretion and energy feedback rates. Even small displacements with respect to the centre of the potential well can have notable effects. We have studied four artificial advection algorithms, each yielding different results. Since the results presented in the rest of this paper are implicitly coupled to the behaviour of the advection algorithm, we discuss this issue first. See Fig. 2.5, where we have isolated the path of one black hole in Models SDH, ONB and DQM.

Without any artificial advection, low mass black hole particles are easily dragged by the local particles (whose mass may be comparable or greater than the mass of the black hole); even with artificial advection, some black hole ‘chaotic’ motions (or oscillations) persist, depending on the algorithm. The smoothest path is from the tracer mass (Model DQM); however, the increased mass of the galaxy slightly adjusts its trajectory, decreases its evolution time compared to the rest of the models, and impacts the disc morphology (i.e. prevents bar formation). The least smooth path is from coupling the black hole to the gas particle with the minimum potential energy, provided that $v_{\mathrm{rel}} < 0.25 c_{\mathrm{s}}$ (Models SDH and BS). Frequently, there is no gas particle satisfying the velocity criterion, thus the black hole oscillates about

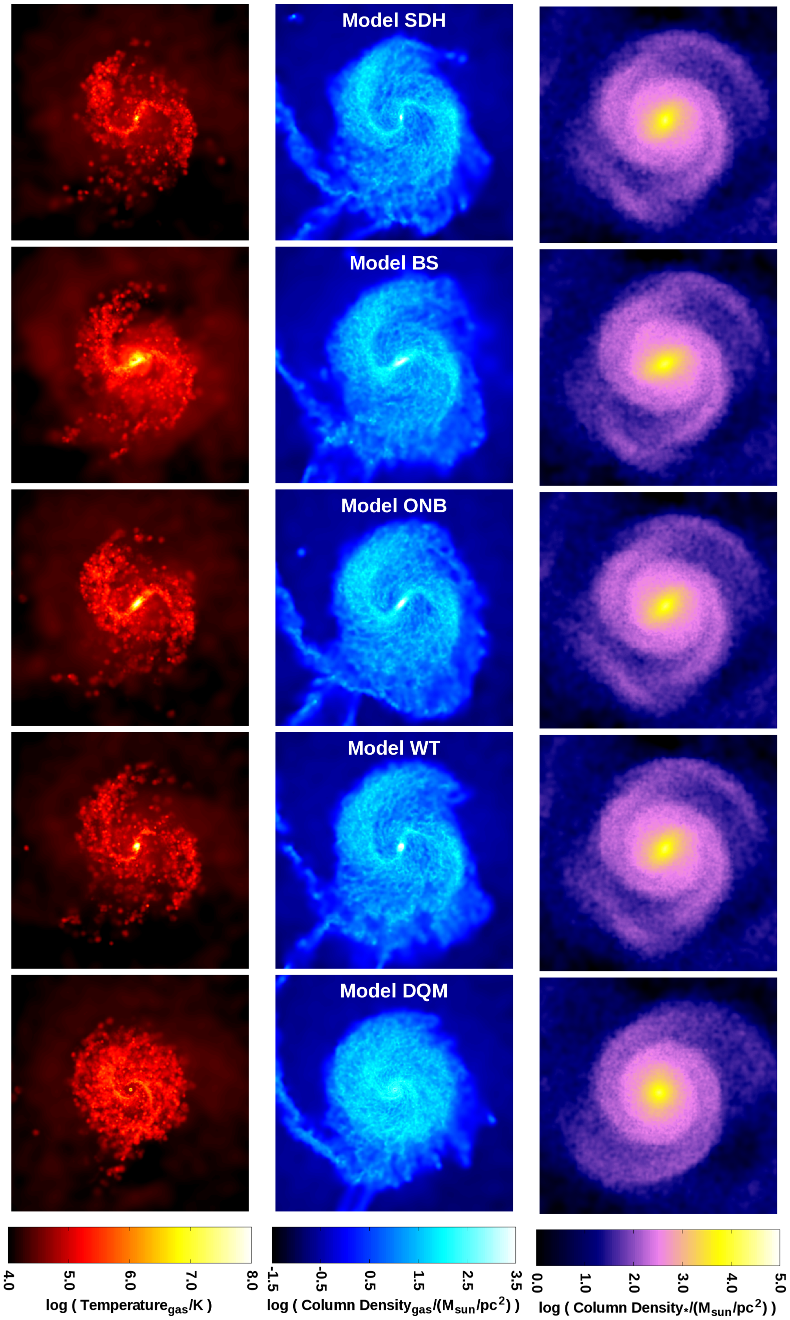

Figure 2.3: *Left to right*: Gas temperature, gas column density and stellar column density of the top right galaxy of each model at apoapsis. Varying morphologies for the different models emerge as the galactic discs reform after first periapsis. The lack of bar in Model DQM is a result of the more massive black hole particle (i.e. the tracer mass). Each frame measures 20 kpc per side, with an image resolution of 39 pc pixel^{-1}.

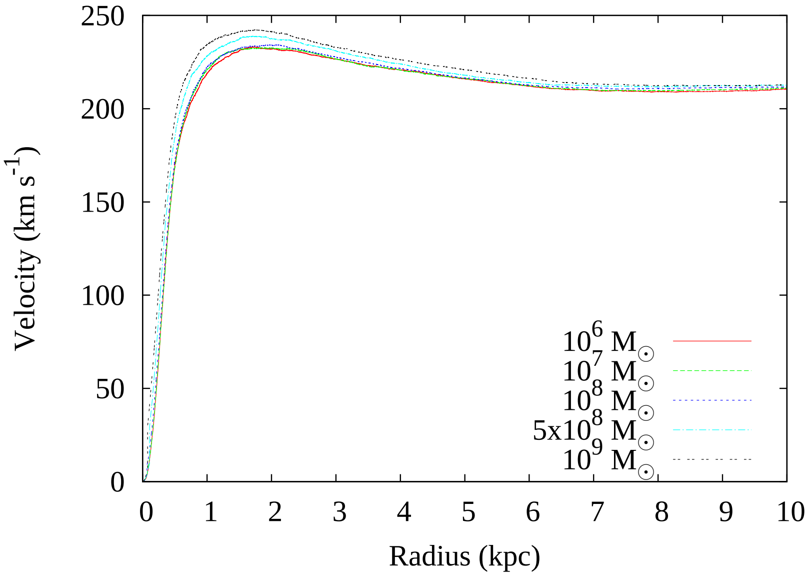

Figure 2.4: The rotation curves for five low resolution test models, where the mass of the tracer mass has been varied. For each model, the rotation curve is for the top right galaxy, and is calculated at 0.25 Gyr just prior to the onset of bar formation. The parent model is Model WT$_\mathrm{l}$.

the galactic core. When there is a gas particle satisfying the criteria, it is likely near the periphery of r_inf since the inner particles are typically too hot. Thus, the stringent velocity criterion permits both dragging by two-body forces and large artificial jumps in position. In Models SDH and BS, the artificial advection is turned off when $m_\mathrm{BH} > 10m_\mathrm{g}$; in the fiducial (low) resolution, the motions become smaller (larger) and more chaotic. We note that SDH05 and BS09 both use a multiphase star formation model, which produces a smoother temperature profile around the black hole than our star formation model. This difference may explain the poor advection in Models SDH and BS.

From the simulations, the advection methods in Models ONB and WT appear to have some advantages; they do not add mass to the galaxy as in the tracer mass method, nor do they couple to gas particles. By associating the direction of motion to stellar densities (Model ONB) or the local centre of mass within r_inf (Model WT), undue influence of gas particles, which are dynamically and continuously affected by

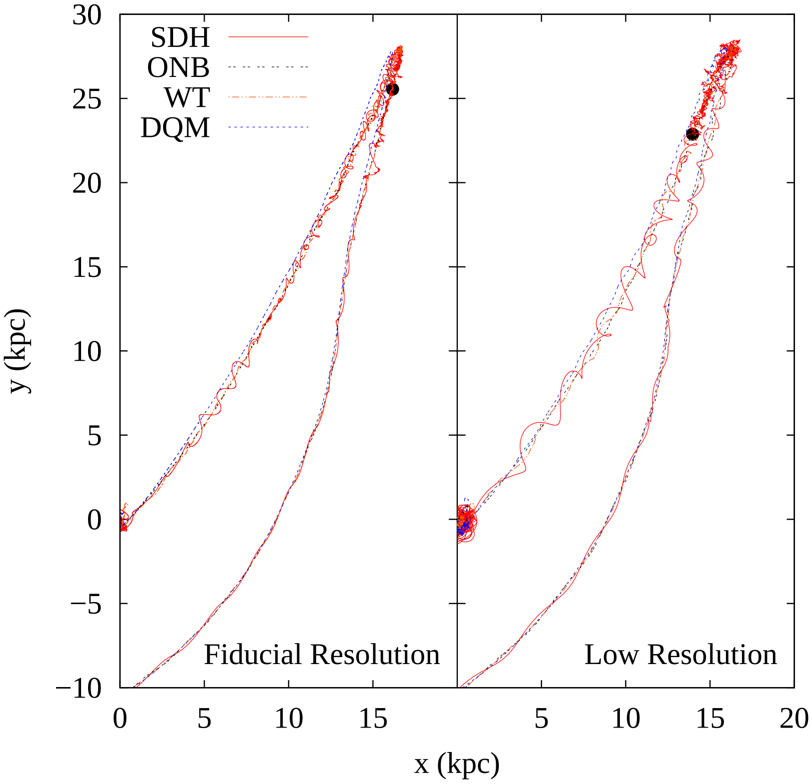

Figure 2.5: A portion of the unaveraged black hole path (including the turnaround point at apoapsis) in Models SDH, ONB and DQM for the fiducial (left) and low resolution (right) simulations. The dot indicates where the black hole advection algorithm turns off for Model SDH. The origin of the system is $(x, y, z) = (0, 0, 0)$ and the black hole originates at $(-27.6, -21.9, 0.0)$.

the AGN feedback, is avoided. Lastly, by limiting the distance a black hole can be artificially advected per iteration, it is possible for it to remain in the centre of a void.

The advection algorithms in Models DQM, ONB and WT are comparatively unaffected by resolution; this is expected since the tracer mass is independent of the local gas particles, and local averages vary little with resolution. The advection algorithm in Models SDH and BS are more resolution dependent; with lower resolution comes a larger $r_{\rm inf}$, thus the black hole has a larger distance it can be artificially displaced. It is worth noting that Fig. 2.5 clearly shows that the oscillations of Model SDH are damped with higher resolution, but are not completely removed.

Due to the notable black hole motion in Model BS, we ran a variation, Model BSw, which uses the black hole advection algorithm of Model WT. In this model, the black hole had smoother accretion rates and more continuous gas densities and temperatures near the black hole. The outbursts near apoapsis were stronger and more symmetric between the two galaxies than in Model BS. Ironically, although we might argue that Model BSw is inherently better than Model BS because of the better black hole trajectories, both models yield remnants with similar total black hole masses and stellar velocity dispersions, even though the black holes in Model BS never merge and the feedback history of the two models is different.

2.3.2 Accretion rate

The mass evolution of the black hole is a key aspect of the AGN feedback models and is an important diagnostic since it sets the $M_{\rm BH}$–σ results. In the left panel of Fig. 2.6, we show the total black hole mass over time. In the right panel, we show the accretion rates (geometrically averaged over both black holes and plotted in bins of 10 Myr). In the top panel of each figure, we show when a black hole is accreting at its Eddington limit. There are three major epochs of black hole growth: at the beginning (Models ONB, WT and DQM), at apoapsis (Models SDH, BS and WT), and at core merger (Models SDH, BS and DQM). It is typically at these times

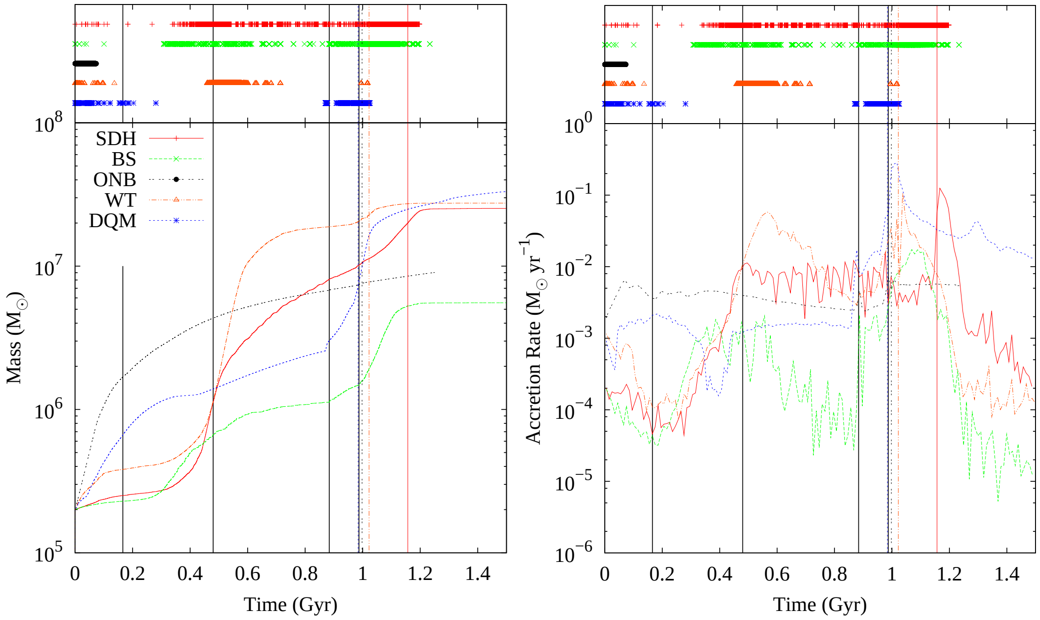

Figure 2.6: *Left*: The total black hole mass in each fiducial resolution simulation. *Right*: The accretion rates for each of the fiducial resolution models geometrically averaged over both black holes and plotted in bins of 10 Myr. *Top of each panel*: Points represent when a black hole is accreting at $\dot{M}_{\rm Edd}$. The vertical line of the same linestyle indicates when the black holes merge. The four black vertical lines indicate the time of first periapsis, apoapsis, second periapsis and core merger.

	Pre-BH Merger	Merged BH
Model SDH	8.32±1.88 (6.82±0.50)	1.95 (0.04)
Model BS	5.87±0.43 (2.26±0.19)	— (—)
Model ONB	5.78±0.06 (3.17±0.02)	0.00 (0.00)
Model WT	9.99±0.97 (5.75±0.07)	0.00 (0.00)
Model DQM	2.35±1.06 (8.22±2.03)	6.86 (1.42)
Model BSw	2.11±0.15 (1.18±0.31)	0.00 (0.00)
Model ONBc	0.00±0.00 (0.37±0.00)	0.00 (0.00)
Model WTh	8.78±0.64 (6.94±0.60)	2.10 (0.00)
Model DQMe	17.72±0.08 (15.74±0.15)	1.20 (0.00)

Table 2.5: Percent of time fiducial (low) resolution black holes are accreting at their Eddington limit; the range of times includes the data for both pre-merged black holes. Dashed lines indicate that the black holes did not merge prior to 1.5 Gyr. The percentages for fiducial resolution Models ONB and ONBc are taken at 1.25 Gyr.

when a black hole is undergoing Eddington accretion; see Table 2.5 for the percent of time that a black hole is accreting at its Eddington limit.

Three models use the Eddington-limited Bondi accretion rate: Models SDH, BS and WT. In SDH05 (see bottom panel of their fig. 14), the accretion rate increases from the onset of the simulation until prior to second periapsis, at which point there is only a slight decrease. At core merger, there is an increase of approximately 1.8 dex, followed by a sudden drop as the system is totally disrupted. Since our initial conditions and our Model SDH were constructed to mimic SDH05, we expect similar results which, within reason, are obtained. In both Models SDH and WT, there is an initial decline in accretion rate as the galaxies are relaxing. This initial relaxation does not occur in SDH05 since the vertical structure of the gas is set in hydrostatic equilibrium, thus this initial difference is expected. After first periapsis, gas is funnelled into the core, thus, in agreement with SDH05, there is an increasing accretion rate. At apoapsis, there is a plateau in Model SDH, but a short-lived spike in Model WT. At core merger, there is an increase followed by a rapid decrease as the systems are totally disrupted.

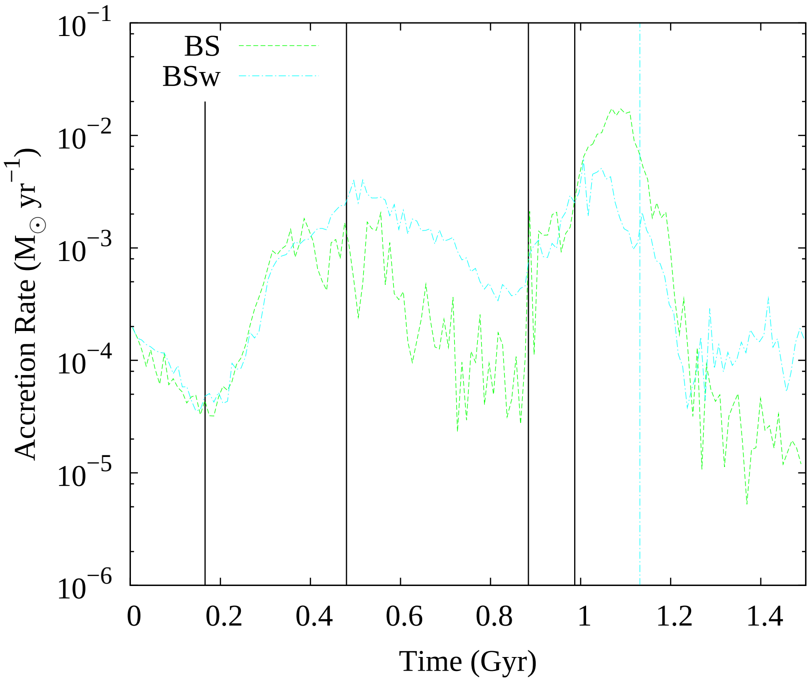

Figure 2.7: The accretion rate for Models BS and BSw, geometrically averaged over both black holes and plotted in bins of 10 Myr. The vertical line of the same linestyle indicates when the black holes merge. The four black vertical lines indicate the time of first periapsis, apoapsis, second periapsis and core merger.

For the first 400 Myr, the accretion rate of Model BS follows the same trends as Models SDH and WT. During this time, $\alpha(n_{\rm H}) > 100$, which explains why $\dot{M}_{\rm Model\ BS} > \dot{M}_{\rm Models\ SDH\ \&\ WT}$ for $230 \lesssim t/{\rm Myr} \lesssim 400$. After this point, $\dot{M}_{\rm Model\ BS}$ decreases, which is a result of the strong outflows from feedback and the motion of the black holes; the latter prevents the black holes from remaining in a steady environment, resulting in rapidly varying gas characteristics around the black hole. The accretion rates in Model BSw continue to increase until apoapsis, after which they decrease due to strong outflows, but with a smoother accretion profile that is slightly higher than in Model BS; see Fig. 2.7.

In DQM11, there is a large jump in $\dot{M}_{\rm visc}$ followed by a slow decline shortly after first periapsis and again starting at second periapsis; see the bottom panel of their fig. 1. Their initial galactic separation is approximately twice that of ours, thus their evolution times are longer, which may account for differences between our models and theirs. Also, their mass and spatial resolution are slightly better than in the models presented here, thus their feedback is likely distributed amongst fewer particles which keeps their void relatively smaller (see discussion in §2.3.3).

In Model DQM, there is not the accretion epoch between first periapsis and apoapsis that occurs in DQM11. This is a result of both a shorter time during which gas can fall into the galactic cores, and the slightly larger r_{inf} which allows for efficient feedback to maintain the void during non-cataclysmic events. At second periapsis, there is an increase of approximately 2.2 dex in Model DQM compared to DQM11's increase of approximately 3 dex. After the merger, both accretion rates drop off, but DQM11 falls off faster.

Unlike Models SDH and WT, Model DQM has a decrease in accretion rate just prior to apoapsis rather than a stead increase. All cases are a result of a decrease in gas temperature (see §2.3.3), but $\dot{M}_{\text{visc}} \propto c_{\text{s}}^2$ whereas $\dot{M}_{\text{Bondi}} \propto 1/c_{\text{s}}^3$. Thus, drastically different accretion histories are obtained from similar trends in gas temperature. Like the other models, there is a large peak in accretion at core merger, but the final accretion rate does not drop as in the other models.

ONB08 is a cosmological simulation run from $z = 49$ to $z = 0$. Over the final 7 Gyr of their simulation, there are no significant galaxy mergers and there is negligible black hole growth (see their fig. 8). During this time, their accretion rate lies comfortable within the RIAF regime by more than an order of magnitude. In Model ONBc, there is a low accretion rate that is continually decreasing and comfortably within the RIAF regime; however, this model uses a very conservative search algorithm to calculate $\dot{M}_{\text{drag}}$, thus the low accretion rate is likely artificially low because of the numerical scheme. When we use a less stringent search algorithm that is better suited for use in HYDRA at the resolutions we present, the accretion rate quickly rises to $\dot{M}_{\text{drag}} \sim 0.005$ M$_{\odot}$yr^{-1} and remains approximately constant for the remainder of the simulation. This relatively constant rate is a result of the feedback energy being deposited into the halo gas rather than modifying the galactic core. Since the feedback is being returned to the halo gas, there are negligible core differences between Models ONB and ONBc, except for the accretion rate.

Model ONB has a noticeably different accretion profile than the other models. Except over the first ∼10 Myr and again at core merger, this model has no prominent features, whereas the other models have strong initial features up to first periapsis, and more features at apoapsis and again at core merger. Thus, this model has the most consistent accretion, which is likely a result of the feedback begin delivered to the halo and not affecting the nuclear region.

2.3.3 Energy feedback algorithm

The two broad categories of returning the feedback energy are thermal, $\dot{E}$, and kinetic, $\dot{p}$. Thermal energy is returned to gas particles in Models SDH, BS, ONB and WT by increasing the internal energy of the particles, while kinetic energy is returned to gas particles in Model DQM by increasing the momentum of the particles. Although these two approaches are related by $\dot{E} = \dot{p}c$, both forms of feedback yield drastically different results which are readily apparent on both large scales and small scales. See Fig. 2.8 for gas density and temperatures around the black holes.

The feedback in Model ONB is returned to the gas particles with $\rho < 5 \times 10^{-26}$ g cm^{-3}. The gas density around the black hole, as shown in the left hand panel of Fig. 2.8, is orders of magnitude higher than this threshold, and the core and ultimately the plane of the disc also have densities higher than this threshold. Thus, this feedback energy is typically distributed to gas that is out of the core and the disc, hence resides in the halo with distances $0.5 \lesssim r/\text{kpc} \lesssim 3.5$ ($7 \lesssim r/r_{\text{inf}} \lesssim 48$) from the black holes. This leaves the galactic cores relatively unmodified by AGN feedback. As gas falls towards the galactic cores (due to tidal interactions at first periapsis), it remains there since the AGN feedback is not local enough to remove it. Hence, these models have the highest core density. The major core heating events in this case are from shock heating of the infalling gas after first periapsis and from the final core collisions.

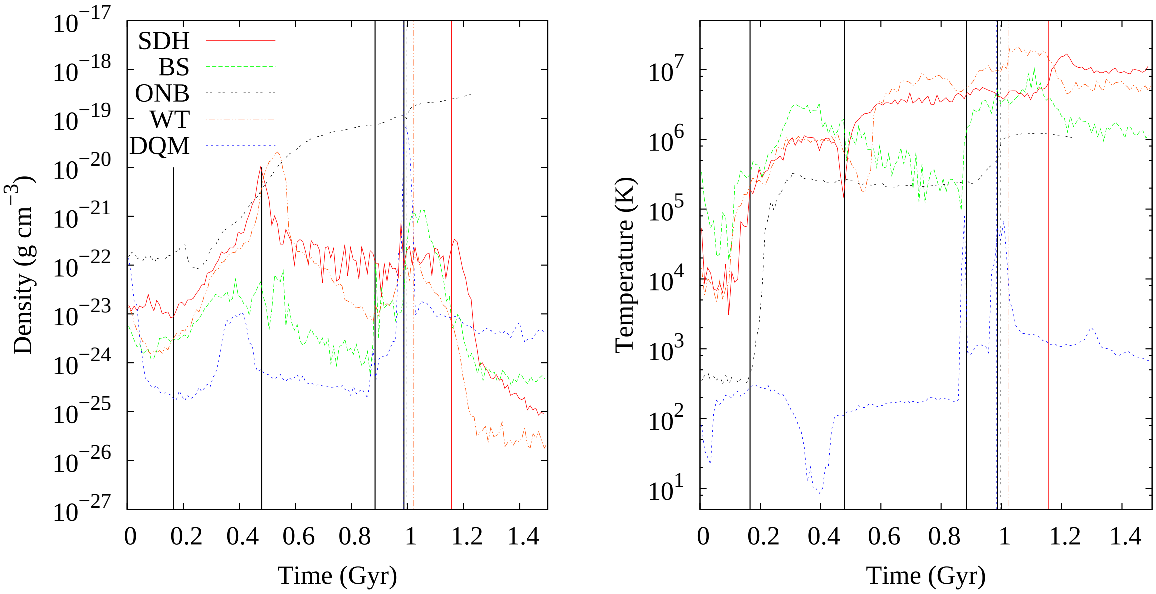

Figure 2.8: Gas density (left) and temperature (right) within r_{inf} of the black holes, geometrically averaged over both black holes and plotted in bins of 10 Myr. The vertical line of the same linestyle indicates when the black holes merge.

The AGN feedback in the remaining models is delivered directly to the core region, leading to a more distinct modification of the entire system. From the onset of the remaining thermal feedback simulations, there is a higher core temperature and a lower core density than in Model ONB. Tidal interactions at first periapsis cause gas to be funnelled towards the cores but, unlike Model ONB, the temperature continues to rise from AGN heating and the density remains moderated. Shortly after first periapsis, a galactic bar starts to form and persists strongly for approximately 200 Myr. As it dissipates, there is a nuclear inflow of gas accounting for the local density maxima near apoapsis in Models SDH and WT. After the dissipation of the bar, the galaxies begin to eject gas, preferentially along the polar axis. As the cores merge, there is a final set of feedback events as the gas is heated and blown away; after this, accretion rates and core densities drop while core temperature remains approximately constant.

Kinetic feedback affects the galactic core in different quantitative and qualitative ways than thermal feedback. In this model, the energy is returned radially to gas particles as a momentum boost, which quickly and efficiently forms a void around the black holes; in Model DQM, a void of $r \sim 0.55 r_{\rm inf}$ is formed within the first 60 Myr. Once the void is formed, it persists for the remainder of the simulation. Strong events, such as the infalling gas after first periapsis or the collision at core merger, can briefly decrease the void radius, increasing the core density. Otherwise, the void and core characteristics are held constant, as we can see by an approximately constant temperature and density profile between first periapsis and core merger.

Model DQMe uses the same kinetic feedback algorithm as in Model DQM, but instead $r_{\rm inf} \equiv 4\epsilon_{\rm S2}$, which leads to an initially higher accretion rate. The increased amount of feedback energy is returned to more particles, delaying the formation of the void. When the void forms after 140 Myr, it has a radius of $r \sim 0.85 r_{\rm inf} \sim 1$ kpc, which is highly unrealistic; moreover, there are no observational indications of a void such as this. Further, when observing molecular rings around the centre of galaxies, they do not define a gas void and have been observed to have radii of less than 1 kpc (e.g. Storchi-Bergmann et al. 2012; König et al. 2013). This void in Model DQMe is more rigid than the void in Model DQM, only being affected at second periapsis and core merger. The unrealistically large $r_{\rm inf}$ in Model DQMe also leads to a premature merger of the black holes, which is poorly handled by the merger subroutine. Thus, the importance of choosing a physical $r_{\rm inf}$ is clear: catastrophic and unphysical results will ensue if it is not chosen appropriately.

2.3.4 Particle accretion algorithm

A particle accretion algorithm should accrete particles such that the internal mass, $M_{\rm BH}$, and dynamical mass, $m_{\rm BH}$, of any given black hole remain similar for all time. In Model DQM, a tracer mass is used to represent the black hole particle, rendering the comparison between internal and dynamic masses moot. The tracer mass model uses a continual-conditional algorithm to remove 'accreted' gas, thus any conclusions we make regarding this category can be applied. In the remainder of our fiducial resolution models, the first accretion event will increase the dynamical mass by 36 per cent since $m_{\rm BH} = 0.36 m_{\rm g}$. All subsequent accretion events will add relatively less mass to the black hole particle. Thus we expect the ratio $\Delta m/M_{\rm BH}$, where $\Delta m = m_{\rm BH} - M_{\rm BH}$, to start at $|\Delta m/M_{\rm BH}| \lesssim 0.36$ and decay to zero with time. In the top panel of Fig. 2.9, we plot $\Delta m/M_{\rm BH}$ for one black hole in Models SDH, BS, ONB and WT. The expected behaviour is obtained in Models BS, ONB and WT; the decline in Models ONB and WT is smoother than in Model BS since there is no stochastic component to the accretion. The expected decline is not observed in Model SDH, where the ratio has no apparent trend, and at late times $\Delta m/M_{\rm BH} \to -0.01$ rather than zero.

The black holes do not all grow at the same rate. Thus, for a normalised comparison, we plot $\Delta m/m_{\rm g}$ in the bottom four panels of Fig. 2.9 for Models SDH, BS, ONB and WT, respectively. Since every accretion event adds mass $m_{\rm g}$ or $m_{\rm g}/2$ to the dynamical mass, we expect $|\Delta m/m_{\rm g}| \leq 1$ for all time, unless multiple particles are accreted in one step, which can occur in the stochastic models.

In Model SDH, particle accretion events are only dependent on the environment. This lack of $M_{\rm BH}$–$m_{\rm BH}$ coupling permits the internal and dynamic masses to follow different histories, as seen by the lack of trend in the second panel of Fig. 2.9. The discontinuity in $\Delta m/m_{\rm g}$ at core merger is a result of both black holes following different mass growth histories, both internally and dynamically.

The stochastic-conditional accretion algorithm in Model BS allows for fluctuations in an otherwise smooth process, and the probability's dependence on Δm forces good agreement between the internal and dynamic masses. Finally, by design, Model ONB (WT) always maintains $0.0 \leq \Delta m/m_{\rm g} \leq 1.0$ ($-0.5 \leq \Delta m/m_{\rm g} \leq 0.5$), displaying the effectiveness of the continual-conditional particle accretion methods.

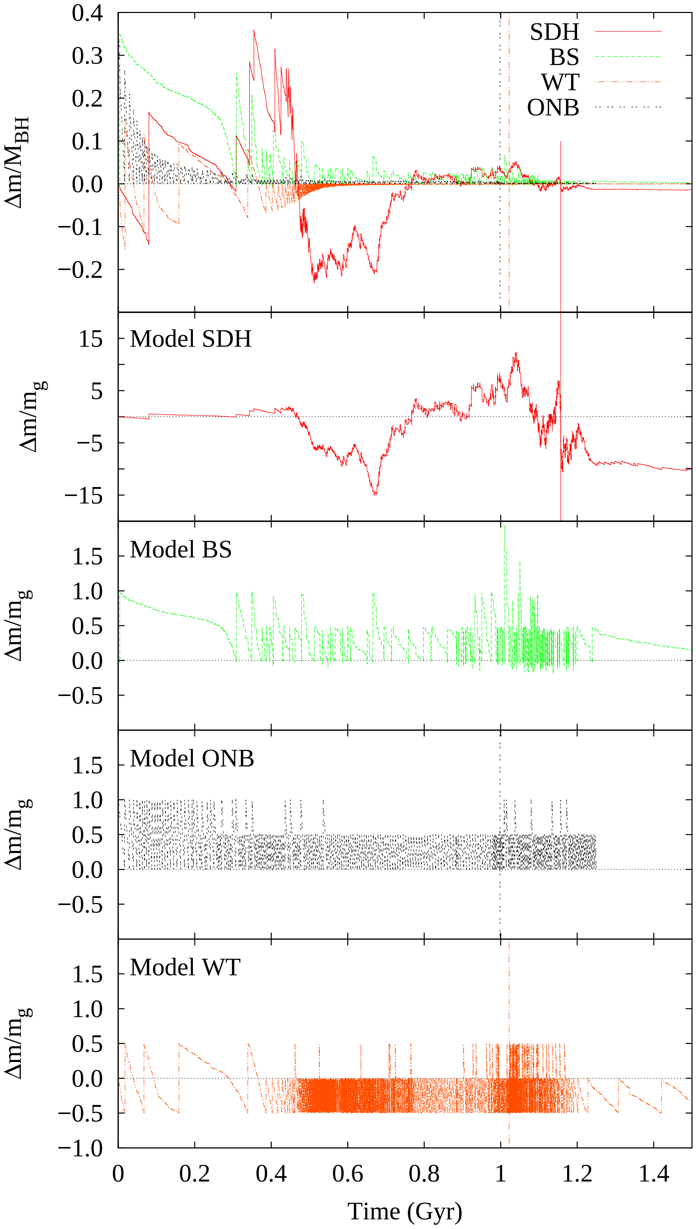

Figure 2.9: A comparison of internal mass, M_{BH}, and dynamical mass, m_{BH}, for one black hole in selected fiducial runs. *Top*: The ratio $\Delta m/M_{\mathrm{BH}}$, where $\Delta m = m_{\mathrm{BH}} - M_{\mathrm{BH}}$. *Bottom Four Panels (top to bottom)*: The ratio $\Delta m/m_{\mathrm{g}}$ for Model SDH (stochastic-unconditional), Model BS (stochastic-conditional), Model ONB (continual-conditional) and Model WT (continual-conditional particle accretion). The vertical line of the same linestyle in the top panel indicates when the black holes merge.

	Time (Gyr)	
	Fiducial Resolution	Low Resolution
Model SDH	1.16	1.31
Model BS	—	—
Model ONB	1.00	1.00
Model WT	1.02	1.00
Model DQM	0.98	0.98
Model BSw	1.13	1.10
Model ONBc	1.10	1.04
Model WTh	1.02	1.01
Model DQMe	0.87	0.86

Table 2.6: Merger time of the black holes, as measured from the beginning of the simulation. Dashes indicate that the black holes did not merge within our 1.5 Gyr simulation time.

2.3.5 Black hole merger algorithm

All of the models include a black hole merger prescription, which conserves internal, dynamical and tracer mass; see Table 2.6 for precise merger times. Thus, the merger should have limited gravitational impact on the surrounding environment. However, the amount of feedback energy returned pre- and post-merger will vary depending on the model, which we analyse below.

Consider two identical black holes in the merged core during the black hole merger. First, the total region of influence of the unmerged black holes will be between $V = \frac{4}{3}\pi r_{\rm inf}^3$ and $2V$ depending on the separation of the black holes. Since $r_{\rm inf}$ is independent of black hole mass, the total region of influence after the merger will simply be V. In all cases, $\dot{E} \propto \dot{M}$, so the amount of feedback energy available prior to the merger will be proportional to $\dot{M}_{\rm BH_1} + \dot{M}_{\rm BH_2}$; after the merger, we will have energy proportional to $\dot{M}_{\rm BH_1+BH_2}$; if we define $\dot{M}$ to be the accretion rate of one black hole prior to the merger, then for each accretion rate we studied, across the merger we have

$$\begin{aligned} 2\dot{M}_{\rm Edd} &\rightarrow 2\dot{M}_{\rm Edd}, \\ 2\dot{M}_{\rm B} &\rightarrow 4\dot{M}_{\rm B}, \\ 2\dot{M}_{\rm drag} &\rightarrow \dot{M}_{\rm drag}, \\ 2\dot{M}_{\rm visc} &\rightarrow \dot{M}_{\rm visc}. \end{aligned}$$

We can clearly see that the only total accretion rate in the core that remains unchanged by the merger is $\dot{M}_{\rm Edd}$; the total Bondi accretion rate doubles and the total viscous and drag accretion rates halves. Thus, in Models SDH, BS and WT (which use Bondi accretion), there is more feedback energy available after the merger than before, and this increased amount of energy will be distributed to a smaller region. Likewise, there is less feedback energy available in Models ONB and DQM after the merger, which will also be distributed within a smaller volume. Thus, we can argue that the galactic core becomes more energetic assuming Bondi accretion, but less energetic assuming viscous or drag accretion when two black holes merge.

In the models, Model DQM has the least stringent merger prescription, with only a separation criteria. As expected, this is the first model to merge. The most stringent merging criteria is in Model BS, which is never met. The circular velocity at the more massive black hole's smoothing length is typically ten times smaller than the local sound speed, and the relative velocity between the black holes never drops below this threshold. Moreover, the chaotic motion and two-body interactions of the black holes typically keeps them further apart than the separation criteria.

2.3.6 Global star formation rates

During a major merger, there is typically a burst of star formation at apoapsis and again during core merger due to the infall of gas on to the galactic core (e.g. Mihos & Hernquist 1996; SDH05; DQM11). There are several characteristics that can modify the star formation rate at these epochs, including initial conditions and

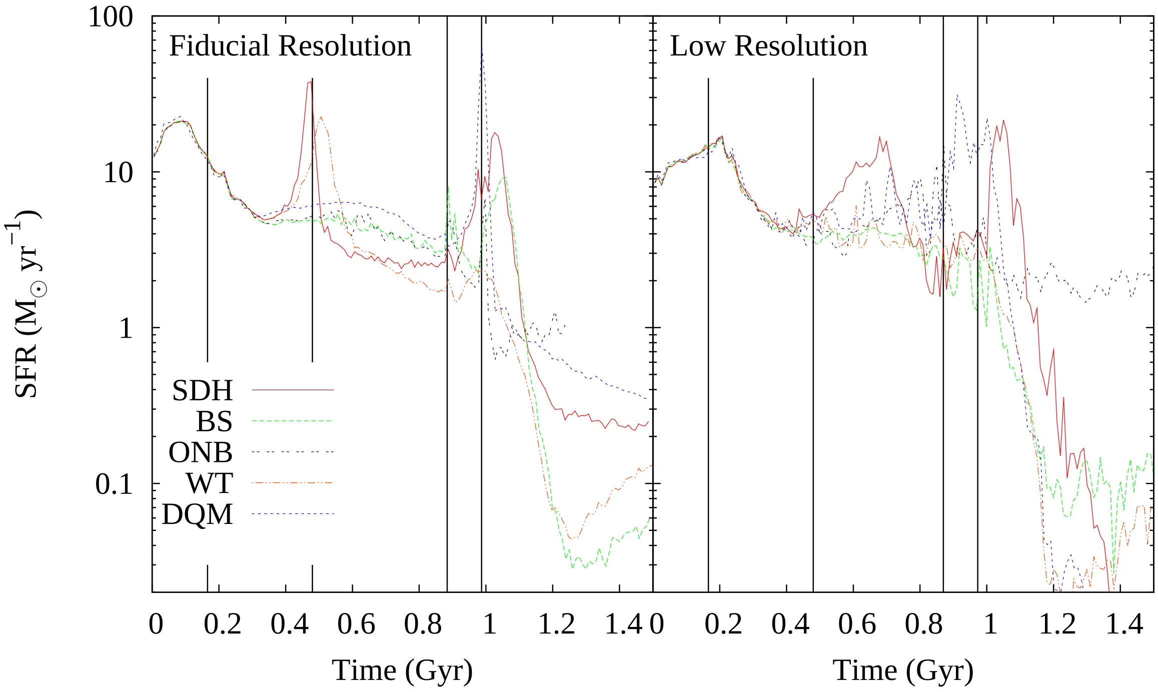

Figure 2.10: Global star formation rate for the fiducial (left) and low resolution (right) runs. The vertical lines represent the times of first periapsis, apoapsis, second periapsis and core merger for the dynamic black hole mass models, as given in Table 2.4.

the inclusion of a galactic bulge and/or AGN feedback (SDH05). In Hydra, the star formation algorithm differs from those used in SDH05, BS09, ONB08 and DQM11, so we do not expect an exact reproduction of their results. However, any differences in SFRs amongst our models will be solely the result of the AGN feedback algorithm and its interaction with the star formation algorithm. The time-averaged SFR for the fiducial (left panel) and the low resolution (right panel) are plotted in Fig. 2.10.

In these models, there are notable star formation bursts shortly after the beginning of the simulation, at apoapsis and again at core merger. In all cases, the initial burst is a result of the gas disc relaxing (Williamson & Thacker 2012). This initial burst also exists in simulations of an isolated galaxy that is constructed in a similar manner to the one presented here. SDH05 and DQM11 create the vertical structure of their gas disc by assuming hydrostatic equilibrium after setting their equation of state. Although cooling is not considered during this process, it means that their initial conditions and simulations are more equivalent than ours. Thus, as expected, this initial burst of star formation is missing from their results. This initial burst is resolution dependent, being higher and shorter lived in the fiducial resolution models. After this epoch in the low resolution models, the only outstanding features are post-apoapsis burst in Model SDH$_{\mathrm{l}}$, the core merger burst for Models SDH$_{\mathrm{l}}$ and DQM$_{\mathrm{l}}$, and the expected drop in SFRs for all models (except Model ONB$_{\mathrm{l}}$) shortly after core merger. The low resolution features do not necessarily have counterparts in the fiducial resolution simulations and vice versa, as a result of the stellar feedback being resolution dependent. Low resolution star formation events extend over a considerably larger volume and mass than fiducial resolution events due to the larger gas particle mass and lower spatial resolution. Thus, a low resolution event has an unavoidably greater impact on its environment, and causes comparatively large regions of the galaxy to undergo a cooling delay. This explains the delayed star formation peak after apoapsis in Model SDH$_{\mathrm{l}}$, the lack of peak in Model WT$_{\mathrm{l}}$ after apoapsis, and generally lower SFRs at core merger.

In Model SDH, the SFR increases by 0.9 dex at both apoapsis and core merger. In SDH05, there is no burst at apoapsis and there is an increase of 1 dex at core merger. This burst at core merger exists in all the models, except Model WT, where the high feedback rate of thermal energy prevents the gas from cooling in to the regime where star formation can commence. After the core merger burst, the SFRs drop, as in SDH05, due to the heating and total disruption of the system.

In Model WTh, the star formation burst at apoapsis peaks approximately 50 Myr earlier than in Model WT. The apoapsis burst is a result of a nuclear inflow of gas, and the lower value of h_{min} allows higher densities to be resolved sooner; thus inflowing gas enters the permissible density regime of star formation for Model WTh before Model WT. For the same resolution argument, Model WTh also has a small burst of star formation (an increase of 0.6 dex) at core merger. This difference in the SFR highlights one of the well known drawbacks of resolution dependency in the star formation algorithm, although developing a model that is independent of resolution awaits a full understanding of star formation in a global context.

The SFR in Model ONB remains relatively smooth until a small increase of 0.6 dex at core merger. Even after core merger, the SFR remains relatively unchanged due to high core densities and moderate core temperatures.

In DQM11, there is a major star formation burst shortly after first periapsis and again starting at second periapsis (see their fig. 1, middle panel). Model DQM reproduced the burst at second periapsis. The hot ring around the void means that the star formation must occur in the galactic disc, which results in the lack of peak after first periapsis. At second periapsis, the merger is efficient enough to create a galactic core, causing the core merger star formation burst. After this final burst, the SFR drops to small values, agreeing with DQM11.

2.4 Final States

We evolved our galaxy merger simulations for 1.5 Gyr, and the characteristics of the remnants are presented here. The exception is the fiducial resolution Model ONB, which was evolved for 1.25 Gyr. From our analysis of Model $\mathrm{ONB_l}$, we do not expect any significant evolution between 1.25 and 1.5 Gyr. Therefore, for the final remnant of Model ONB, we present a combination of data from 1.25 Gyr, data extrapolated to 1.5 Gyr, and data from Model $\mathrm{ONB_l}$. We will clearly state where the data comes from in each instance.

The final remnant in all models is a reformed gas and stellar disc surrounded by a fragmented hot gas halo. The radial profiles for gas temperature, gas density and stellar column density (averaged over all azimuthal and polar angles) for each remnant are similar, as seen in Fig. 2.11; the values typically span 0.5 dex at any given radius. In Figs. 2.12 and 2.13, we have plotted the final gas temperature, gas column density and stellar column density for frames of 100 and 20 kpc per side, respectively.

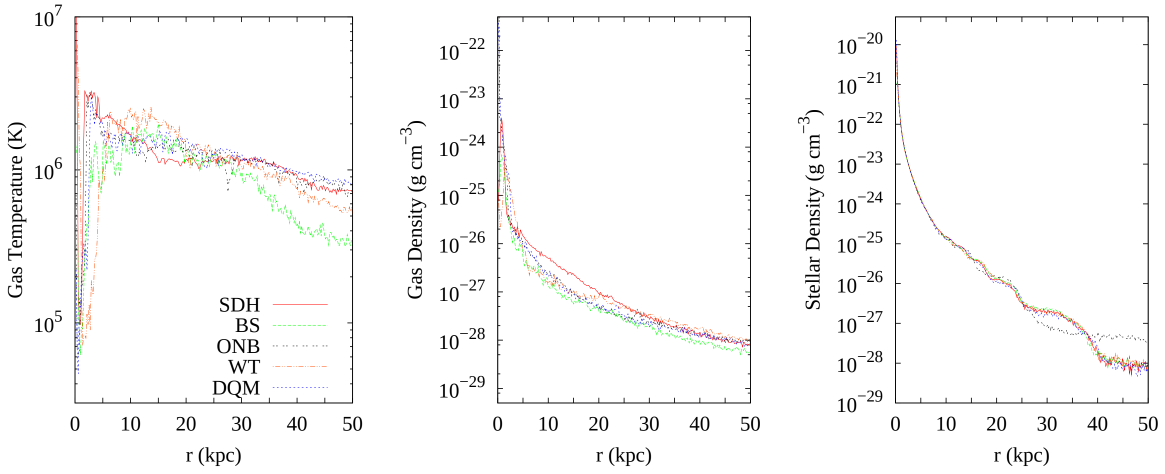

Figure 2.11: Radial profiles of the remnants, averaged over all azimuthal and polar angles. From left to right, we show gas temperature, gas density, and stellar density. The profile for Model ONB is taken at 1.25 Gyr.

2.4.1 Gas properties

By the end of the simulation, the gas that was originally in a galactic disc is heavily depleted while the majority of the gas that was originally in the halo remains. The fraction of remaining gas for each fiducial resolution model is given in Table 2.7. The majority of the depleted gas has been converted in to stars as opposed to being accreted on to a black hole. The gas that is ejected from the disc has temperatures and pressures a few orders of magnitude greater than the halo gas, thus it can easily escape from the system. Therefore, the gas halo does not play a role in recycling the ejected gas in to stars.

The amount of substructure varies considerably amongst remnants. Model ONB's remnant is a well-formed disc in a smooth halo, while Models BS and WT have a loosely reformed disc in a fragmented halo. Shortly after core merger, Model BS undergoes an outburst event which expels most of the gas and, by 1.5 Gyr, this gas is starting to recondense on to the core. In Model WT, the remaining gas cools and fragments, and then begins to recondense on to the core. Thus, in both models there

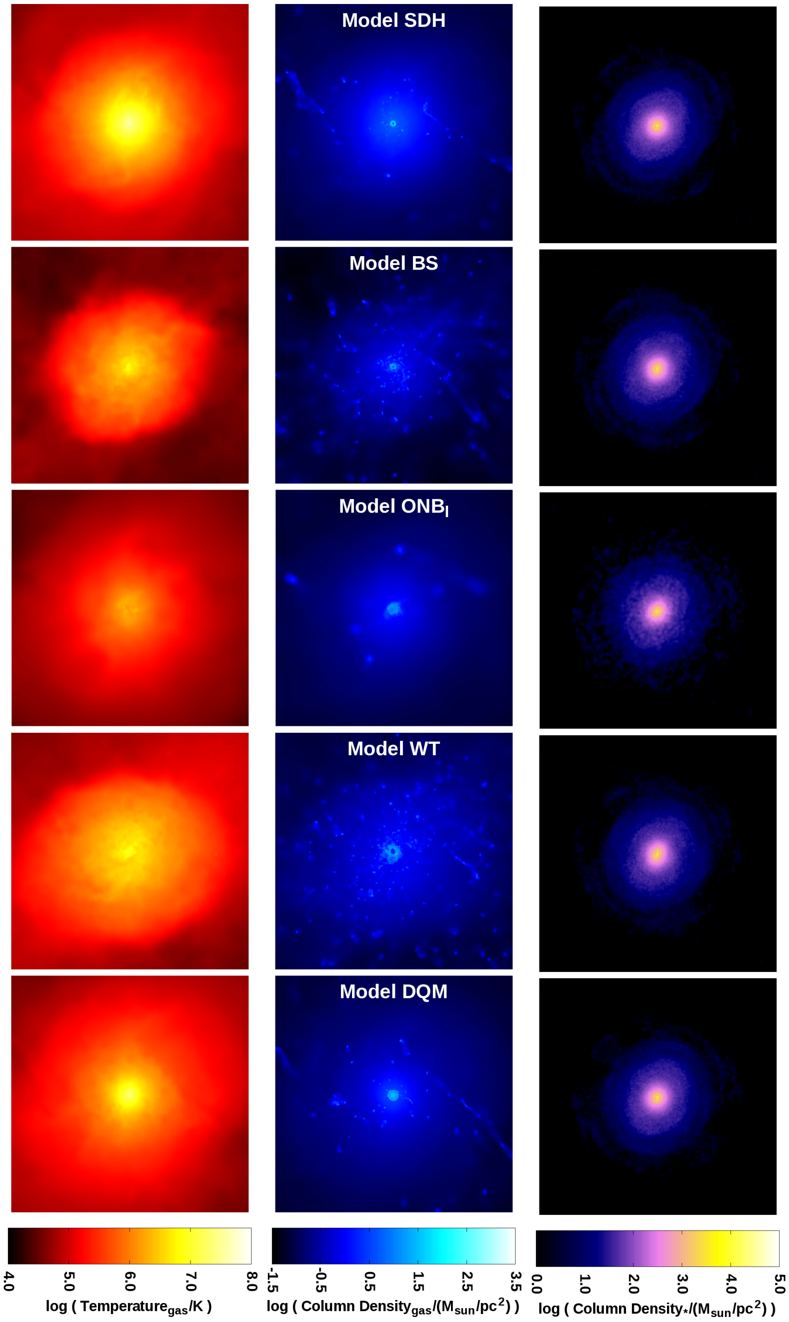

Figure 2.12: *Left to right*: Face-on gas temperature, gas column density, and stellar column density of each remnant. Each frame measures 100 kpc per side, with an image resolution of 195 pc pixel^{-1} (391 pc pixel^{-1}) for the fiducial (low) resolution models.

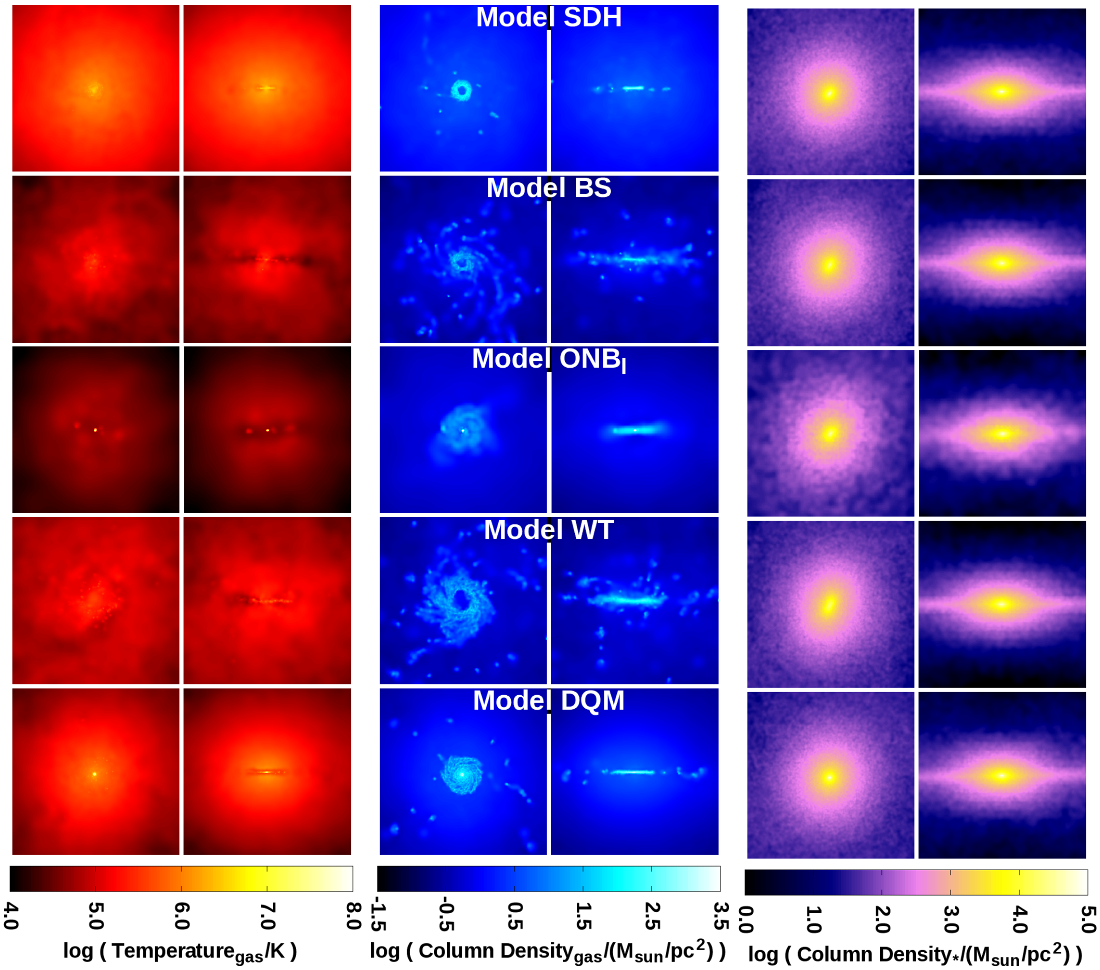

Figure 2.13: *Left to right*: Face-on and edge-on gas temperature, face-on and edge-on gas column density, and face-on and edge-on stellar column density of each remnant. Each frame measures 20 kpc per side, with an image resolution of 39 pc pixel^{-1} (78 pc pixel^{-1}) for the fiducial (low) resolution models.

Model	$\frac{M_{\rm stars,f}}{M_{\rm stars,i}}$	$\frac{M_{\rm gas,f}}{M_{\rm gas,i}}$	$\frac{M_{\rm disc\ gas,f}}{M_{\rm disc\ gas,i}}$	$\frac{M_{\rm halo\ gas,f}}{M_{\rm halo\ gas,i}}$	$\frac{M_{\rm BH,f}}{M_{\rm BH,i}}$	$\frac{M_{\rm acc}}{\Delta M_{\rm gas}}$
SDH	1.089	0.615	0.205	0.988	124.7	0.00286
BS	1.056	0.756	0.497	0.992	27.9	0.00096
ONB	1.053	0.772	0.527	0.996	66.8	0.00251
WT	1.061	0.734	0.452	0.992	137.6	0.00450
DQM	1.098	0.577	0.127	0.987	165.9	0.00339
BSw	1.046	0.802	0.592	0.992	16.6	0.00069
ONBc	1.055	0.766	0.513	0.996	1.4	0.00000
WTh	1.065	0.716	0.415	0.991	169.8	0.00521
DQMe	1.064	0.720	0.423	0.991	615.1	0.01917

Table 2.7: Ratios of final to initial global mass components for each of our fiducial resolution models; black hole masses are dynamic masses (except for Model DQM) since gas is removed in discrete amounts of $m_{\rm gas}$. Gas labelled as disc gas or halo gas is based upon its initial position. We define $M_{\rm acc}$ as the total mass of gas (dynamically) accreted by black holes and $\Delta M_{\rm gas} = M_{\rm gas,i} - M_{\rm gas,f}$. Depleted gas that is not accreted on to a black hole has been converted into stars. The values for Models ONB and ONBc are extrapolated to 1.5 Gyr based upon data from the final output and their low resolution counterparts. Specifically, we assume an average SFR of 1.0 $\rm M_\odot$ $\rm yr^{-1}$ (1.6 $\rm M_\odot$ $\rm yr^{-1}$) and $\dot{M}_{BH} = 5.3\times10^{-3}\rm M_\odot$ $\rm yr^{-1}$ ($6.0\times10^{-8}\rm M_\odot$ $\rm yr^{-1}$) for the remainder of the simulation for Model ONB (ONBc).

are similar remnants at 1.5 Gyr but different histories prior to this time. In all cases, a small disc begins to reform; the surface density profile for the reformed fiducial resolution discs is plotted in Fig. 2.14. The scale lengths of the discs embedded within the stellar remnant are approximately 0.5 kpc, compared to the initial value of 2.46 kpc. There are voids in the centre of the discs in Models SDH, BS and WT, thus the peak surface density occurs at 0.7–1.5 kpc from the centre. The voids persist from the residual angular momentum of the gas and from the weak (but remaining) AGN feedback.

2.4.2 Stellar remnant

As is a common test in numerical simulations of mergers (e.g. Di Matteo et al. 2005; Debuhr et al. 2011), we calculate the stellar velocity dispersion, σ, around the black hole for each remnant. Since the final result is a supermassive black hole in a stellar bulge, it is expected that — even after one merger — there would be some

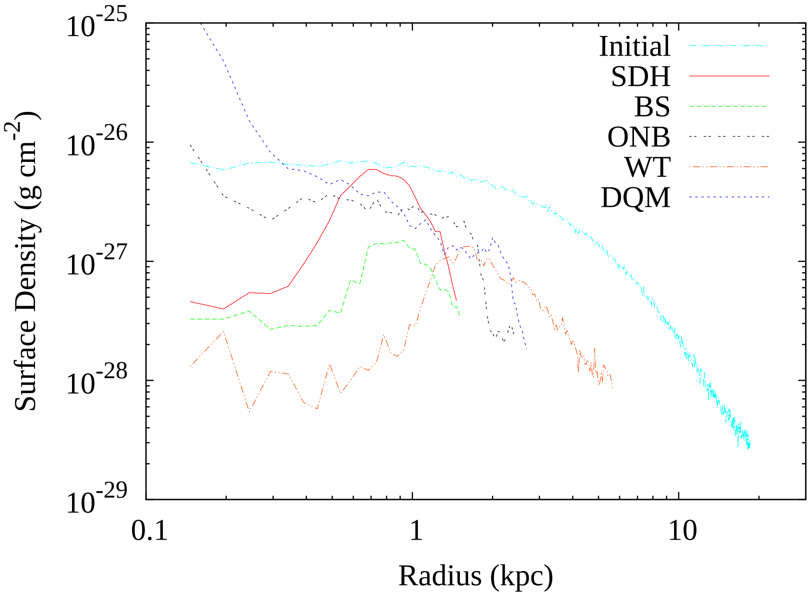

Figure 2.14: Gas surface density profile, averaged over all azimuthal angles, for the initial and final discs of the fiducial resolution models. The profiles are truncated at the edge of the disc, and plotted in bins of 49 pc. The remnant profile for Model ONB is taken at 1.25 Gyr.

agreement to the observed $M_{\rm BH}$–σ since the evolution of the black hole and bulge is coincident throughout the merger. To mimic observations, we calculate the velocity dispersion using

$$\sigma^2 = \frac{\int_0^{R_{\rm e}} \sigma_{\rm los}^2(r) I(r) r \, {\rm d}r}{\int_0^{R_{\rm e}} I(r) r \, {\rm d}r}, \tag{2.25}$$

where $\sigma_{\rm los}$ is the line of sight velocity dispersion, $I(r)$ is the projected 2D stellar density profile, and $R_{\rm e}$ is the half-light (mass) radius. This is similar to what is done numerically in DQM11 and observationally in Gültekin et al. (2009). Since the final stellar configuration is highly triaxial (see the two right-most columns in Fig. 2.13), the σ we present in Fig. 2.15 is averaged over 1000 random lines of sight. We have also included the full range of σ's calculated, as well as the preferentially chosen lines of sight along the $\pm x-$, $\pm y-$ and $\pm z-$directions.

The velocity dispersions are all very similar, with the five primary, fiducial resolution models having an average velocity dispersion of $161.8^{+19.2}_{-14.6}$ km s^{-1}. For the

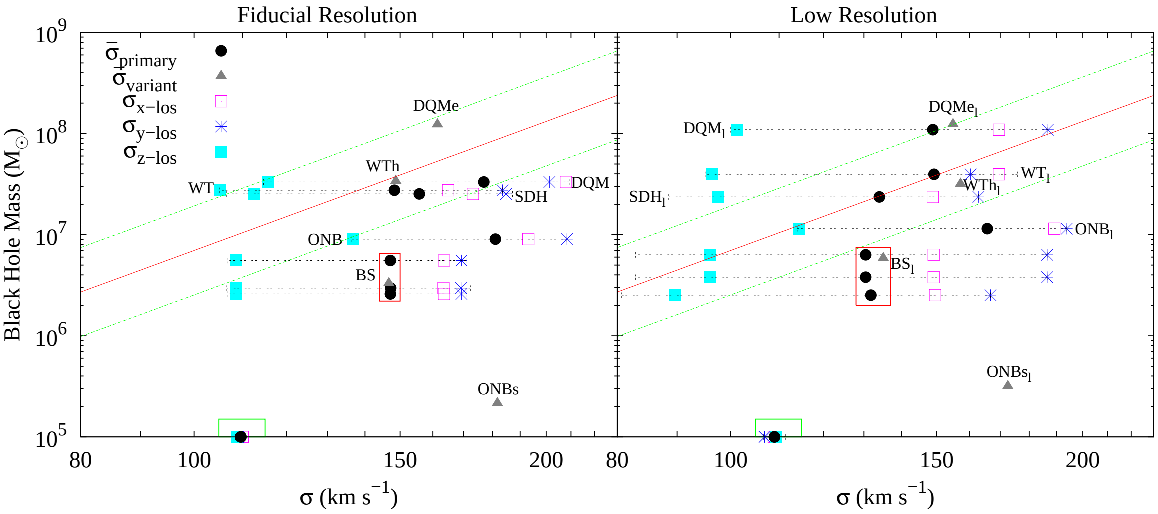

Figure 2.15: The $M_{\rm BH}$–σ relation for our simulations, along with the observed relation (red) and the one-sigma scatter (dashed) from Gültekin et al. (2009). For our five primary models at each resolution, the dot represents the average σ of 1000 random lines of sight, the horizontal bars represent the range of all calculated σs, and the remaining three symbols on the horizontal line represent σ taken along the $\pm x-$, $\pm y-$ and $\pm z-$lines of sight. For our variant models, we have only plotted the average σ of 1000 random lines of sight (solid triangles). We have explicitly labelled which points/set of points corresponds to which models. The black dots in the red rectangles represent the black holes in Model BS; the lower two points represent the actual black holes, and the upper point is calculated assuming one black hole with $M_{\rm BH} = M_{\rm BH_1} + M_{\rm BH_2}$ at the centre of mass of the black hole system. The solid triangle in the red rectangle is the result for Model BSw. The points in the green box are our initial relationships. The data for Models ONB and ONBc are taken at 1.25 Gyr.

fiducial (low) resolution models, the velocity dispersion spans a range of $\sim 75 \pm 15$ km s^{-1} ($\sim 90 \pm 15$ km s^{-1}), and is latitude dependent. Since the remnant reforms a disc, there is a large σ if the line of sight lies in the plane of the disc, and σ decreases as the elevation increases. Except for Models BS and ONB, the average σ lies within the one-sigma scatter of the observational relation.

Since the feedback in Models ONB and ONBc is delivered to the halo gas, the nuclear region is relatively unmodified by AGN feedback. Thus, we can expect a velocity dispersion of $\sim$180 km s^{-1} resulting from the merger of the two galaxies. When thermal AGN feedback is delivered to the core, the velocity dispersion is reduced by $\sim$30 km s^{-1}, which indicates that the method of thermal feedback has little impact on the final value of the velocity dispersion. Thus, how the feedback affects the *growth* of the black hole is likely the primary cause of whether or not the final result lies on the observed $M_{\rm BH}$–σ relation. Another test (not presented here) would be the $M_{\rm BH}$–$M_{\rm bulge}$ relation to see if this indicated that the bulge mass was also relatively independent of feedback mechanism. Lastly, with larger black hole masses typically comes more feedback energy, which has ultimately has a greater effect on the stars. Thus, it is not unreasonable that the more massive black holes have a tighter fit to the relation.

In Model BS, the black holes never merge and do not fall within one-sigma of the observed relation; the black holes in Model BSw merge, but still do not fall within one-sigma of the observed relation. This indicates that the difference from observational expectations is not a result of the lack of merger for the model parameters we have implemented. In these models, between apoapsis and second periapsis, the accretion rates are lower than the other models, which hinders black hole growth and is the likely cause of the lack of agreement with the observed $M_{\rm BH}$–σ relation.

In Model ONB, the black hole mass is 9.5 times lower than predicted by the $M_{\rm BH}$–σ relation, assuming the stellar velocity dispersion remains constant; a mass 3.4 times larger would bring the point within the one-sigma scatter of the relation. Since the feedback energy is returned far from the galactic core, gravity is the only influence the black hole has on the nearby stars. Thus, the self-regulating feedback mechanism is never fully realised, which could explain the lack of agreement with the observed relation. This is also true for Model ONBc, but to a more extreme extent since the low accretion rate means that the black hole only negligibly grows and cannot couple to the stellar system.

2.5 Conclusions

This chapter details a study of five different AGN feedback algorithms, which were all run using the numerical code Hydra, started from the same initial conditions, and implemented the same star formation algorithm. Two resolutions were tested for each model. The AGN feedback algorithms used in Models SDH, BS, ONB and DQM were previously found in the literature and the algorithm used in Model WT was developed specifically for this study. We also ran four additional models, each of which was a slight variation of one of the primary models to study a specific aspect of the model.

We have performed a full analysis of all models, but only presented fiducial resolution results of the five primary models and selected other results. Although the low resolution models run considerably faster, their results are noisy, and some of the physics is essentially lost. However, the low resolution studies are a good test of the varying feedback models, and provide a first-order comparison between the models. Furthermore, the continued implementation of cosmological simulations mean these resolutions will inevitably be used in the future.

By comparing these models using the same initial conditions, star formation algorithm and numerical code, any differences obtained are a direct result of the AGN feedback. Although we have tried to isolate each component of the AGN feedback algorithm, we accept that they are all intimately intertwined, and the effects cannot necessarily be disentangled from one another. We also accept that every simulation we run involves free parameters. Although we have — as best as possible — matched them to their source simulations from the literature, it is possible that we can modify these parameters such that all simulations will return similar final states. Since the goal of this chapter was to compare different feedback models and not to analyse any given model in great detail, we defer to the source literature for discussions on the sensitivity of the results to the free parameters. We thus refrain from making strong statements about the 'accuracy' of given models.

Our principal conclusions of the five key components are as follows:

1. The black hole advection algorithm plays a key role since small displacements can cause great changes in the accretion rate. Coupling the black hole to a gas particle can allow for oscillations or chaotic motion if a void is formed around the black hole, or if the nearby gas does not meet the velocity criteria. Using a tracer mass yields smooth movement of the black hole, but the evolution time of the merger is decreased and disc morphology is altered in non-trivial ways such as preventing the formation of a bar. This obviously impacts other physical properties, most notably the SFR. Clearly, evolving the mass of the black hole in a way that does not overly impact the expected evolution of the disc is an important goal. The algorithms that limit the distance a black hole can be displaced per iteration and where the direction is based upon the local stellar or total mass distribution appear to be optimal.

2. We test four different accretion rates: $\dot{M}_{\rm B}(\alpha = 100)$, $\dot{M}_{\rm B}(\alpha \equiv \alpha(n_{\rm H}))$, $\dot{M}_{\rm drag}$ and $\dot{M}_{\rm visc}$. Each model yields a different accretion history, with substantially different qualitative profiles and quantitative differences of up to a factor of three orders of magnitude at any given time. The total black hole mass in the remnants varies by factor of 6.9, with Model BS being the least massive, and DQM being the most massive. The three models that fall within one-sigma scatter of the $M_{\rm BH}$–σ relation have final black hole masses that differ by less than 30 per cent.

3. The form of feedback can drastically modify the large- and small-scale systems. Delivering the feedback to the halo gas leads to little modification of the core

region, resulting in high core densities and nominal temperatures. Thermal feedback delivered to the core region can drive strong outflows. Kinetic feedback delivered to the core region efficiently creates a void around the black hole, resulting in low gas temperature and density. This feedback is persistent and efficient, keeping the core properties nearly constant for all time. Only a cataclysmic event, such as a core merger, can modify these characteristics.

4. We tested three categories of particle accretion algorithms: stochastic-unconditional, stochastic-conditional and continual-conditional. Two of the three continual-conditional algorithms randomly selected *which* particles were accreted but never *how many* or *how often*. The continual-conditional cases gives the best agreement between the dynamical and internal mass; here, the discrepancy is never more than $2m_{\mathrm{g}}$. The stochastic-unconditional algorithm of Model SDH, however, contains discrepancies up to $15m_{\mathrm{g}}$. Thus, for agreement between dynamical and internal masses, continual-conditional algorithms appear optimal.

5. In Models BS and BS_{l}, the black holes never merge. In these models, there is considerable chaotic movement of the black holes in the remnant core, preventing both merger criteria from being simultaneously met. In the remainder of the models, the black holes merge during or shortly after core merger, as one would reasonably expect. The importance of a ‘reasonable’ merger time is that the amount of feedback energy available increases across the merger for Bondi accretion and decreases for drag and viscous accretion.

The models presented here do not represent an exhaustive list. For example, an accretion rate suggested by Hobbs et al. (2012) is an interpolation between Bondi accretion and a free-fall accretion rate. Power et al. (2011) suggest using an accretion disc particle. In this two-tier accretion process, gas is first accreted on to an accretion disc, and then the gas is accreted from the disc on to the black hole using a viscous time-scale. The accretion disc particle method of accretion has recently been implemented in major merger simulations similar to those presented here (Wurster & Thacker 2013b); see Chapter refADPaccretion.

Lastly, while it is possible that free parameters in different models can be adjusted such that all yield similar final states, it is very clear that this will not produce agreement throughout the evolution. While we have a vast amount of observational data of many stages of major mergers — including final remnants — it is difficult to build these various snapshots into an obvious picture of the evolutionary processes, and the fundamental theoretical development of AGN modelling still has much to contribute in this regard. As we have shown here, given the many different models of AGN feedback, building an understanding of the evolution of mergers is an important and challenging task.

Chapter 3

Accretion Disc Particle Accretion in Major Merger Simulations

This chapter is published as Wurster & Thacker (2013b). We have removed text and details regarding the set up of the numerical simulation, and Models SDH and DQM that have previously been presented in Chapter 2, to which we will simply refer. We have also removed figures that have been made redundant by the inclusion of the previous chapter.

Abstract

A recent approach to simulating localized feedback from active galactic nuclei (AGN) by Power et al. (2011) uses an accretion disc particle to represent both the black hole and its accretion disc. We have extrapolated and adapted this approach to simulations of Milky Way-sized galaxy mergers containing black holes and explored the impact of the various parameters in this model as well as its resolution dependence. The two key parameters in the model are an effective accretion radius, which determines the radius within which gas particles are added to the accretion disc, and a viscous time-scale which determines how long it takes for material in the accretion disc to accrete on to the black hole itself. We find that there is a limited range of permitted accretion radii and viscous time-scales, with unphysical results produced outside this range. For permitted model parameters, the nuclear regions of simulations with the same resolution follow similar evolutionary paths, producing final black hole masses that are consistent within a factor of two. When comparing the resolution dependence of the model, there is a trend towards higher resolution producing slightly lower mass black holes, but values for the two resolutions studied again agree within a factor of two. We also compare these results to two other AGN feedback algorithms found in the literature. While the evolution of the systems vary, most notably the intermediate total black hole mass, the final black hole masses differ by less than a factor of five amongst all of our models, and the remnants exhibit similar structural parameters. The implication of this accretion model is that, unlike most accretion algorithms, a decoupling of the accretion rate on to the black hole and the local gas properties is permitted and obtained; this allows for black hole growth even after feedback has prevented additional accretion events on to the disc.

Key words: black hole physics – galaxies: interactions – galaxies: active – methods: numerical

3.1 Introduction

Observational evidence suggests that supermassive black holes exist at the centre of all galaxies with stellar spheroids (e.g. Kormendy & Richstone 1995; Ferrarese & Merritt 2000). Further evidence, such as the M_{BH}–σ relationship (e.g. Silk & Rees 1998; Ferrarese & Merritt 2000; Gebhardt et al. 2000; Tremaine et al. 2002; King 2003; Gültekin et al. 2009) and the M_{BH}–M_{bulge} relationship (Magorrian et al. 1998; McLure & Dunlop 2002; Marconi & Hunt 2003), suggests that the black hole and spheroid evolution are related. Moreover, galaxies are less luminous today than might be naively predicted from the hierarchical model of galaxy formation, indicating that some mechanism has limited the growth of these galaxies (e.g. Silk & Mamon 2012). One favoured explanation is that, during mergers, gas from the merger fuels both star formation and AGN activity (e.g. Sanders et al. 1988; Scannapieco et al. 2005). The latter is likely a self-regulated process: outflows from the black hole following a strong accretion event interact with the surrounding gas, inhibiting further accretion events, and hence limiting black hole growth (e.g. Silk & Rees 1998; Fabian 1999b; Scannapieco & Oh 2004; King 2005; King 2010). Ultimately, the feedback from the increased AGN activity blows away some or possibly all the gas, truncating the star formation and leading to an elliptical galaxy (e.g. Springel et al. 2005a).

Using various models, AGN feedback has been implemented in many numerical simulations (e.g. Springel et al. 2005b; Thacker et al. 2006; Okamoto et al. 2008; Booth & Schaye 2009; Kurosawa et al. 2009; Debuhr et al. 2011). The goals of this research have been varied, from reproducing the observed relationships between the black hole and spheroid, to other factors impacted by AGN activity, such as galaxy cluster properties (e.g. Puchwein et al. 2008) or even the impact on CMB foregrounds (e.g. Scannapieco et al. 2008). In all these simulations, the accretion rate of gas on to the black hole is dependent on extrapolating the macroscopic gas properties to the microscopic scale around the black hole. This is true for viscous accretion (e.g. Debuhr et al. 2011; Hopkins & Quataert 2011), drag accretion (Okamoto et al. 2008), and the form of the Bondi accretion rate (Bondi 1952) modified for numerical simulations,

$$\dot{M}_{\rm Bondi} = \frac{4\pi\alpha G^2 M_{\rm BH}^2 \rho}{(c_{\rm s}^2 + v_{\rm rel}^2)^{3/2}}, \tag{3.1}$$

where α is a numerical parameter used to account for the limited dynamic range in the simulations, ρ and $c_{\rm s}$ are the gas density and sound speed around the black hole, $v_{\rm rel}$ is the relative velocity between the gas and the black hole, and $M_{\rm BH}$ is the mass of the black hole. This accretion rate has been used in merger (e.g. Springel et al. 2005b; Di Matteo et al. 2005) and in cosmological (e.g. Sijacki et al. 2007; Booth & Schaye 2009) simulations.

Most algorithms also limit the mass accretion to be no greater than the Eddington accretion rate,

$$\dot{M}_{\rm Edd} \equiv \frac{4\pi G M_{\rm BH} m_{\rm p}}{\epsilon_{\rm r} \sigma_{\rm T} c}, \tag{3.2}$$

where $m_{\rm p}$ is the proton mass, $\sigma_{\rm T}$ is the Thomson cross section, and $\epsilon_{\rm r}$ is the radiative efficiency (i.e. the mass-to-energy conversion efficiency); we set $\epsilon_{\rm r} = 0.1$ (Shakura & Sunyaev 1973). This rate differs from the previously considered accretion rates in that it depends only on the black hole mass, and not the local gas properties.

One of the assumptions frequently used in these models is that any accreted gas is immediately transferred to the black hole. This is clearly an unrealistic assumption as material must first shed its angular momentum. Indeed some models argue that understanding this process is one of the key factors in modelling AGN feedback; for example, the viscous accretion rate in Debuhr et al. (2011) accounts for angular momentum of the gas. However, the gas in this model is nonetheless instantly accreted on to the black hole. In reality the gas would be expected to settle on to a circular orbit of radius R_{circ}, which is set by the angular momentum of the gas and whatever processes cause it to shed angular momentum while collapsing (cf. Hobbs et al. 2011), resulting in an accretion disc around the black hole. The gas with the lowest angular momentum would then travel through the disc and eventually be accreted on to the black hole (e.g. King 2010).

Motivated by these ideas, Power et al. (2011) (hereafter PNK11) have implemented a two-stage accretion algorithm using an accretion disc particle (ADP), which models both the black hole and accretion disc. In the first stage, nearby gas, the bulk of which will have shed large amounts of angular momentum to reach this radius, is accreted on to the accretion disc; this accretion rate is dependent only on the relative positions of the black hole and the gas particle. In the second stage, the gas is accreted from the accretion disc on to the black hole. This method incorporates the delay between the time gas is accreted on to the disc and when it is finally accreted on to the black hole, and at the same time decouples the black hole's accretion rate from the instantaneous gas properties around the black hole.

While the ADP model implemented in Power et al. (2011) relies upon resolving scales far smaller than those that can be resolved in merger simulations, the two stage approach, and perhaps more specifically the incorporation of a delay period before accreting on to the black hole, is an issue worthy of investigation in merger simulations which can have time-steps in the few thousand year range. But this consideration highlights the fact that resolution dependence must be considered. For example, at very low mass resolution and the associated low time resolution, concerns about accretion delays are likely less significant as the ratio of time-step and delay time get closer to unity. Therefore investigating the precise resolution dependence is important. We also emphasize that the ADP model needs additional features to be implemented in a merger simulation, and we have drawn on prior work and use methods that have been well studied in the literature.

The layout of this chapter is as follows: In section 3.2 we discuss salient details of the simulation including the PNK11 model and how we have augmented it to allow for black hole tracking. In section 3.3 we compare the behaviour of the merger simulations and the sensitivity of final state diagnostics, specifically the black hole mass, as a function of the model parameters. We end with a brief review.

3.2 Numerical Simulations

We test the ADP method in a simulation of a major merger of two Milky Way-sized galaxies, as described in §2.2.

To implement an AGN feedback algorithm motivated by the PNK11 model, we have had to make some modifications and additions. We have modified how feedback is returned to the local gas, and added both a black hole advection algorithm and a black hole merger algorithm. None of the issues related to black hole advection or mergers are addressed within the PNK11 paper since they consider accretion of gas on to a black hole that is embedded within an initially spherical gas cloud.

3.2.1 Implementing the PNK11 model: Approach to accretion

The black hole accretion algorithm is the same as in PNK11. In this method the accretion disc particle (ADP) is a collisionless sink particle containing both the black hole and its tightly bound accretion disc. The mass of the ADP is given by

$$M_{\mathrm{ADP}} = M_{\mathrm{BH}} + M_{\mathrm{disc}}, \tag{3.3}$$

where M_{BH} is the mass of the black hole and M_{disc} is the mass of the accretion disc. As in PNK11, we initialise $M_{\mathrm{disc}} = 0$, while we choose the initial black hole mass in each galaxy to be 10^5 $\mathrm{M}_{\odot}$. The ADP has an associated 'smoothing length', h_{ADP}, which is calculated at every iteration by $h_{\rm ADP} = \max\left(h_{\rm ADP}, h_{\rm min}\right)$, where a sphere with radius $2h_{\rm ADP}$ around the ADP includes 60 gas particles, and $h_{\rm min}$ is the smallest resolved smoothing length in the SPH solver. The smoothing length is used to calculate the gas properties at the location of the ADP, which is used for analysis and returning feedback energy. The ADP is also given an accretion radius, $R_{\rm acc}$, which is a free parameter of the model that determines at what radii particles are considered to have accreted on to the accretion disc. Nominally, and indeed in PNK11, this radius is expected to be on the order of a pc. While merger simulations can reach these small radii by considering arbitrarily small values of $R_{\rm acc}$, it is worth emphasizing that the properties of the gas on these scales is not resolved. Indeed this is a generic problem with feedback models in general, namely that they use input parameters at the edge of model resolution. However, since this is an unavoidable problem, we continue on with this issue noted and examine the impact of varying the value of $R_{\rm acc}$ by up to a factor of 10.

Whenever a gas particle comes within $R_{\rm acc}$ of the ADP, it is instantly accreted on to the accretion disc, thus $M_{\rm disc} \rightarrow M_{\rm disc} + m_{\rm gas}$, where $m_{\rm gas}$ is the mass of the gas particle. The accreted particle's mass and momentum are added to the ADP, and then the accreted particle is removed from the simulation. This capture rate is not limited in any way, and solely depends on the particles' relative locations. Once accreted on to the accretion disc, it takes time for the gas to be transported through the disc so that it can finally be accreted on to the black hole. This time delay is on order of the disc viscous time, $t_{\rm visc}$, which must be larger than the dynamical time at the accretion radius; PNK11 set $t_{\rm visc}$ as a free parameter, but argue that it should be $t_{\rm visc}$ ∼10–100 Myr in galaxy formation simulations.

The mass accretion rate on to the black hole from the accretion disc is given by,

$$\dot{M}_{\rm BH} = \min\left(\frac{M_{\rm disc}}{t_{\rm visc}}, \dot{M}_{\rm Edd}\right). \qquad (3.4)$$

To preserve mass continuity, the mass added to the black hole is removed from the accretion disc although the overall ADP mass remains the same. As in most numerical implementations of AGN feedback, the accretion rate on to the black hole is Eddington-limited; this moderates the growth of the black hole based upon a physical limit rather than just from the numerical accretion on to the disc.

3.2.2 Implementing the PNK11 model: Changes and additions for merger simulations

3.2.2.1 Feedback

PNK11 use the same feedback scheme as described in Nayakshin & Power (2010). In this scheme, feedback energy is returned by adding wind particles which are radially directed away from the black hole; the wind particles have momentum $p_{\text{wind}} = 0.1 m_{\text{gas}}\sigma$, where σ is the velocity dispersion of the host galaxy. In our simulation, it is impractical to continually add wind particles since the particle load in the solver will climb rapidly. Instead follow the wind prescription used in Debuhr et al. (2011), where the feedback rate is given by

$$\dot{p} = \tau \frac{L}{c}, \tag{3.5}$$

and where $\tau = 10$ is the assumed infrared optical depth, $L = \epsilon_{\text{r}} \dot{M}_{\text{BH}} c^2$ is the luminosity, and $\epsilon_r = 0.1$ is the radiative efficiency. The momentum is returned radially, such that every gas particle within the ADPs radius of influence, $r_{\text{inf}} \equiv 2h_{\text{ADP}}$, receives an equal acceleration. We reiterate that r_{inf} has no explicit dependence on R_{acc} and is being recalculated at every iteration.

3.2.2.2 Black hole advection and mergers

The black hole advection algorithm is a modified version of that presented in Okamoto et al. (2008) and used in Model WT in Wurster & Thacker (2013a). Here, the ADP is displaced towards the centre of mass of the sphere with radius r_{inf} which is centred on the ADP. The distance it is displaced is

$$\Delta l = \min(0.10 h_{\rm ADP}, 0.30\,|\boldsymbol{v}|\,{\rm d}t, d_{\rm CM}), \tag{3.6}$$

where $\boldsymbol{v}$ is the velocity of the black hole, ${\rm d}t$ is the time-step, and $d_{\rm CM}$ is the distance from the black hole to the centre of mass. The coefficients are based upon those in Okamoto et al. (2008), but modified for our higher resolution. Following the approach of Okamoto et al. (2008), we have selected the parameters to suppress the oscillations of the black hole particles such that the maximum amplitude of the black hole oscillation between the start of the simulation and first periapsis is less than 0.25 per cent of the core radius. This method continually displaces the black hole towards the centre of mass to counter any two-body interactions that may try to displace the black hole from the bottom of the potential well. Limiting the distance preserves the possibility of the black hole remaining in a gas void. One option we considered but did not implement was to couple the ADP to the gas particle that has the lowest potential energy, is within $r_{\rm inf}$ of the ADP and satisfies $v_{\rm rel} < 0.25 c_{\rm s}$, where $v_{\rm rel}$ is the relative velocity between the ADP and the gas particle and $c_{\rm s}$ is the local sound speed. Generally, this can lead to large artificial displacements and prohibits the black hole from remaining in a gas void, but with this specific accretion algorithm, it would artificially increase the accretion rate by arbitrarily moving the ADP within $R_{\rm acc}$ of a gas particle. A second option we considered was to use a tracer particle whose mass is ∼100–1000 times greater than any other particle. Although this method produces a smooth black hole trajectory, the additional mass affects the evolution time when compared to non-tracer particle models.

Finally, when the ADPs pass within each others smoothing lengths and have a relative velocity less than the local sound speed, they are assumed to merge instantly. The merged black hole has the combined mass of the progenitor black holes, and the merged accretion disc has the combined mass of the progenitor discs, thus all masses are conserved. This is similar to the numerical merger procedure used in Springel et al. (2005b).

3.2.3 Parameter space and resolution dependence

To understand the impact of the two free parameters, $R_{\rm acc}$ and $t_{\rm visc}$, we ran a suite of simulations within this parameter space and considered two separate resolutions for a total of 17 simulations. We plot where the simulations lie in the parameter space in Fig. 3.1, where each point corresponds to a model. Our parameter space is

1. resolution $\in \{\text{low}, \text{fiducial}\}$,
2. $R_{\rm acc}/h_{\rm min} \in \{0.02, 0.05, 0.10, 0.20\}$, and
3. $t_{\rm visc}/\text{Myr} \in \{1, 5, 10\}$.

In Table 3.1, we convert the accretion radius to physical units for both resolutions. The choices of $R_{\rm acc}$ were primarily for numerical considerations. At these radii, the dynamical time-scale varies from a few dozen kiloyears to a Megayear, assuming a black hole of mass $10^5\text{M}_\odot$, and the fiducial resolution time-step is typically a few tens of kiloyears. Given these considerations, and the only criterion that the viscous time-scale must larger than the dynamical time-scale, we chose the three values given above. Our model naming convention is understood as follows: ‘$\text{PNK}_{\text{resolution}}\text{r}(100R_{\rm acc}/h_{\rm min})\text{t}(t_{\rm visc}/\text{Myr})$’. If we do not include a resolution when referring to a model, then we are referring to both resolutions. In terms of wall-clock time, despite having a modest particle content, the fiducial resolution models still take over a month to run on 16 processors due to the large number of time steps required, the lack of multiple time-steps in the HYDRA solver and also an $\mathcal{O}(n^2)$ slowdown that occurs as large numbers of SPH particles reach the minimum smoothing length of the solver. We thus have a limited number of fiducial resolution simulations.

R_{acc} (h_{min})	Fiducial resolution (pc)	Low resolution (pc)
0.02	0.731	1.827
0.05	1.827	4.567
0.10	3.654	9.133
0.20	Not run	18.266

Table 3.1: The accretion radii, R_{acc}, in our parameter space, given in simulation and physical units.

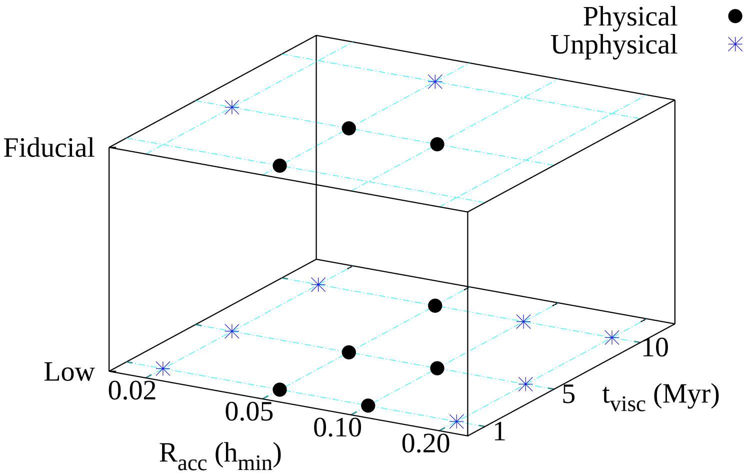

Figure 3.1: The parameter space that we tested. Each point corresponds to a model; the physical/unphysical designation will be discussed in §3.3.

3.3 Results

3.3.1 General evolution

Each of our models was evolved for 1.5 Gyr through a merger event, similar to that of Springel et al. (2005b). We found that each model followed a similar qualitative history to that presented in Chapter 2; see Figs. 2.1 and 2.2 for the typical evolution of the gas column density and gas temperature, respectively.

There are four significant evolutionary epochs: first periapsis, apoapsis, second periapsis and core merger, occurring at $\sim$170, 480, 880 and 990 Myr, respectively; the low resolution models reach second periapsis and core merger 25 and 6 Myr, respectively, earlier than their fiducial resolution counterparts. In all our fiducial resolution models, the black holes merge at 1.01 Gyr, and their low resolution counterparts merge 10–60 Myr later. The later merger in the low resolution models is a result of the binary black holes oscillating about one another with a greater amplitude than in the fiducial resolution models; this is from both the low resolution black holes being more massive by this epoch (see section 3.3.6), and there being fewer particles to induce drag on the black hole system.

The final remnant is a reformed gas disc and flattened stellar ellipsoid surrounded by a hot gas halo; the remnant is further discussed in section 3.3.7. The final gas discs in the fiducial resolution models have scale lengths of approximately 0.5 kpc, compared to the initial scale length of 2.46 kpc and are essentially an order of magnitude less massive than the discs in the initial conditions. Of the gas that was initially in a disc, 89 per cent of it is either accreted on to the black hole or converted into stars. With a final star formation rate of less than 0.5 $\mathrm{M}_{\odot}$/yr, the final configuration is a red and dead elliptical, as expected (Springel et al. 2005a).

To quantify this evolution, we have plotted the total black hole mass, the accretion rates on to the black hole, and the gas density and gas temperature within r_{inf} of the ADP for Model PNKr05t05 in Fig. 3.2; the accretion rates and gas properties are geometrically averaged over both black holes and plotted in bins of 10 Myr.

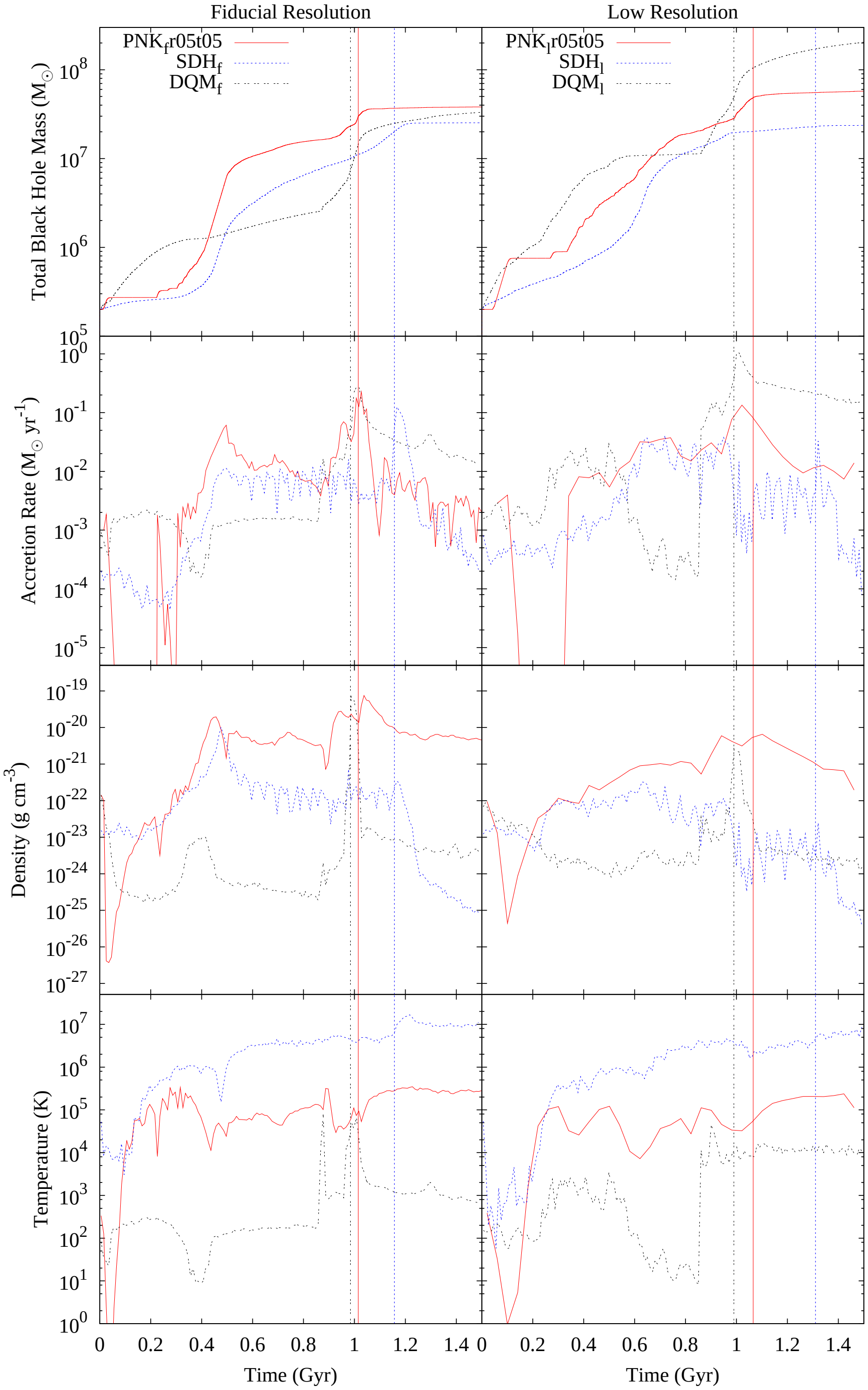

Figure 3.2: *Top to bottom*: Total black hole mass, accretion rates on to the black hole, gas density and gas temperature within $r_{\rm inf}$ of the ADP/black hole particle. The bottom three rows are geometrically averaged over both black holes in bins of 10 Myr. The left panels are from the fiducial resolution simulations and the right panels are from their low resolution counterparts. The vertical line of the same linestyle indicates when the black holes merge.

For the first ∼300 Myr, $r_{\mathrm{inf}} > 2h_{\mathrm{min}}$, and there are only 60 gas particles within this radius. After ∼300 Myr, $r_{\mathrm{inf}} = 2h_{\mathrm{min}}$, and there are several thousand particles within this radius. There is an increasing accretion rate after first periapsis, which peaks near apoapsis, and a second peak at core merger. The gas density in the core also increases from first periapsis to apoapsis, and again at core merger. The core temperature stays relatively moderated after first periapsis. The initial decline in gas density and temperature is a result of the feedback energy carving out a void around the black hole in the initial density field which is quite symmetric. The SPH particles that contribute to the density and temperature at the location of the black hole are at $r \sim 0.9r_{\mathrm{inf}}$, thus provide only a minimal contribution. Thus, these low densities and temperatures are essentially a result of the smoothing kernel breaking down due to a poor distribution of the particles within $2h_{\mathrm{ADP}}$. An ideal distribution would have particles distributed throughout $2h_{\mathrm{ADP}}$ and not just in a ring near the edge of the volume. Also, when calculating properties at the location of a gas particle, the properties of the particle itself are included; this is not true in this case since the black hole particle itself does not have any intrinsic gas properties. At later times the number of particles increases and symmetry is lost which prevents any spurious temperature and density values from being calculated.

3.3.2 Comparison to other models in the literature

We briefly compare Model PNKr05t05 to two other models found in the literature, namely Model SDH (see §2.2.5.1) and Model DQM (see §2.2.5.4). We plot the total black hole mass, the accretion rates on to the black hole, and the gas density and gas temperature within r_{inf} of the black hole for Models SDH and DQM in Fig. 3.2.

Although all three accretion and feedback algorithms make different physical assumptions, the final total black hole masses in the fiducial (low) resolutions are equal within a factor of 1.52 (4.62). The accretion histories, however, vary considerably. As expected, Models SDH and DQM have continual accretion which starts immediately, but the accretion rate in PNKr05t05 is punctuated by periods of nearly zero accretion, especially at early times. The latter is a result of feedback from the first few accretion events creating a small and transient void around the ADP, as can be seen in the core density profile. After first periapsis, tidal torques are large enough and feedback energy is low enough to allow additional accretion events.

The core density of Model DQM is the lowest of these three models. In Model $\mathrm{DQM_f}$, kinetic feedback builds up in the gas and, after 60 Myr, a void of $\sim 0.55 r_{\mathrm{inf}}$ is formed and maintained for the duration of the simulation. Although Model PNKr05t05 uses the same feedback algorithm, the initially lower accretion rate prevents this build up of kinetic feedback, thus this void never forms, hence the higher core density. The core temperature is highest for Model SDH, where thermal feedback energy directly increases the temperature of the gas. The core heating of Models PNK and DQM is from shock heating and star formation. The higher accretion and star formation (not shown) rates in PNKr05t05 after first periapsis results in more heating than in Model DQM.

3.3.3 Acceptable parameter ranges

We ran 12 low resolution simulations to probe our entire R_{acc}–t_{visc} parameter space. At our fiducial resolution we only tested five models because of the time required to complete individual simulations. After analysing the results, each simulation was classified as either physical or unphysical, as indicated by the dot type in Fig. 3.1. The basis for our definition of physical or unphysical relies upon a combination of structural evolution and how close the final remnant lies to the M_{BH}–σ relationship. We note that relying upon the M_{BH}–σ relationship is perhaps not a strong constraint because the masses of the seed black holes could be changed. However it remains a commonly used approach in these simulations and we thus proceed cautiously with this issue noted.

For R_{acc} values that are very small, the accretion rate on to the black hole will be limited. The expectation in this case is that the resulting remnant will fall below the $M_{\rm BH}$–σ relation. Our numerical experiments show this to be true for all the models with $R_{\rm acc} = 0.02h_{\rm min}$, with the black hole mass in PNK$_{\rm f}$r02t05 being 4.5 times lower than expected, assuming the velocity dispersion remains constant. These models also suffer from sensitivity to operation ordering in the solver. At a given resolution, we would expect the absorption of particles to occur at the same time provided that the operations in the solver are executed in the same order, and hence produce the same round-off. However, when running in parallel with dynamic load-balancing this is no longer the case since the calculations will be shared amongst all the processors in a different way each time. Round-off errors will be different for each calculation order, and will accumulate to produce subtle differences around or just above machine precision. Thus, with too small of an accretion radius, pseudo-random issues due to machine precision dominate the accretion, and the results of a given simulation are not easily reproducible. On the basis of lying beneath the $M_{\rm BH}$–σ relation and the exhibited numerical sensitivity, we classify all of our $R_{\rm acc} = 0.02h_{\rm min}$ models as 'unphysical'.

At the other extreme of our parameter space, there can be unphysical results if the accretion rate on to the disc is too high. If $R_{\rm acc}$ is too large, then many particles can pass within this radius and be accreted on to the disc, regardless of the amount of feedback. Likewise, a large $t_{\rm visc}$ means that the feedback energy is being returned at a lower rate, thus particles have less of an obstacle to overcome to pass within $R_{\rm acc}$ when influenced by outside forces (i.e. tidal torques from the interacting galaxies). Both result in a large accretion rate on to the disc, where the accretion disc mass can surpass the mass of the black hole (see right-most panel of Fig. 3.3; the remaining three panels show the profiles for physical models, where the peak accretion disc mass is $\sim 5\times10^{6}{\rm M}_{\odot} < M_{\rm BH}$). This unreasonably large accretion rate on to the disc yields a large and continual accretion rate from the disc on to the black hole, which results in a vast amount of feedback energy. Once a critical amount of kinetic feedback is injected into the gas, namely that sufficient to overcome the nuclear gravitational binding energy, a large, unphysical void (i.e. there are no observational counterparts

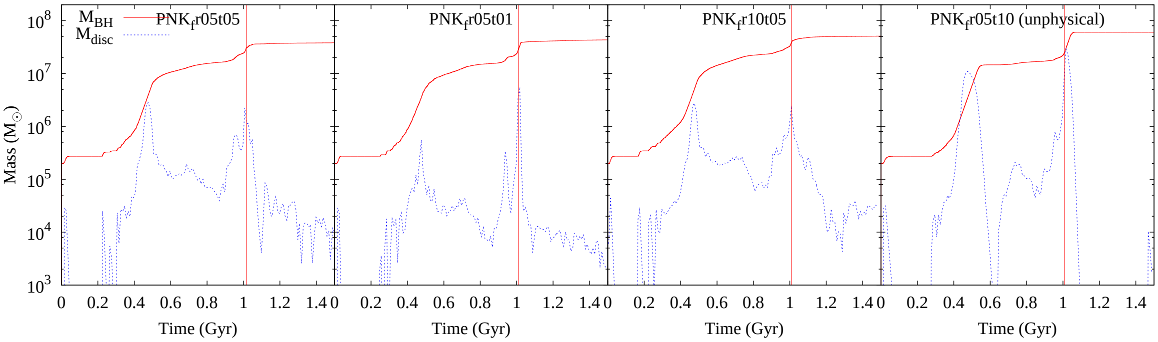

Figure 3.3: Total black hole mass (solid red line) and total accretion disc mass (dashed blue line; geometrically averaged over both black holes and plotted in bins of 10 Myr) for four fiducial resolution models. The vertical line indicates when the black holes merge.

to these voids) is formed in the galaxy. This in turn suppresses the accretion rate on to the ADP, but not from the disc on to the black hole. The accretion disc is ultimately depleted, the feedback ends and the void recollapses to begin another cycle. In situations where a large radius and large viscous time-scale are included it is possible to remove the gas from the system.

These unphysical voids often foreshadow the total disruption of the remnant. Starting at 1.04 Gyr in Model PNK$_\mathrm{f}$r05t10, there is a catastrophic explosion, and the system is totally disrupted within 60 Myr. In other models, specifically our low resolution models, the core merger causes an increase in the accretion rate, leading to a final feedback episode that disrupts the system, although often less catastrophically than Model PNK$_\mathrm{f}$r05t10. While the system is highly disrupted, there are often no noticeable voids, and the process is ‘gentle’ enough that the gas begins to recondense into a disc and cloud. We cautiously and liberally classify these results as physical.

In Fig. 3.4, we have plotted the actual and the Eddington accretion rates for six models; we also give the length of time each system is undergoing Eddington-limited accretion in the top right corner of each panel. The unphysical model PNK$_\mathrm{f}$r05t10 is undergoing Eddington-limited accretion for 11.7 per cent of the time, thus a (relatively) high percentage is a possible indicator of an unphysical model. However, the

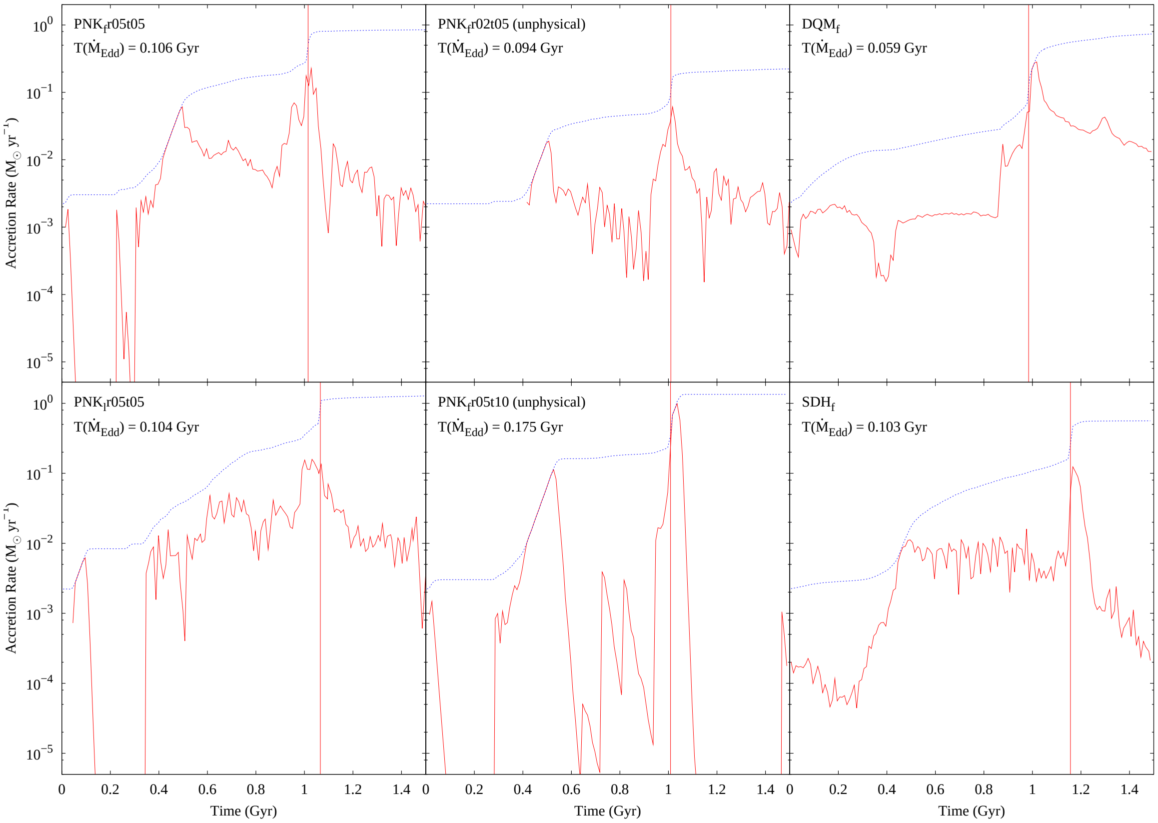

Figure 3.4: Actual (solid red line) and Eddington (dashed blue line) accretion rates for six models, geometrically averaged over both black holes and plotted in bins of 10 Myr. The vertical line indicates when the black holes merge. Model names and length of time the system is undergoing Eddington accretion are listed in the top right of each panel.

unphysical Model $\mathrm{PNK_f}$r02t05 undergoes Eddington-limited accretion 6.3 per cent of the time, which is higher than the per cent of time the physical Model $\mathrm{DQM_f}$ is undergoing Eddington-limited accretion. While there is a correlation between the amount of time spent in Eddington-limited accretion and the final black hole mass for the PNK models, this is not true when comparing across different models. Further, these numbers indicate that relying upon the M_{BH}–σ relationship appears to place the amount of time in Eddington-limited accretion in a comparatively narrow band. It is thus difficult for us to draw detailed conclusions about using the amount of time spent in Eddington-limited accretion as a strong discriminant between the physical or unphysical nature of models.

Ultimately, the amount of time spent accreting at the Eddington limit is very closely related to the duty cycle of the quasar. In the context of models such as Small & Blandford (1992), where the population of SMBH is predicted as a function of luminosity (or mass) and time, the duty cycle directly impacts the global population because the luminosity function is a product of the number density, mass and duty cycle. Models of this type have been extensively developed by Shankar (e.g. Shankar et al. 2013; Shankar et al. 2010) and show that while Eddington accretion is likely to be more common at lower masses ($M < 10^{7.5}$ $\mathrm{M}_{\odot}$), once the SMBH reaches 10^{8} $\mathrm{M}_{\odot}$, matching the luminosity function requires that growth at the Eddington rate must be considerably less frequent or radiative efficiencies must be low. While obviously not directly equivalent, matching the M_{BH}–σ relationship appears to place a very similar constraint on the allowed duty cycle.

Lastly, the gas discs in the simulation are quite stable and in the absence of any additional supply of infalling gas actually decrease their mass during the simulation by 63 per cent prior to the start of the main merger. The stability of the discs is a product both of our choosing a comparatively stable initial configuration and also that the SN feedback routine keeps the gas comparatively well supported against cold collapse. Thus the discs do not fuel the black hole through large scale fragmentation due to them becoming unstable.

3.3.4 Parameter sensitivity: $R_{\rm acc}$

We have four models (two models each of fiducial and low resolution) with $t_{\rm visc} = 5$ Myr that produce physically plausible results. In Fig. 3.5, we have plotted total black hole mass, the accretion rates on to the black hole, and the gas density and gas temperature within $r_{\rm inf}$ of the ADP. As expected, the first accretion event occurs in Model PNKr10t05, and this model has a slightly higher accretion rate for most of the simulation. By increasing the radius of accretion by a factor of two (hence the volume in which a particle can be accreted, $V_{\rm acc}$, by a factor of eight), there is only a factor of 1.35 and 1.70 increase in final total black hole mass for fiducial and low resolutions, respectively. The gas density and temperature behaviour within $r_{\rm inf}$ are very similar at both resolutions. The value of $r_{\rm inf}$ has no explicit dependence on $R_{\rm acc}$ and all models produce the same qualitative behaviour for $r_{\rm inf}$, which settles to $\sim 2h_{\rm min}$ between first periapsis and apoapsis. We find that $R_{\rm acc}$ has negligible influence on $r_{\rm inf}$ and a minimal impact on the final black hole masses. Thus, we conclude that, as long as the parameters are in the physically acceptable range results are not overly sensitive to the exact value of $R_{\rm acc}$; see Fig. 3.6 for a plot of final black hole masses at various accretion radii.

3.3.5 Parameter sensitivity: $t_{\rm visc}$

We have five models with $R_{\rm acc} = 0.05h_{\rm min}$ (two at the fiducial resolution and three at low resolution). In Fig. 3.7, we have again plotted total black hole mass, the accretion rates on to the black hole, and the gas density and gas temperature within $r_{\rm inf}$ of the ADP. The total black hole masses in the fiducial resolution simulations are similar throughout the simulations, and their final masses differ by 13 per cent. At low resolution, the total black hole masses for models PNK$_{\rm l}$r05t05 and PNK$_{\rm l}$r05t01 match within 18 per cent at the end of the simulation; if we include PNK$_{\rm l}$r05t10 (a model that produces unphysical behaviour at the fiducial resolution), then the low resolution black hole masses differ at most by a factor of 1.68.

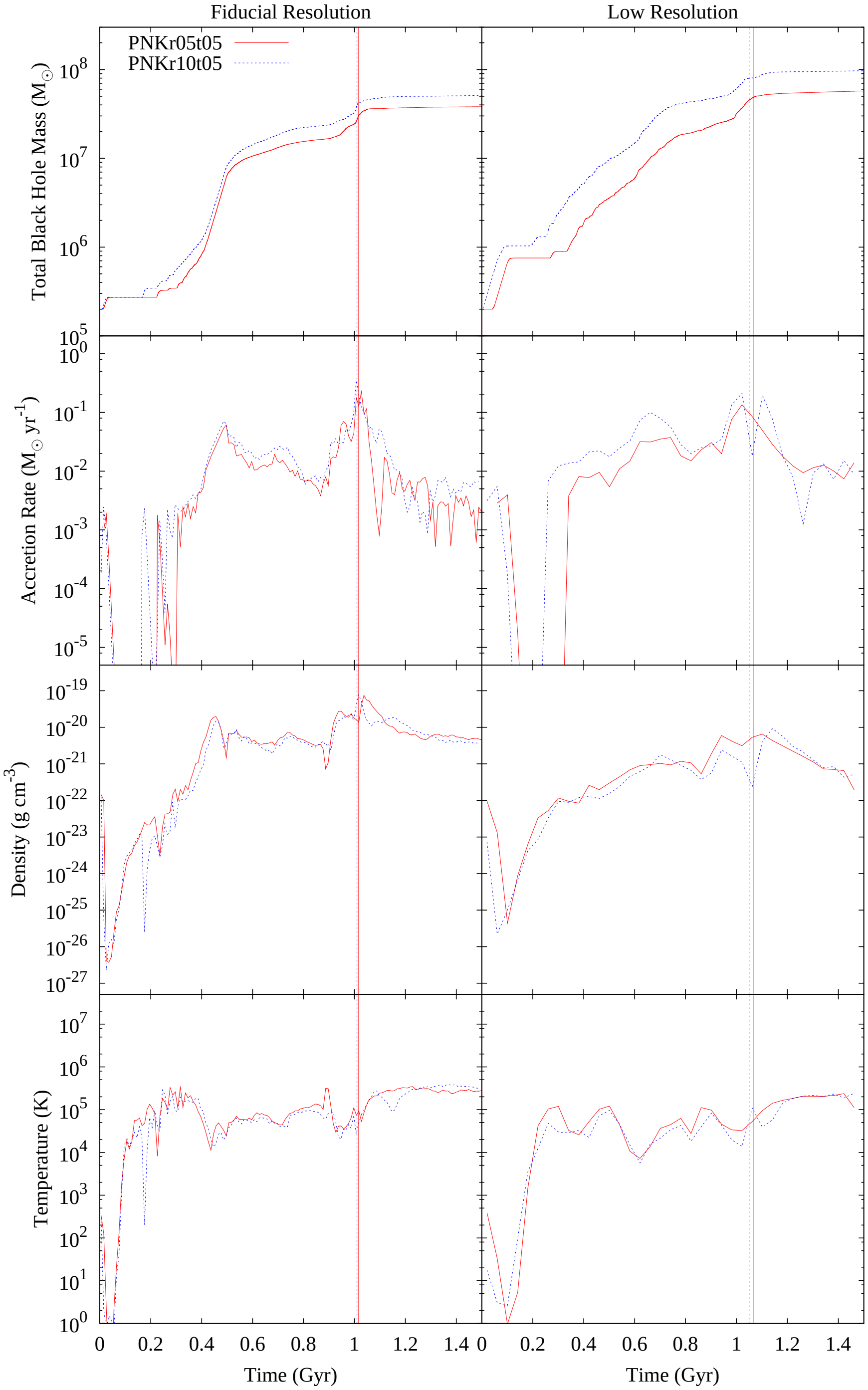

Figure 3.5: The total black hole mass, accretion rates on to the black hole, gas density and gas temperature within $r_{\rm inf}$ of the ADP, as in Fig. 3.2; we fix $t_{\rm visc} = 5$ Myr and vary $R_{\rm acc}$.

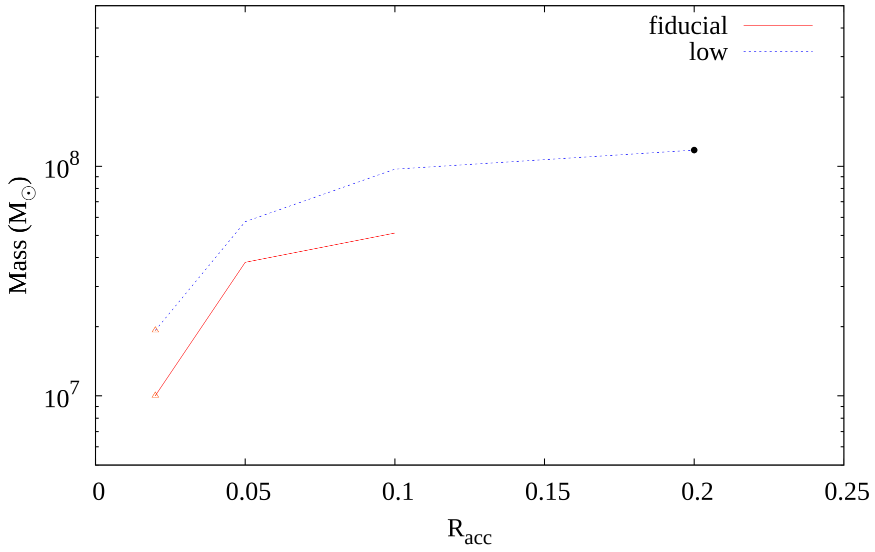

Figure 3.6: The final black hole mass for various accretion radii and $t_{\rm visc} = 5$ Myr. The open triangle represents models we deemed unphysical on basis of it laying far below the $M_{\rm BH}$–σ, and the closed black dot represents models we deemed unphysical for morphological reasons.

In Fig. 3.8, we plot two segments of the accretion rate for one black hole in our three low resolution models with $R_{\rm acc} = 0.05h_{\rm min}$. As expected, the first accretion event happens simultaneously in each model (left panel). This is followed by a period of Eddington accretion, which stops first for $t_{\rm visc} = 10$ Myr and last for $t_{\rm visc} = 1$ Myr depending upon when the $M_{\rm disc}/t_{\rm visc}$ rate falls below the Eddington rate. Once the Eddington accretion has stopped, the rate of feedback (where $\dot{p} \propto \dot{M}$) differs for each model, but at least at this early time the accretion rate on to the black hole can still be calculated: an exponentially decaying rate with the time dependence given by $t/t_{\rm visc}$. Although PNKr05t01 accretes at the Eddington limit very slightly longer than the other two models, the faster decrease in the accretion rate means that feedback effectively stops sooner, thus giving particles more time to slow down and fall within $R_{\rm acc}$.

At late times, each accretion event does not add enough mass to the disc to permit Eddington accretion (right panel); however, there is a local accretion peak

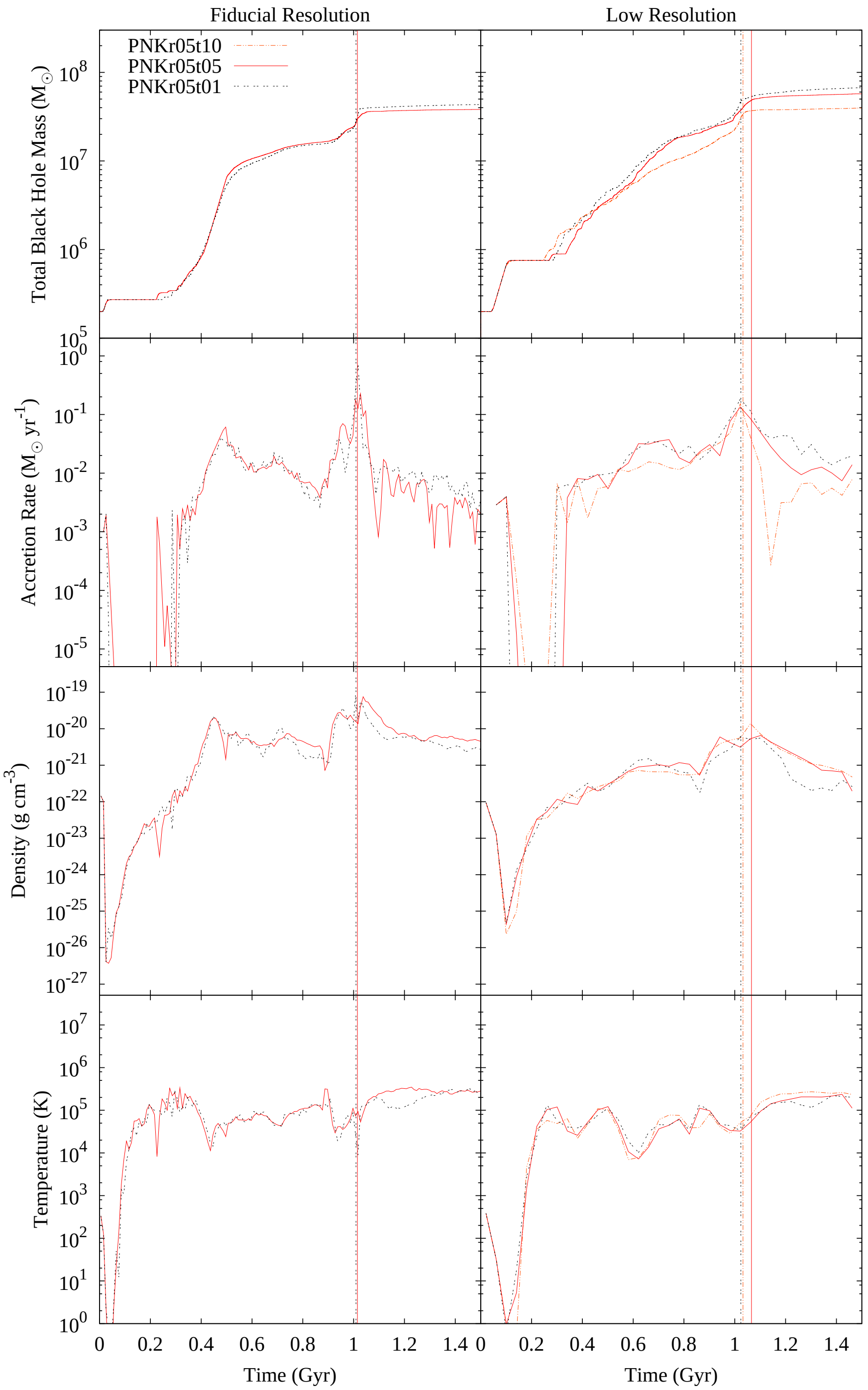

Figure 3.7: The total black hole mass, accretion rates on to the black hole, gas density and gas temperature within $r_{\rm inf}$ of the ADP, as in Fig. 3.2; we fix $R_{\rm acc} = 0.05h_{\rm min}$ and vary $t_{\rm visc}$.

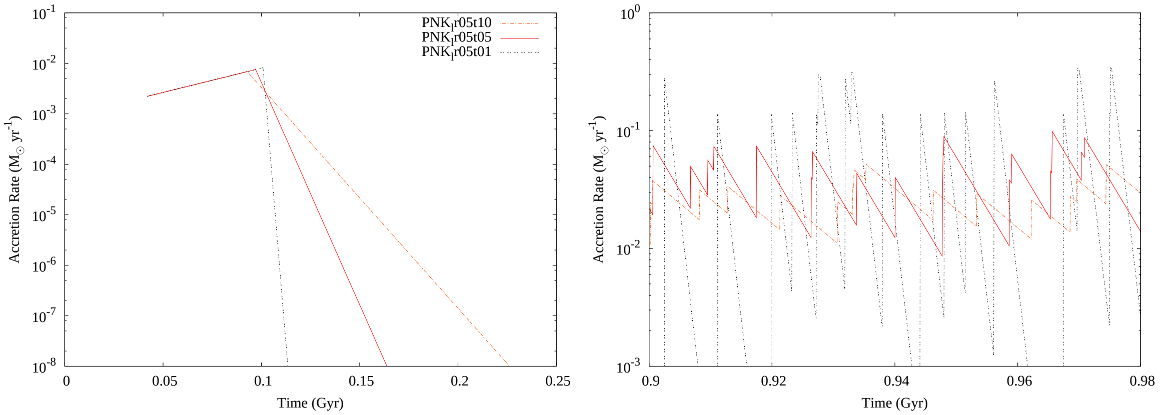

Figure 3.8: The gas accretion rate on to one black hole for three low resolution models, holding $R_{\rm acc} = 0.05h_{\rm min}$. We show the initial accretion event (left) and the accretion just prior to core merger (right).

followed by exponential decay. As previously discussed, the faster decay of $t_{\rm visc} = 1$ Myr allows for rapid accretion events on to the disc. This creates large variances in the accretion rates, spanning a few orders of magnitude. The slower decay of $t_{\rm visc} = 10$ Myr yields a moderated accretion rate, and there is only a factor of a few between the local peak accretion rate and the minimum rate prior to the next accretion event. The time-average accretion rate yields a higher accretion rate for the lower viscous time-scales, resulting in more feedback being returned to the gas which can, at least temporarily, expel considerable amounts of gas from the system. Summarising, we find a general trend to more massive black holes with decreasing $t_{\rm visc}$.

The torques from the interacting galaxies modify this argument by introducing disc instabilities. Although the feedback rate of the $t_{\rm visc} = 10$ Myr models can hinder gas from accreting on to the disc during a quiescent phase, there is not enough cumulative feedback to prevent a large gas flow on to the disc produced by the disc instabilities. This results in a large accretion epoch, followed by powerful outbursts of feedback energy. Thus, the tidal torques at first periapsis and core merger are strong enough to over come the feedback and cause a catastrophic (or near catastrophic) outburst, as in Model PNK$_{\rm f}$r05t10.

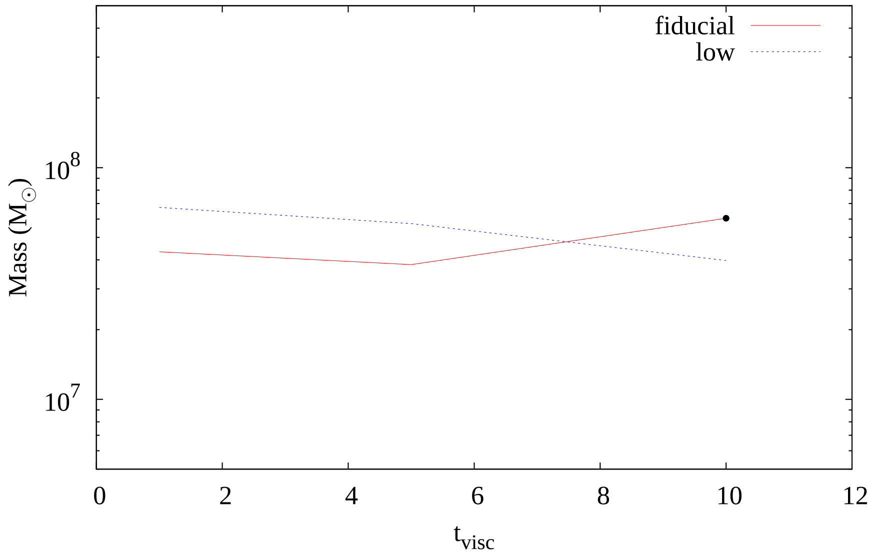

Figure 3.9: The final black hole mass for various viscous time-scales and $R_{\mathrm{acc}} = 0.05h_{\mathrm{min}}$. The closed black dot represents models we deemed unphysical for morphological reasons.

Similar to our discussion in section 3.3.4, we find quantitatively similar gas behaviour within r_{inf}, which is a result of the values of r_{inf} being similar across all models. As with R_{acc}, we conclude that as long as t_{visc} lies with the physically acceptable range, then the simulations are comparatively insensitive to its exact value (at least to within 1/2 an order of magnitude at the fiducial resolution); see Fig. 3.9 for a plot of final black hole masses at various viscous time-scales. .

3.3.6 Resolution sensitivity

We have three models that are deemed to have physically plausible results at both resolutions. In Fig. 3.10, we have plotted total black hole mass, the accretion rates on to the black hole, and the gas density and gas temperature within r_{inf} of the ADP. When we directly compare two models at different resolutions, there are significantly more differences in accretion and evolution histories than when the model parameters are changed (at least for the acceptable range). As would be expected, in all cases the fiducial resolution model accretes the first particle, while the lower

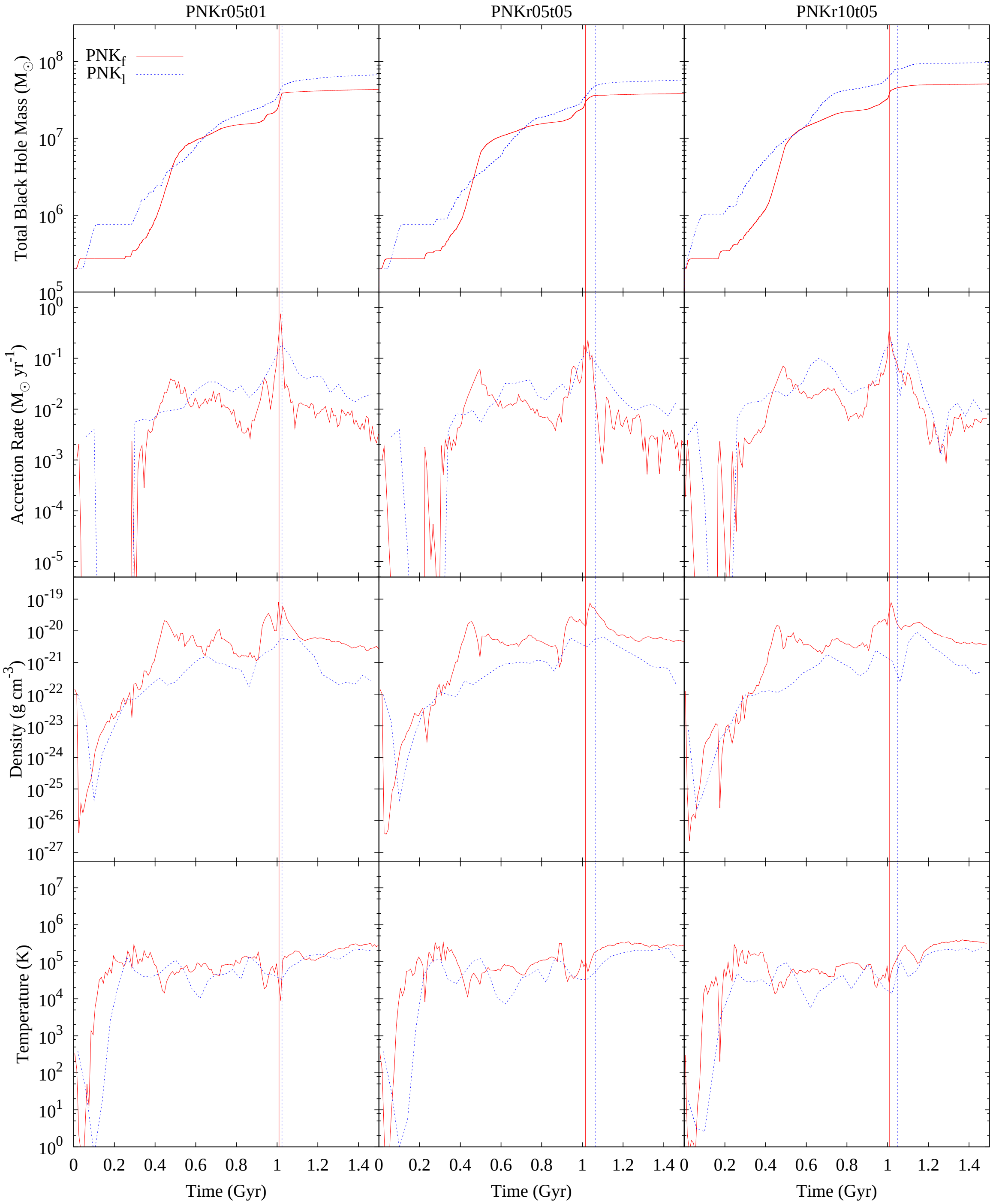

Figure 3.10: The total black hole mass, accretion rates on to the black hole, gas density and gas temperature within $r_{\rm inf}$ of the ADP, as in Fig. 3.2. Each column plots data for a different set of $R_{\rm acc}$ and $t_{\rm visc}$.

resolution simulations produce a larger jump in the accretion rate at early times due to the particles in those simulations being more massive. By the time the galaxies reach first periapsis at 166 Myr, the low resolution gas has a greater kinetic feedback obstacle to overcome before it can pass within R_{acc} of the ADP. Thus, the first low resolution accretion event immediately begins to moderate the accretion on to the disc, and this moderation continues to persist after first periapsis.

Because it has a smaller kinetic feedback obstacle to overcome, the fiducial resolution gas can more easily fall within R_{acc} of the ADP after first periapsis, leading to a large and essentially unmoderated accretion on to the disc. As the gas accretes from the disc on to the black hole, it modifies the environment to suppress further accretion events on to the disc. However, the disc remains massive from the previous accretion episode. Thus, there is a decrease in gas density in the core, but the accretion on to the black hole continues as the gas in the disc is continually transferred to the black hole. This major epoch of accretion on to the disc after first periapsis results in a steeper black hole growth between first periapsis and apoapsis for the fiducial resolution models.

For all three models, the fiducial resolution models have the expected higher core gas densities. Since the feedback is being returned kinetically, shock heating and star formation are the primary heating mechanisms, and both scale with resolution in turn producing similar core temperatures.

Thus, based upon the two resolutions we test, we can conclude that resolution has a greater impact on the results than the values of the free parameters, R_{acc} and t_{visc}. However, these differences are predictable since there are more epochs of discrete behaviour in the fiducial resolution models than in the low resolution models, allowing for a more continuous modelling of the evolution. Also, each fiducial–low resolution pair is more similar to one another than to Models SDH or DQM of the same resolution, indicating that the model can be distinguished from other models even at low resolution. However, we acknowledge that two resolutions are not enough for a proper resolution comparison, and, ideally, we would perform simulations at yet higher resolution.

3.3.7 Final states

3.3.7.1 Stellar remnant

A common test of numerical accretion and feedback algorithms is the $M_{\rm BH}$–σ relation. For all of our physical models, we have calculated the stellar velocity dispersion around every black hole using the method described in Debuhr et al. (2011). These velocity dispersions are averaged over 1000 random lines of sight, and are plotted on the $M_{\rm BH}$–σ relation in Fig. 3.11. For the six models in Fig. 3.10, we also plot the full range of velocity dispersions, as well as those taken preferentially along the $\pm x$-, $\pm y$- and $\pm z$-lines of sight. The large range of σ is a result of the highly triaxial stellar remnant; see Fig. 3.12, where we have plotted a fiducial and low resolution stellar remnant. The fiducial resolution models have average values very near the observed $M_{\rm BH}$–σ relation, and a range that nearly stays within the one-sigma scatter. The low resolution stellar remnants are more elliptical than their fiducial resolution counterparts, thus they have a greater range of values for σ. While some of the average σs fall outside of the one-sigma range, they all obtain σs near the observed $M_{\rm BH}$–σ relation if the line of sight is near the plane of the disc. To verify these results, we have recalculated the velocity dispersions of the fiducial resolution models based upon the gravitational potential of the black hole, and found these values to be consistent within five per cent of the average values reported above.

3.3.7.2 Gas properties

In Figs. 3.13 and 3.14, we plot the gas column density of ten remnants at 1.5 Gyr. These show, respectively, the inner 100 and 20 kpc of six PNK models (three models at each resolution) and Models DQM and SDH. As discussed in sections 3.3.4 and 3.3.5, there is much qualitative similarity amongst the three fiducial remnants

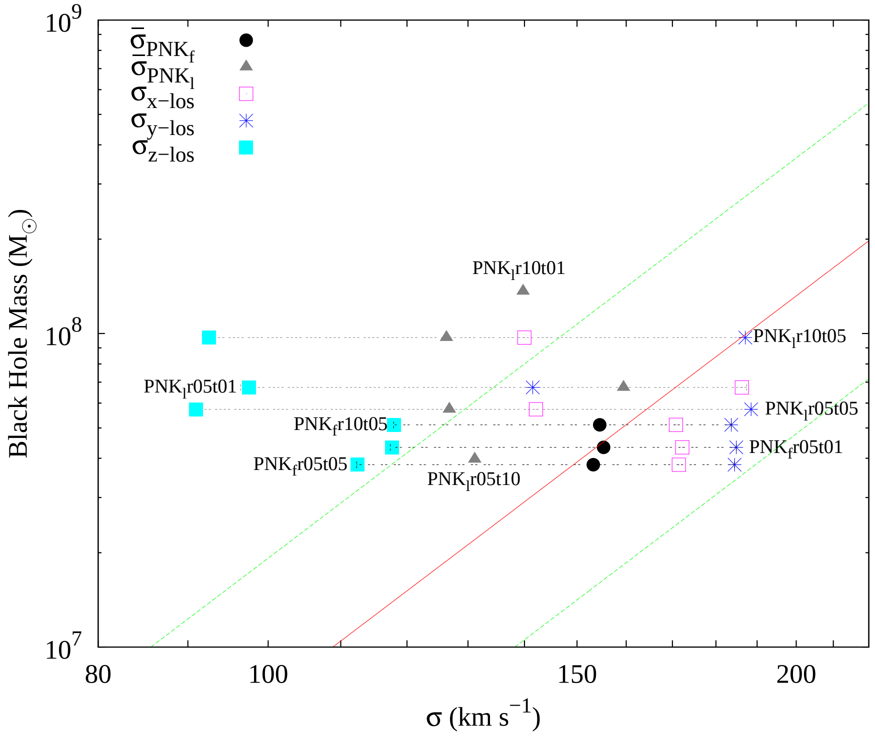

Figure 3.11: Our numerical $M_{\rm BH}$–σ relation, along with the observed relation (red solid line) and the one-sigma scatter (green dashed line) from Gültekin et al. (2009). For six selected models, the solid dot/triangle represents the average σ of 1000 random lines of sight, the horizontal bars represent the range of all calculated σs, and the remaining three symbols on the horizontal line represent σ taken along the $\pm x-$, $\pm y-$ and $\pm z-$lines of sight. For the remainder of our physical PNK models, we have only plotted the average σ of 1000 random lines of sight. We have explicitly labelled which points/set of points corresponds to which models.

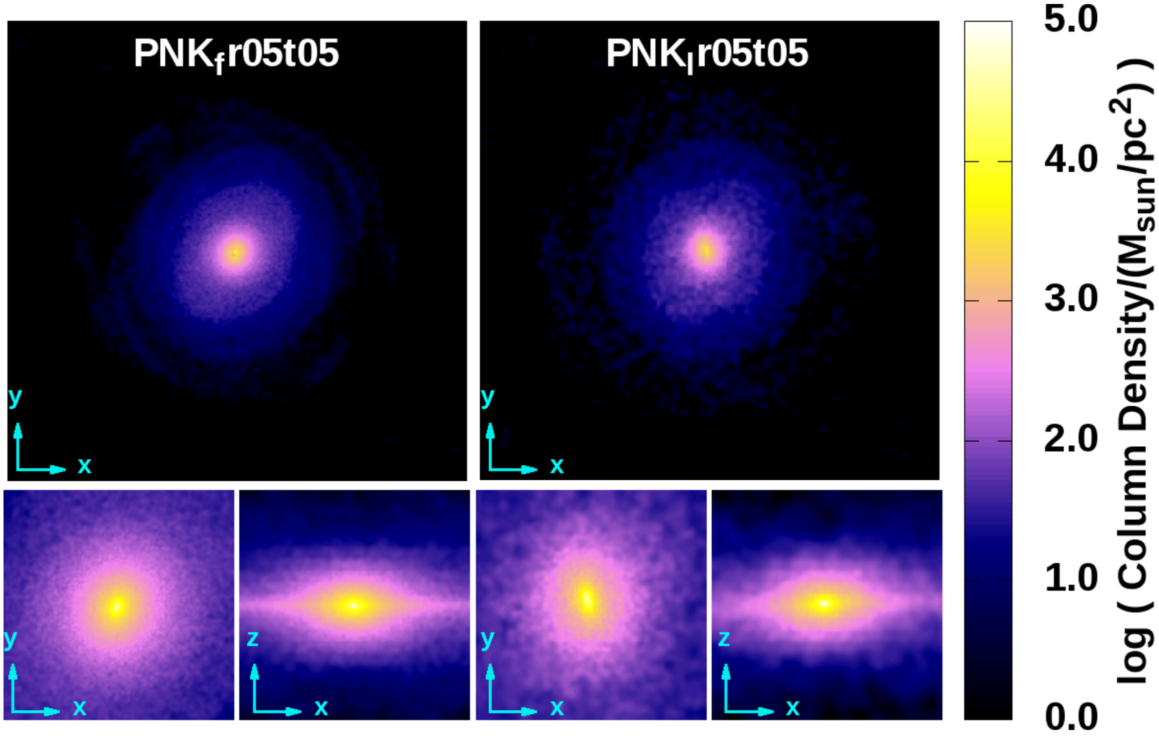

Figure 3.12: Stellar column density of the remnants of PNK$_f$r05t05 (left) and PNK$_l$r05t05 (right), taken at 1.5 Gyr. All stellar remnants (including Models DQM and SDH) of each resolution are similar, with the low resolution remnants yielding more elliptical bulges than their fiducial resolution counterparts. *Top Row*: Face-on view with each frame measuring 100 kpc per side, with image resolution of 195 pc/pixel (left) and 390 pc/pixel (right). *Bottom*: Face-on and edge-on view of both models, with each frame measuring 20 kpc per side, and image resolution of 39 pc/pixel (78 pc/pixel) for the fiducial (low) resolution models.

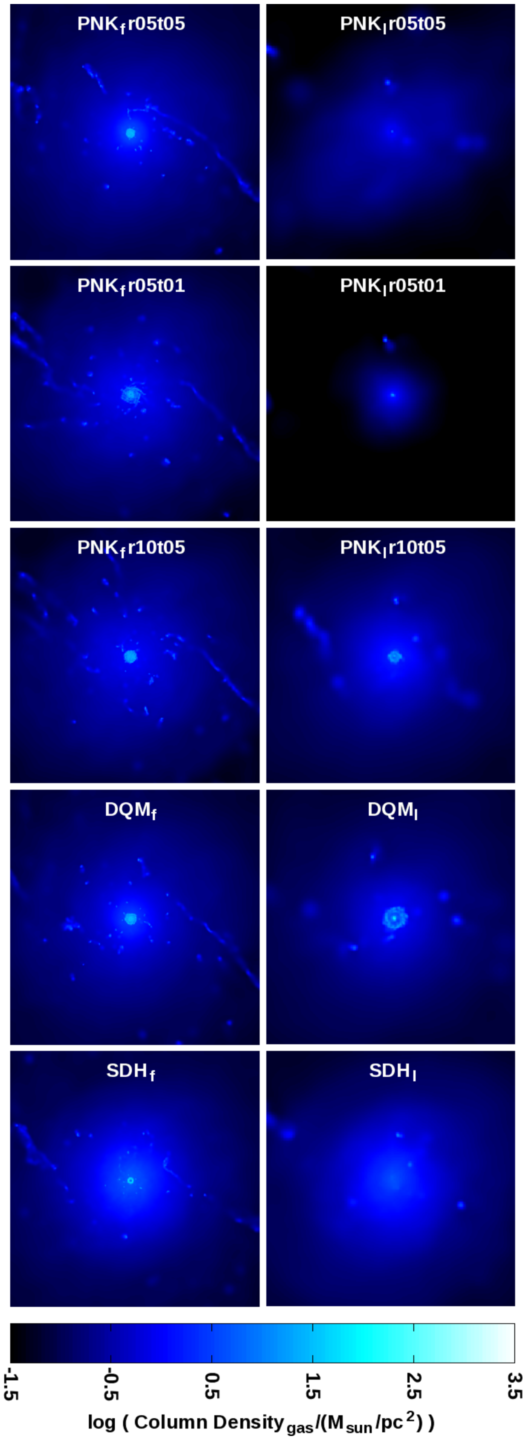

Figure 3.13: Gas column density of ten remnants, taken at 1.5 Gyr. Each frame measures 100 kpc per side, with image resolution of 195 pc/pixel (390 pc/pixel) for the fiducial (low) resolution models.

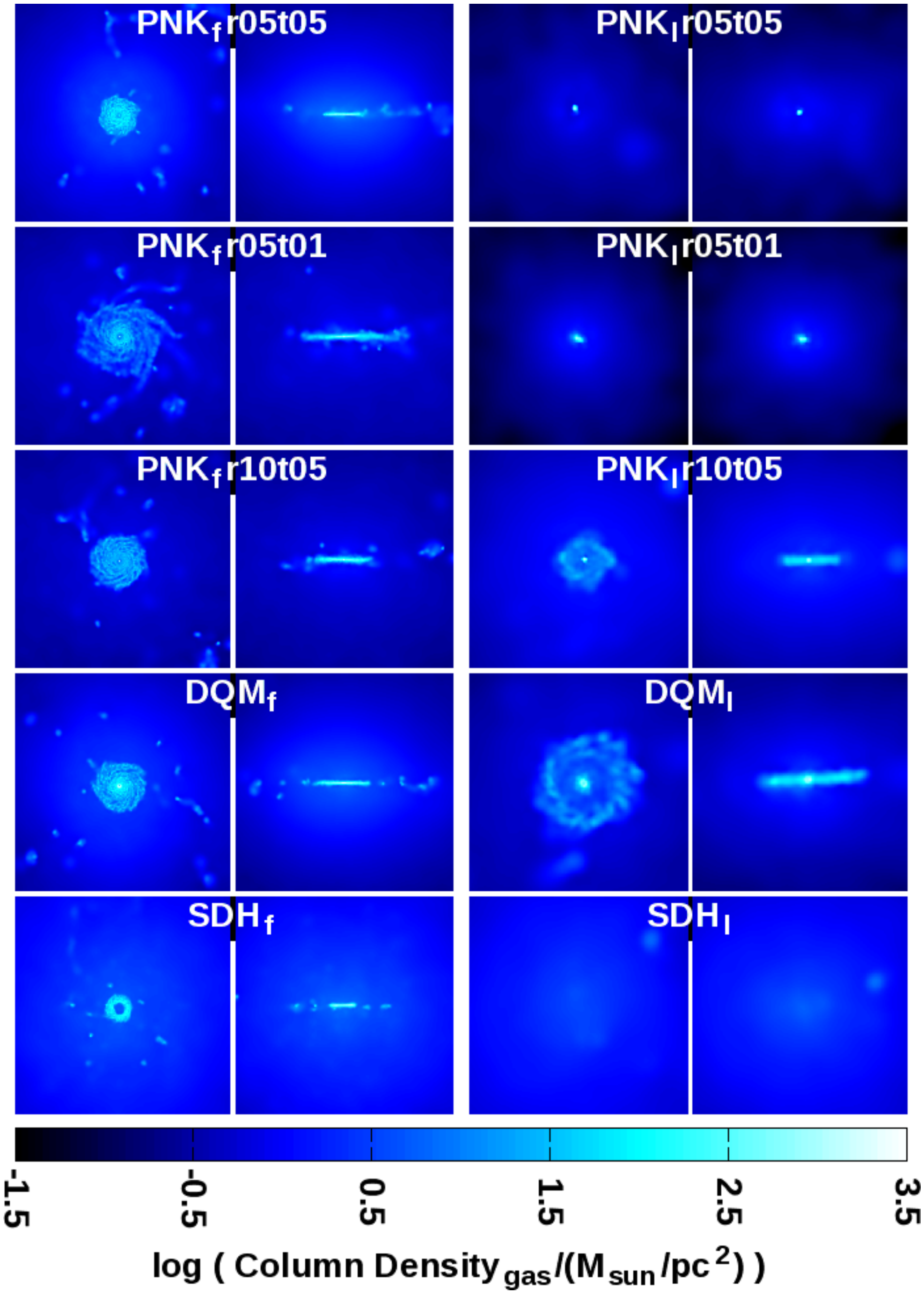

Figure 3.14: Gas column density of ten remnants, taken at 1.5 Gyr. Each pair contains a face-on and edge-on view of the central 20 kpc. The image resolutions are 39 pc/pixel (78 pc/pixel) for the fiducial (low) resolution models.

Model	Disc mass (10^8 $M_\odot$)
PNK_fr05t05	4.18
PNK_fr05t01	3.93
PNK_fr10t05	3.31
DQM_f	6.42
SDH_f	2.70

Table 3.2: The gas mass of the reformed discs at 1.5 Gyr for five fiducial resolution models.

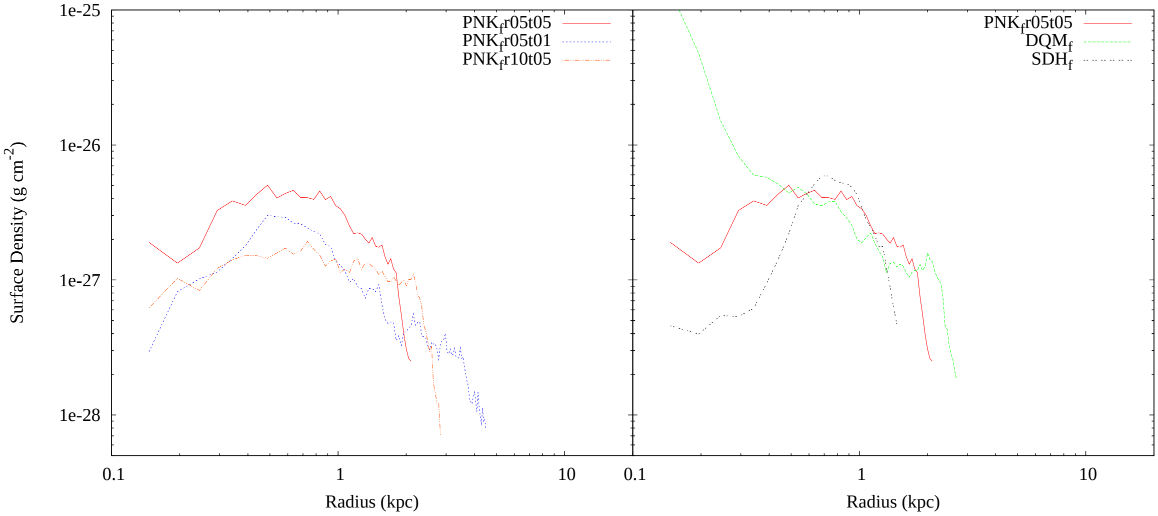

Figure 3.15: Gas surface density profile, averaged over all azimuthal angles, for the reformed disc of three fiducial resolution remnants. The profile is truncated at the edge of the disc, and plotted in bins of 49 pc.

of the PNK models, as well as Models DQM_f and SDH_f. In all cases, there is a condensing gas cloud with a reformed disc.

The radius, surface density profiles and total gas mass of the reformed discs in the PNK models are only slightly dependent on the free parameters. The surface density profile is plotted in the left panel of Fig. 3.15 and the gas disc masses are given in Table 3.2.

After core merger, PNK_fr10t05 has a slightly larger accretion rate than PNK_fr05t05 due to its larger accretion radius. This leads to more feedback energy and a slightly extended disc with lower surface density. Model PNK$_\mathrm{f}$r05t01 has a higher accretion rate at core merger than PNK$_\mathrm{f}$r05t05, which results in a small outburst at 1 Gyr expelling some gas from the system. By 1.5 Gyr, the remaining gas is less bound leading to the slightly larger radius and lower surface density.

The fiducial resolution PNK models have different surface density profiles than Models DQM$_\mathrm{f}$ and SDH$_\mathrm{f}$; see the right panel of Fig. 3.15. The disc in Model DQM$_\mathrm{f}$ has a dense core and a moderately dense torus (resulting in a high-mass disc), whereas the profile for Model SDH$_\mathrm{f}$ is a torus due to low level feedback activity carving out a region of the disc.

The three fiducial resolution PNK remnants are qualitatively more similar to one another than to their low resolution counterparts. Both PNK$_\mathrm{l}$r05t01 and PNK$_\mathrm{l}$r05t05 underwent a major outburst starting at 1.05 Gyr, blowing away much of the gas and preventing the reformation of the gas disc. In the subsequent few 100 Myrs, the gas begins to recondense into the cloud presented here. In PNK$_\mathrm{l}$r10t05, this major outburst never occurs, thus allowing the disc to reform.

3.4 Conclusion

We have implemented the accretion disc particle (ADP) method of Power et al. (2011) into a major merger simulation of two Milky Way-sized galaxies. We ran five fiducial resolution simulations and twelve low resolution simulations varying the free parameters R_acc and t_visc. Our primary conclusions are as follows:

1. For accretion radii that are too small (i.e. $R_\mathrm{acc} = 0.02h_\mathrm{min}$), the final black hole mass is far smaller than predicted from the M_BH–σ relationship. Thus all of our $R_\mathrm{acc} = 0.02h_\mathrm{min}$ models are classified as unphysical.

2. For accretion radii that are too large (i.e. $R_\mathrm{acc} = 0.20h_\mathrm{min}$), the accretion rate on to the accretion disc (hence on to the black hole) is unreasonably large. The resulting feedback is enough to catastrophically disrupt the system. We thus classify all of our $R_\mathrm{acc} = 0.20h_\mathrm{min}$ models as unphysical.

3. For large viscous time-scales (i.e. $t_{\rm visc} = 10$ Myr), feedback from an accretion event persists long enough to hinder secular accretion. Tidal forces from the interacting galaxies can overcome the low amount of feedback and funnel considerable amounts of gas on to the accretion disc. Depending on resolution and accretion radius, this short accretion epoch can be large enough such that its resulting feedback energy can catastrophically disrupt the system. Thus a few of our $t_{\rm visc} = 10$ Myr models are classified as unphysical.

4. The values of $R_{\rm acc}$ and $t_{\rm visc}$, assuming they were in the allowed parameter space, had minimal effect on the gas properties within $r_{\rm inf}$ of the black hole. This result was expected since $r_{\rm inf}$ had no explicit dependence on $R_{\rm acc}$ or $t_{\rm visc}$.

5. The exact value of $R_{\rm acc}$ has only a minimal effect on the resulting system, assuming that it is in the allowed parameter space. By doubling the accretion radius from $0.05h_{\rm min}$ to $0.10h_{\rm min}$, the final black hole mass increases by only a factor of 1.35 (1.70) for our fiducial (low) resolution simulations.

6. As we decrease the value of $t_{\rm visc}$ the final black hole mass increases; the final range of black hole masses spans a factor of 1.13 (1.68) for our fiducial (low) resolution models. Thus, the exact value of $t_{\rm visc}$ has only a minimal effect on the resulting (physical) system.

7. Decreasing the resolution increases the final black hole mass. For any given fiducial–low resolution pair, the final black hole mass differs by at most a factor of 1.90. The fiducial resolution models experience steeper black hole growth between first periapsis and apoapsis, and the lower resolution models are more prone to major outburst events shortly after core merger. Given the parameters tested here, resolution has the largest impact on the outcome of the model. We understand that these differences are unavoidable and are a result of a single accretion event in the low resolution models returning 7.6 times more energy to the gas than the fiducial resolution models.

In AGN feedback models where the accretion rate is dependent on the gas properties near the black hole, the accretion and energy feedback rates are never zero, and span only a few orders of magnitude. In our simulations, the accretion and feedback begins immediately. In Model DQM, an initially high accretion rate leads to an immediate and dramatic modification of the black hole's environment. In Model $\mathrm{SDH_f}$, the accretion rate does not become significant until apoapsis, at which point the black hole undergoes a major accretion epoch, with its mass increasing by a factor of 20.5 in 470 Myr.

With the ADP model, the initial accretion rate is zero or very small. The minimal modification of the ADP's environment by first periapsis allows a large accretion event on to the disc, which results in a large accretion rate on to the black hole, leading to a very rapid black hole growth. In the case of Model $\mathrm{PNK_f}$r05t05, the black hole mass increases by a factor of 19.6 in 200 Myr. Although these three models, Models SDH, DQM and PNK, have very different algorithms and different evolution histories, there are similar remnants in all three cases.

The ADP algorithm decouples the accretion rate on to the black hole from the gas properties around it and allows a high accretion rate even after feedback has prevented additional accretion events on to the disc. Yet to have confidence in this conceptual model, a precise observational strategy for determining parameters is necessary (essentially looking at the correlation, or lack of, between activity and the nuclear gas environment). Recent observational work (Wild et al. 2010) has unveiled how star formation activity and black hole growth appear tied together in spheroids. These results undoubtedly give useful hints on how black hole growth proceeds outside of rapid accretion phases, but fueling of black hole via cold gas accretion remains the biggest uncertainty in our models currently. To date, studies of nuclear CO morphology such as the NUGA project (e.g. García-Burillo et al. 2005; van der Laan et al. 2011) have found no obvious morphological links between local AGN activity and mid-scale CO morphology. However, such studies are obviously limited by resolution concerns, as well as probing an entirely different AGN luminosity regime.

ALMA, in its full configuration with the largest baselines, will provide resolutions that are sufficient to study the nuclear regions of the nearest active quasar systems, and observe distinctions between models describing the formation of the clumpy region around the black hole (i.e. was it formed outflows from the accretion disc or from stellar winds and supernovae; the latter will make the medium thick). The kinematics observered from ALMA will also be able to provide information on the stability and origin of the circumnuclear medium, as well as provide detailed measurements of the black hole mass and stellar velocity dispersions (Maiolino 2008). Thus, this should give great insight into the evolution of AGN, and place constraints on the models and the parameters therein.

Chapter 4

AGN Triggered Star Formation

4.1 Introduction

Supermassive black holes are expected to to reside at the centre of galaxies that have stellar spheroids (e.g. Kormendy & Richstone 1995; Ferrarese & Merritt 2000). From the empirical black hole mass – stellar velocity dispersion relationship (M_{BH}–σ; e.g. Silk & Rees 1998; Ferrarese & Merritt 2000; Gebhardt et al. 2000; Tremaine et al. 2002; King 2003; Gültekin et al. 2009) and the black hole mass – bulge mass relationship, (M_{BH}–M_{b}; Magorrian et al. 1998; McLure & Dunlop 2002; Marconi & Hunt 2003), it is inferred that the black hole and spheroidal evolution is related. This interrelationship likely occurs as a result of feedback from the black hole interacting with the surrounding environment. Although the exact interaction mechanism is not yet well understood, feedback has several profound impacts on the host galaxy and beyond. First, it can lead to a self-regulated black hole feedback/accretion system: Outflows from the black hole following a strong accretion event inhibit further accretion events, hence limiting black hole growth (e.g. Silk & Rees 1998; Fabian 1999b; Scannapieco & Oh 2004). Next, feedback can drive large fractions of the gas from the host galaxy, leaving a red and dead galaxy (e.g. Silk & Rees 1998; King 2005; Zubovas & King 2012). A third result is to quench star formation (i.e. via 'negative feedback'), as demonstrated numerically in e.g. Springel et al. (2005b) and Debuhr et al. (2011) and is observationally supported in e.g. Maiolino et al. (2012).

However, rather than just suppressing star formation, it is possible that feedback from active galactic nuclei (AGN) may actually trigger star formation (i.e. via 'positive feedback'), as first suggested by Silk & Norman (2009). If a shock is travelling through a gas-rich bulge and the shocked gas cools faster than the shock can propagate through the bulge, then the shocked gas will be swept up into a geometrically thin shell. If the shell is denser than the tidal density (which is a reasonable assumption), then the shell can fragment into star forming clumps (e.g. Zubovas et al. 2013). Jet-triggered star formation has been observed in both nearby (Croft et al. 2006; Rodríguez Zaurín et al. 2007) and distant (Feain et al. 2007; Elbaz et al. 2009) galaxies.

Triggered star formation may also help to explain why high-redshift galaxies are more compact than today's counterparts (Daddi et al. 2005; Trujillo et al. 2007; van Dokkum et al. 2008; Bezanson et al. 2009; van Dokkum et al. 2010; Patel et al. 2013). Since the central densities are similar, it has been suggested that this growth (substantial in radius but minimal in mass) occurs at the outer radii (Bezanson et al. 2009; van Dokkum et al. 2010; Patel et al. 2013). This argument is consistent with stars forming in expanding shells. Moreover, as the shell advects outward, the stars are ultimately expected to drop out of the shell and begin to follow their own orbit within the potential. If the shell's velocity is not initially exceeding the escape velocity of the host, then the stars will remain bound to the host, increasing the radius of the galaxy and the stellar mass in the outer regions (Ishibashi & Fabian 2012; Ishibashi et al. 2013). This description predicts that the stars are born with radial velocities in the outer regions, as observed by Romanowsky et al. (2003) and Gerhard (2010). This also implies that the stars spend the majority of their life in the outer regions of the host where their velocity is small. Observationally, this would suggest that the outer regions of the galaxy have a bluer colours and a negative colour gradient (i.e. a redder core); however, these may imply metallicity gradients, and the two effects must be disentangled (Ishibashi et al. 2013).

There have been several studies of triggered star formation (e.g. Ishibashi et al. 2013 in 1-D; Liu et al. 2013 in 2-D; Zubovas et al. 2013 in 3-D). The 1-D analytical studies of Ishibashi & Fabian (2012) (herein IF12) and Ishibashi et al. (2013) assume that the gas is embedded in a dark matter potential with a luminous central source; this is based upon the feedback study of McQuillin & McLaughlin

(2012). The luminous source imparts thermal momentum on to the gas, pushing it outwards. Realistically, the thermal momentum would likely be imparted on the dust around the source, and the momentum would be transferred to the gas through the strong coupling between the gas and the dust (Murray et al. 2005), efficiently dragging both outward. The end result is gas being swept up into a thin shell that propagates outward, leaving a cavity near the black hole. In these studies, the shell properties are entirely defined by the properties of the system, including the luminosity of the central source. If the black hole is less luminous than some critical luminosity, then the shell will fall back on to the black hole since the radiation pressure will be unable to support the gas against the gravitational force of the dark matter. If the central luminosity is greater than the critical luminosity, then the shell's velocity will surpass the escape velocity and the shell will expand indefinitely.

The goal of this chapter is to study numerically triggered star formation in 3-D. Specifically, we will simulate a luminous source in a gas-rich environment, and track the stars that are formed, concentrating on trajectories and distributions. We acknowledge that this is an idealised study since we consider AGN feedback solely as a central luminosity source and we neglect stellar feedback. These caveats do not, however, affect our goal of tracking the stellar trajectories or distributions.

The chapter is organised as follows: In Section 4.2, we will discuss the theory of expanding shells and the relevant star formation equations. In Section 4.3, we will describe our numerical methods. In Section 4.4, we will describe our results and we will conclude in Section 4.5.

4.2 Theory of expanding shells

Assuming that radiation pressure from the black hole is the only feedback mechanism and assuming that the black hole has a negligible gravitational impact, the equation of motion for the shell is given by

$$\frac{\mathrm{d}}{\mathrm{d}t}\left[M_{\mathrm{g}}(r)\dot{r}\right] = \frac{L}{c} - \frac{GM_{\mathrm{g}}(r)M_{\mathrm{DM}}(r)}{r^2} \tag{4.1}$$

where $M_{\rm g}(r)$ is the mass of the shell (which contains all of the gas interior to r), L is the luminosity of the source, c is the speed of light, G is Newton's gravitational constant, and $M_{\rm DM}(r)$ is the mass of the dark matter halo interior to r. From (4.1), we calculate the the shell's velocity at any given radius to be

$$\begin{aligned} v^2(r) = & \frac{1}{M_{\rm g}(r)^2}\int_{r_0}^{r}\frac{2M_{\rm g}(r)L}{c}{\rm d}r \\ & -\frac{1}{M_{\rm g}(r)^2}\int_{r_0}^{r}\frac{2GM_{\rm g}(r)^2M_{\rm DM}(r)}{r^2}{\rm d}r \\ & +\frac{M_{\rm g}(r_0)^2}{M_{\rm g}(r)^2}v_0^2, \end{aligned} \tag{4.2}$$

where r_0 is the launching radius of the shell and v_0 is the shell's initial velocity. Thus, it is a relatively simple task to determine the critical luminosity ($L_{\rm crit}$; the minimum luminosity for which a shell can escape), and the stalling radius, $r_{\rm stall}$ (i.e. $v(r > r_{\rm stall}) = 0$ if $L < L_{\rm crit}$). These velocity profiles have been studied by IF12 using various matter distributions, including isothermal, Hernquist and NFW profiles for both gas and the dark matter.

To account for the triggered star formation in the shell, IF12 adopt a simple star formation prescription of

$$\dot{M}_* \sim \epsilon_*\frac{M_{\rm g}(r)}{t_{\rm flow}(r)}, \tag{4.3}$$

where ϵ_* is the star formation efficiency and $t_{\rm flow}(r) = \frac{r}{v(r)}$ is the local flow time, assuming a steady state flow.

For an isothermal mass profile given by

$$M(r) = \frac{2f_{\rm g}\sigma^2}{G}r, \tag{4.4}$$

where $f_{\rm g}(= 0.16)$ is the gas fraction compared to the dark matter mass and $\sigma(= 200\ {\rm km\ s^{-1}})$ is the velocity dispersion, the position-dependent star formation rate (SFR) is

$$\dot{M}_* \sim \epsilon_*\frac{2f_{\rm g}\sigma^2}{G}v(r). \tag{4.5}$$

Integrating over a Salpeter time ($\sim 5 \times 10^7$ yr) and assuming a critical luminosity of $\sim 4.6 \times 10^{46}$ erg s^{-1}, IF12 calculate that on order of several 10^9 M$_\odot$ of stars would be formed by the expanding shell.

Depending on motivation, there are several other possible time-scales to use in the star formation rate equation. Silk (2013) discusses the star formation rate in a galactic disc, thus uses the dynamical time-scale of the disc, $t_{\rm dyn} \equiv R_{\rm d}/\sigma$ where $R_{\rm d}$ is the disc scale length and σ is the circular velocity. In scenarios where the disc fragments and collapses into star forming giant molecular clouds, the Schmidt law is well fit provided that the local free-fall time, $t_{\rm ff} = \sqrt{\frac{3\pi}{32G\rho}}$, where ρ is the local gas density, is used and not $1/\sqrt{G\rho_{\rm d}}$ (Krumholz et al. 2012), where $\rho_{\rm d}$ is the mean disc density.

In the scenario we will study, a steady state flow is not reached, nor is there a coherent rotation of a disc, thus $t_{\rm flow}$ and $t_{\rm dyn}$ will not be well-defined. Since we expect fragmentation, we will use the local free fall time, $t_{\rm ff}$, as the characteristic time-scale. Thus, as is common in numerical simulations, our SFR will be dependent on local properties such as temperature and density, rather than (locally unknown) global properties. Using this time scale, the SFR becomes

$$\dot{\rho_*} \sim \epsilon_* \frac{\rho_{\rm g}(r)}{t_{\rm ff}(r)}, \tag{4.6}$$

which can be simplified to

$$\dot{\rho_*} = \epsilon_* \sqrt{\frac{32G}{3\pi}} \rho(r)^{\frac{3}{2}}. \tag{4.7}$$

This form matches the accepted SFR from the Schmidt law (e.g. Katz 1992; Kennicutt 1998) of

$$\dot{\rho_*} \propto \rho(r)^{\alpha}, \tag{4.8}$$

with $\alpha = \frac{3}{2}$. In addition to forming stars in shocks, this algorithm will induce star formation in high density nuclear regions, but this is a reasonable representation of what would naturally occur. This SFR has not been explored by IF12 or Ishibashi et al. (2013), but provides us with a route for comparison.

4.3 Numerical Methods

4.3.1 Hydrodynamic equations used in ZEUS-3D

To perform our simulations, we use the Eulerian grid code ZEUS-3D (Clarke 1996; Clarke 2010). Our simulation neglects magnetic fields, thus the hydrodynamic equations solved by ZEUS-3D are

$$\frac{\partial \rho}{\partial t} + \boldsymbol{\nabla} \cdot (\rho \boldsymbol{v}) = 0 \tag{4.9a}$$

$$\frac{\partial (\rho \boldsymbol{v})}{\partial t} + \boldsymbol{\nabla} \cdot (\rho \boldsymbol{v} \boldsymbol{v}) = -\boldsymbol{\nabla} p - \rho \boldsymbol{\nabla} \phi \tag{4.9b}$$

$$\frac{\partial e}{\partial t} + \boldsymbol{\nabla} \cdot (e \boldsymbol{v}) = -p \boldsymbol{\nabla} \cdot \boldsymbol{v} \tag{4.9c}$$

where ρ, $\boldsymbol{v}$, p and e are the gas density, velocity, pressure and thermal energy density, respectively. The equations are closed with the equation of state, $p = (\gamma - 1)e$. The gas is allowed to undergo compressional heating and cooling, where the latter is determined from the cooling tables of MacDonald & Bailey (1981). Although there are more modern cooling tables (e.g. Sutherland & Dopita 1993; see fig. 1 of Schure et al. (2009) for a comparison of the MacDonald & Bailey (1981) and Sutherland & Dopita (1993) cooling curves), the key point is to allow the gas to cool such that it will build up in the shell. Also, since the width of the shock is limited by the resolution of the grid, we necessarily cannot follow cooling as accurately as we would like.

4.3.2 Particle solver

To model shocks, grid codes are typically superior to particle codes, hence our choice of ZEUS-3D. However, to track stellar trajectories, star particles are required, thus we have implemented a particle solver in the ZEUS-3D code. In a non-ideal scenario, star forming regions and stellar motions would be influenced by more than just an expanding shell of gas. Thus, for added fidelity, we have added two additional particle types to provide the additional influences on the star particles. Our three particle types are

1. External potential particle,
2. Dwarf satellite particle, and
3. Star particle.

The possible interactions are {satellite, star}-gas, {satellite, star, gas}-external and {satellite, star, gas}-satellite, where the latter member of each pair is the massive gravitational source and the former member is (at least momentarily) treated as massless. To calculate the net force for the particle-particle interactions, we simply perform a brute force N^2 calculation; the stars are always treated as massless particles, so this reduces to a reasonable $N \times (N_{\text{satellite}} + N_{\text{external}})$ calculation, where $N_{\text{satellite}}$ is the number of satellite particles, N_{external} is the number of external potential particles, and N is the total number of particles. For the particle-gas/gas-particle interactions, we first discretise the gas into a set of extended points (spheres) located at each cell's centre, where the sphere has the same density and volume as the grid cell. For each cell that contains at least one particle, we place one particle at the centre of the cell and calculate the particle-gas/gas-particle interactions for all non-doubly adjacent cells. Finally, for every particle at its true location within the cell, we supplement this force with the exact short-range force from the doubly-adjacent cells.

Although the gas is evolved on a pre-defined grid, the particles are not bound to this domain; if they leave this domain, then the total gas mass is treated as a point source. There can be small force discrepancies as a particle nears the boundary of the gas; however, the gas density is typically low in these regions and thus has a minimal effect on the net motion of the particle. As is standard in particle codes, all forces are softened to prevent extreme accelerations caused by small impact parameters, and the satellite particles are given an effective mass distribution (described by a Hernquist profile). Lastly, at all radii, all particles feel the force of the host's dark matter halo.

Each particle type has a different purpose and behaves as described below.

4.3.2.1 External potential particle

This particle represents an external potential to account for tidal effects of a passing galaxy. The particle has the same total mass as the initial gas and dark matter within r_{max} (see §refZic), and is placed on an elliptical orbit about the centre of the grid with a periapsis of 100 kpc and an apoapsis of 300 kpc. The particle is initially placed 90° from apoapsis moving counterclockwise towards periapsis. This particle does not deviate from its elliptical path, and all other particles and gas feel its gravitational force. This creates a maximal tidal scenario as compared to a single hyperbolic ‘flyby’.

4.3.2.2 Dwarf satellite particles

These particles represent a host galaxy’s dwarf satellite system. Each dwarf satellite is small compared to the host (with a mass 0.35% of the host’s total mass), but the localised gravitational sources are of importance if stars are projected towards them, or if the dwarf satellite passes through its host, exciting the gas.

In this simulation, we add 40 dwarf satellite particles, with each one representing a Small Magellanic Cloud-size dwarf satellite with a Hernquist (Hernquist 1990) dark matter profile of

$$M(r) = M_{\text{total}} \frac{r^2}{(r + r_{\text{a}})^2}, \tag{4.10}$$

where $M_{\text{total}} = 5.3 \times 10^9$ $\text{M}_\odot$ and the scale radius is $r_{\text{a}} = 1$ kpc. The particles are placed throughout the halo using output from GalactICs (Kuijken & Dubinski 1995; Widrow & Dubinski 2005; Widrow et al. 2008); specifically, GalactICs is used to create a 40-particle dark matter halo with the desired characteristics, and then those particles are converted into satellite particles and given a circular velocity about the origin. The spin parameter of the satellite system can be calculated using

$$\lambda = \frac{J\sqrt{|E|}}{GM^{5/2}}, \tag{4.11}$$

where J is the magnitude of the angular momentum, E is the total energy of the system and M is the mass of the system. For our satellite system, the spin parameter is $\lambda \sim 0.02$ about the z-axis, which essentially imparts a small net rotational velocity on the particle system. For all time and radii, the satellite particles feel the gravitational force from the external potential particle, the dark matter halo, and the other satellite particles. If the satellite particle is within the domain of the gas, then there is also a mutual gravitational force between the satellite and the gas.

4.3.2.3 Star particle

These particles are massless tracers, but represent a pre-defined mass of stars, each of which represents 200 $\mathrm{M}_{\odot}$ in our fiducial simulation. When we refer to the 'mass' of a star particle, we refer to the stellar mass it represents, not the actual mass of the particle. The star particles do not gravitationally affect their environment but, like the satellite particles, they feel the gravitational force from the external potential particle, the dark matter halo, and the satellite particles. If the star particle is within the domain of the gas, then it also feels the gravitational attraction of the gas. The simulation is initialised with zero star particles, but star particles are spawned as described in §4.3.3

4.3.3 Star formation

We have added a star formation algorithm to spawn star particles. Using (4.7), the amount of gas that has been converted to stars in each cell on each iteration is calculated. For every 200 $\mathrm{M}_{\odot}$ of stars formed in a cell, one star particle is placed in that cell on a pre-defined shell. The star particle's initial velocity is set equal to the velocity of the gas within that cell. To numerically conserve mass, gas is not removed from the simulation when a star is born. We do not include stellar feedback, so energy is not returned to the gas when a star is born.

4.3.4 Initial conditions

We define our problem on a Cartesian grid with linear spacing. The simulation has a grid containing 128^3 cells, and physical dimensions of 60 kpc per side with the origin of the system at the centre of the box. We thus have a maximal sphere of $r_{\rm max} = 30$ kpc embedded in the grid.

We have performed test that show at our modest resolution of 128^3, a spherical shell launched from the centre of the Cartesian computational domain will lose its spherical symmetry as we approach $r_{\rm max}$ due to interactions with the boundary. Likewise, with inflow boundary conditions, a gravitational source at the centre of the grid will lose spherical symmetry since there is a longer distance to the fixed boundary along a diagonal than along the axis, which results in a cross-shaped pattern. To maintain spherical symmetry within $r_{\rm max}$, we impose $\rho(r > r_{\rm max}) = 0.01 \times \rho(\sqrt{3}r_{\rm max}) = 1.9 \times 10^{-29}$ g cm^{-3} and $0.01 \times e(r > r_{\rm max}) = e(\sqrt{3}r_{\rm max}) = 3.8 \times 10^6$ K. While we admit that this creates a discontinuity at $r_{\rm max}$, spherical symmetry is well maintained and, in the outflow test, waves are not reflected. The values imposed outside $r_{\rm max}$ help control the quantity of remaining gas in the scenario where a source evacuates the gas. These values are set low enough that minimal mass will be added to the simulation. We further impose a density and temperature floors of $\rho_{\rm floor} = 10^{-40}$ g cm^{-3} and $e_{\rm floor} = 10$ K, and impose outflow boundary conditions at all boundaries.

We set the initial gas profile to follow the observationally motivated β-profile (e.g. Cavaliere & Fusco-Femiano 1976):

$$\rho(r) = \rho_0 \left[1 + \left(\frac{r}{r_{\rm c}}\right)^2\right]^{-\frac{3}{2}\beta}, \tag{4.12}$$

where ρ_0 is the central density, $r_{\rm c}$ is the core radius, and β is the outer slope parameter; we set $\rho_0 = 1.67 \times 10^{-24}$ g cm^{-3} and we choose $r_{\rm c} = 1.75$ kpc and $\beta = 2/3$ as done in Moster et al. (2011). The total gas mass within 30 kpc is 2.5×10^{10} M$_\odot$ and, for simplicity, has no initial angular momentum. The temperature profile of the gas is given by (Kaufmann et al. 2007)

$$T(r) = \frac{\mu m_{\mathrm{p}}}{k_{\mathrm{B}}} \frac{1}{\rho(r)} \int_{r}^{\infty} \rho(r) \frac{GM(r)}{r^2} \mathrm{d}r, \tag{4.13}$$

where μ is the mean molecular weight, m_{p} is the proton mass, k_{B} is the Boltzmann constants, and $M(r)$ is the total mass interior to r. Using the equation of state and the ideal gas law, $p = \frac{k_{\mathrm{B}}}{\mu m_{\mathrm{p}}} \rho T$, the temperature is converted into internal energy density via

$$e(r) = \frac{3}{2} \frac{k_{\mathrm{B}}}{\mu m_{\mathrm{p}}} \rho(r) T(r), \tag{4.14}$$

assuming $\gamma = 5/3$.

We add an external potential (i.e. the dark matter halo) by modifying (4.9b). The external potential is centred on the origin and describes an NFW dark matter halo (Navarro et al. 1996),

$$M_{\mathrm{DM}}(r) = 4\pi\delta\rho_{\mathrm{c}} r_{\mathrm{s}}^3 \left[\ln\left(1 + \frac{r}{r_{\mathrm{s}}}\right) - \frac{r}{r + r_{\mathrm{s}}} \right], \tag{4.15}$$

where r_{s} is the scale radius, ρ_{c} is the critical density and δ is the over-density, which is given by

$$\delta = \frac{\Delta}{3} \frac{c_{\Delta}^3}{\ln(1 + c_{\Delta}) - \frac{c_{\Delta}}{1 + c_{\Delta}}}, \tag{4.16}$$

where c_{Δ} is the concentration parameter for a density contrast of Δ. We set $r_{\mathrm{s}} = 16.1$ kpc, $\Delta = 200$ and $c_{\Delta} = 20.1$, to reproduce a Milky Way-size dark matter halo (Nesti & Salucci 2013). The total dark matter mass within 30 kpc is 7.8×10^{11} $\mathrm{M}_{\odot}$.

To create the shock, we assume there is a luminous source, with $L = 4 \times 10^{46}$ erg s^{-1}, at the origin of the grid (as in McQuillin & McLaughlin 2012 and IF12); this adds additional source terms to (4.9b). The final equation of motion we use is

$$\frac{\partial \boldsymbol{v}}{\partial t} = -\frac{1}{\rho(r)} \boldsymbol{\nabla} p - \frac{GM_{DM}(r)}{r^2} + \frac{L}{M_{\mathrm{g}}(r) c} - \frac{\boldsymbol{v}}{M_{\mathrm{g}}(r)} \frac{\partial M_{\mathrm{g}}(r)}{\partial t}, \tag{4.17}$$

where the first term on the right hand side is from the hydrodynamic equations (equation 4.9b), the second term is from the dark matter halo, and the third and fourth terms are from the luminosity source. We explicitly note that, while the remainder of the system is loosely based upon the Local Group, the luminosity of the AGN is $\sim 10^7$ times more luminous than Sgr A*.

In their analytical calculations, IF12 assume that the luminous source is on for all time; results for up to 1 Gyr are presented in their figures. However, the lifetime of AGN are uncertain. The upper limit is $\sim 10^9$ yr, during which time entire quasar populations rise and fall (e.g. Osmer 1998). The lower limit of $\sim 10^5$ yr is based upon indirect requirements (e.g. Bajtlik et al. 1988; Bechtold 1994). The former lifetime would indicate that AGN are rare phenomena, while the latter would suggest that they are common and that a large fraction of present-day galaxies have gone through AGN episodes in their past.

In their various models, Martini & Weinberg (2001) obtain lifetimes of 10^7–10^8 yr, which is similar to the Salpeter time. Their models rely on the ratio of the quasar being on and the total age of the host dark matter halo in which it resides. Thus, they cannot distinguish between one episode or several shorter episodes of activity totalling the same length. Hopkins & Hernquist (2009) further show that the same final black hole mass can be achieved through one quasar episode, or several episodes of shorter duration.

For our simulation, we will adopt the episodic model to study the effect of AGN activity both on creating stars and on the dynamics of existing stars. Our luminous source will be on for 2×10^7 yr, and then off for 2×10^8 yr. When the luminous source is off, the final two terms in (4.17) are set to zero.

4.3.5 Additional models

In addition to the fiducial model described above, we have run several variations in order to determine the effect of the various components. Specifically, we have run simulations without the satellites and the external potential particles to

Name	Luminosity of AGN (10^{46} erg s^{-1})	Duty Cycle (on/off; Myr)	'Mass' per Star Particle ($M_\odot$)	Number of Satellites	Number External of Potential Particles	Resolution
Fid	4	20/200	200	40	1	128^3
Fid400	4	20/200	400	40	1	128^3
NoAGN	0	0/ 0	200	40	1	128^3
NoSat	4	20/200	200	0	1	128^3
NoSatE	4	20/200	200	0	0	128^3
NoEP	4	20/200	200	40	0	128^3
HiRes	4	20/200	50	40	1	256^3

Table 4.1: The various models. The fiducial model is Fid.

determine their respective tidal influences, we have tested a quiescent model with no AGN feedback to determine the properties of the system under the maximal star formation rate, and we have varied the resolution of the system and the star formation threshold. The full list of simulations is given in Table 4.1. In the remainder of the text, if we do not refer to a specific model, we are referring to the fiducial model, Fid.

4.4 Results

We have evolved our system for 7 Gyr in order to track the evolution of the stellar distributions over half a Hubble time. The luminous source is on for 20 Myr, then off for 200 Myr, and thus there are ∼32 cycles (one complete cycle is 220 Myr). During the first three cycles, 98% of all the stars in our simulation are born. During this same time, ∼97% of all the gas is blown out of the system. After 2 Gyr, the system equilibriates with ∼0.2% of the initial gas mass as a result of the numerically imposed density floor. The external potential particle reaches periapsis at 665 Myr.

It is inevitable that the AGN will produce negative feedback on star formation within the core region. Although the negative feedback has a profound evolution on the system as a whole, we are focusing on the positive feedback that occurs in the shells. In our analysis, we will consider both the stellar system as a whole, and the subset of the first generation stars that were formed as a result of positive feedback.

4.4.1 Gas evolution

In Figs. 4.1 and 4.2, we plot snapshots of the $x-y$ plane of the gas density and temperature, respectively, over the first cycle. The central void at 10 and 20 Myr is driven by the luminous source. The void continues to increase until ∼30 Myr from residual linear momentum of the gas. As the shock propagates, the shocked gas cools, and the overall temperature and density of the system decreases. Shortly after 30 Myr, the gas begins to collapse and, by 40 Myr, there is low-density, high-temperature gas in the nuclear region. The central densities and temperatures then increase as the gas returns to the core. By the end of the first cycle, the reformed central density peak (prominent at 80 Myr) has dissipated, and the density and temperature profiles are moderately stable. The initial gas has zero angular momentum, but rotation (with $v \lesssim 100$ km s^{-1}) and a weak spiral structure has developed by the end of the cycle as a result of the satellite particles dragging the gas; the spiral structure is more prominent in NoAGN since it is not periodically destroyed by AGN feedback. The satellite particles likely lead to more heating than is feasible since they are not permitted to be disrupted. Energy that would otherwise be dissipated via disrupting a satellite is instead transferred to or kept in the gas.

The next several cycles are qualitatively similar, but with less gas mass in each successive cycle. The cycles after ∼1 Gyr are less coherent due to the substantially reduced gas mass. The net rotation persists, but the density spirals and approximate spherical symmetry do not reform.

In the absence of the satellite particles (model NoSat), asymmetries initially form as a result of the gravitational influence from the external potential, and they grow over time; the external potential particle does not excite a coherent rotation (model NoSatE).

4.4.2 Star formation

The star formation algorithm added to Zeus-3D calculates the amount of gas converted to stars at each iteration in every cell. We acknowledge that there are no

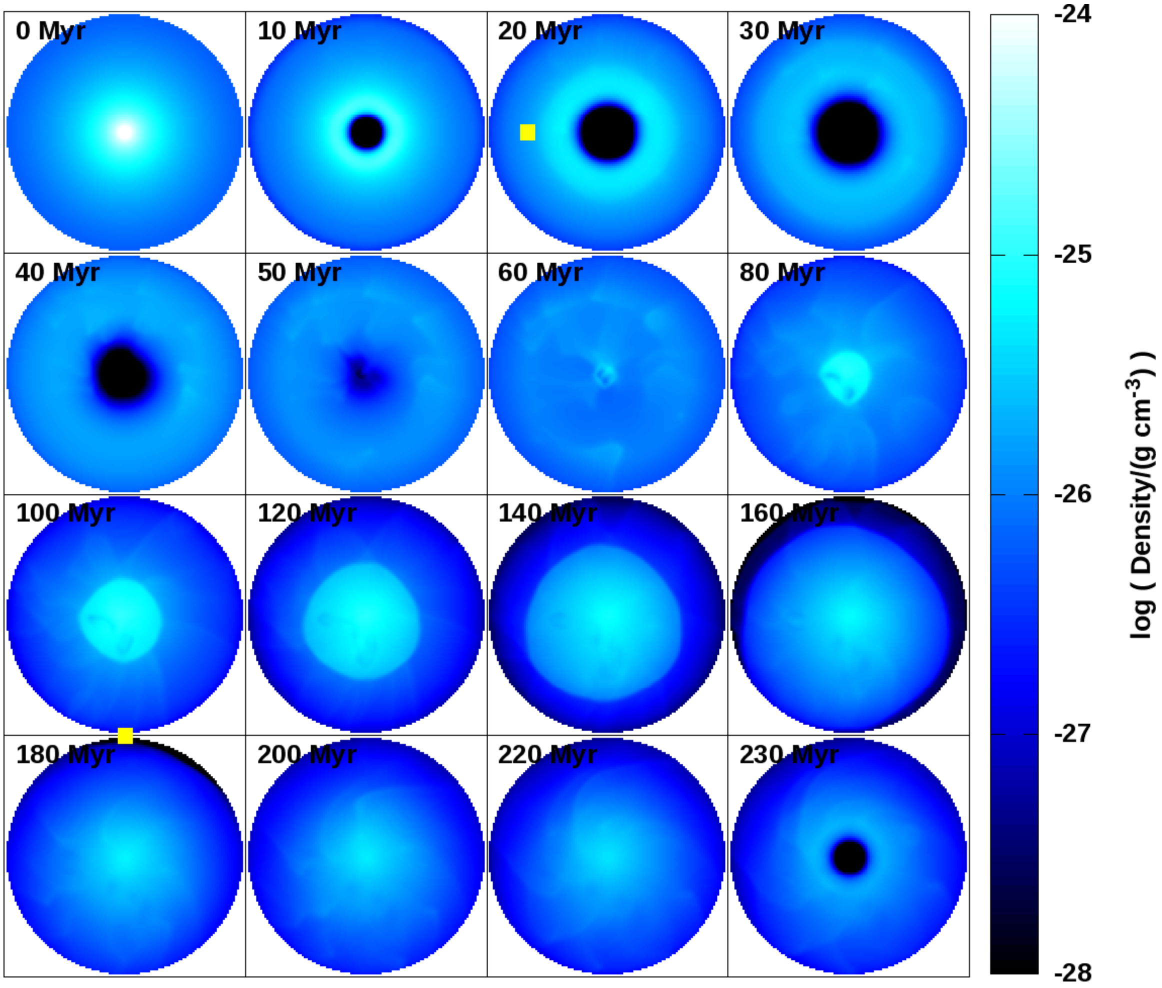

Figure 4.1: Evolution of the gas density over one cycle. Times from the onset of the simulation are listed in each frame. Each frame is a slice at $z = 0$, with $x = y = 0$ in the centre of the frame; each frame measures 60 kpc per side. The total gas mass at 0 Myr is 2.53×10^{10} $M_{\odot}$ and at 220 Myr is 7.3×10^{9} $M_{\odot}$. The numerically imposed density floor is 10^{-40} g cm^{-3}. Relative to the frame at 0 Myr, the yellow square in the first column represents the initial location of the external potential particle, and the yellow square in the top row represents the location of the external potential at apoapsis, which occurs at 665 Myr.

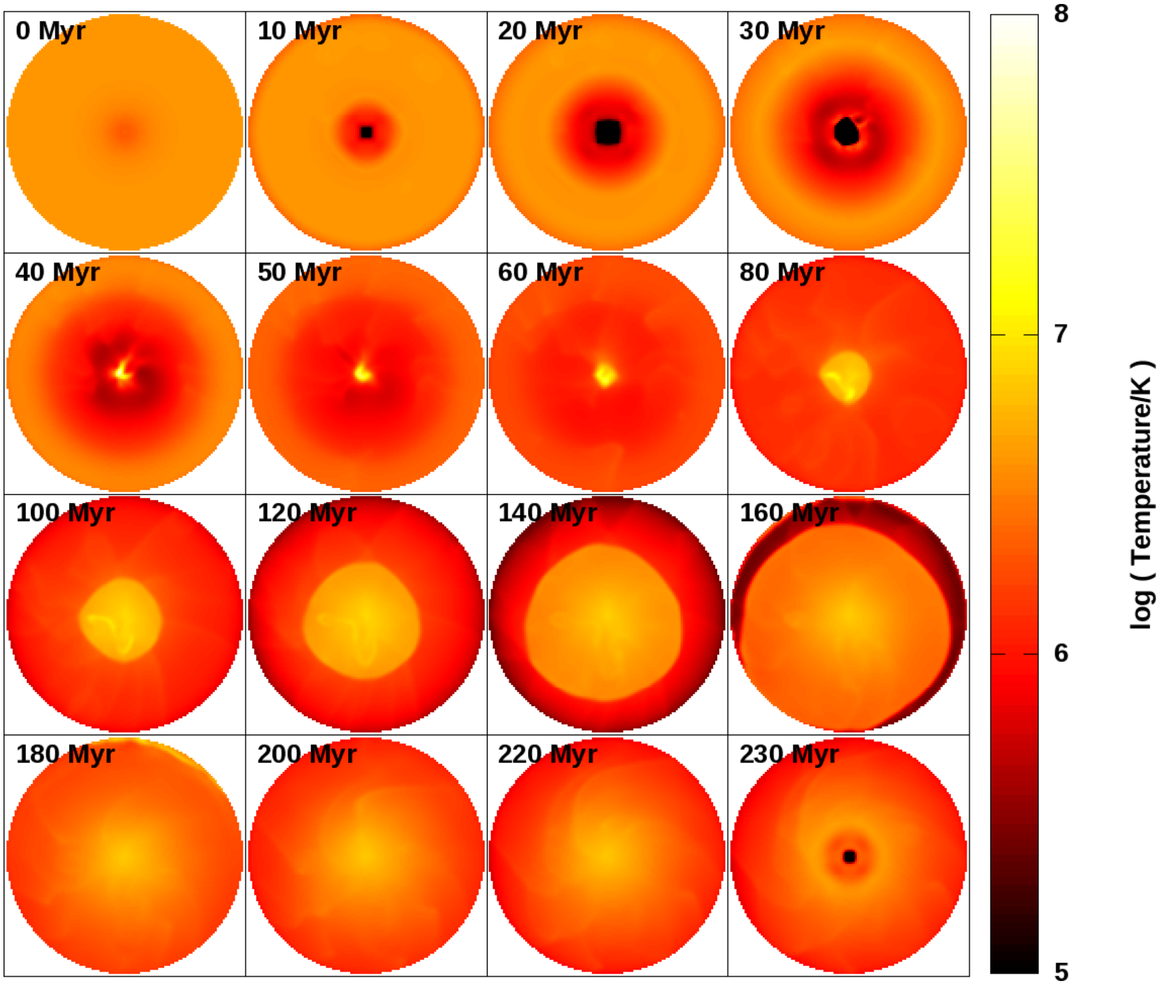

Figure 4.2: Evolution of the gas temperature over one cycle. Times from the onset of the simulation are listed in each frame. Each frame is a slice at $z = 0$, with $x = y = 0$ in the centre of the frame; each frame measures 60 kpc per side. The numerically imposed temperature floor is 10 K.

restrictions on this algorithm, such as flow convergence or temperature limits, thus we are likely over-producing the number of stars. We tested the algorithm with a reasonable density floor of 2×10^{-26} g cm^{-3} (i.e. stellar mass was created only in cells with density greater than the density floor; e.g. Thacker & Couchman 2000; Dubois et al. 2012), and the stellar mass produced was within a factor of two of the unrestricted algorithm. Likewise, in the absence of stellar feedback and a temperature ceiling, we are also over-producing the number of star particles since the algorithm allows stars to spawn in regions that are hotter than physically justified (e.g. Springel & Hernquist 2003). However, if the shock is not sufficiently well resolved, then we will be over-estimating its width and underestimating its density. This combination will likely lead to an under-production of stars in the shocks. We are also underestimating the temperature of the shock, thus if a temperature ceiling was imposed on the star formation algorithm, then this would reduce the number of stars formed in the shock. Thus, our discussion will be limited to predictions on distributions of stars, but not on the quantity. Indeed, the emphasis of this investigation is to see how a distribution of massless tracers, sourced with an initial velocity, eventually disperses into the overall halo. Thus, the overall star formation rate normalization, provided it is not anticipated to be excessively large, is actually not a significant contributor to the evolution of the simulated system.

We calculate the SFR using two methods: discrete and continuous. For the discrete method, we use $Nm_{\rm s}/dt$, where $m_{\rm s}$ is the mass associated with a star particle and N is the number of stars spawned during the time interval dt; we use $dt = 5$ Myr. In the continuous method, we calculate the amount of gas mass that has been converted to stellar mass as per the Schmidt Law and perform this calculation at 5 Myr intervals. Ideally, both of these rates should be similar, but we accept that the discrete rate will typically be lower since a critical mass of gas must be converted to stars in a given cell prior to a particle being spawned. In Fig. 4.3, we plot the discrete and continuous SFRs and the number of star particles over time. In Fig. 4.4, we plot

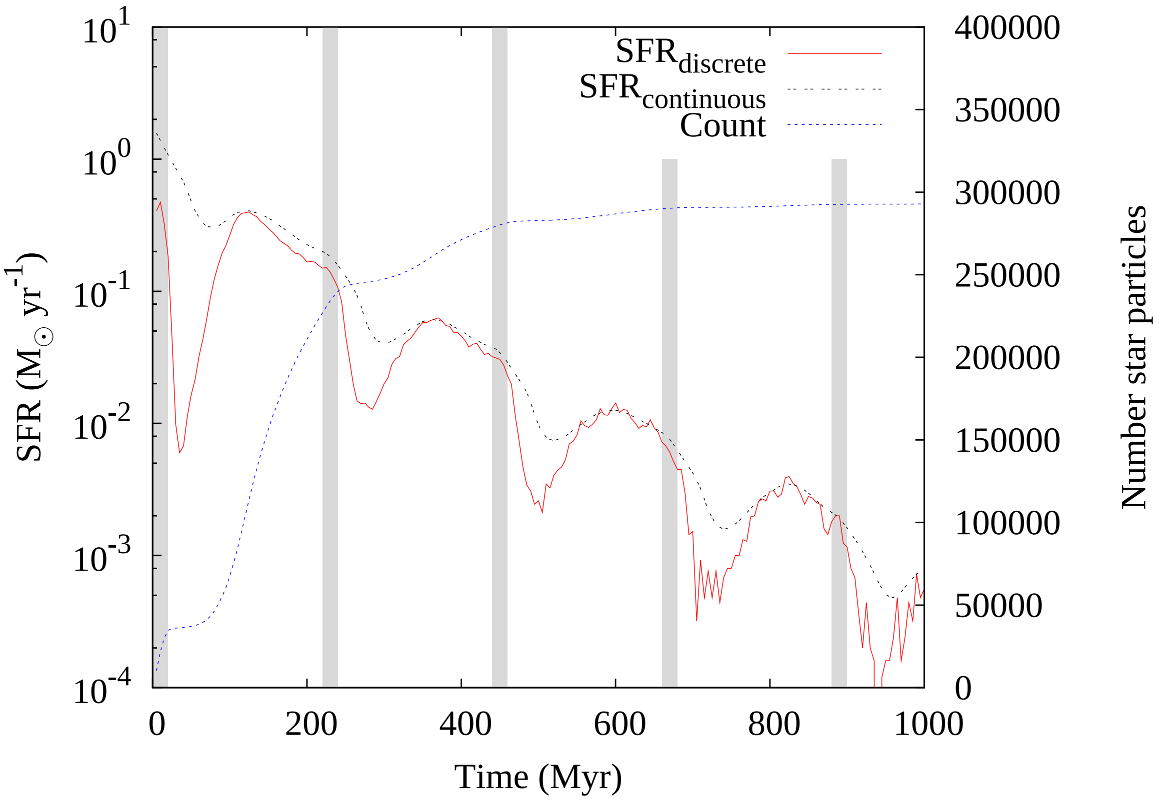

Figure 4.3: Discrete SFR (based upon particle production), continuous SFR (based upon mass conversion) and star particle count for the first 1 Gyr of the simulation. The gray stripes indicate when the luminous source is on.

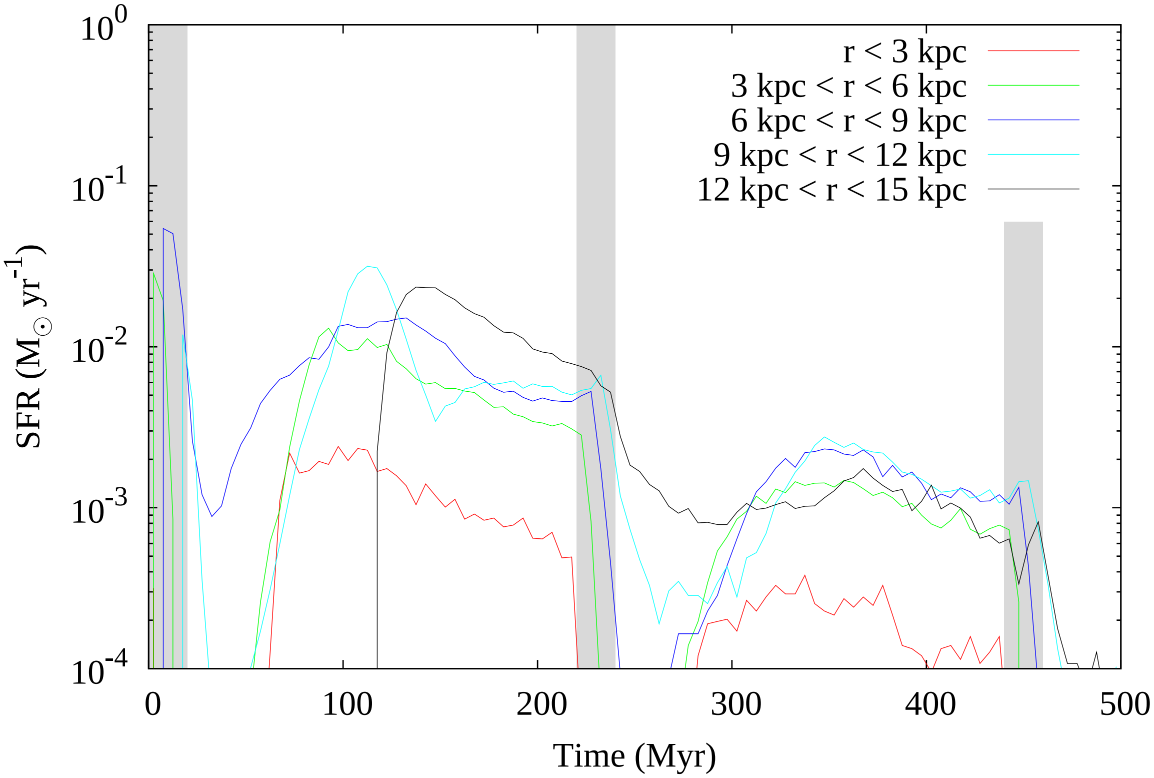

Figure 4.4: Discrete SFR for Fid separated by radius. The gray stripes indicate when the luminous source is on.

the discrete SFR for five radial bins over the first 500 Myr; although each bin has the same width, the volume is increasing with each subsequent bin.

In the first 20 Myr, there is a strong, but brief, star formation epoch, with the first stars being spawned within 200 kyr. These stars are born in the shells created by the AGN feedback, and will be discussed in detail in §4.4.3.

The second epoch of star formation follows a quiescent star formation period and peaks at 115 Myr. During this epoch, gas is returning to the inner regions, which naturally increases the SFR. Strong star formation begins in the range $6 < r/\mathrm{kpc} < 9$, since this is the first region the collapsing gas passes through. Larger radii feel only weak feedback and may not be shocked. However, their gas density is low and thus it takes considerable time before any star particles are spawned, hence the delayed star formation in the outer regions. At all radii, the gas density is slowly decreasing as the system relaxes, hence the systematic decrease in SFR.

This second star formation epoch occurs when the luminous source is off, and thus the stars are spawned at all radii and not in expanding shells. They are spawned with velocities that cover the full range of $v_{\rm t}^2/v^2 \in [0,1]$, where $v_{\rm t}$ is the tangential velocity and v is the total velocity. Although the peak SFR is similar to the first epoch, its duration allows a considerable number of star particles to be spawned. The stars from this star formation epoch dominate the dynamics of the stellar system.

The second AGN event displays both positive and negative feedback. Once the AGN is turned on, star formation is quenched in the core ($r < 3$ kpc). The quenching extends to larger radii as the effects of the AGN feedback expand outwards; by 240 Myr, most of the star formation within 12 kpc has been quenched. However, prior to the negative feedback quenching star formation at these larger radii, positive feedback triggers weak star formation in the shells created by the AGN. There is a clear rise in star formation between $6 < r/\text{kpc} < 9$, peaking at $\sim$227 Myr. This shell expands outwards, and the SFR for $9 < r/\text{kpc} < 12$, peaks at $\sim$232 Myr. Although these peaks are small, they represent positive feedback.

The above cycle is repeated with varying strengths until $\sim$1.5 Gyr, with each subsequent SFR peak being smaller. During each 'on' phase, new stars are formed in the expanding shell and not near the black hole. This can be seen in Fig. 4.4 at $\sim$450 Myr, where there are slight increases in the SFRs during the AGN episode for each geometric region; the results are noisier than the second episode due to the smaller number of stars being born. After $\sim$1.5 Gyr, the gas mass has been substantially depleted, and the location of where stars are spawned is nearly stochastic, with no preference to shocks or post-shock over-densities.

Although the AGN feedback triggers star formation in expanding shells, it also highly quenches the global star formation rate. This is a result of feedback being returned spherically in our model, blowing the gas out of the simulation domain in all directions. If feedback was radially directed (i.e. a jet), then most of the central gas would be unmodified. Thus, the SFR in the core would also remain mostly unmodified during an AGN episode. Applying radially directed feedback energy may prevent the significant quenching of star formation in our model.

Over the first Gyr, the peak discrete (continuous) SFR drops by ∼2.7 dex (∼3.3 dex), while the total gas mass drops by ∼2.2 dex over the same time period. In the absence of AGN feedback (model NoAGN), the discrete (continuous) SFR drops by ∼1.3 dex (∼1.6 dex) over the first Gyr, and the total gas mass decreases by ∼1 dex (by gas flowing out through the boundaries as the system is relaxing). Thus, both with and without AGN feedback, the SFR loosely traces the evolution of the total gas mass, and the AGN quickly depletes the gas from the system. By 1 Gyr, there is 5.9×10^7 $\mathrm{M}_\odot$ of stellar mass represented by particles in Fid, and 20.4×10^7 $\mathrm{M}_\odot$ in NoAGN. See Fig. 4.5 for the SFRs of models Fid and NoAGN.

4.4.3 First generation stars

We define first generation stars to be those born in the first shell and explicitly note that we do not use this term to refer to Population III stars. These stars are spawned prior to 35 Myr, have $v_\mathrm{t}^2/v^2 \leq 0.005$, and constitute 7.0×10^6 $\mathrm{M}_\odot$ of stellar mass.

In Fig. 4.6, we plot the discrete SFR for both Fid and NoAGN for five radial bins. The peak SFR in Fid moves outwards with time, indicating an expanding shell. Moreover, for the ranges of $3 < r/\mathrm{kpc} < 6$, $6 < r/\mathrm{kpc} < 9$ and $9 < r/\mathrm{kpc} < 12$, the peak SFR occurs in Fid before NoAGN indicating that these stars were born as a result of triggered star formation.

The early stellar distributions evolve rapidly, as shown in Figs. 4.7, 4.8 and 4.9, where we plot the evolution of the profiles for stellar density, velocity and v_t^2/v^2 over the first 200 Myr.

As expected, the $t = 20$ Myr density profile shows a narrow distribution of stars, all of which have a highly radial trajectory. The slow stars quickly begin to fall back into the core, while the outer stars and newly spawned stars (born at

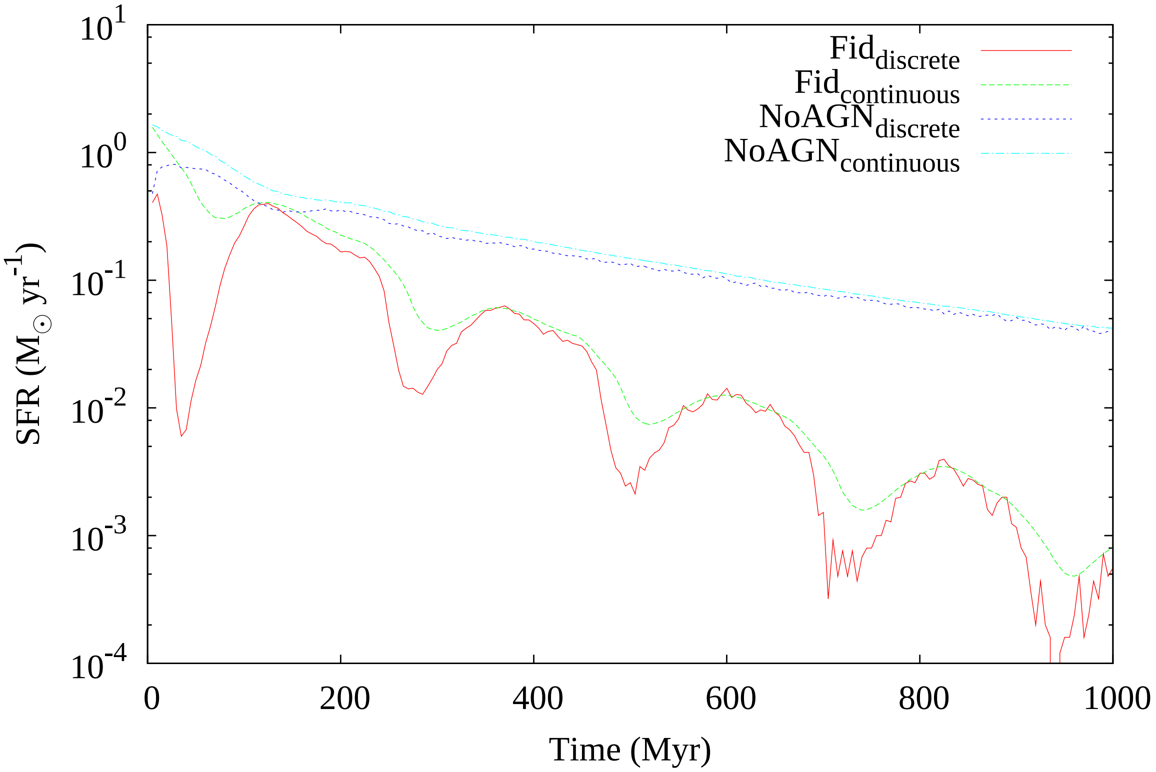

Figure 4.5: Discrete and continuous SFRs for models Fid and NoAGN over the first Gyr.

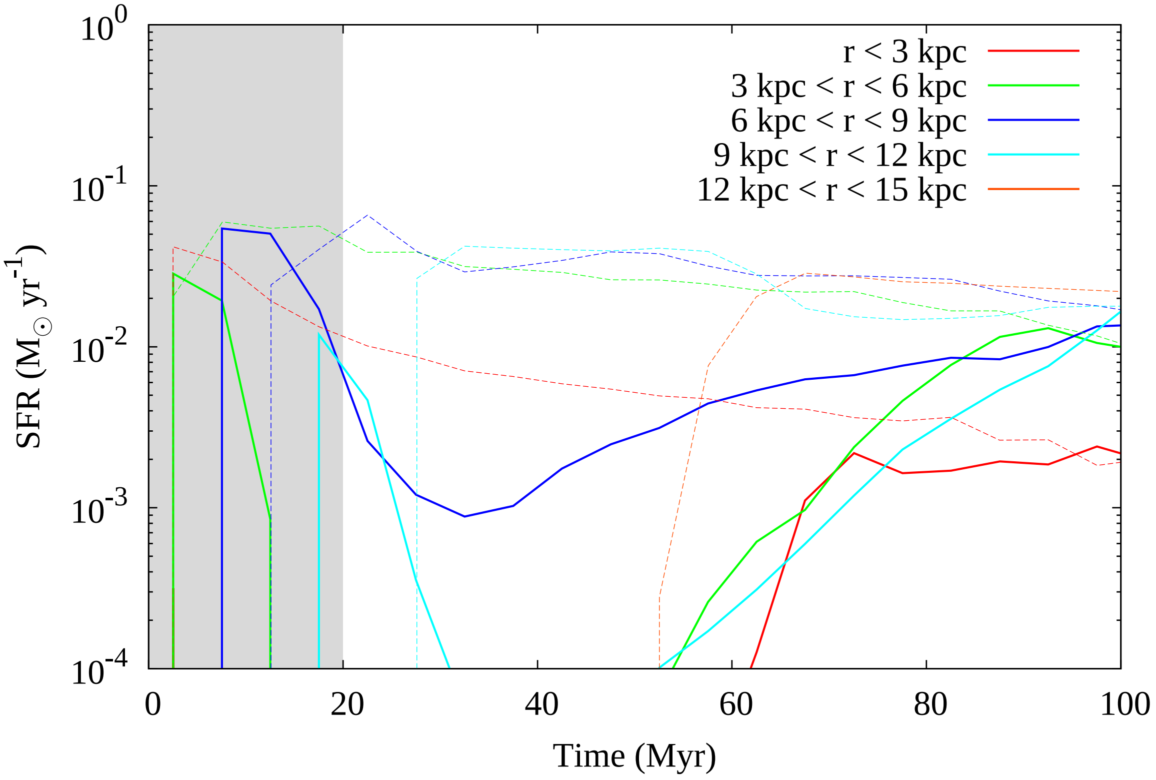

Figure 4.6: Discrete SFR for Fid (thick solid lines) and NoAGN (thin dashed lines) separated by radius. The gray stripe indicates when the luminous source is on. Triggered star formation is most notable between $6 < r/\mathrm{kpc} < 12$, where the star formation stars later in NoAGN.

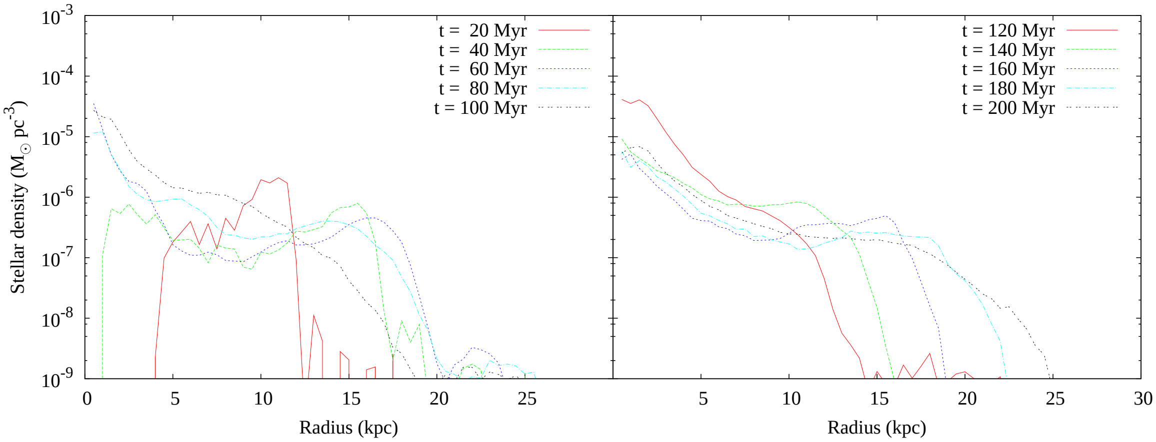

Figure 4.7: Stellar density profile of the first generation stars for the first 200 Myr. Times are from the beginning of the simulation.

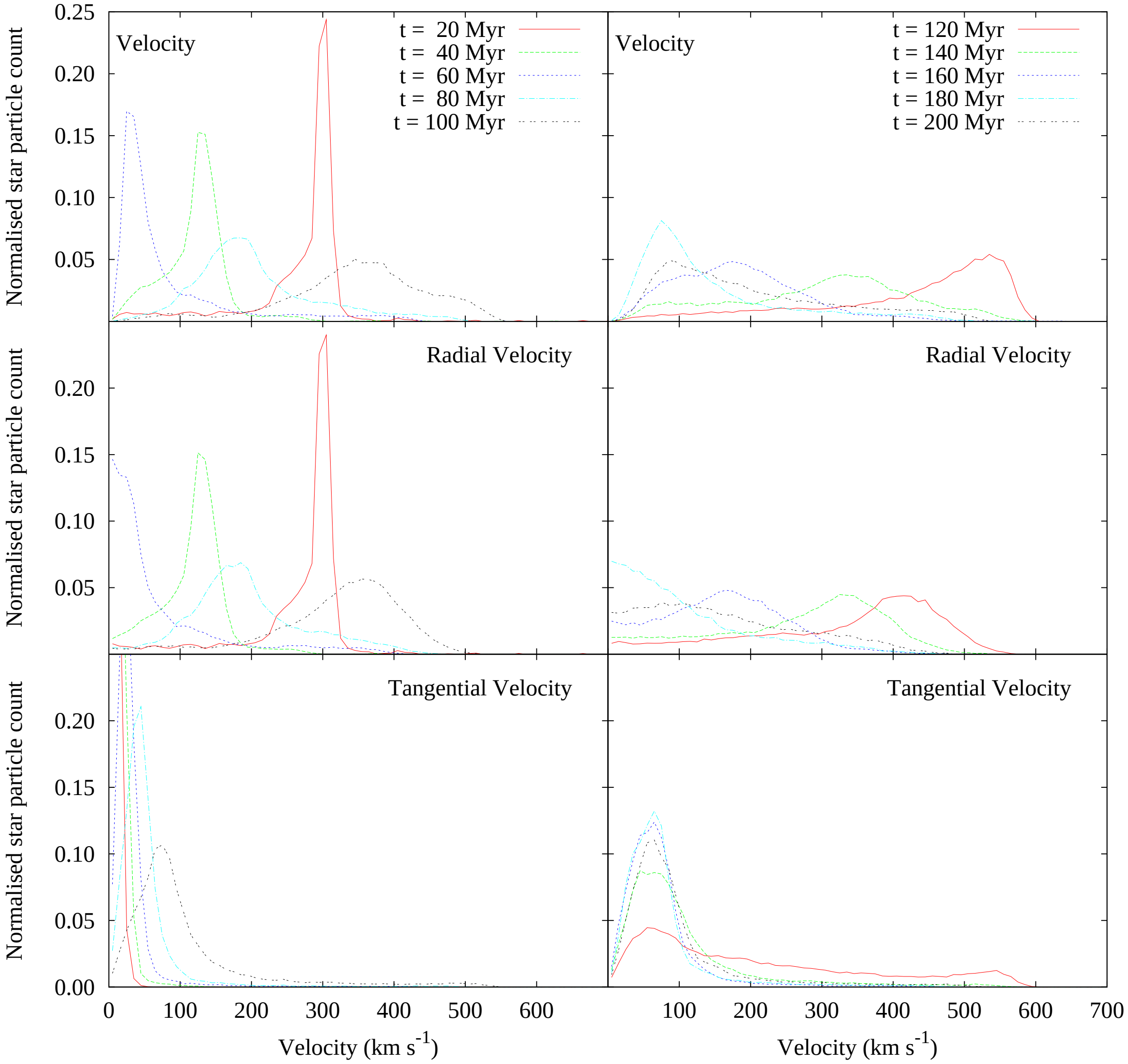

Figure 4.8: Stellar velocity profiles of the first generations stars for the first 200 Myr. Counts have been normalised such that the area under each curve is 1, regardless of the total number of stars at that time. Times are from the beginning of the simulation. Velocities are plotted in bins of 10 km s^{-1}. *Top row*: total velocity distribution. *Middle row*: radial component of the velocity. *Bottom row*: tangential component to the velocity.

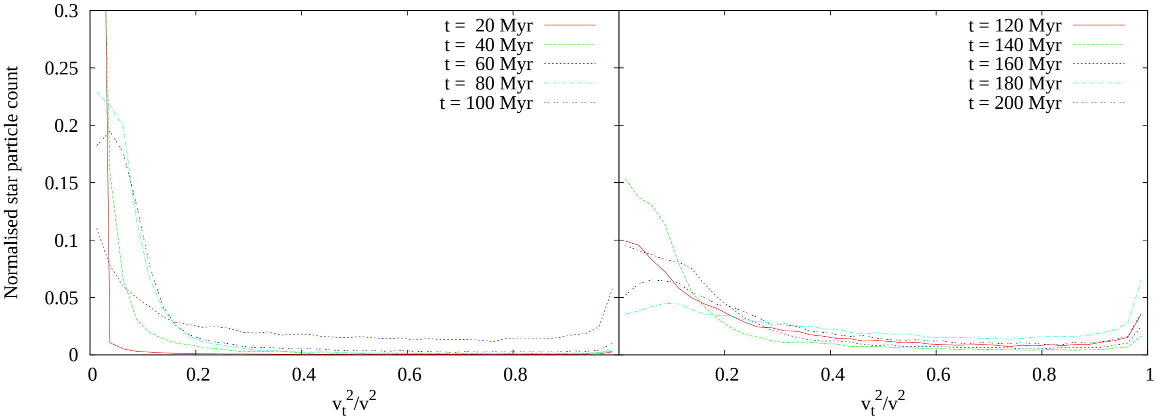

Figure 4.9: Ratio of v_t^2/v^2 for the first generations stars for the first 200 Myr. Counts have been normalised such that the area under each curve is 1, regardless of the total number of stars at that time. Times are from the beginning of the simulation. Values are plotted in bins of 0.025.

$20 < t/\mathrm{Myr} < 35$) continue on their radial trajectory outwards, hence the broadening of the stellar distribution by 40 Myr. With no outward acceleration, these stars slow down and reach their maximum distance and minimum velocity at $t \sim 60$ Myr. When the stars are at their greatest distance from the core, they are most susceptible to the gravitational influences of the satellites. Thus, this is when the tangential component to the velocity begins to increase (notable by the increase in number of stars at each value of $v_\mathrm{t}^2/v^2 \gtrsim 0.2$). This is equally noticeable in the broadening of the radial velocity profile.

With even a slight gravitational influence, the radial trajectory of a star is perturbed into an ellipse. As the stars plunge towards the core, the radial component again increases. As the stars approach the core, they pass by it with some non-zero impact parameter, thus there is again a high v_t^2/v^2 for $120 \lesssim t/\mathrm{Myr} \lesssim 140$ when the stars are at periapsis. With each oscillation, the v_t^2/v^2 distribution spreads out, with a greater number of stars permanently occupying larger values of v_t^2/v^2.

This distortion of a radial trajectory can be clearly seen in the top left panel of Fig. 4.10, where we plot the path of one first generation star (projected onto the

$x - y$ plane) over 1.5 Gyr; in the bottom left panel, we plot $v_{\rm t}(t)^2/v(t)^2$ for the same particle. The trajectory of this particle is oscillatory about the core with a random component to the precession caused by the gravitational influence of the additional gravitational sources. Moreover, the satellite particles accelerate the stars such that they oscillate with larger amplitudes than with which they were spawned and prevent them from maintaining a 'stable' orbit. The local maxima of $v_{\rm t}^2/v^2$ occur at both periapsis and apoapsis. However, the value of the local minima and maxima change on every orbit as a result of continual perturbations.

In comparison, the middle and right columns show more stable stellar orbits. There is a slight precession caused by the external potential particle in the absence of satellite particles (middle column). With a growing minor axis of the elliptical orbit, the local minima of $v_{\rm t}^2/v^2$ slowly increases. There is minimal precession when there are no external influences (right column). In both of these cases, the amplitude of the oscillations is approximately constant with time.

4.4.4 Stellar distributions

By 660 Myr, 98% of all the stars have been born, accounting for 5.9×10^7 $M_\odot$ of stellar mass. The age distribution of the star particles at 7 Gyr is plotted in Fig. 4.11. The early evolution is strongly affected by the properties of the gas from which the stars were spawned, the first encounters with the satellites, and the close passage of the external potential; this will be discussed in §4.4.4.1. The remainder of the evolution to 7 Gyr will be discussed in §4.4.4.2.

4.4.4.1 The first Gyr

Over the first Gyr, the first generation stars continue to oscillate about the core, spending a large portion of their time in the outer regions. Thus, the stellar distribution becomes more extended, and the central densities decrease; see the left panel in Fig. 4.12. The peak velocity decreases, and the tangential component to the velocity increases; see the left column in Figs. 4.13 and 4.14.

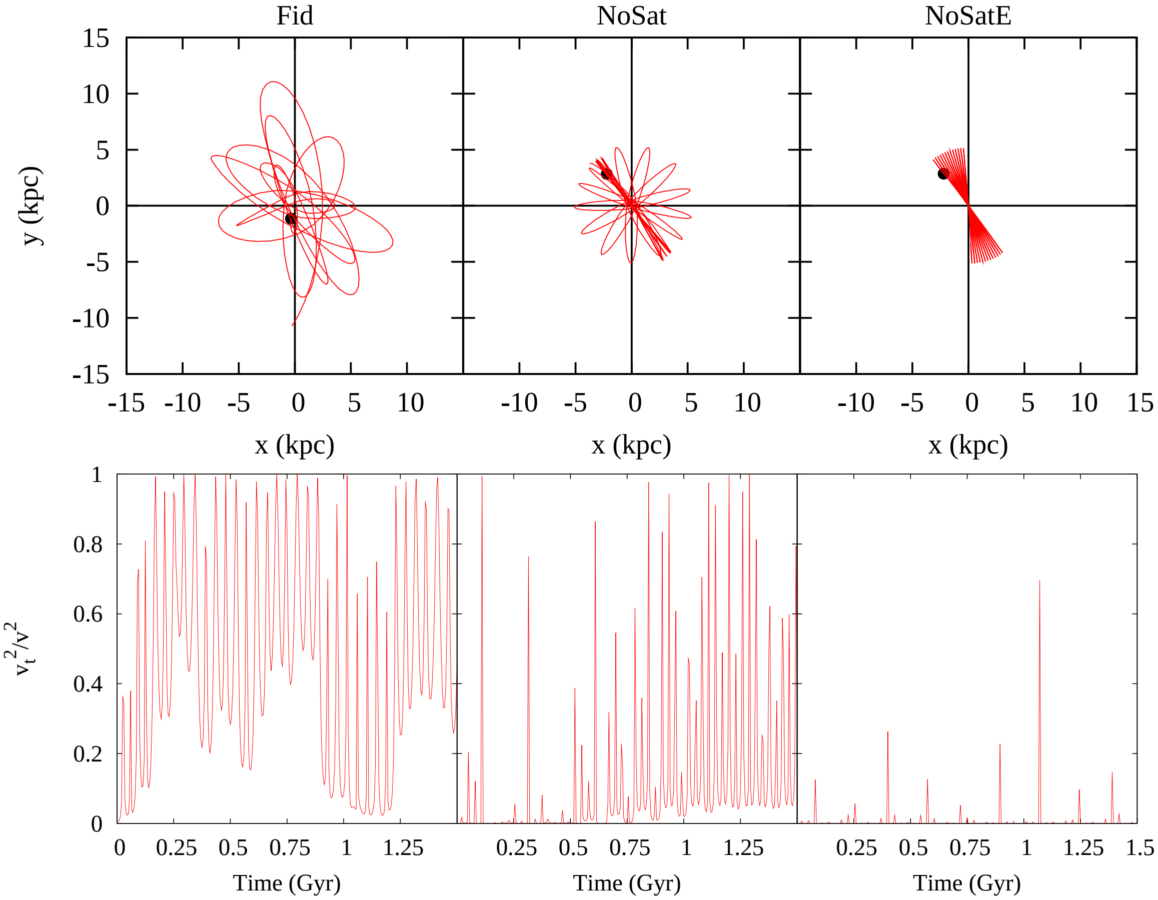

Figure 4.10: Projected stellar path (top row) and evolution of $v_{\rm t}^2/v^2$ (bottom row) for one first generation star for models Fid, NoSat, and NoSatE for 1.5 Gyr. The black dot in the top row indicates the spawning location of the star. The stars are born in an expanding shell with initially outward radial velocity and $v_{\rm t}^2/v^2 \sim 0$.

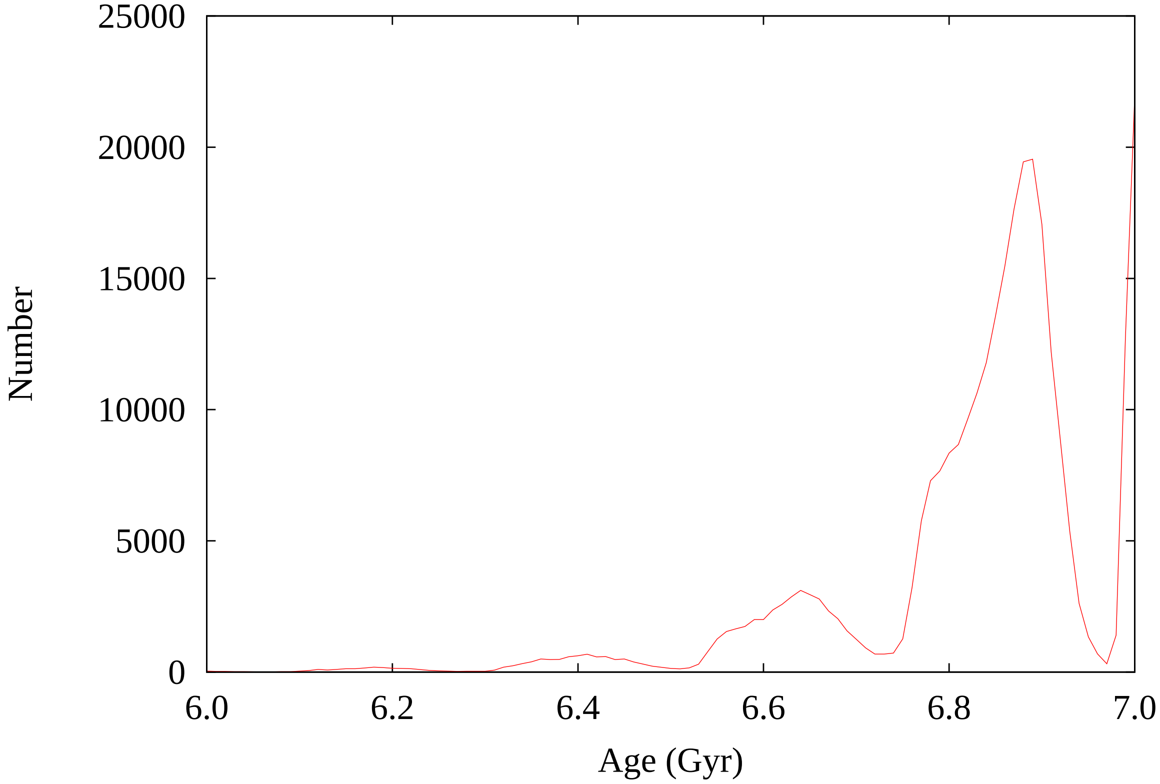

Figure 4.11: Age distribution of the stars at 7 Gyr, plotted in bins of 10 Myr.

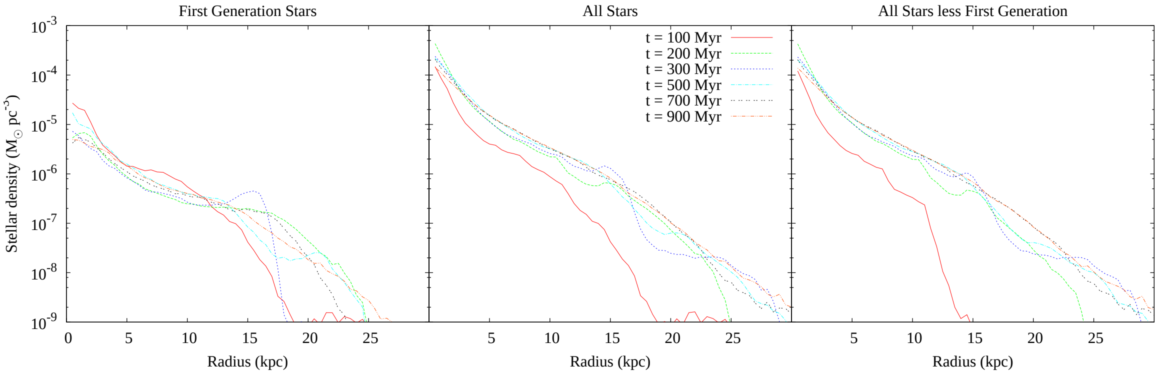

Figure 4.12: Stellar density profiles for the first Gyr for the first generation stars (left), the total stellar population (centre) and the non-first generation stars (right). Times are from the beginning of the simulation.

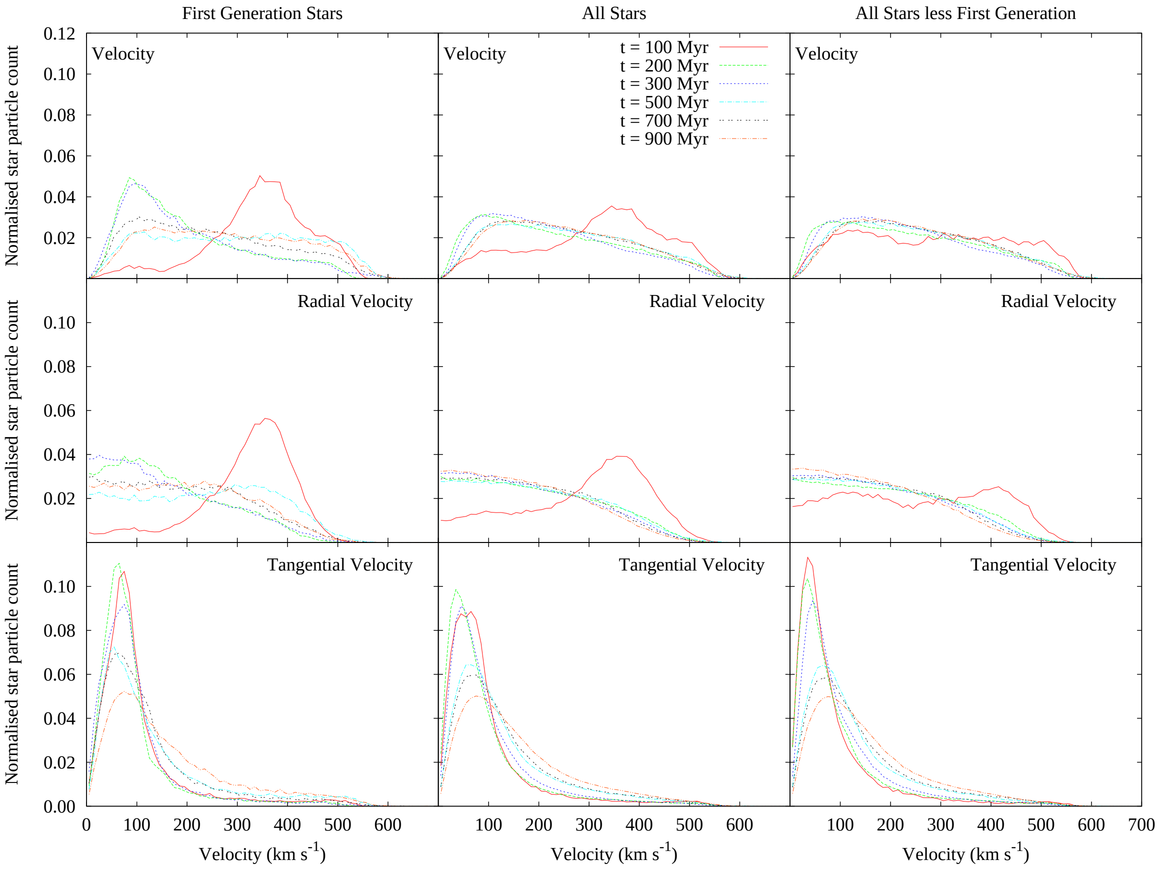

Figure 4.13: Stellar velocity profiles for the first Gyr for the first generation stars (left column), the total stellar population (middle column) and the non-first generation stars (right column). Counts have been normalised such that the area under each curve is 1, regardless of the total number of stars at that time. Times are from the beginning of the simulation. Velocities are plotted in bins of 10 km s^{-1}. *Top row*: total velocity distribution. *Middle row*: radial component of the velocity. *Bottom row*: tangential component to the velocity.

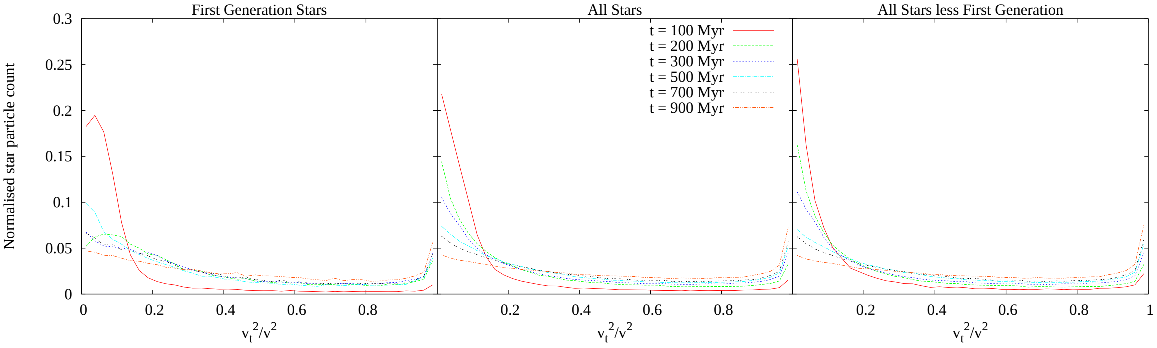

Figure 4.14: Ratio of v_{t}^2/v^2 for the first Gyr for the first generation stars (left column), the total stellar population (middle column) and the non-first generation stars (right column). Counts have been normalised such that the area under each curve is 1, regardless of the total number of stars at that time. Times are from the beginning of the simulation. Values are plotted in bins of 0.025.

At 100 Myr, 51.8% of the stars are first generation stars, thus the total distributions are heavily influenced by this population. The non-first generation stars were born in the core, hence there is a sharp decline in stellar density for $r \gtrsim 10$ kpc; see the right panel in Fig. 4.12. These stars have an approximately uniform distribution of radial and tangential velocities at 100 Myr (right column of Fig. 4.13), but the majority of the stars have $v_{\mathrm{t}}^2/v^2 \lesssim 0.2$ (right column of Fig. 4.14). By 200 Myr, the first generation stars represent only 16.5% of the total stellar population, thus the total and non-first generation profiles are similar. Over the first Gyr, the stellar density continues to increase at all radii due to stars being spawned. The increase in the outer regions ($r > 15$ kpc) is from low velocity stars spending much of their time there. The ratio $v_{\mathrm{t}}^2/v^2 \lesssim 0.2$ tends to flatten, with more stars obtaining a higher ratio.

By 1 Gyr, the first generation stars comprise 11.6% of the total population.

4.4.4.2 The final six Gyrs

The stellar distributions continue to evolve on both short time-scales (i.e. an orbital period), and on long time-scales, which we will discuss here. As the simulation

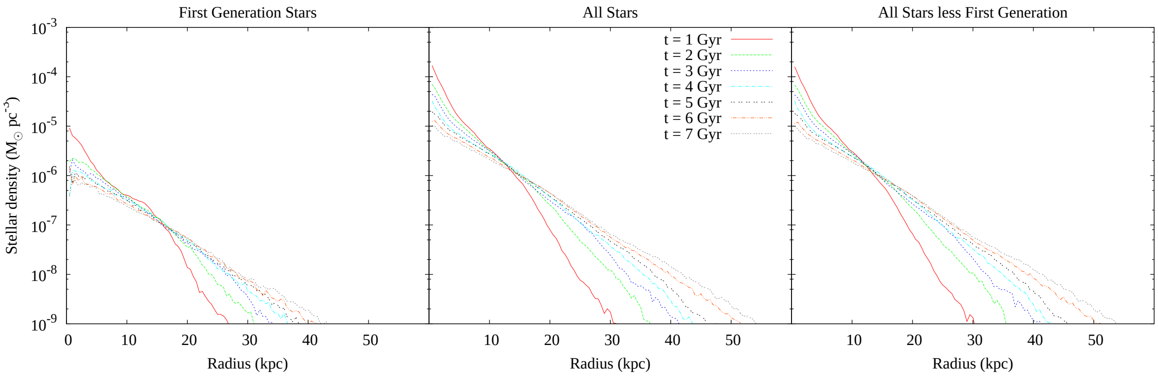

Figure 4.15: Stellar density profiles every Gyr for the first generation stars (left), the total stellar population (middle) and the non-first generation stars (right). Times are from the beginning of the simulation.

evolves from 1 to 7 Gyr, the stellar density profile becomes shallower, as seen in Fig. 4.15. This is a result of gravitational influences from the nearby satellites perturbing the stellar orbits, systematically boosting them outwards. This flattening of the density profile is not seen in models NoSat and NoSatE, but is observed in model NoEP, confirming that this is a result of the satellite system. The flattening systematically occurs for both the total distribution and the distribution of the first generation of stars since they are well-mixed by this time.

Although the density profile continually flattens, the evolution of the velocity profile drastically slows down after 3 Gyr, as seen in Figs. 4.16 and 4.17. At 1 Gyr, most of the stars have a small tangential component. As the system evolves, the stars continue to be affected by the satellites and the orbits will become more circularised, with the average tangential velocity increasing and radial velocity decreasing. By 3 Gyr, an equilibrium has been reached in the stellar distributions, and the velocity profile remains approximately constant. There is a slight diffusion of stars to higher tangential velocities between 3 and 7 Gyr. The increase in number of stars with $v_\mathrm{t}^2/v^2 \gtrsim 0.9$ is from the stars spending more time in the outer regions. In NoSat, NoSatE and NoEP, the velocity distribution also becomes approximately constant after 3 Gyr. In the absence of the satellite particles (model NoSat), 73.4% have

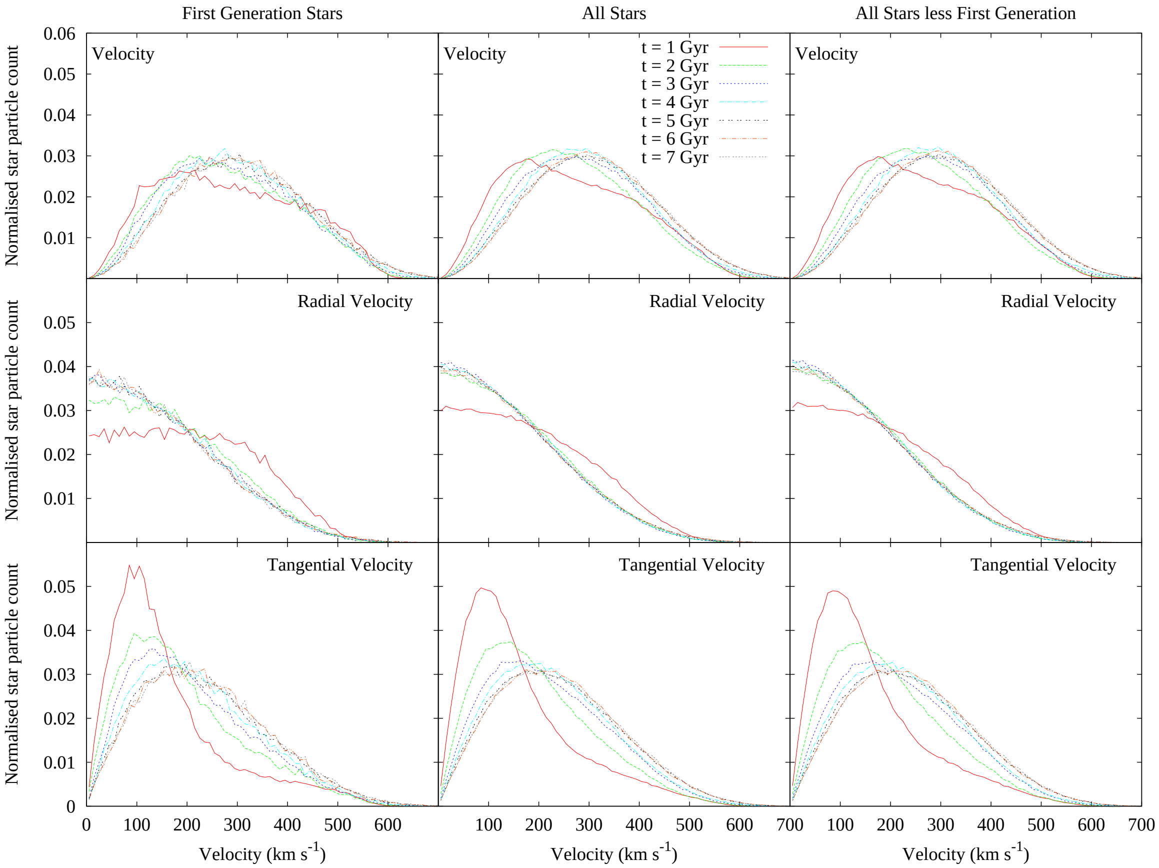

Figure 4.16: Stellar velocity profiles every Gyr for the first generation stars (left column), the total stellar population (middle column) and the non-first generation stars (right column). Counts have been normalised such that the area under each curve is 1, regardless of the total number of stars at that time. Times are from the beginning of the simulation. Velocities are plotted in bins of 10 km s^{-1}. *Top row*: total velocity distribution. *Middle row*: radial component of the velocity. *Bottom row*: tangential component to the velocity.

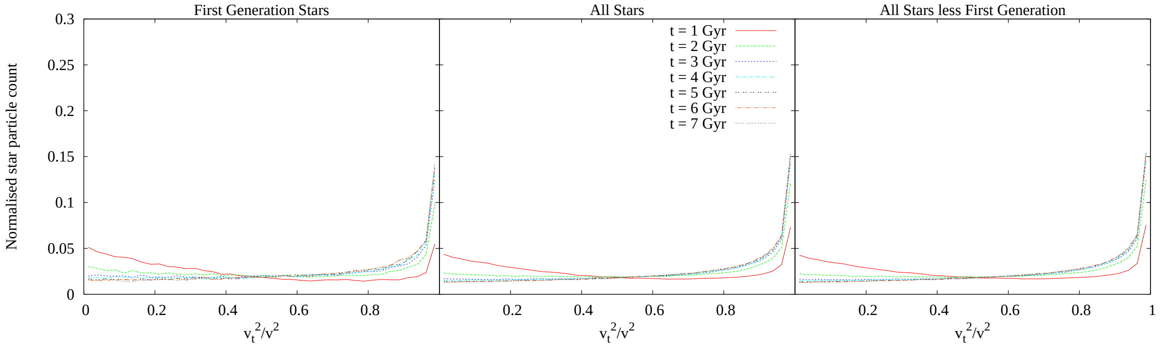

Figure 4.17: Ratio of v_{t}^2/v^2 for every Gyr for the first generation stars (left column), the total stellar population (middle column) and the non-first generation stars (right column). Counts have been normalised such that the area under each curve is 1, regardless of the total number of stars at that time. Times are from the beginning of the simulation. Values are plotted in bins of 0.025.

$v_{\mathrm{t}} < 100$ km s^{-1} and 89.7% have $v_{\mathrm{t}} < 200$ km s^{-1}. In the absence of both the satellite particles and external potential particle (model NoSatE), 97.5% have $v_{\mathrm{t}} < 100$ km s^{-1}. Thus, the satellite particles are primarily responsible for the circularisation of the stellar orbits.

Observationally, the intensity profile of spiral bulges and elliptical galaxies can be fit with a Sérsic profile (Sérsic 1963; Sérsic 1968),

$$I(R) = I_{\mathrm{e}} \exp\left\{ -b_n \left[\left(\frac{R}{R_{\mathrm{e}}} \right)^{1/n} - 1 \right] \right\}, \qquad (4.18)$$

where R_{e} is the half-light radius, I_{e} is the intensity at R_{e}, and b_n describes the shape of the profile. Following this motivation, we numerically fit our stellar distribution with a Sérsic profile to determine its evolution over time. The numerical Sérsic profile is calculated from the age-dependent bolometric luminosity of each star particle, which is obtained from a lookup table generated by PEGASE2 (Fioc & Rocca-Volmerange 1997). We then fit the curve using a least-squares fitting routine. The evolution of the numerical Sérsic profile, along with its best fit curve, is plotted in Fig. 4.18, and the parameters of the best fit are given in Table 4.2. The galaxy gets dimmer

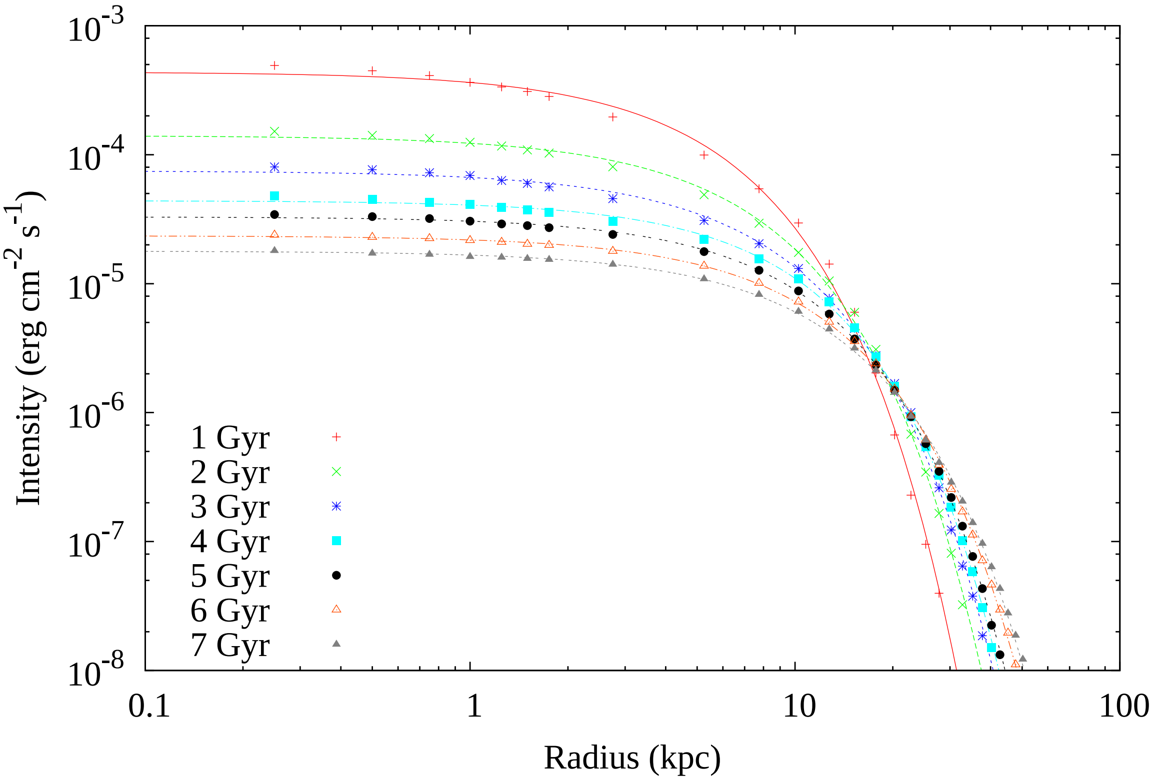

Figure 4.18: Sérsic profile evolving over time. The dots represent the numerical intensity, and the line of the same colour represents the best fit from a least-squares fitting routine. Only every tenth point was plotted after 2 kpc for easier viewing.

over time (i.e. I_e is constantly decreasing), as expected, since the bulk of the star formation occurred within the first 200 Myr. Also, the effective radius increases with time, indicating an increase in the galactic radius and an increase in the stellar mass in the outer regions; this agrees with observations that galaxies today have larger radii and more stellar mass in the outer regions compared to galaxies at $z \sim 2$, as discussed in IF12 and Ishibashi et al. (2013).

4.4.5 Tidal stripping from external potential

The external potential particle is initialised at $x = z = 0$, $y = -150$ kpc (i.e. the yellow square in the first column of Fig. 4.1, relative to the frame at 0 Myr).

Time (Gyr)	I_{e} (10^{-5} erg cm^{-2} s^{-1})	R_{e} (kpc)	n
1	10.1	5.48	0.853
2	3.54	7.19	0.854
3	1.88	8.29	0.854
4	1.23	9.37	0.803
5	0.896	10.0	0.815
6	0.617	11.1	0.833
7	0.461	12.1	0.842

Table 4.2: The best-fit parameters for the Sérsic profiles, from a least-squares fitting routine.

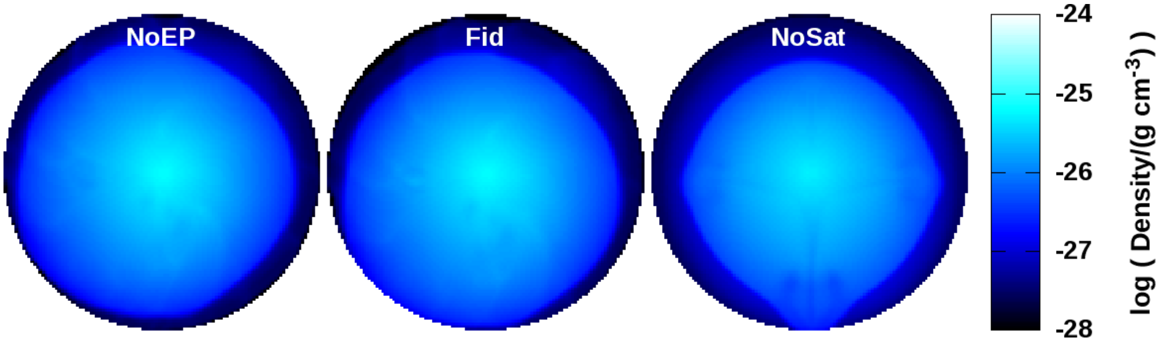

Figure 4.19: Gas density at 160 Myr for NoEP (left), Fid (centre) and NoSat (right). Each frame is a slice at $z = 0$, with $x = y = 0$ in the centre of the frame; each frame measures 60 kpc per side.

The external potential produces asymmetries in the gas, but the effects are minimal compared to the effects caused by the satellite particles. In the absence of satellite particles (model NoSat), the gas is slightly deformed, with a bulge in the direction of the external potential. With the satellites present, the gas distribution is similar for both NoEP and Fid, with the entire distribution slightly offset in Fid. See Fig. 4.19, where we plot the gas density at 160 Myr for Fid, NoEP and NoSat.

The evolution of the radially averaged stellar density profiles (e.g. Fig. 4.15 for Fid) for Fid and NoEP are similar for all time, while there is negligible evolution for NoSat. The actual stellar distributions are not symmetric, as can been seen in Fig. 4.20, where we plot the stellar column density for five different times for models Fid, NoSat and NoEP. As the stars oscillate about the core, there is an apparent

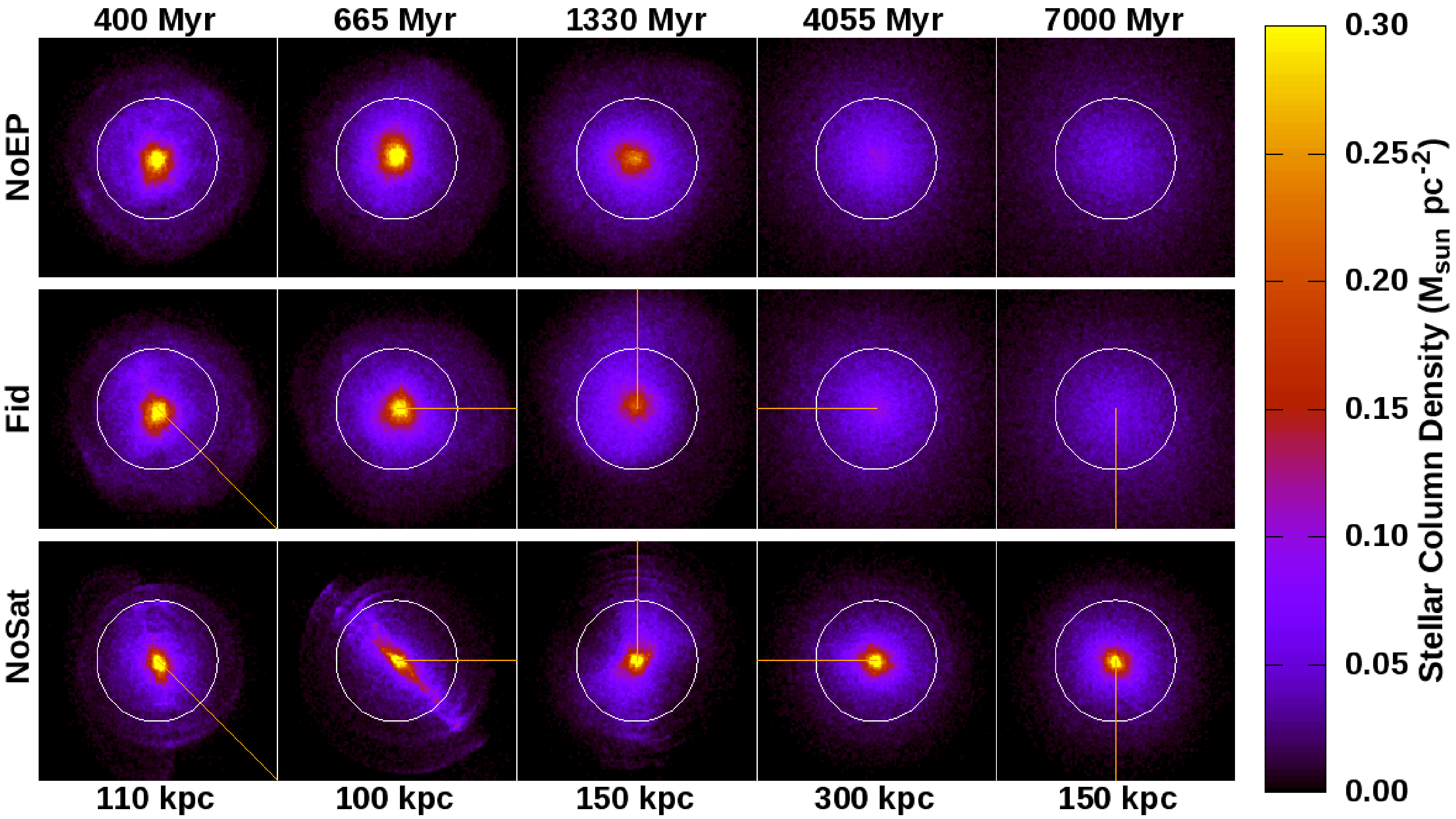

Figure 4.20: Stellar column density for five times for NoEP (top row), Fid (middle row) and NoSat (bottom row). The time since the beginning of the simulation is listed above each column, and the distance to the external potential particle (for Fid and NoSat) is listed below each column; the orange line is in the direction of the external potential particle. Each frame measures 40 kpc with a resolution of 250 pc pixel^{-1}. The white reference circle has a radius of 10 kpc.

net pulsation. With each ‘pulsation’, the stars closer to the satellite particles are accelerated by them. At 400 Myr, there are more satellites on the lower right than elsewhere in the domain, hence the surplus of stars in that region. In Fid, the lower right is also the direction of the external potential, so the additional gravitation force slightly increases the number of stars in that region. At this time, the stars are still young, thus are more strongly affected by the short-range forces (i.e. of the satellites) rather than the long-range forces (i.e. of the external potential).

The pulsating continues, and the stellar system begins to undergo a net rotation. This rotation is caused by the satellites dragging the stars, and the asymmetry of the satellite system causes the rotation axis of the stellar system to become offset from the centre of the dark matter halo. In Fid, the external potential exerts its gravitational influence on the precession of the stellar distribution such that there is a stellar bulge in the direction of the external potential at 1330 Myr. As the system ages, the rotation axis aligns with the centre of the dark matter halo, and the stellar distribution becomes spherical. By 4055 Myr, when the external potential has reached apoapsis, there is negligible difference in the stellar distributions of Fid and NoEP. We should note that the radial orbit instability (ROI) may contribute to the rotation and distortion of the stellar system. The ROI can cause a spherical, N-body system of particles, whose orbits are predominantly radial, to become prolate or triaxial over time (Barnes et al. 2009); however, the system can become spherical again on timescales of the relaxation time (Theis & Spurzem 1999).

In the absence of the satellite particles, the external potential’s influence on the stellar system is more apparent. The stellar system becomes elliptical by 400 Myr, with the major axis of the ellipse lagging behind the vector pointing towards the external potential. The ellipse persists and precesses, as can be seen at 665 Myr and 1330 Myr, with the major axis continuing to lag behind the direction to the external potential. As in Fid, as the external potential approaches apoapsis, the stellar distributions become spherical. The high core density remains throughout the simulation since there are no satellites to disrupt it.

In all simulations with the external potential, the external potential captures many stars and seven satellite particles to create its own system. While some of the stars are artificially slingshot away from the system, all the captured satellites remain bound to the external potential, often on highly elliptical orbits. The simulations end prior to the host reclaiming any of its satellites.

4.4.6 Resolution study

There are two important resolution-dependent quantities in this simulation: the grid resolution and the star formation threshold. Each of these quantities will briefly be discussed below.

4.4.6.1 Increasing the star formation threshold

In Fid400, we increased the threshold at which star particles can be spawned to 400 $M_\odot$; thus, each star particle represents 400 $M_\odot$ of stellar mass rather than 200 $M_\odot$. After 7 Gyr, Fid400 produced 3.2 times fewer stars than Fid; this corresponds to 1.6 times less stellar mass represented by particles.

For all time, the continuous SFR is the same for both models since the star particles have no impact on the gas dynamics that determine the continuous SFR. The discrete SFR is typically lower in model Fid400, especially at early times, since it takes longer for a cell to acquire the critical amount of stellar mass to spawn a star particle; see Fig. 4.21 where we plot the SFR for Fid and Fid400. The most noticeable difference is the quiescent period between 15 and 45 Myr. In Fid400, no stars are formed, but the lower threshold in Fid allows stars to be spawned, albeit at a greatly reduced rate.

With more stellar mass represented by stars in Fid, the stellar density is higher for Fid at all radii; the qualitative profiles, however, are similar. See Fig. 4.22, where we plot the stellar density for both models at 3 and 7 Gyr. Both distributions are qualitatively similar, thus we can be confident in the general trends. However, the total stellar mass represented by particles at 1 Gyr is ~2.1 times lower than predicted

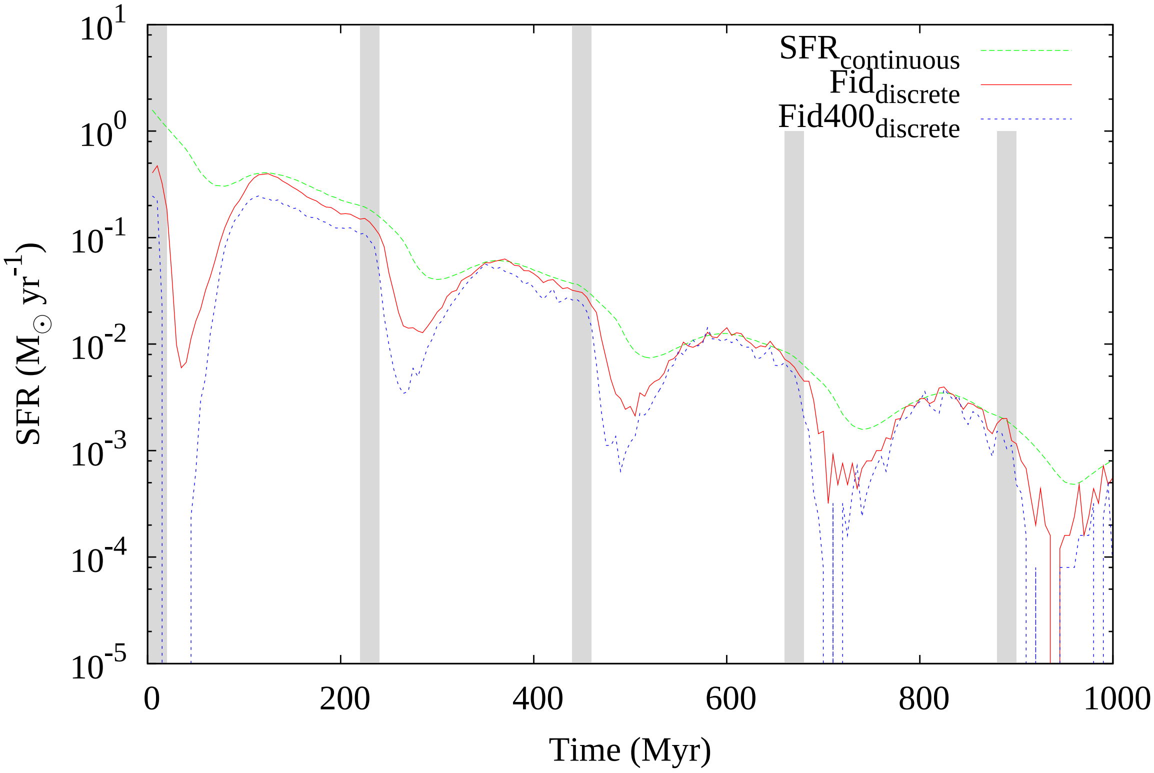

Figure 4.21: Star formation rate for models Fid and Fid400 for the first Gyr of the simulation. The continuous SFR is the same for both models. The gray stripes indicate when the luminous source is on.

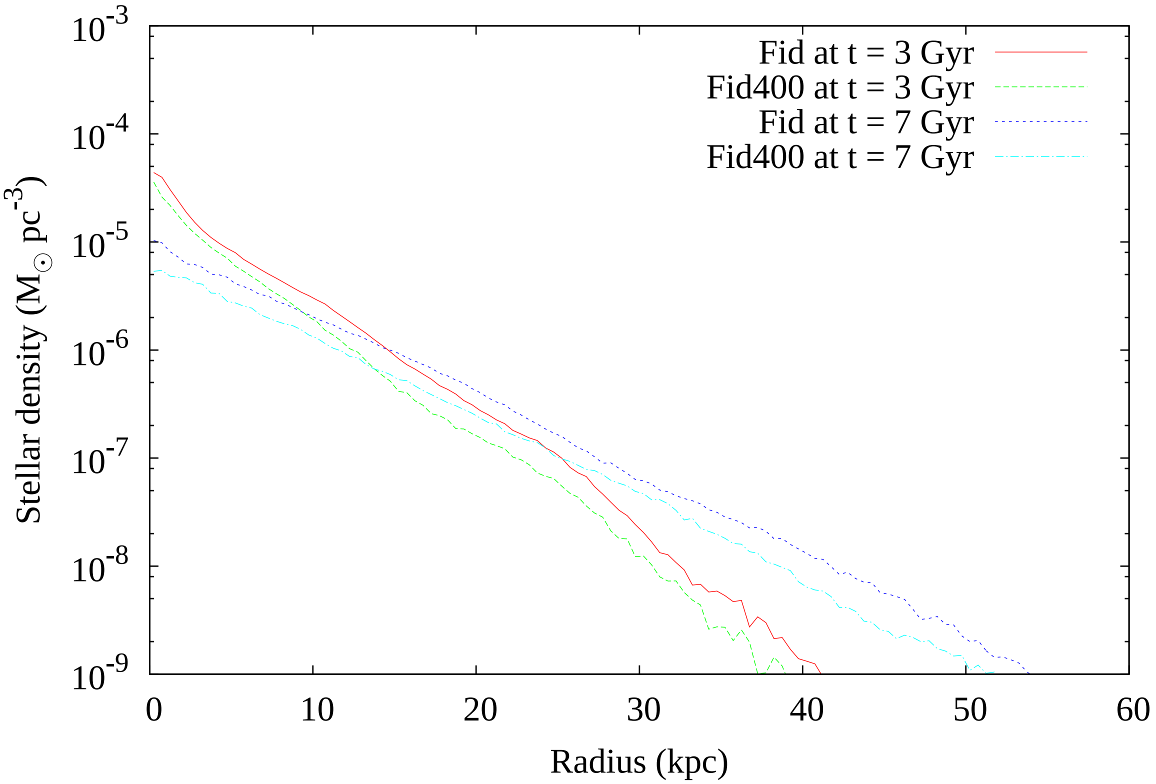

Figure 4.22: Stellar density profiles at 3 and 7 Gyr for Fid and Fid400, where times are from the beginning of the simulation.

by the Schmidt Law for Fid, and ∼3.3 times lower for Fid400. Thus, an even lower star formation threshold should be tested to verify that these trends hold in a simulation where the mass represented by particles is within a few percent of the mass represented by the Schmidt Law.

4.4.6.2 Increasing the grid resolution

To test the grid resolution, we ran our model at 256^3 (model HiRes). In Fig. 4.23, we plot four frames of the gas evolution during the first cycle for both Fid and HiRes. The gas features are slightly more pronounced in HiRes, but Fid captures these features very well.

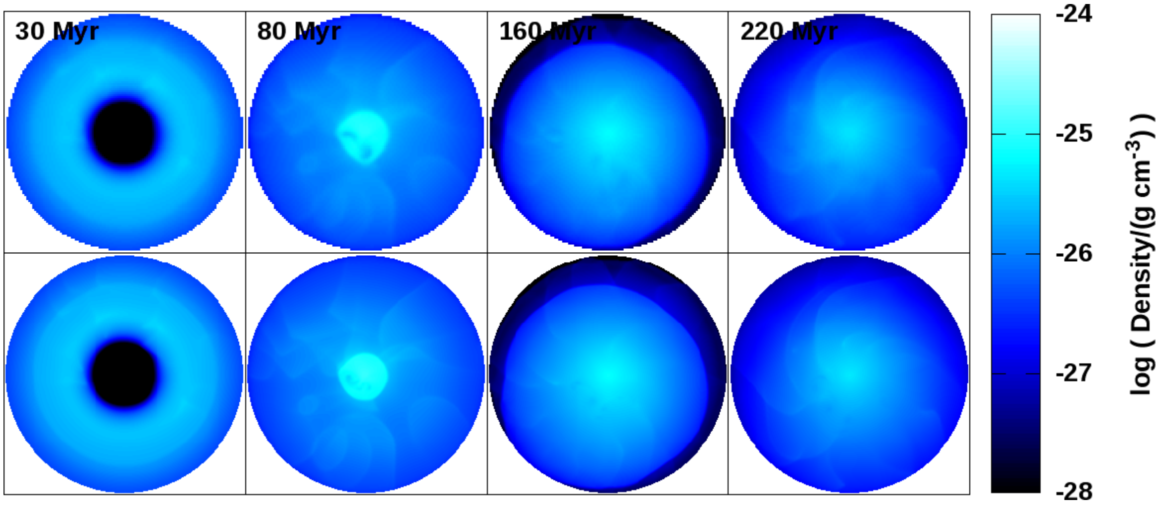

Figure 4.23: Gas density at four times for models Fid and HiRes during the first cycle. Times from the onset of the simulation are listed in each frame. Each frame is a slice at $z = 0$, with $x = y = 0$ in the centre of the frame; each frame measures 60 kpc per side. *Top Row*: Model Fid. *Bottom Row*: Model HiRes.

To compare stellar distributions, it is better to compare HiRes to Fid400 since both grid cell volume and the stellar mass represented by a particle are 8 times lower in HiRes than Fid400. By 1 Gyr, there are 7.22 times as many stars in HiRes than Fid400, so total stellar mass represented by particles is similar in both models. In Figs. 4.24 and 4.25, we compare the SFR and the stellar density distribution at 1 Gyr, respectively. Again, there is very good agreement at both resolutions, with features at lower resolutions clearly visible at the resolution.

4.5 Conclusions

This chapter details a study of AGN triggered star formation and the resulting stellar distributions. Using Zeus-3D augmented with a particle solver, we created a gas sphere embedded in a Milky Way-sized dark matter halo. Analogous to the Milky Way, we added 40 dwarf satellites and an external potential (an M31-analogue). The AGN, represented as a luminous point source, was turned on for 20 Myr every 200 Myr. Our principle conclusions are as follows.

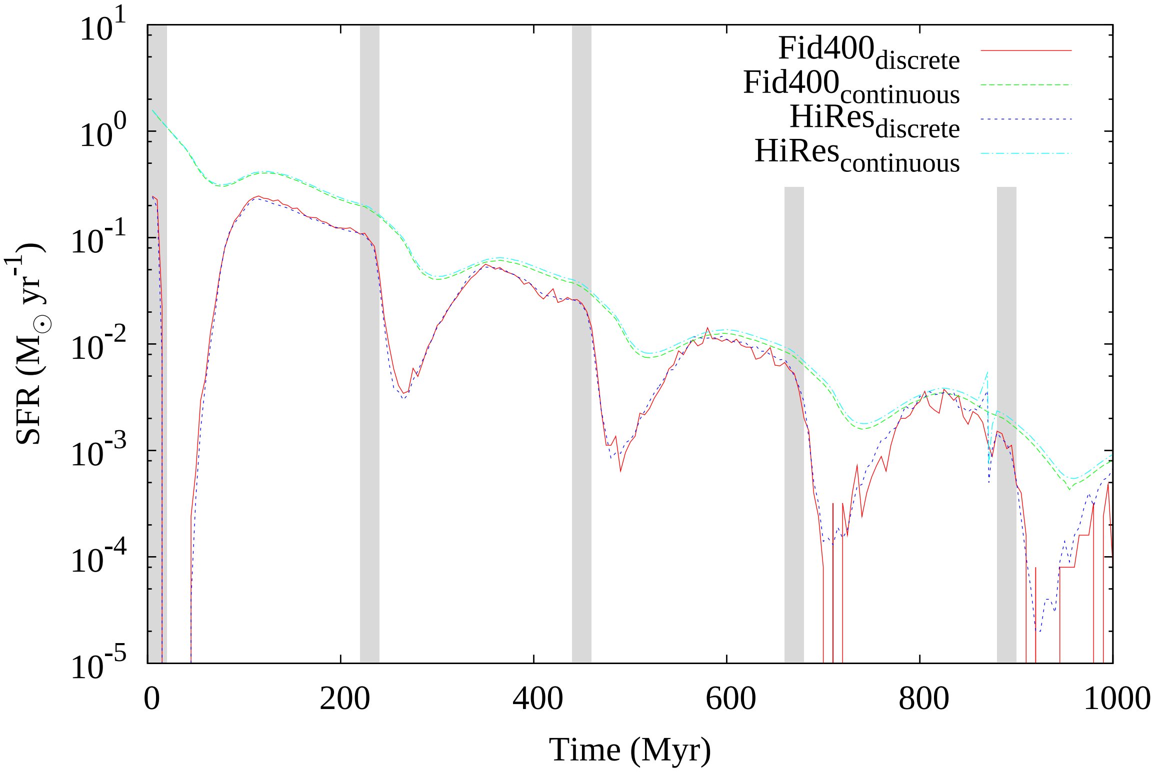

Figure 4.24: Star formation rate for models Fid400 and HiRes for the first Gyr of the simulation. The gray stripes indicate when the luminous source is on.

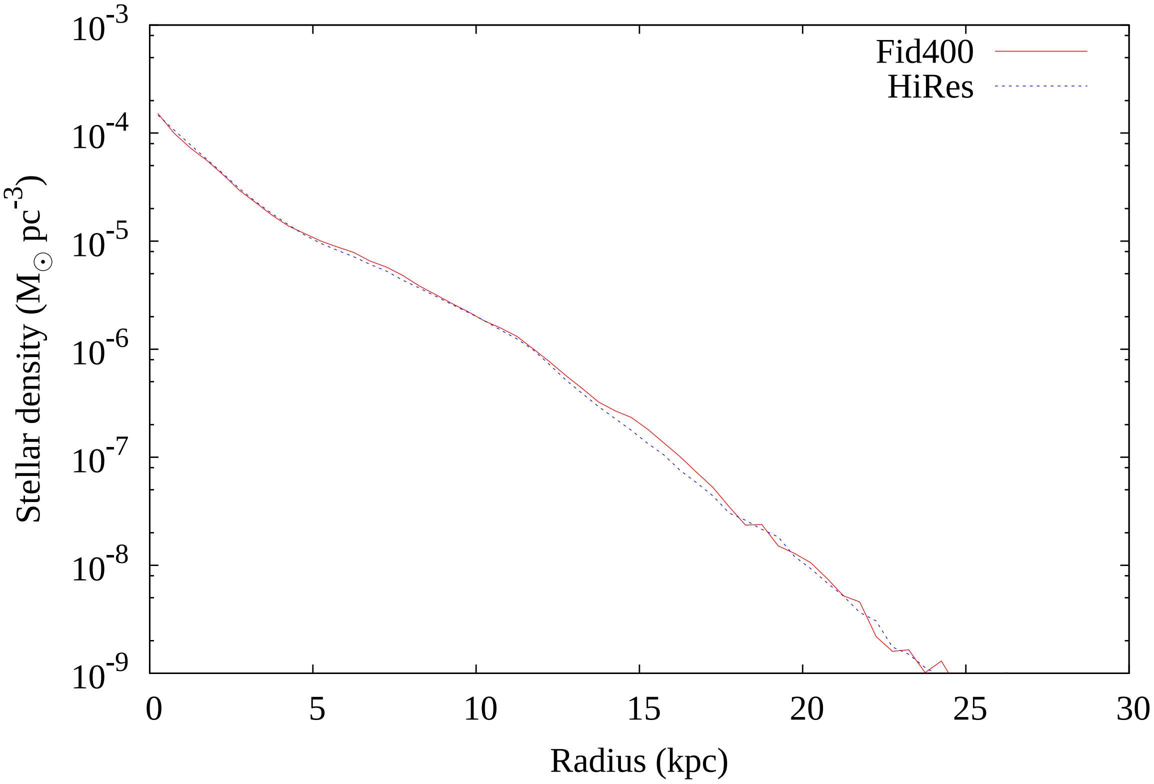

Figure 4.25: Stellar density profiles at 1 Gyr for Fid400 and HiRes, where times are from the beginning of the simulation.

1. During the first 660 Myr, 98% of all the stars in our simulation are born. By 7 Gyr, there are $\sim 3 \times 10^5$ star particles representing 5.9×10^7 $M_\odot$ of stellar mass. The stellar distributions of the first generation stars are similar to the distributions of the total stellar population after a few 100 Myr; by 1 Gyr, the first generation stars comprise 11.6% of the total population.

2. At all times, the stellar system can be represented with a Sérsic profile. The profile evolves with time, decreasing in surface brightness and increasing in effective radius. There is no coherent evolution in the overall shape of the profile. This expansion in effective radius is confirmed in the stellar density profile, where the slope gets shallower with time.

3. The stars spawned in shocks are born with a large radial velocity component, but most are perturbed on to an elliptical orbit during their first approach to apoapsis. The stars born in the nuclear region are born with all values of $v_{\rm t}^2/v^2$, but most have $v_{\rm t}^2/v^2 < 0.2$. After 3 Gyr, the slow expansion of the stellar system yields a slow increase in the tangential velocity component of the stars.

4. The dwarf satellite system causes the stellar system to undergo a net rotation, and the external potential causes the rotation to precess, with a bulge in the direction of the external potential. In the absence of a dwarf satellite system, the stellar system undergoes a slow orbital rotation; the stellar system is elliptical with the major axis lagging behind the direction of the external potential. The individual stellar orbits are perturbed into precessing elliptical orbits. In the absence of both the dwarf satellite system and the external potential, the particles oscillate radially through the core. In the latter two cases, the amplitude of the oscillation is constant for the duration of the simulation.

5. The AGN provides both negative and positive feedback. Positive feedback triggers star formation in shells, with the most prominent shell occurring during the first AGN episode. The peak SFR expands outwards from $\sim$3 kpc to $\sim$12 kpc over the first 20 Myr, with the peak value decreasing with radius. Over

this range, the star formation in Fid starts prior to the star formation in model NoAGN, indicating that this star formation has been triggered by the AGN. The second AGN episode arrests the declining SFR and weakly triggers star formation in the expanding shells. The negative feedback quenches star formation in inner regions during each AGN episode. Moreover, the repeated AGN episodes expel 97% of the gas from the system by 660 Myr, highly quenching the global star formation rate after this point, leaving the system 'red and dead.'

6. Increasing the resolution of the gas grid allows for the gas features to be better resolved, but has a negligible influence on the dynamics of the stellar system. Decreasing the threshold at which a star particle is spawned creates more star particles, thus more stellar mass is represented in the particles. The quantitative values (e.g. stellar density) necessarily change with the number of particles, but the qualitatively results remain unchanged.

In agreement with observations, our simulation of AGN triggered star formation suggests that galaxies get larger over time, with the stellar mass in the outer regions increasing; recall that the simplifications used our model prevent strong quantitative statements, hence we can only qualitatively relate our results to observations. However, contrary to suggestions (Bezanson et al. 2009; van Dokkum et al. 2010; Patel et al. 2013), our long-term radial growth is from a slow relaxation of the stellar system rather than continual star formation in the outer regions. This results in a dimmer core and elliptical stellar orbits, which is contrary to the observations, hence gives credence to the previous suggestions. Although the end result of a more extended galaxy is the same, the process through which this is achieved is different.

At early times (i.e. within the first Gyr), our results better match observations, with only a minimal dimming of the core, and 77% of all the stars having a strong radial component ($v_\mathrm{t}^2/v^2 < 0.8$). However, even by 3 Gyr, the core has become dimmer and the number of stars with a strong radial component has decreased to 59%.

The simulated galaxy has expelled most of its gas within the first 660 Myr (i.e. pushed it out of a 30 kpc radius). Thus, there is simply not enough gas at later epochs to create new stars, either in the nuclear region or in expanding shells. If the galaxy were to replenish its gas supply, from either adding more gas into the simulation or modelling a larger sphere thus allowing gas to return from the larger radii, then the star formation would continue. As with the first 660 Myr, this would likely occur both in shocks (leading to new stars being born in the expanding shocks and travelling to the outer regions of the galaxy) and in the nuclear region when the luminous source is off (maintaining the central luminosity and stellar densities). Thus, our simulation may be more consistent with the observations if our gas supply were not so quickly expelled or if it were replenished.

Acknowledgments

Use of Zeus-3D, developed by D.A. Clarke at the Institute for Computational Astrophysics (www.ica.smu.ca) with financial support from the Natural Sciences and Engineering Research Council of Canada (NSERC), is hereby acknowledged.

Chapter 5

Conclusions and Future Work

In Chapter 2, we presented a comparative study of five AGN feedback algorithms using the AP^{3}M SPH code HYDRA. In Chapter 3, we discussed a sixth AGN feedback model in our HYDRA simulations based upon the accretion disc particle (ADP) method of Power et al. (2011) and performed a parameter study on resolution and two free parameters. The ADP parameter study was treated as a separate chapter since the ADP method was published after the comparison of Chapter 2 was well in progress, and because we expected the free parameters to analytically play a much larger role in dictating the accretion rate than in the models in Chapter 2. In Chapter 4, we modelled star formation in shocks using an augmented version of the Eulerian code ZEUS-3D and analysed the resulting stellar distributions. Given the direct relation between the studies in Chapters 2 and 3, we summarise them together for completeness in §5.1, and discuss future work in §5.1.2. We summarise the star formation in expanding shells and discuss future extensions to this study in §5.2.

5.1 Major merger simulations

5.1.1 Summary

AGN feedback has been implemented in many numerical simulations throughout the literature (e.g. Kawata & Gibson 2005; Di Matteo et al. 2005; Springel et al. 2005b; Thacker et al. 2006; Sijacki et al. 2007; Okamoto et al. 2008; Kurosawa et al. 2009; Booth & Schaye 2009; Debuhr et al. 2011; Dubois et al. 2012) on both galactic and cosmological scales. However, these AGN feedback algorithms differed in the underlying physics and were implemented in different numerical codes. Thus, given the current literature, it was not possible to compare and contrast the effects of the various AGN feedback algorithms. Thus, in Chapter 2, we chose four AGN feedback algorithms from the literature and implemented them in a major merger simulation of two Milky Way-sized galaxies, which we ran using HYDRA. The algorithms were Model SDH (based upon Springel et al. 2005b), Model ONB (based upon Okamoto et al. 2008), Model BS (based upon Booth & Schaye 2009) and Model DQM (based upon Debuhr et al. 2011). We then created and tested a fifth model, Model WT, that was designed specifically for this study for use in HYDRA. We also ran four additional simulations, each of which examined a variation of one of the primary algorithms in order to study a specific aspect of the physical model. By implementing each feedback algorithm in HYDRA, we were able to control the initial conditions of the simulation as well as all other algorithms (e.g. star formation) and underlying physics. Thus, any differences were a direct result of the AGN feedback algorithm. Our analysis focused on the five key components of AGN feedback algorithms:

1. The accretion rate on to the black hole,
2. The SPH particle accretion algorithm,
3. The energy feedback algorithm,
4. The black hole advection algorithm, and
5. The black hole merger algorithm.

As a separate study, we created an AGN feedback algorithm based upon the model in Power et al. (2011); Power et al. (2011) tested their model in a small-scale simulation that started from spherically symmetric initial conditions, so we were required to add a black hole advection and merger algorithm, as well as modify the feedback algorithm. This model, Model PNK, includes two primary free parameters, the accretion radius, $R_{\rm acc}$, and the viscous timescale, $t_{\rm visc}$, which directly affect the accretion rate of gas onto the black hole. We thus ran a parameter study consisting of five fiducial resolution simulations and twelve low resolution simulations varying $R_{\rm acc}$ and $t_{\rm visc}$. The primary purpose of this study was to determine the impact of these two free parameters, but we also briefly compared the results to Models SDH and DQM from Chapter 2.

Although we tried to isolate each component of the AGN feedback algorithm, we accept that they were all intimately intertwined, and that the effects could not necessarily be disentangled from one another. Based upon the large number of free parameters included in the simulations, and that we have not performed a thorough comparison to observational data, we have refrained from making strong statements about the 'accuracy' of given models.

For the major merger simulations, our principle conclusions were as follows:

1. The black hole advection algorithm played a key role since small displacements could cause great changes in the accretion rate. The three methods we tested were to couple the black hole to a nearby gas particle if the relative velocity was below $0.25c_\mathrm{s}$, displace the black hole based upon local mass distributions, and use a tracer mass. The coupling method allowed for oscillations or chaotic motion if a void formed around the black hole, or if the nearby gas did not meet the velocity criteria. In Model PNK, this method would artificially inflate the accretion rate since a gas particle would be arbitrarily placed within R_acc. The tracer mass method yielded a smooth trajectory of the black hole, but affected the evolution time of the merger and the disc morphology (i.e. the extra particle mass prevented a bar from forming in the galaxy at apoapsis). The algorithms that limited the distance a black hole could be displaced per iteration and where the direction was based upon the local stellar or total mass distribution appeared to be optimal since they did not overly impact the expected evolution of the disc or adversely affect the accretion rate.

2. We tested five different accretion rates: $\dot{M}_\mathrm{B}(\alpha = 100)$, $\dot{M}_\mathrm{B}(\alpha \equiv \alpha(n_\mathrm{H}))$, $\dot{M}_\mathrm{drag}$, $\dot{M}_\mathrm{visc}$ and $\dot{M}_\mathrm{ADP}$. The first four models (from Chapter 2) yielded continual accretion on to the black hole (even if the rate was small), whereas $\dot{M}_\mathrm{ADP}$ from Model PNK could decrease to a negligible rate if the accretion disc had

been depleted of gas, which occurred near the beginning of the simulation. Each model yielded a different accretion history, with substantially different evolutionary profiles. The final masses for the six models that fell within the one-sigma scatter of the $M_{\rm BH}$–σ relation (three continual accretion and three PNK models) had final black hole masses that differed by less than a factor of two. The final masses from the PNK models were consistently larger than the masses from the continual accretion rates, but they agreed with the $M_{\rm BH}$–σ to a high precision.

3. In our simulations, we tested thermal (Models SDH, BS, ONB and WT) and kinetic (Models DQM and PNK) feedback. In Model ONB, feedback was delivered to the halo gas, which lead to little modification of the core region and resulted in high core densities and nominal temperatures. Thermal feedback delivered to the core region could drive strong outflows. The kinetic feedback delivered to the core region in Model DQM quickly and efficiently created a void around the black hole, which resulted in a low gas temperature and density. This feedback was persistent and efficient, and kept the core properties nearly constant for all time. The kinetic feedback of Model PNK did not create the initial void around the black hole, thus the gas density around the black hole remained high throughout the simulation. The gas temperature near the black hole was comparable to the temperature of Model ONB, which received its heating from collisions and stellar feedback only. Thus, as expected, the form of feedback drastically modified the large- and small-scale systems.

4. We tested three categories of particle accretion algorithms: stochastic-unconditional, stochastic-conditional and continual-conditional. The continual-conditional cases gave the best agreement between the dynamical and internal

mass, since the discrepancy was never more than $2m_{\mathrm{g}}$. With the stochastic-unconditional algorithm, we obtained discrepancies up to $15m_{\mathrm{g}}$. Thus, for agreement between dynamical and internal masses, continual-conditional algorithms appeared optimal.

5. In most cases, the two black holes merged during or shortly after core merger, as one would reasonably expect. Moreover, all models that used the advection algorithm of Model WT (i.e. Models WT, WTh and PNK) had black holes that merged at 1.01–1.02 Gyr, which showed that this merger time was independent of the accretion and feedback algorithms. In Models BS and BS_{l}, the black holes never merged, and there was considerable chaotic movement of the black holes in the remnant core which prevented both merger criteria from simultaneously being met. The importance of a 'reasonable' merger time is motivated by the fact that the feedback energy available increases across the merger for Bondi accretion and decreases for drag, viscous, and ADP accretion.

The specific results that related to the parameter study of Model PNK were as follows:

1. If the accretion radii was too small (i.e. $R_{\mathrm{acc}} = 0.02h_{\mathrm{min}}$), then the final black hole mass was far smaller than predicted from the M_{BH}–σ relationship. If the accretion radii was too large (i.e. $R_{\mathrm{acc}} = 0.20h_{\mathrm{min}}$), then the accretion rate on to the accretion disc (hence on to the black hole) was unreasonably large; the resulting feedback was enough to catastrophically disrupt the system. Thus, for the accretion radii tested, we obtained physical results for only $R_{\mathrm{acc}} = 0.05$ and $0.10h_{\mathrm{min}}$.

2. If the viscous time-scale was too large (i.e. $t_{\mathrm{visc}} = 10$ Myr), then feedback from an accretion event persisted long enough to hinder secular accretion. Tidal forces from the interacting galaxies could overcome the low amount of feedback and funnel considerable amounts of gas on to the accretion disc. Depending

on resolution and accretion radius, this short accretion epoch could be large enough such that its resulting feedback energy could catastrophically disrupt the system. Thus, a few of our $t_{\rm visc} = 10$ Myr models were classified as unphysical. We encountered no scenarios where a short viscous time-scale contributed to a model being classified as unphysical.

3. Assuming that the free parameters $R_{\rm acc}$ and $t_{\rm visc}$ were in the allowed parameter space, the exact value had only a minimal effect on the results. When the accretion radius was doubled from $0.05h_{\rm min}$ to $0.10h_{\rm min}$, the final black hole mass increased by only a factor of 1.35 for our fiducial resolution simulations. When $t_{\rm visc}$ decreased, the final black hole mass increased, although, the final range of black hole masses spanned only a factor of 1.13 for our fiducial resolution models. The gas properties within $r_{\rm inf}$ of the black hole were essentially unaffected by the free parameters as expected, since $r_{\rm inf}$ had no explicit dependence on them.

4. When the mass and spatial resolution was decreased, the final black hole mass increased. This was generally true for the continual accretion algorithms presented in Chapter 2 as well. For any given fiducial–low resolution pair of PNK models, the final black hole mass differed by less than a factor of two. Given the parameters tested here, resolution had the largest impact on the outcome of the model.

5.1.2 Future work

There are many natural extensions to the major merger simulations, as are described below.

1. All of the models contained free parameters in the AGN feedback algorithms, thus a proper parameter study can be done to determine the impact these parameters have on the results. In Table 5.1, we list the free parameters associated with each model that would be ideal for a parameter study. We note that most of the free parameters suggested for the parameter study directly or

Model	Free Parameters
SDH	$\alpha,\ \epsilon_{\rm f}$
BS	$\beta,\ \epsilon_{\rm f},\ \Delta T$
ONB	$\epsilon_{\rm drag},\ M_{\rm c}$
DQM	$\delta,\ \tau$
WT	$\alpha,\ \epsilon_{\rm f}$
PNK	$R_{\rm acc},\ t_{\rm visc},\ \tau$

Table 5.1: Free parameters for the merger simulations ideal for a full parameter study. All variables are described in Chapters 2 and 3. Note that models may contain additional parameters that are not on the above list, but it would not be efficient to perform a parameter study with them.

indirectly impact the amount of energy being fed back in to the system. Thus, this study would be a test of self-regulation, and to determine physical limits on the amount of feedback energy a system can receive without being totally disrupted. The resulting analysis would be similar to the parameter study for Model PNK presented in Chapter 3.

2. An extension to the previous point is to vary the parameters of each model to determine if it is possible to obtain similar results at a given epoch (e.g. at apoapsis or the final remnant). If this is true, then this would indicate a numerical degeneracy and that the results can be independent of the exact AGN feedback algorithm (although this seems unlikely). If this is not possible, then comparing the numerical results to observational data (e.g. Wild et al. 2010 who studied the link between star formation and black hole growth; García-Burillo et al. 2005 and van der Laan et al. 2011 who studied the link between CO morphology and local AGN activity; and Chen et al. 2013 who compared star forming rates to black hole accretion rates) could provide hints as to the actual algorithms and the values of the free parameters.

3. As is standard in SPH for gas particles, our black holes have a time-dependent smoothing length, defined as $h_{\rm BH} = \max(h_{60}, h_{\rm min})$, where a sphere with radius

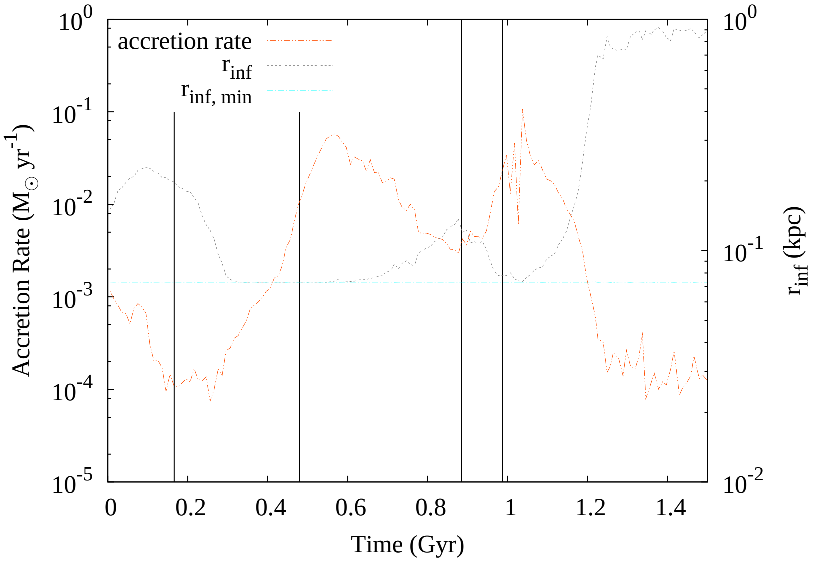

Figure 5.1: The accretion rate and radius of influence for Model WT, geometrically averaged over both black holes and plotted in bins of 10 Myr. The four black vertical lines indicate the time of first periapsis, apoapsis, second periapsis and core merger, as given in Table 2.4.

$2h_{60}$ around the black hole particle includes 60 gas particles, and $h_{\rm min}$ is the smallest resolved smoothing length in the SPH solver. The black hole's radius of influence is then defined as $r_{\rm inf} \equiv 2h_{\rm BH}$. Most of the time, the smoothing length is defined by h_{60}, but during apoapsis and core merger, it is typically defined by $h_{\rm min}$. As expected, it is during these two epochs that the black holes are accreting at a high rate; see Fig. 5.1 for the accretion rate and $r_{\rm inf}$ for Model WT.

Since the black hole's gravitational field is dependent on its mass and not the local gas density, it would be intriguing to run the simulation with a fixed $r_{\rm inf}$. Although this was done in Model DQMe, that model used an unrealistically large $r_{\rm inf}$. We would thus require a fixed radius that is more suited for our simulations in HYDRA. In determining the fixed $r_{\rm inf}$, we can drawn upon our results from the parameter study of $R_{\rm acc}$ for Model PNK.

4. The galaxy mergers presented in this thesis were confined to a plane. Although this matched the primary results presented in Springel et al. (2005b), it is highly unrealistic that this orientation would occur in reality. Thus, it would be ideal to test a variety of initial orientations and rotations (e.g. prograde–prograde, prograde–retrograde, retrograde–retrograde), which would provide data for realistic comparisons to observed mergers. From the orientation tests presented in (Springel et al. 2005b), we do not expect that orientation will have a large influence on the results presented here, although we would expected to obtain a more isotropic stellar distribution.

5. Given that AGN feedback plays a major role in galaxy formation, it would be useful to perform these studies in a cosmological simulation, or to consider a number of different merger scenarios to probe different mass haloes. This would provide a large scale picture as to how the various algorithms affect galaxy assembly and the evolution of entire clusters, and also provide direct comparison to observational ensemble statistics. The low resolution simulations presented in this thesis have resolution that would be comparable to a cosmological simulation, so we have proof-of-concept that a comparison would be possible.

   Models BS and ONB were designed for cosmological simulations, thus they would effortlessly be translated to the new scale. Models SDH, DQM and WT would likewise easily be modified for the cosmological scale, provided resolution criteria are met. Model PNK, however, would not be as simple to translate to a cosmological simulation. First, the seed black hole will likely be orders of magnitude smaller than the mass of a gas particle. Thus, the first accretion event would be unrealistic, yielding an accretion disc mass, M_{disc}, that is greater than the black hole mass, M_{BH}. The massive gas particles would likely yield $M_{\text{disc}} > M_{\text{BH}}$, for all time (Muldrew et al. 2013). Second, it would be a challenge to choose an appropriate accretion radius, R_{acc}. As discussed in Chapter 3, if R_{acc} is too small compared to the minimum smoothing length, then the results are unrealistic and fraught with numerical instabilities, while if it is too large, then the accretion rate is unrealistically high and feedback can disrupt the entire system. In a cosmological simulation where (e.g.) a galaxy consists of ∼100 SPH particles, it is possible that both critical issues can be met simultaneously. Thus, additional research would be required to determine if it is possible to implement Model PNK in a cosmological simulation. One possible option could be to use a larger (thus numerically stable) accretion radius and then add a probability or velocity condition on whether or not the SPH particle will be accreted. Although the parameters here could be modified to yield stable and realistic results, it is in contradiction of the spirit of the algorithm presented by Power et al. (2011).

Model WT has already been expanded to track $n > 2$ black holes, thus it is ready for implementation in a cosmological simulations.

6. In all our simulations, we initialised the black holes with seed masses of $M_{\rm BH} = 10^5$ M$_\odot$. Our justification was that this seed mass is standard throughout the literature (e.g. Springel et al. 2005b; Debuhr et al. 2011) and that it gave the black holes ample room to grow. Our simulations yielded final black hole masses on order of 10^7 M$_\odot$, thus we were able to analyse the black hole growth — and corresponding feedback — over two orders of magnitude. A useful study would be to run simulations with initial black hole masses of 10^6 and 10^7 M$_\odot$ to track their growth throughout the merger. A key point of interest would be to compare the final black hole masses to determine if all simulations yield similar final black hole masses on order of 10^7 M$_\odot$ or similar black holes growths of $\Delta M_{\rm BH} \sim 2$ dex.

   As briefly discussed at the end of §2.3, the mass of the tracer mass has a direct impact on the morphology of the galaxy. Specifically, our tracer mass of $m_{\rm BH} = 10^9$ M$_\odot$ was able to prevent a bar from forming at apoapsis, which was a result of the higher peak velocity of the galactic rotation curve just after first periapsis. Given the morphological differences caused by the large tracer mass, it would be prudent to run a suite of models varying the tracer mass in the range $m_{\rm BH} \in \{10^7~{\rm M}_\odot, 10^9~{\rm M}_\odot\}$, where $10^7~{\rm M}_\odot$ is approximately the final black hole mass and $10^9~{\rm M}_\odot$ is the tracer mass used in this thesis. Key points of interest would be the final black hole (internal) mass and the impact on the gas properties and star formation rate throughout the evolution of the simulation.

In all our simulations and suggested extensions, we did not make the distinction between the quasar and radio modes of AGN. Except for Okamoto et al. (2008), the literature sources for our algorithms also did not make this distinction. We also do not effectively represent radiative transfer, which is a challenge both theoretically and numerically. However, improvements are continually being made to codes and more realistic simulations are under development. For example, Vogelsberger et al. (2013) uses AREPO to study galaxy formation in a cosmological simulation using both radio and quasar modes, plus a simple model of the impact of the photoionization field. Thus, with the next generation of codes, and comparisons similar to the one presented here, we will obtain a better understanding of the evolution of AGN feedback and its impact on the environment.

5.2 AGN Triggered Star Formation

5.2.1 Summary

Motivated by recent analytical (e.g. Silk & Norman 2009; Ishibashi & Fabian 2012; Silk 2013) and numerical (e.g. Liu et al. 2013; Zubovas et al. 2013) work on triggered star formation, Chapter 4 presented our study of AGN triggered star formation. We used the Eulerian grid code ZEUS-3D, which we augmented with a particle solver. The grid code was optimal for resolving shocks, and the particle solver was required to track stellar distributions and add local and global gravitational sources.

The system we studied consists of a gas sphere embedded in a Milky Way-sized dark matter halo, 40 dwarf satellite particles, and an external potential (an

M31-analogue). The AGN, represented as a luminous point source, is turned on for 20 Myr every 200 Myr. Star formation is allowed to proceed in all cells following the Schmidt Law, and a star particle is spawned when a critical mass of gas has been converted in to stars in any given cell. Our simulations do not include any conditions on the star formation requirements (i.e. density floor, temperature ceiling, flow convergence) or any stellar feedback, thus we likely over-produced the number of stars. However, we also do not resolve the true density of the shell, thus we likely under-produced the number of stars born in the shells. Given that our purpose was to study the stellar distributions, these issues did not affect our goal of tracking stellar trajectories or distributions.

During the first 660 Myr, 98% of all the stars in our simulation were born, and 97% of the total gas mass had been expelled from the system as the system relaxes. By 2 Gyr, the gas system had reached an equilibrium with ~0.2% of the initial gas mass. By 7 Gyr, there were $\sim 3 \times 10^5$ star particles representing 5.9×10^7 $M_\odot$ of stellar mass. The stellar distributions of the first generation stars (those stars born within the first 35 Myr with $v_t^2/v^2 \leq 0.005$, where v_t is the tangential velocity and v is the total velocity), was similar to the distributions of the total stellar population after a few 100 Myr. By 1 Gyr, the first generation stars comprised 11.6% of the total stellar population.

The principle conclusions of this study were as follows.

1. The stellar system could be represented with a Sérsic profile, which evolved with time. As the system aged, the surface brightness decreased and the effective radius increased. There was no coherent evolution in the overall shape of the profile. The increase in effective radius was consistent with observations, but the decrease in central surface brightness was not.

2. The stars spawned in shocks were born with a large radial velocity component, $v_t^2/v^2 \leq 0.005$, but most were perturbed on to an elliptical orbit during their first approach to apoapsis. The stars born in the nuclear region were born with

all values of v_t^2/v^2, but most had $v_t^2/v^2 < 0.2$. After 3 Gyr, the slow expansion of the stellar system yielded a slow increase in the tangential velocity component of the stars.

3. The dwarf satellite system and the external potential caused the stellar system to undergo a net rotation with the entire system precessing about the centre of the dark matter halo. In the absence of a dwarf satellite system, the stellar system underwent a slow orbital rotation, but was elliptical in distribution with the major axis lagging behind the direction of the external potential. The individual stellar orbits were perturbed into precessing elliptical orbits, while in the absence of both the dwarf satellite system and the external potential, the particles oscillated radially through the core.

4. The AGN provided both negative and positive feedback. Positive feedback triggered star formation in expanding shells, and the most prominent shell occurred during the first AGN episode. The peak SFR expanded outwards from ∼3 kpc to ∼12 kpc over the first 20 Myr. Over this range, the star formation in Fid started prior to the star formation in model NoAGN, which indicated that this star formation had been triggered by the AGN. The second AGN episode arrested the declining SFR and triggered star formation in the expanding shell. The negative feedback quenched star formation in inner regions during each AGN episode. The repeated AGN episodes expelled 97% of the gas from the system by 660 Myr, which highly quenched the global star formation rate, leaving the system 'red and dead.'

   The AGN provided both negative and positive feedback. As predicted, star formation was triggered in expanding shells ('positive feedback') and nuclear star formation was quenched when the luminous source was on ('negative feedback'). The AGN feedback globally quenched star formation ('negative feedback') since it expelled most of the gas from the system within the first Gyr.

5.2.2 Future work

There are many natural extensions to our model of AGN triggered star formation, as will be described below.

1. Our primary simulation was run on a grid of 128^3 with linear spacing. Given the nature of this project, migrating it to an adaptive mesh code (AMR), such as AZEuS (Ramsey et al. 2012), would allow for better resolution of the gas shocks and local over-densities caused by the satellite and external potential particles. From our analysis of model HiRes, however, we do not expect the results obtained with this modification to alter our primary conclusions.

2. Our current star formation algorithm is based upon the Schmidt Law and has no conditions on the gas. In most numerical star formation algorithms, star formation only proceeds in regions where given criteria are met. The most common condition is a density floor, which we briefly discussed in §4.4.2; this is the only condition used by Dubois et al. (2012), who run a cosmological simulation using the AMR code Ramses (Teyssier 2002). In the SPH code Hydra, there are density, temperature and velocity conditions, as discussed in §2.2.3. By constraining the star formation algorithm, we would be able to make estimates on stellar masses in addition to the estimates of stellar distributions presented here.

   A necessary counterpart to the star formation algorithm is the stellar feedback algorithm. Returning (kinetic or thermal) energy whenever a star is formed will modify the star's environment and future history. This stellar feedback may trigger star formation by creating small shocks, or it may quench local star formation by modifying the region such that the criteria for forming stars are no longer met.

3. Our external potential particle reaches periapsis at 665 Myr. This was chosen in order for the external potential to have a maximal affect on the newly formed

stars, as well as influence the distribution of the gas before the majority of it was expelled from the system. It would thus be intriguing to perform a parameter study where the external potential was initialised at various points along its orbit. This would allow us, for example, to determine the effect that the external potential has on an evolved stellar system. The orbit could also be modified to a smaller periapsis distance in order to study stronger tidal interactions.

4. Our current system, while loosely based upon the Local Group, is still an idealised system (i.e. there is a non-rotating, spherically symmetric gas cloud embedded in the dark matter halo). To better mimic the Local Group, the gas cloud should be given an initial angular momentum, and a rotationally supported gas disc should be placed at the centre of the sphere. The gas disc would be given temperatures that better represent a gas disc than a hot gas halo. Then, if the improved star formation algorithm is implemented as described above, we would obtain a more realistic picture of how triggered star formation occurs in a disc, and whether or not these stars get ejected in to the halo.

5. The amount of AGN activity is pre-set with 20 Myr on and 200 Myr off. Although the values are justified by observational and analytical arguments (e.g. Martini & Weinberg 2001 and references therein), they are independent of the physics occurring in the simulation. Thus, more realistic results would be obtained by implementing a self-consistent method of controlling the AGN activity. This could be done by treating the central cell(s) as a proxy for the black hole and tracking the net increase of mass in the cell(s). A portion of this accreted mass could then be converted in to energy and returned as the luminous source. This method would likely yield a continuous, low-level luminosity that would not create strong shocks.

In order to obtain strong shocks, a second method is to track the net increase of mass in the central cell(s), and when a given threshold is met, convert the mass to energy and return a portion of it at a pre-set rate over a pre-set time. Although this is conceptually the same as our simulation, the period between AGN episodes would be dependent on the system, and the black hole would have acquired enough mass during the quiescent period to physically account for its luminosity.

6. The gas is quickly depleted from our system, thus we are only able to trigger star formation during the first few AGN episodes. In order for star formation to occur throughout the duration of the simulation, we need to prevent the near total loss of gas from the numerical domain or replenish the system's reservoir.

   The former is a numerical challenge which could be addressed in several methods. First, the computational domain could be increased such that the gas is expelled from the central regions of the host but not the computational domain. Although plausible, this method is computationally expensive with little return. A second option would be to modify the boundary conditions such that they are outflow when the AGN is active and expelling gas from the system, and inflow when the AGN is in a quiescent phase and gas is relaxing back on to the system.

   The first method to physically replenishing the gas reservoir is to allow accretion of gas from the intergalactic medium, but this essentially results in a modification of the boundary conditions described above. The second method is to simulate minor mergers. Periodically, a satellite galaxy could 'merge' with the host and deposit its gas in the computational domain. This would be a small amount of gas, thus many mergers would be required to fully replenish the reservoir. The third option is to simulate a major merger, where a host's worth of gas is deposited in to the computational domain. However, without modifying the boundary conditions, the majority of this gas would also likely be evacuated within a Gyr.

If the gas reservoir were to be replenished using one of the above methods, then star formation would likely occur throughout the entire simulation, possibly leading to different results than presented here.

Simulating the improved model described above with an AMR code and a full accretion history is likely something that can be accomplished in the near future. Furthermore, the particle algorithm could be adapted to account for particle mergers, tidal stripping of the satellites (where the particle scale length increases and mass decreases), and possible minor mergers with the host galaxy. With the added fidelity, however, comes the difficulty of disentangling the triggered star formation from the effects of minor mergers depositing outerlying stellar features, including shells. Disentangling the two mechanisms may prove to be quite challenging.

Bibliography

Agertz O. et al., 2007, MNRAS, 380, 963

Aird J. et al., 2010, MNRAS, 401, 2531

Alexander D. M. et al., 2011, ApJ, 738, 44

Alexander D. M. et al., 2008, ApJ, 687, 835

Alexander D. M., Hickox R. C., 2012, New A Rev., 56, 93

Bajtlik S., Duncan R. C., Ostriker J. P., 1988, ApJ, 327, 570

Balsara D. S., 1995, Journal of Computational Physics, 121, 357

Barai P., Proga D., Nagamine K., 2012, MNRAS, 424, 728

Barnes E. I., Lanzel P. A., Williams L. L. R., 2009, ApJ, 704, 372

Barnes J., Hut P., 1986, Nature, 324, 446

Barnes J. E., Hernquist L., 1996, ApJ, 471, 115

Barnes J. E., Hernquist L. E., 1991, ApJ, 370, L65

Barrow J. D., Saich P., 1993, MNRAS, 262, 717

Bauer F. E., Alexander D. M., Brandt W. N., Schneider D. P., Treister E., Hornschemeier A. E., Garmire G. P., 2004, AJ, 128, 2048

Bechtold J., 1994, ApJS, 91, 1

Begelman M. C., Volonteri M., Rees M. J., 2006, MNRAS, 370, 289

Behroozi P. S., Wechsler R. H., Conroy C., 2013, ApJ, 770, 57

Bekki K., Couch W. J., 2011, MNRAS, 415, 1783

Belokurov V. et al., 2006, ApJ, 642, L137

Benson A. J., Bower R. G., Frenk C. S., Lacey C. G., Baugh C. M., Cole S., 2003, ApJ, 599, 38

Berentzen I., Preto M., Berczik P., Merritt D., Spurzem R., 2009, ApJ, 695, 455

Bezanson R., van Dokkum P. G., Tal T., Marchesini D., Kriek M., Franx M., Coppi P., 2009, ApJ, 697, 1290

Bîrzan L., Rafferty D. A., McNamara B. R., Wise M. W., Nulsen P. E. J., 2004, ApJ, 607, 800

Blecha L., Cox T. J., Loeb A., Hernquist L., 2011, MNRAS, 412, 2154

Bode T., Bogdanović T., Haas R., Healy J., Laguna P., Shoemaker D., 2012, ApJ, 744, 45

Boehringer H., Voges W., Fabian A. C., Edge A. C., Neumann D. M., 1993, MNRAS, 264, L25

Bondi H., 1952, MNRAS, 112, 195

Bondi H., Hoyle F., 1944, MNRAS, 104, 273

Booth C. M., Schaye J., 2009, MNRAS, 398, 53 (BS09)

Bournaud F., Jog C. J., Combes F., 2005, A&A, 437, 69

Bromm V., Loeb A., 2003, ApJ, 596, 34

Brook C. B., Kawata D., Gibson B. K., Freeman K. C., 2004, ApJ, 612, 894

Bucciantini N., Del Zanna L., 2011, A&A, 528, A101

Buff J., McCray R., 1974, ApJ, 189, 147

Cabrit S., Edwards S., Strom S. E., Strom K. M., 1990, ApJ, 354, 687

Castor J. I., Abbott D. C., Klein R. I., 1975, ApJ, 195, 157

Cavagnolo K. W., McNamara B. R., Nulsen P. E. J., Carilli C. L., Jones C., Bîrzan L., 2010, ApJ, 720, 1066

Cavaliere A., Fusco-Femiano R., 1976, A&A, 49, 137

Chen C.-T. J. et al., 2013, ApJ, 773, 3

Churazov E., Sunyaev R., Forman W., Böhringer H., 2002, MNRAS, 332, 729

Ciotti L., Ostriker J. P., 2001, ApJ, 551, 131

Clarke D. A., 1996, ApJ, 457, 291

Clarke D. A., 2010, ApJS, 187, 119

Colella P., Woodward P. R., 1984, Journal of Computational Physics, 54, 174

Couchman H. M. P., 1991, ApJ, 368, L23

Couchman H. M. P., Thomas P. A., Pearce F. R., 1995, ApJ, 452, 797

Cowie L. L., Ostriker J. P., Stark A. A., 1978, ApJ, 226, 1041

Cowie L. L., Songaila A., Hu E. M., Cohen J. G., 1996, AJ, 112, 839

Croft R. A. C., Di Matteo T., Springel V., Hernquist L., 2009, MNRAS, 400, 43

Croft S. et al., 2006, ApJ, 647, 1040

Crowther P. A., 2007, ARA&A, 45, 177

Daddi E. et al., 2007, ApJ, 670, 173

Daddi E. et al., 2005, ApJ, 626, 680

Dasyra K. M. et al., 2006, ApJ, 638, 745

Debuhr J., Quataert E., Ma C.-P., 2011, MNRAS, 412, 1341 (DQM11)

Di Matteo T., Springel V., Hernquist L., 2005, Nature, 433, 604

Djorgovski S., Davis M., 1987, ApJ, 313, 59

Dressler A., Lynden-Bell D., Burstein D., Davies R. L., Faber S. M., Terlevich R., Wegner G., 1987, ApJ, 313, 42

Dubois Y., Devriendt J., Slyz A., Teyssier R., 2012, MNRAS, 420, 2662

Edwards D., Heath D., 1976, Ap&SS, 41, 183

Efstathiou G., Eastwood J. W., 1981, MNRAS, 194, 503

Elbaz D., Jahnke K., Pantin E., Le Borgne D., Letawe G., 2009, A&A, 507, 1359

Escala A., Larson R. B., Coppi P. S., Mardones D., 2004, ApJ, 607, 765

Fabian A. C., 1999a, Proceedings of the National Academy of Science, 96, 4749

Fabian A. C., 1999b, MNRAS, 308, L39

Fabian A. C., 2012, ARA&A, 50, 455

Feain I. J., Papadopoulos P. P., Ekers R. D., Middelberg E., 2007, ApJ, 662, 872

Ferrarese L., Merritt D., 2000, ApJ, 539, L9

Fioc M., Rocca-Volmerange B., 1997, A&A, 326, 950

Fragile P. C., Meier D. L., 2009, ApJ, 693, 771

Frank J., King A., Raine D. J., 2002, Accretion Power in Astrophysics: Third Edition

Fukumura K., Kazanas D., Contopoulos I., Behar E., 2010, ApJ, 715, 636

García-Burillo S., Combes F., Schinnerer E., Boone F., Hunt L. K., 2005, A&A, 441, 1011

Gaspari M., Brighenti F., Temi P., 2012, MNRAS, 424, 190

Gastaldello F., Buote D. A., Temi P., Brighenti F., Mathews W. G., Ettori S., 2009, ApJ, 693, 43

Gebhardt K. et al., 2000, ApJ, 539, L13

Gerhard O., 2010, in Galaxies and their Masks, Block D. L., Freeman K. C., Puerari I., eds., p. 339

Gerritsen J. P. E., Icke V., 1997, A&A, 325, 972

Gillessen S., Eisenhauer F., Trippe S., Alexander T., Genzel R., Martins F., Ott T., 2009, ApJ, 692, 1075

Gilli R., Comastri A., Hasinger G., 2007, A&A, 463, 79

Gingold R. A., Monaghan J. J., 1977, MNRAS, 181, 375

Godunov S. K., 1959, Mat. Sb.

Goodman J., 2003, MNRAS, 339, 937

Governato F., Willman B., Mayer L., Brooks A., Stinson G., Valenzuela O., Wadsley J., Quinn T., 2007, MNRAS, 374, 1479

Gültekin K. et al., 2009, ApJ, 698, 198

Hao L. et al., 2005, AJ, 129, 1795

Hartigan P., Edwards S., Ghandour L., 1995, ApJ, 452, 736

Hartwick F. D. A., Schade D., 1990, ARA&A, 28, 437

Heckman T. M., Kauffmann G., Brinchmann J., Charlot S., Tremonti C., White S. D. M., 2004, ApJ, 613, 109

Hernquist L., 1989, Nature, 340, 687

Hernquist L., 1990, ApJ, 356, 359

Hernquist L., Mihos J. C., 1995, ApJ, 448, 41

Hernquist L., Spergel D. N., Heyl J. S., 1993, ApJ, 416, 415

Hickox R. C. et al., 2007, ApJ, 671, 1365

Ho L. C., 2008, ARA&A, 46, 475

Hobbs A., Nayakshin S., Power C., King A., 2011, MNRAS, 413, 2633

Hobbs A., Power C., Nayakshin S., King A. R., 2012, MNRAS, 421, 3443

Hockney R. W., Eastwood J. W., 1981, Computer Simulation Using Particles

Hopkins P. F., Cox T. J., Younger J. D., Hernquist L., 2009, ApJ, 691, 1168

Hopkins P. F., Hernquist L., 2009, ApJ, 698, 1550

Hopkins P. F., Hernquist L., Cox T. J., Kereš D., 2008, ApJS, 175, 356

Hopkins P. F., Hernquist L., Cox T. J., Robertson B., Krause E., 2007, ApJ, 669, 45

Hopkins P. F., Quataert E., 2010, MNRAS, 407, 1529

Hopkins P. F., Quataert E., 2011, MNRAS, 415, 1027

Hoyle F., Lyttleton R. A., 1939, PCPS, 35, 405

Huang J.-S., Cowie L. L., Gardner J. P., Hu E. M., Songaila A., Wainscoat R. J., 1997, ApJ, 476, 12

Ishibashi W., Fabian A. C., 2012, MNRAS, 427, 2998 (IF12)

Ishibashi W., Fabian A. C., Canning R. E. A., 2013, MNRAS, 431, 2350

Islam R. R., Taylor J. E., Silk J., 2003, MNRAS, 340, 647

Johansson P. H., Naab T., Burkert A., 2009, ApJ, 690, 802

Katz N., 1992, ApJ, 391, 502

Kaufmann T., Mayer L., Wadsley J., Stadel J., Moore B., 2007, MNRAS, 375, 53

Kawakatu N., Umemura M., 2002, MNRAS, 329, 572

Kawata D., Gibson B. K., 2005, MNRAS, 358, L16

Kennicutt, Jr. R. C., 1998, ApJ, 498, 541

Kewley L. J., Dopita M. A., Sutherland R. S., Heisler C. A., Trevena J., 2001, ApJ, 556, 121

Khan F. M., Just A., Merritt D., 2011, ApJ, 732, 89

King A., 2003, ApJ, 596, L27

King A., 2005, ApJ, 635, L121

King A. R., 2010, MNRAS, 402, 1516

Kocevski D. D. et al., 2012, ApJ, 744, 148

König S., Aalto S., Muller S., Beswick R. J., Gallagher J. S., 2013, A&A, 553, A72

Kormendy J., Richstone D., 1995, ARA&A, 33, 581

Krumholz M. R., Dekel A., McKee C. F., 2012, ApJ, 745, 69

Kuijken K., Dubinski J., 1995, MNRAS, 277, 1341

Kurosawa R., Proga D., Nagamine K., 2009, ApJ, 707, 823

Lacy M. et al., 2004, ApJS, 154, 166

Lambas D. G., Tissera P. B., Alonso M. S., Coldwell G., 2003, MNRAS, 346, 1189

Landau L. D., Lifshitz E. M., 1959, Fluid mechanics

Liu C., Gan Z.-M., Xie F.-G., 2013, Research in Astronomy and Astrophysics, 13, 899

Loeb A., Rasio F. A., 1994, ApJ, 432, 52

Loveday J., Peterson B. A., Efstathiou G., Maddox S. J., 1992, ApJ, 390, 338

Lucy L. B., 1977, AJ, 82, 1013

Lynden-Bell D., 1967, MNRAS, 136, 101

MacDonald J., Bailey M. E., 1981, MNRAS, 197, 995

Madau P., Ferguson H. C., Dickinson M. E., Giavalisco M., Steidel C. C., Fruchter A., 1996, MNRAS, 283, 1388

Madau P., Rees M. J., 2001, ApJ, 551, L27

Magorrian J. et al., 1998, AJ, 115, 2285

Maiolino R., 2008, New A Rev., 52, 339

Maiolino R. et al., 2012, MNRAS, 425, L66

Maller A. H., Katz N., Kereš D., Davé R., Weinberg D. H., 2006, ApJ, 647, 763

Marconi A., Hunt L. K., 2003, ApJ, 589, L21

Marconi A., Risaliti G., Gilli R., Hunt L. K., Maiolino R., Salvati M., 2004, MNRAS, 351, 169

Martini P., Weinberg D. H., 2001, ApJ, 547, 12

McLure R. J., Dunlop J. S., 2002, MNRAS, 331, 795

McNamara B. R., Nulsen P. E. J., 2007, ARA&A, 45, 117

McNamara B. R., Nulsen P. E. J., Wise M. W., Rafferty D. A., Carilli C., Sarazin C. L., Blanton E. L., 2005, Nature, 433, 45

McNamara B. R. et al., 2000, ApJ, 534, L135

McQuillin R. C., McLaughlin D. E., 2012, MNRAS, 423, 2162

Meier D. L., 2001, ApJ, 548, L9

Merloni A., Heinz S., 2008, MNRAS, 388, 1011

Merritt D., Ferrarese L., 2001, MNRAS, 320, L30

Mihos J. C., Hernquist L., 1996, ApJ, 464, 641

Monaghan J. J., 1992, ARA&A, 30, 543

Monaghan J. J., 2005, Reports on Progress in Physics, 68, 1703

Monaghan J. J., Gingold R. A., 1983, Journal of Computational Physics, 52, 374

Monaghan J. J., Lattanzio J. C., 1985, A&A, 149, 135

Mori M., Yoshii Y., Tsujimoto T., Nomoto K., 1997, ApJ, 478, L21

Moster B. P., Macciò A. V., Somerville R. S., Naab T., Cox T. J., 2011, MNRAS, 415, 3750

Muldrew S. I., Pearce F. R., Power C., 2013, ArXiv e-prints

Murray N., Quataert E., Thompson T. A., 2005, ApJ, 618, 569

Narayan R., Mahadevan R., Quataert E., 1998, in Abramowicz M. A., Bjornsson G., Pringle J. E., eds, Theory of Black Hole Accretion Disks. Cambridge Univ. Press, Cambridge, p. 148

Narayan R., Yi I., 1994, ApJ, 428, L13

Navarro J. F., Frenk C. S., White S. D. M., 1996, ApJ, 462, 563

Navarro J. F., White S. D. M., 1993, MNRAS, 265, 271

Nayakshin S., Power C., 2010, MNRAS, 402, 789

Nesti F., Salucci P., 2013, J. Cosmology Astropart. Phys., 7, 16

Nixon C. J., King A. R., Pringle J. E., 2011, MNRAS, 417, L66

Noble S. C., Krolik J. H., 2009, ApJ, 703, 964

Nobukawa M., Ryu S. G., Tsuru T. G., Koyama K., 2011, ApJ, 739, L52

Okamoto T., Nemmen R. S., Bower R. G., 2008, MNRAS, 385, 161 (ONB08)

Orban de Xivry G., Davies R., Schartmann M., Komossa S., Marconi A., Hicks E., Engel H., Tacconi L., 2011, MNRAS, 417, 2721

Osmer P. S., 1998, in Astronomical Society of the Pacific Conference Series, Vol. 146, The Young Universe: Galaxy Formation and Evolution at Intermediate and High Redshift, D'Odorico S., Fontana A., Giallongo E., eds., p. 1

Patel S. G. et al., 2013, ApJ, 766, 15

Planck Collaboration et al., 2013, ArXiv e-prints

Power C., Nayakshin S., King A., 2011, MNRAS, 412, 269 (PNK11)

Price D. J., Monaghan J. J., 2004, MNRAS, 348, 123

Proga D., 2007, ApJ, 661, 693

Proga D., Stone J. M., Kallman T. R., 2000, ApJ, 543, 686

Puchwein E., Sijacki D., Springel V., 2008, ApJ, 687, L53

Ramsey J. P., Clarke D. A., Men'shchikov A. B., 2012, ApJS, 199, 13

Rasmussen J., Sommer-Larsen J., Pedersen K., Toft S., Benson A., Bower R. G., Grove L. F., 2009, ApJ, 697, 79

Read J. I., Hayfield T., 2012, MNRAS, 422, 3037

Read J. I., Wilkinson M. I., Evans N. W., Gilmore G., Kleyna J. T., 2006, MNRAS, 366, 429

Rees M. J., Begelman M. C., Blandford R. D., Phinney E. S., 1982, Nature, 295, 17

Rees M. J., Ostriker J. P., 1977, MNRAS, 179, 541

Reynolds S. P., 2008, ARA&A, 46, 89

Robertson B., Cox T. J., Hernquist L., Franx M., Hopkins P. F., Martini P., Springel V., 2006a, ApJ, 641, 21

Robertson B., Hernquist L., Cox T. J., Di Matteo T., Hopkins P. F., Martini P., Springel V., 2006b, ApJ, 641, 90

Rodríguez Zaurín J., Holt J., Tadhunter C. N., González Delgado R. M., 2007, MNRAS, 375, 1133

Romanowsky A. J., Douglas N. G., Arnaboldi M., Kuijken K., Merrifield M. R., Napolitano N. R., Capaccioli M., Freeman K. C., 2003, Science, 301, 1696

Salpeter E. E., 1964, ApJ, 140, 796

Sanders D. B., Soifer B. T., Elias J. H., Madore B. F., Matthews K., Neugebauer G., Scoville N. Z., 1988, ApJ, 325, 74

Sarajedini V. L., Koo D. C., Klesman A. J., Laird E. S., Perez Gonzalez P. G., Mozena M., 2011, ApJ, 731, 97

Scannapieco C. et al., 2012, MNRAS, 423, 1726

Scannapieco E., Oh S. P., 2004, ApJ, 608, 62

Scannapieco E., Silk J., Bouwens R., 2005, ApJ, 635, L13

Scannapieco E., Thacker R. J., Couchman H. M. P., 2008, ApJ, 678, 674

Schechter P., 1976, ApJ, 203, 297

Schmidt M., 1968, ApJ, 151, 393

Schneider R., Ferrara A., Natarajan P., Omukai K., 2002, ApJ, 571, 30

Schure K. M., Kosenko D., Kaastra J. S., Keppens R., Vink J., 2009, A&A, 508, 751

Sérsic J. L., 1963, Boletin de la Asociacion Argentina de Astronomia La Plata Argentina, 6, 41

Sérsic J. L., 1968, Atlas de galaxias australes

Shakura N. I., Sunyaev R. A., 1973, A&A, 24, 337

Shankar F., Crocce M., Miralda-Escudé J., Fosalba P., Weinberg D. H., 2010, ApJ, 718, 231

Shankar F., Salucci P., Granato G. L., De Zotti G., Danese L., 2004, MNRAS, 354, 1020

Shankar F., Weinberg D. H., Miralda-Escudé J., 2013, MNRAS, 428, 421

Shaver P. A., Wall J. V., Kellermann K. I., Jackson C. A., Hawkins M. R. S., 1996, Nature, 384, 439

Shima E., Matsuda T., Takeda H., Sawada K., 1985, MNRAS, 217, 367

Shiokawa H., Dolence J. C., Gammie C. F., Noble S. C., 2012, ApJ, 744, 187

Sijacki D., Springel V., Di Matteo T., Hernquist L., 2007, MNRAS, 380, 877

Silk J., 2013, ApJ, 772, 112

Silk J., Mamon G. A., 2012, Research in Astronomy and Astrophysics, 12, 917

Silk J., Norman C., 2009, ApJ, 700, 262

Silk J., Rees M. J., 1998, A&A, 331, L1

Small T. A., Blandford R. D., 1992, MNRAS, 259, 725

Soltan A., 1982, MNRAS, 200, 115

Sommer-Larsen J., Gelato S., Vedel H., 1999, ApJ, 519, 501

Spergel D. N. et al., 2003, ApJS, 148, 175

Springel V., 2010a, MNRAS, 401, 791

Springel V., 2010b, ARA&A, 48, 391

Springel V., Di Matteo T., Hernquist L., 2005a, ApJ, 620, L79

Springel V., Di Matteo T., Hernquist L., 2005b, MNRAS, 361, 776 (SDH05)

Springel V., Hernquist L., 2002, MNRAS, 333, 649

Springel V., Hernquist L., 2003, MNRAS, 339, 289

Springel V. et al., 2005c, Nature, 435, 629

Springel V., Yoshida N., White S. D. M., 2001, New A, 6, 79

Steidel C. C., Hunt M. P., Shapley A. E., Adelberger K. L., Pettini M., Dickinson M., Giavalisco M., 2002, ApJ, 576, 653

Steinmetz M., 1996, MNRAS, 278, 1005

Stinson G., Seth A., Katz N., Wadsley J., Governato F., Quinn T., 2006, MNRAS, 373, 1074

Storchi-Bergmann T., Riffel R. A., Riffel R., Diniz M. R., Borges Vale T., McGregor P. J., 2012, ApJ, 755, 87

Subramanian K., Rees M. J., Chitre S. M., 1987, MNRAS, 224, 283

Sutherland R. S., Dopita M. A., 1993, ApJS, 88, 253

Taffoni G., Mayer L., Colpi M., Governato F., 2003, MNRAS, 341, 434

Teyssier R., 2002, A&A, 385, 337

Thacker R. J., Couchman H. M. P., 2000, ApJ, 545, 728

Thacker R. J., Couchman H. M. P., 2006, Computer Physics Communications, 174, 540

Thacker R. J., Scannapieco E., Couchman H. M. P., 2006, ApJ, 653, 86

Thacker R. J., Tittley E. R., Pearce F. R., Couchman H. M. P., Thomas P. A., 2000, MNRAS, 319, 619

Theis C., Spurzem R., 1999, A&A, 341, 361

Theuns T., Leonard A., Efstathiou G., Pearce F. R., Thomas P. A., 1998, MNRAS, 301, 478

Thomas P. A., Couchman H. M. P., 1992, MNRAS, 257, 11

Toomre A., 1977, in Evolution of Galaxies and Stellar Populations, Tinsley B. M., Larson D. Campbell R. B. G., eds., p. 401

Toomre A., Toomre J., 1972, ApJ, 178, 623

Tozzi P. et al., 2006, A&A, 451, 457

Tremaine S. et al., 2002, ApJ, 574, 740

Trujillo I., Conselice C. J., Bundy K., Cooper M. C., Eisenhardt P., Ellis R. S., 2007, MNRAS, 382, 109

Ueda Y., Akiyama M., Ohta K., Miyaji T., 2003, ApJ, 598, 886

Umemura M., 2001, ApJ, 560, L29

Umemura M., Fukue J., Mineshige S., 1997, ApJ, 479, L97

van Albada T. S., Bahcall J. N., Begeman K., Sancisi R., 1985, ApJ, 295, 305 van der Laan T. P. R. et al., 2011, A&A, 529, A45

van Dokkum P. G. et al., 2008, ApJ, 677, L5

van Dokkum P. G. et al., 2010, ApJ, 709, 1018

van Leer B., 1977, Journal of Computational Physics, 23, 276

Vasudevan R. V., Fabian A. C., 2007, MNRAS, 381, 1235

Veilleux S., Osterbrock D. E., 1987, ApJS, 63, 295

Vogelsberger M., Genel S., Sijacki D., Torrey P., Springel V., Hernquist L., 2013, ArXiv e-prints

Webb W., Malkan M., 2000, ApJ, 540, 652

White S. D. M., Navarro J. F., Evrard A. E., Frenk C. S., 1993, Nature, 366, 429

White S. D. M., Rees M. J., 1978, MNRAS, 183, 341

Widrow L. M., Dubinski J., 2005, ApJ, 631, 838

Widrow L. M., Pym B., Dubinski J., 2008, ApJ, 679, 1239

Wild V., Heckman T., Charlot S., 2010, MNRAS, 405, 933

Williamson D. J., Thacker R. J., 2012, MNRAS, 421, 2170

Willson L. A., 2000, ARA&A, 38, 573

Woods D. F., Geller M. J., Barton E. J., 2006, AJ, 132, 197

Wurster J., Thacker R. J., 2013a, MNRAS, 431, 2513

Wurster J., Thacker R. J., 2013b, MNRAS, 431, 539

Yan R. et al., 2011, ApJ, 728, 38

Zubovas K., King A., 2012, ApJ, 745, L34

Zubovas K., Nayakshin S., Sazonov S., Sunyaev R., 2013, MNRAS, 431, 793

Appendix A

Alternative derivation for $\boldsymbol{\nabla} A_{\mathrm{I}}(\boldsymbol{r})$

Let us begin with the interpolation integral given in (1.9),

$$A_{\mathrm{I}}(\boldsymbol{r}) = \int A(\boldsymbol{r}')W(\boldsymbol{r}-\boldsymbol{r}', h)\mathrm{d}\boldsymbol{r}'. \tag{A.1}$$

To determine the derivative $A_{\mathrm{I}}(\boldsymbol{r})$, replace $A_{\mathrm{I}}(\boldsymbol{r})$ with $\frac{\partial A(\boldsymbol{r})}{\partial \boldsymbol{r}}$ in (A.1), viz.,

$$\frac{\partial A_{\mathrm{I}}(\boldsymbol{r})}{\partial \boldsymbol{r}} = \int \frac{\partial A(\boldsymbol{r}')}{\partial \boldsymbol{r}'}W(\boldsymbol{r}-\boldsymbol{r}', h)\mathrm{d}\boldsymbol{r}'. \tag{A.2}$$

This can be expanded as

$$\frac{\partial A_{\mathrm{I}}(\boldsymbol{r})}{\partial \boldsymbol{r}} = \int \frac{\partial}{\partial \boldsymbol{r}'}\left[A(\boldsymbol{r}')W(\boldsymbol{r}-\boldsymbol{r}', h)\right]\mathrm{d}\boldsymbol{r}' - \int A(\boldsymbol{r}')\frac{\partial}{\partial \boldsymbol{r}'}W(\boldsymbol{r}-\boldsymbol{r}', h)\mathrm{d}\boldsymbol{r}'. \tag{A.3}$$

The first term on the right hand can be converted to a surface integral by the divergence theorem, which then vanishes since $W(\boldsymbol{r}-\boldsymbol{r}', h) = 0$ on the surface. Thus,

$$\frac{\partial A_{\mathrm{I}}(\boldsymbol{r})}{\partial \boldsymbol{r}} = -\int A(\boldsymbol{r}')\frac{\partial}{\partial \boldsymbol{r}'}W(\boldsymbol{r}-\boldsymbol{r}', h)\mathrm{d}\boldsymbol{r}'. \tag{A.4}$$

Using the approximation

$$\boldsymbol{\nabla}_i W(\boldsymbol{r}_i-\boldsymbol{r}_j, h_i) \simeq -\boldsymbol{\nabla}_j W(\boldsymbol{r}_i-\boldsymbol{r}_j, h_j) \tag{A.5}$$

yields

$$\frac{\partial A_{\mathrm{I}}(\boldsymbol{r})}{\partial \boldsymbol{r}} = \int A(\boldsymbol{r}')\frac{\partial}{\partial \boldsymbol{r}}W(\boldsymbol{r}-\boldsymbol{r}', h)\mathrm{d}\boldsymbol{r}'. \tag{A.6}$$

Then, we can multiply and divide the integrand by $\rho(\boldsymbol{r}')$ to obtain

$$\frac{\partial A_{\mathrm{I}}(\boldsymbol{r})}{\partial \boldsymbol{r}} = \int \frac{A(\boldsymbol{r}')}{\rho(\boldsymbol{r}')} \frac{\partial}{\partial \boldsymbol{r}} W(\boldsymbol{r} - \boldsymbol{r}', h) \rho(\boldsymbol{r}') \mathrm{d}\boldsymbol{r}', \tag{A.7}$$

which then can be converted in to a sum, viz.

$$\boldsymbol{\nabla} A_{\mathrm{I}}(\boldsymbol{r}) = \sum_j m_j \frac{A_j}{\rho_j} \boldsymbol{\nabla} W(\boldsymbol{r} - \boldsymbol{r}_j, h), \tag{A.8}$$

where $m_j = \rho(\boldsymbol{r}')\mathrm{d}\boldsymbol{r}'$ is the mass element of the particle, and $\boldsymbol{\nabla} \equiv \frac{\partial}{\partial \boldsymbol{r}}$. This equation matches (1.18), as required.

Appendix B

Additional Figures

In Chapters 2 and 3, we studied AGN feedback algorithms in a major merger simulation. Since each chapter was based upon a published paper (Wurster & Thacker (2013a) for Chapter 2 and Wurster & Thacker (2013b) for Chapter 3), there is very little direct comparison between Models PNK and the continual accretion algorithms in Chapter 2. Thus, in Section B.1, we will replot many of the figures from Chapter 2, and include the data for Model PNKr05t05, which will be shortened to Model PNK for this appendix.

Likewise, in §2.2.5.6, we mentioned four additional models, which were only minimally discussed in Chapter 2. In §B.2 we plot several figures comparing the results of the variant to its parent model. Finally, in §B.3, we compare each of our primary models at the two resolutions run.

B.1 Comparing Model PNK to the continual accretion models

In Figs. B.1–B.3, we plot the gas column density, gas temperature and stellar column density of the top right galaxy in each model at apoapsis. The profiles for Model PNK is similar to that of Model WT (both use the black hole advection of Model WT), as opposed to Model DQM (both use the kinetic feedback of Model DQM). This further supports our claim that the large tracer mass prevents the bar from forming and not the kinetic feedback.

In the left panel of Fig. B.4, we show the total black hole mass over time and, in the right panel, we show the accretion rates (geometrically averaged over both black holes and plotted in bins of 10 Myr). Model PNK has the largest final black

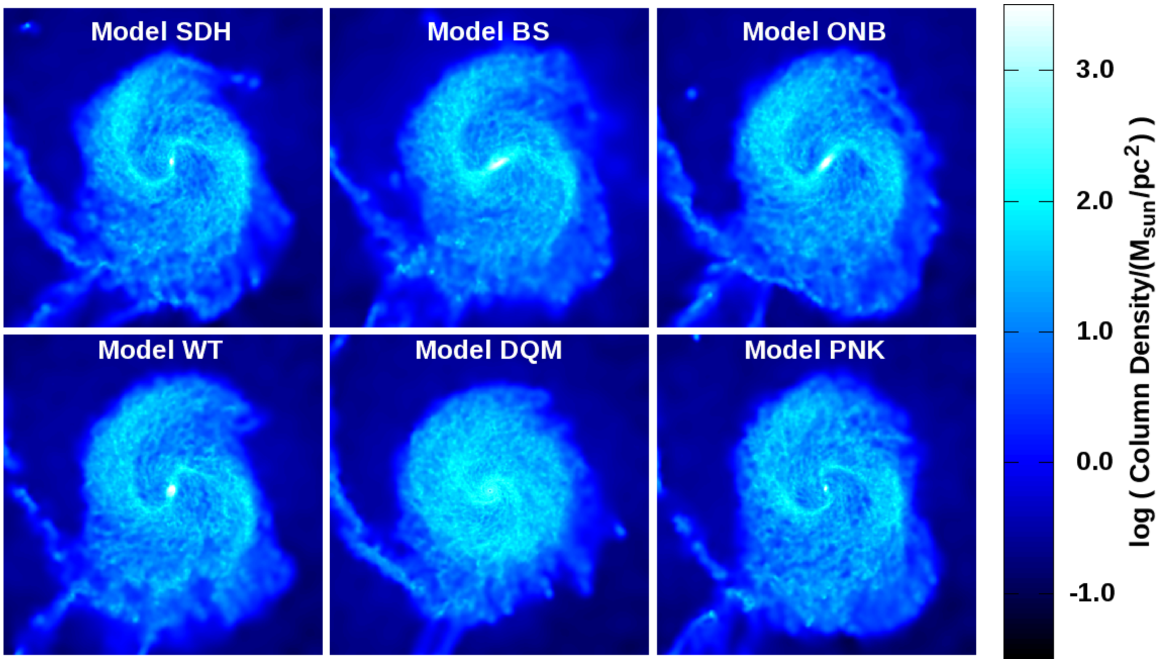

Figure B.1: Gas column density of the top right galaxy of each model at apoapsis. Each frame measures 20 kpc per side, with an image resolution of 39 pc pixel^{-1}.

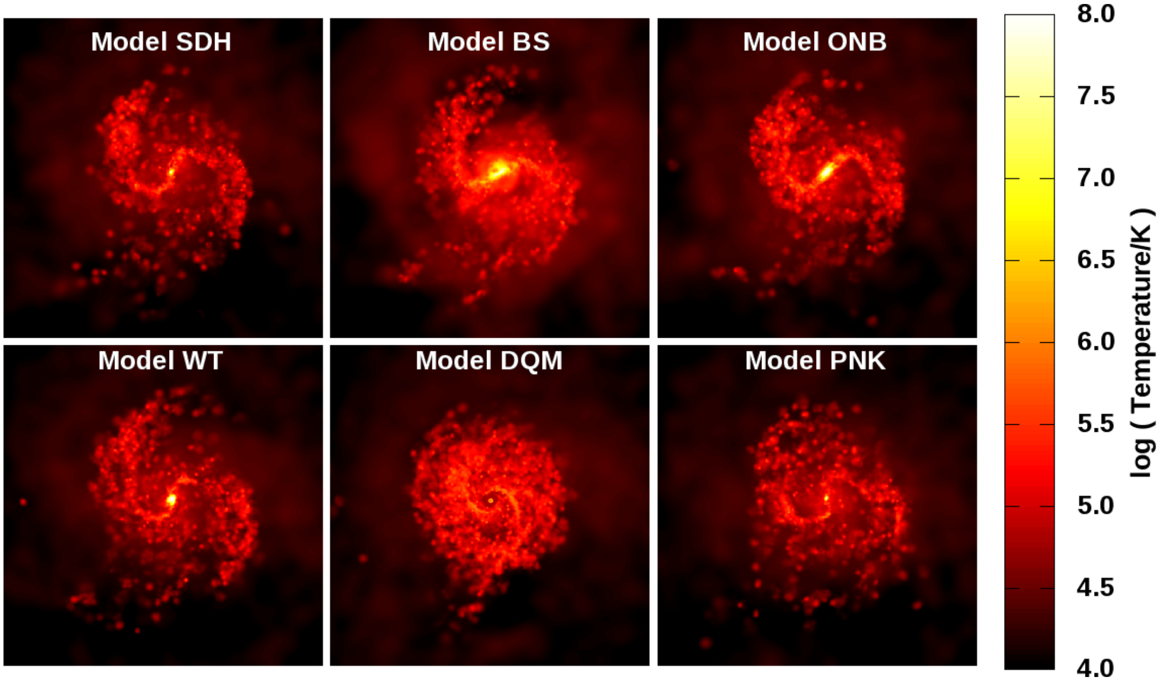

Figure B.2: Same as Fig. B.1, except showing gas temperature.

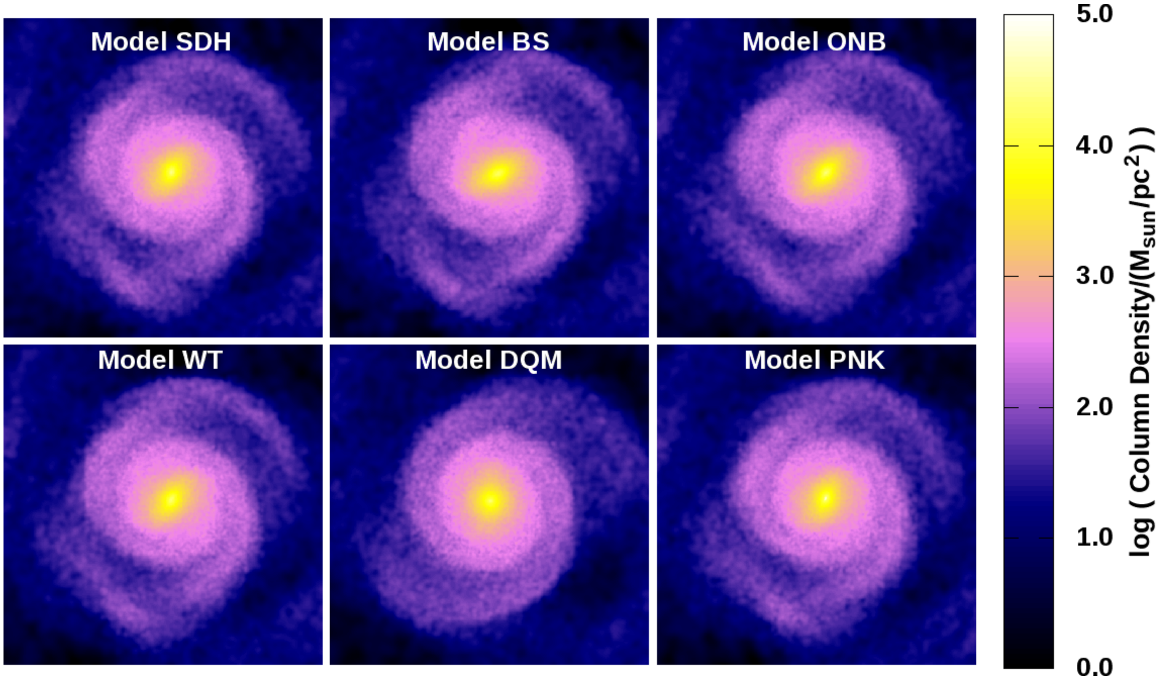

Figure B.3: Same as Fig. B.1, except showing stellar column density.

hole mass of all the simulations, but it still lies within the accepted M_{B}–σ relation, as is shown below. The accretion rate profile of Model PNK is similar to Models SDH and WT, but the apoapsis accretion epoch begins earlier.

In Fig. B.5 we plot the gas density and temperatures around the black holes. The gas density of Model PNK is qualitatively similar to Models SDH and WT, while its temperature profile is slightly lower than Model ONB. Model PNK has a higher temperature than Model DQM, even though both models are using kinetic feedback.

The global star formation rate is plotted in Figure B.6.

The final remnant in all models is a reformed gas and stellar disc surrounded by a fragmented hot gas halo. We plot the final gas column density, gas temperature and stellar column density for frames of 100 and 20 kpc per side, respectively in Figs. B.7, B.8 and B.9. In Fig. B.10, we plot the radial profiles for gas temperature, gas

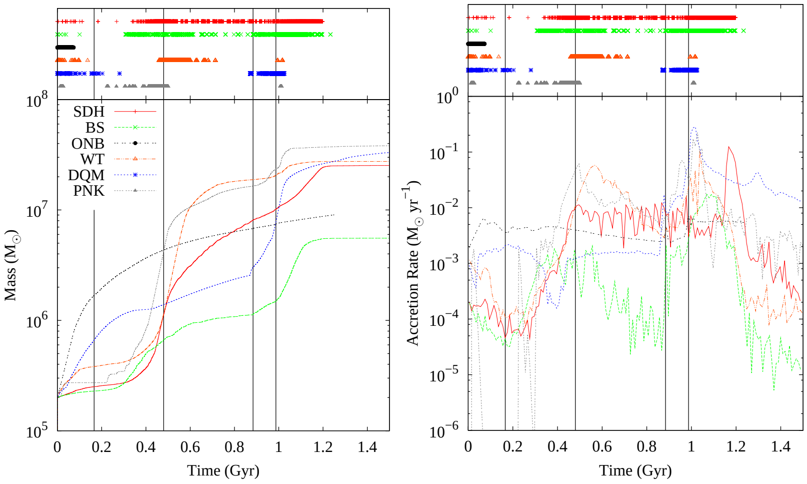

Figure B.4: *Left*: The total black hole mass in each fiducial resolution simulation. *Right*: The accretion rates for each of the fiducial resolution models geometrically averaged over both black holes and plotted in bins of 10 Myr. *Top*: Points represent when a black hole is accreting at $\dot{M}_{\rm Edd}$. The four black vertical lines indicate the time of first periapsis, apoapsis, second periapsis and core merger.

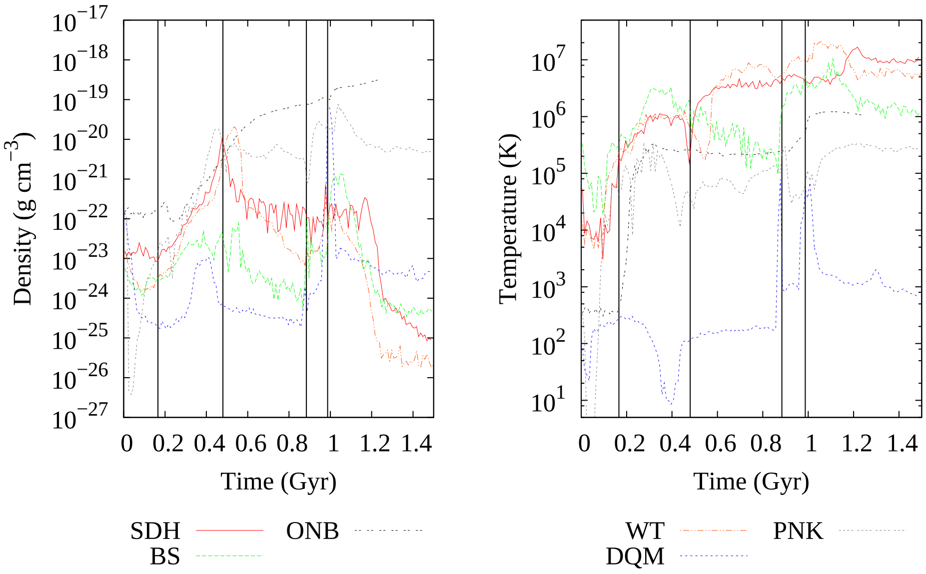

Figure B.5: Gas density (left) and temperature (right) within $r_{\rm inf}$ the black holes, geometrically averaged over both black holes and plotted in bins of 10 Myr.

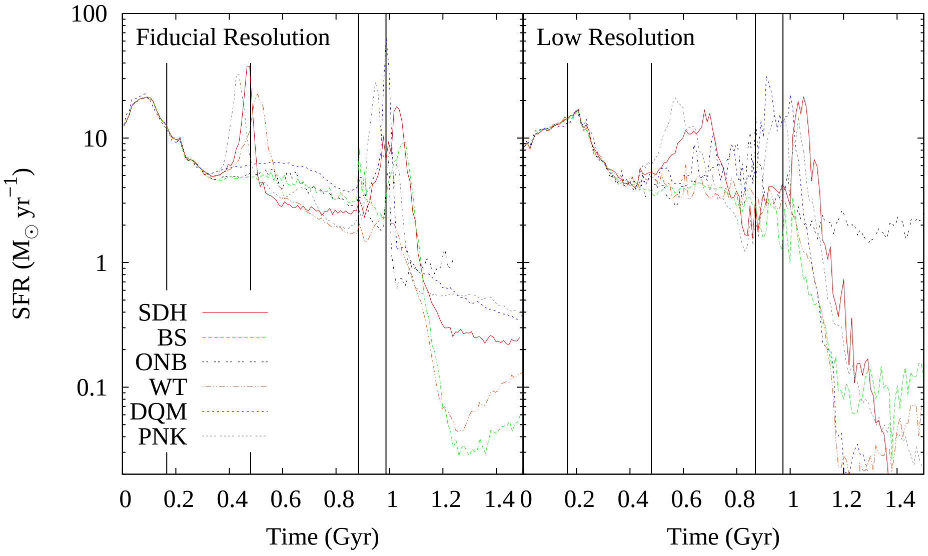

Figure B.6: Global star formation rate for the fiducial (left) and low resolution (right) runs. The vertical lines represent the times of first periapsis, apoapsis, second periapsis and core merger for the dynamic black hole mass models, as given in Table 2.4.

density and stellar column density (averaged over all azimuthal and polar angles) for each remnant.

The surface density profile for the reformed fiducial resolution discs is plotted in Fig. B.11.

Finally, we plot the $M_{\rm BH}$–σ relationship in Fig. B.12.

B.2 Comparing parent and variant models

In Fig. B.13, we plot the total black hole mass, accretion rates, gas density, gas temperature and global star formation rate for our variant models compared to their parent models.

Models BS and BSw differ by the black hole advection algorithm. Although the gas profiles around the black hole are much smoother for Model BSw, both models

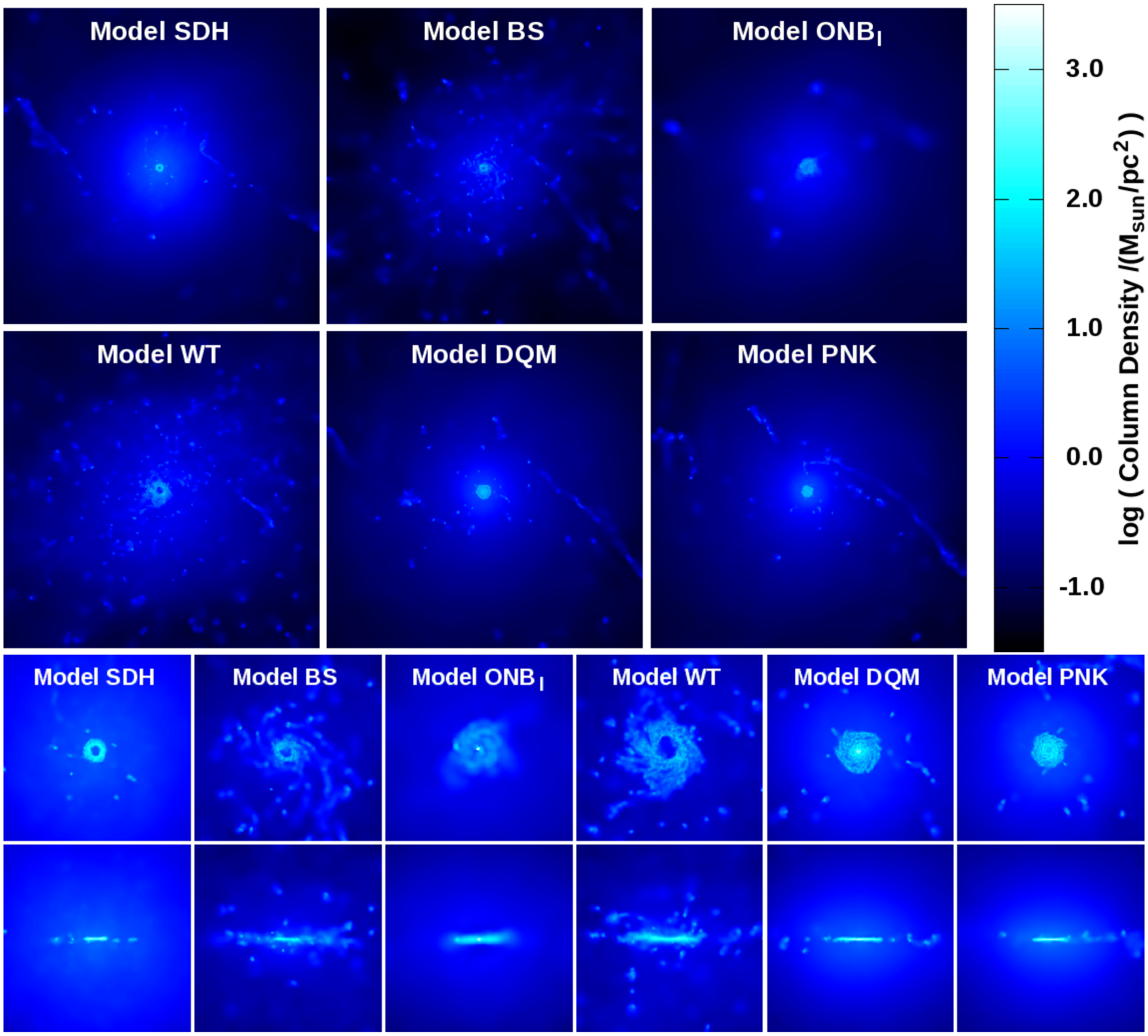

Figure B.7: Gas column density of each model taken at 1.5 Gyr. The frames in the top two rows measure 100kpc per side, with an image resolution of 195 pc pixel^{-1} (391 pc pixel^{-1}) for the fiducial (low) resolution models. The frames in the bottom two rows measure 20kpc per side, with a image resolution of 39 pc pixel^{-1} (78 pc pixel^{-1}) for the fiducial (low) resolution models.

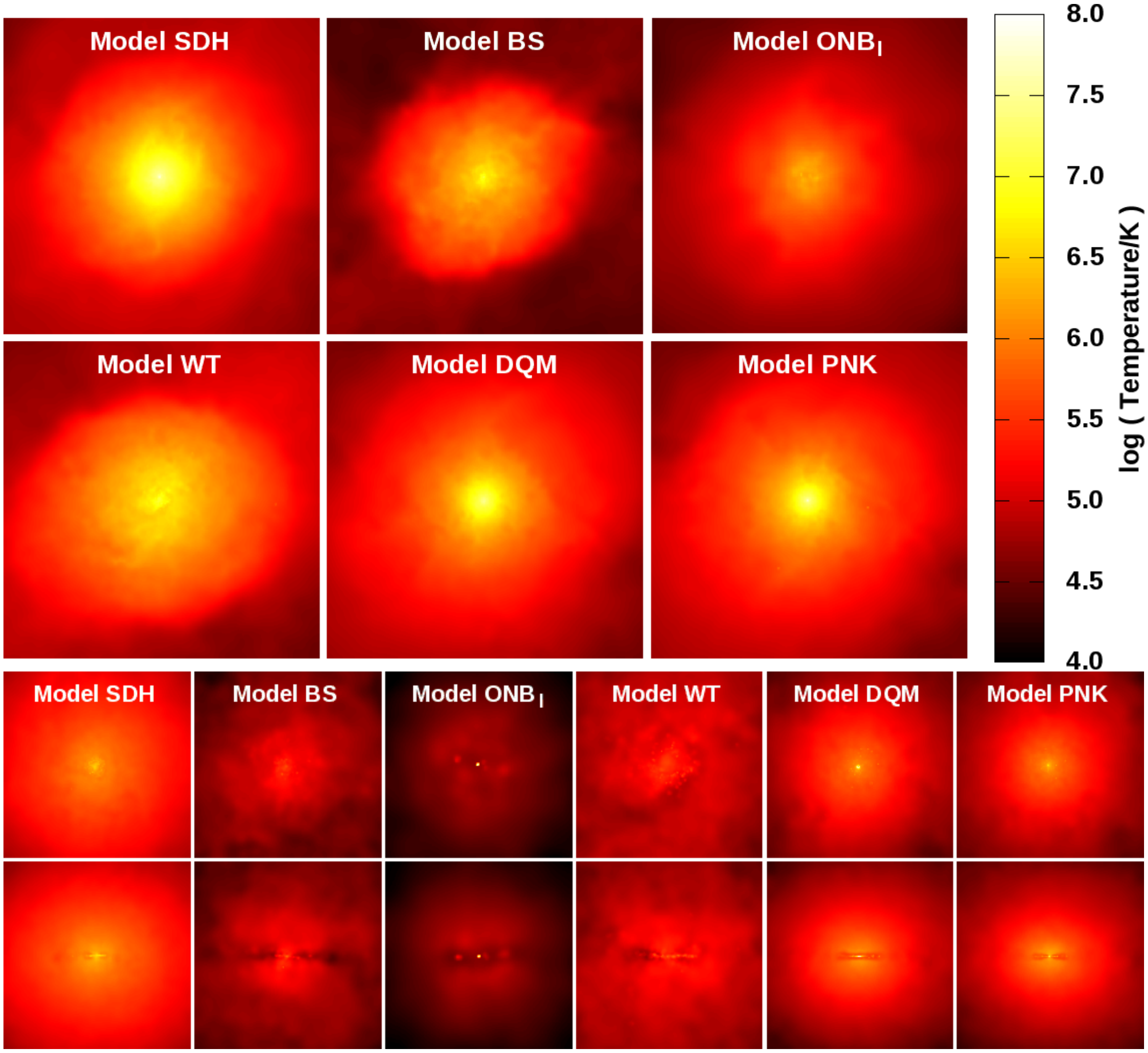

Figure B.8: Gas temperature of each model taken at 1.5 Gyr. The frames in the top two rows measure 100kpc per side, with an image resolution of 195 pc pixel^{-1} (391 pc pixel^{-1}) for the fiducial (low) resolution models. The frames in the bottom two rows measure 20kpc per side, with a image resolution of 39 pc pixel^{-1} (78 pc pixel^{-1}) for the fiducial (low) resolution models.

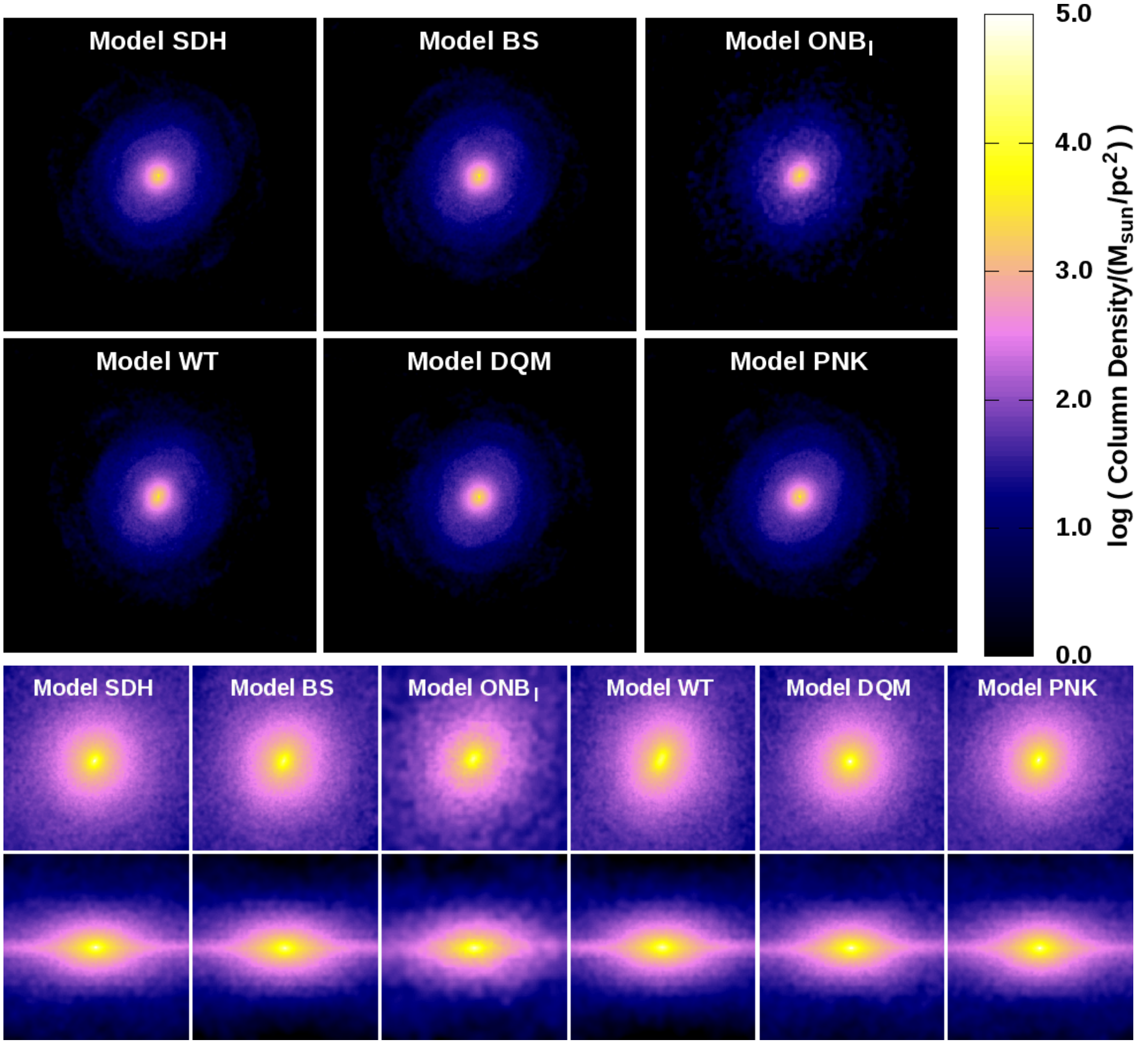

Figure B.9: Stellar column density of each model taken at 1.5 Gyr. The frames in the top two rows measure 100kpc per side, with an image resolution of 195 pc pixel^{-1} (391 pc pixel^{-1}) for the fiducial (low) resolution models. The frames in the bottom two rows measure 20kpc per side, with a image resolution of 39 pc pixel^{-1} (78 pc pixel^{-1}) for the fiducial (low) resolution models.

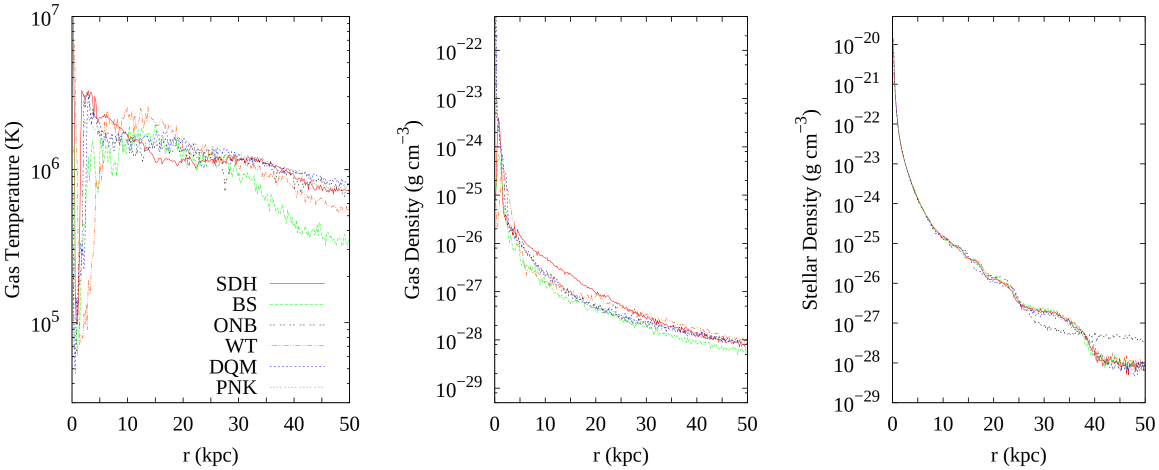

Figure B.10: Radial profiles of our remnants, averaged over all azimuthal and polar angles. From left to right, we show gas temperature, gas density, and stellar density. The profile for Model ONB is taken at 1.25 Gyr.

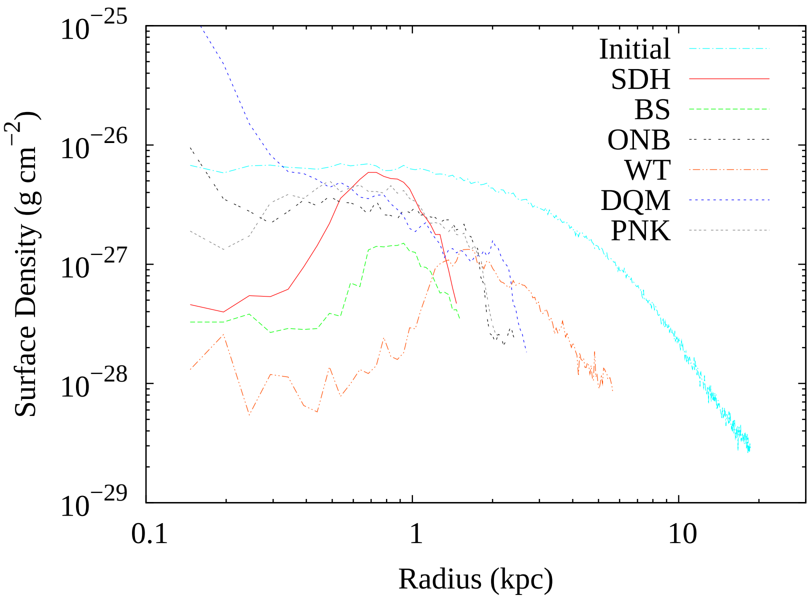

Figure B.11: Gas surface density profile, averaged over all azimuthal angles, for the initial and final discs of the fiducial resolution models. The profiles are truncated at the edge of the disc, and plotted in bins of 49 pc. The remnant profile for Model ONB is taken at 1.25 Gyr.

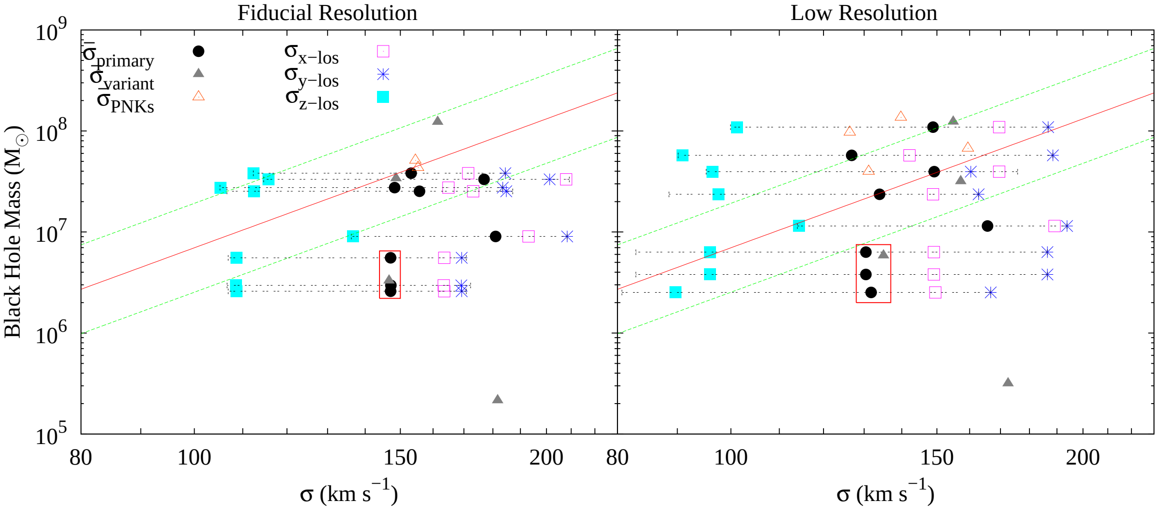

Figure B.12: The M_{BH}–σ relation for our simulations, along with the observed relation (red) and the one-sigma scatter (dashed) from Gültekin et al. (2009). For our six primary models at each resolution, the dot represents the average σ of 1000 random lines of sight, the horizontal bars represent the range of all calculated σ's, and the remaining three symbols on the horizontal line represent σ taken along the $\pm x-$, $\pm y-$ and $\pm z-$lines of sight. For our variant models, we have only plotted the average σ of 1000 random lines of sight (solid triangles). We have removed the labels for clarity; refer to Figs. 2.15 and 3.11 for details concerning the individual data points.

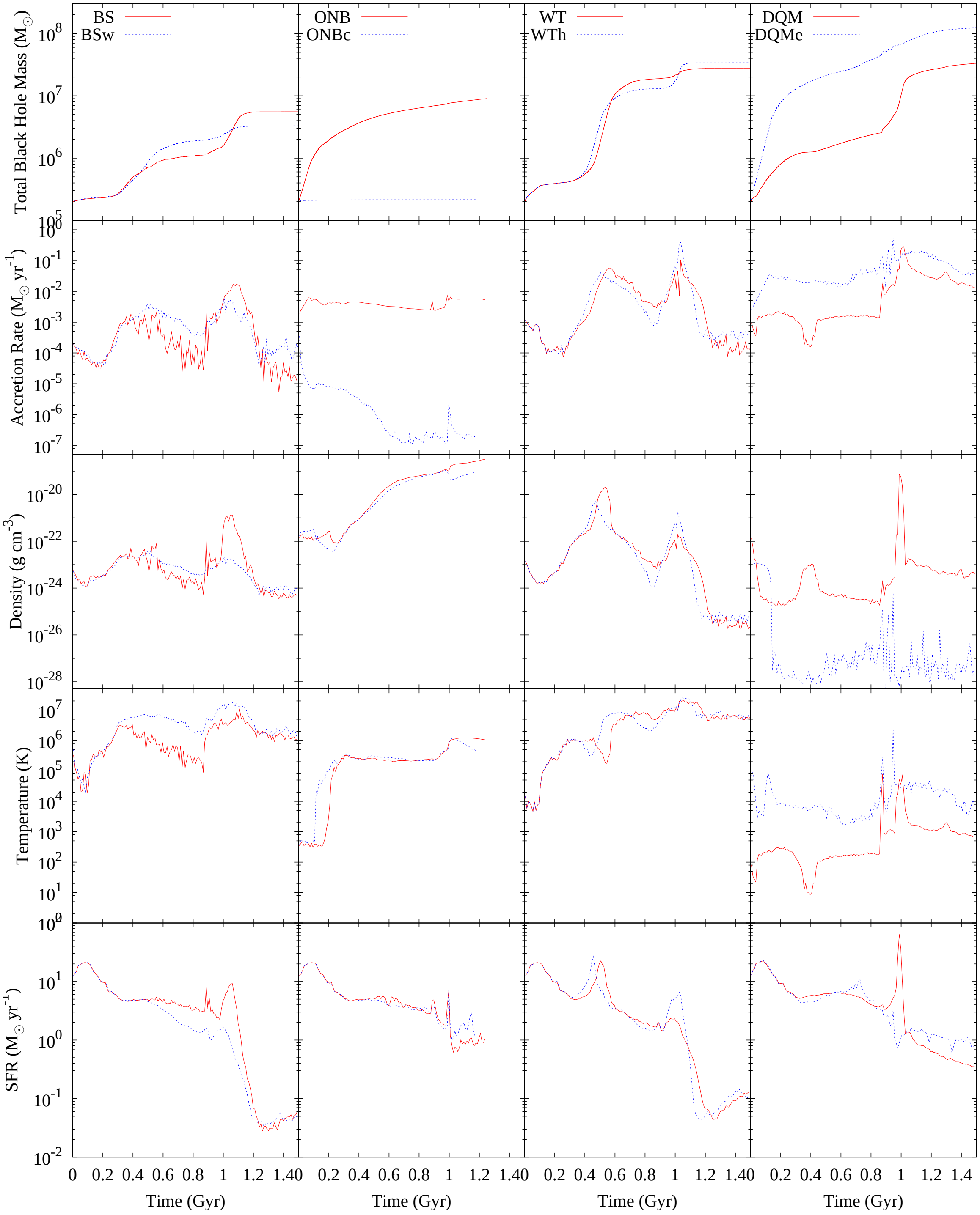

Figure B.13: Total black hole mass, accretion rates, gas density, gas temperature and global star formation rate for our variant models and their parent models. The bottom four rows are geometrically averaged over both black holes in bins of 10 Myr.

yield similar remnants (including black holes that do not lie on the $M_{\rm BH}$–σ relationship). At core merger, the density and accretion rates are not as large in Model BSw, since the black hole motion is better behaved and there is less stirring of the gas.

Model ONBc is essentially a zero-feedback model due to its negligible accretion rate. Since this feedback is returned to the halo in Models ONB and ONBc (leaving the core relatively undisturbed), the gas properties and global star formation rate are very similar. There are deviations between the two models for the secular evolution prior to first periapsis and again after the black holes have merged. The former is a result of gas being accreted on to the black hole, and the latter is likely a result of the black holes having very different masses, hence gravitational influences.

Model WTh has a smaller minimum smoothing length than Model WT. This only becomes relevant for high density regions, such as periapsis and core mergers. At these times, the local maxima are less broad and better well-defined. One notable difference is the star formation peak at core merger in Model WTh, again, a result of a smaller minimum smoothing length permitting higher gas densities. In general, the results are very similar, thus the additional computational time required to run Model WTh is not an efficient trade-off.

Model DQMe has a fixed and unreasonably large radius of influence, $r_{\rm inf}$. This yields unphysical results for this model. The large $r_{\rm inf}$ permits an initial epoch of Eddington accretion, then self-regulates a large void around the black hole. Although self-regulated voids exist for Models DQM and DQMe, the smaller void in DQM permits a reasonable evolution of the system. Also, the large $r_{\rm inf}$ means that the black holes can numerically merge from greater distances. This merger then displaces the merged black hole to the centre of mass of the two black holes, which is outside of their local gas cores, resulting in a drop in gas density. The black hole's motion after this causes shock heating as it collides with and destroys the gas cores of its progenitors. This can be seen and the local gas density and temperature peaks just prior to 1 Gyr.

B.3 Comparing resolutions

In Fig. B.14, we plot the total black hole mass, accretion rates, gas density, gas temperature and global star formation rate for both resolutions of the models presented in Chapter 2.

In Chapter 3, we concluded that of the free parameters tested for Model PNK ($R_{\rm acc}$, $t_{\rm visc}$ and resolution), resolution had the largest impact on the results. From this figure, we can see that the resolution also impacts the results of the models from Chapter 2. In general and as expected, the fiducial resolution results are smoother and display sharper features. Moreover, some of the features are completely smoothed out in the low resolution models. However, loose general trends exist between each fiducial–low resolution pair. Thus, a low resolution comparative analysis can still be performed, although it would be difficult to make observational predictions or quantitative statements from them.

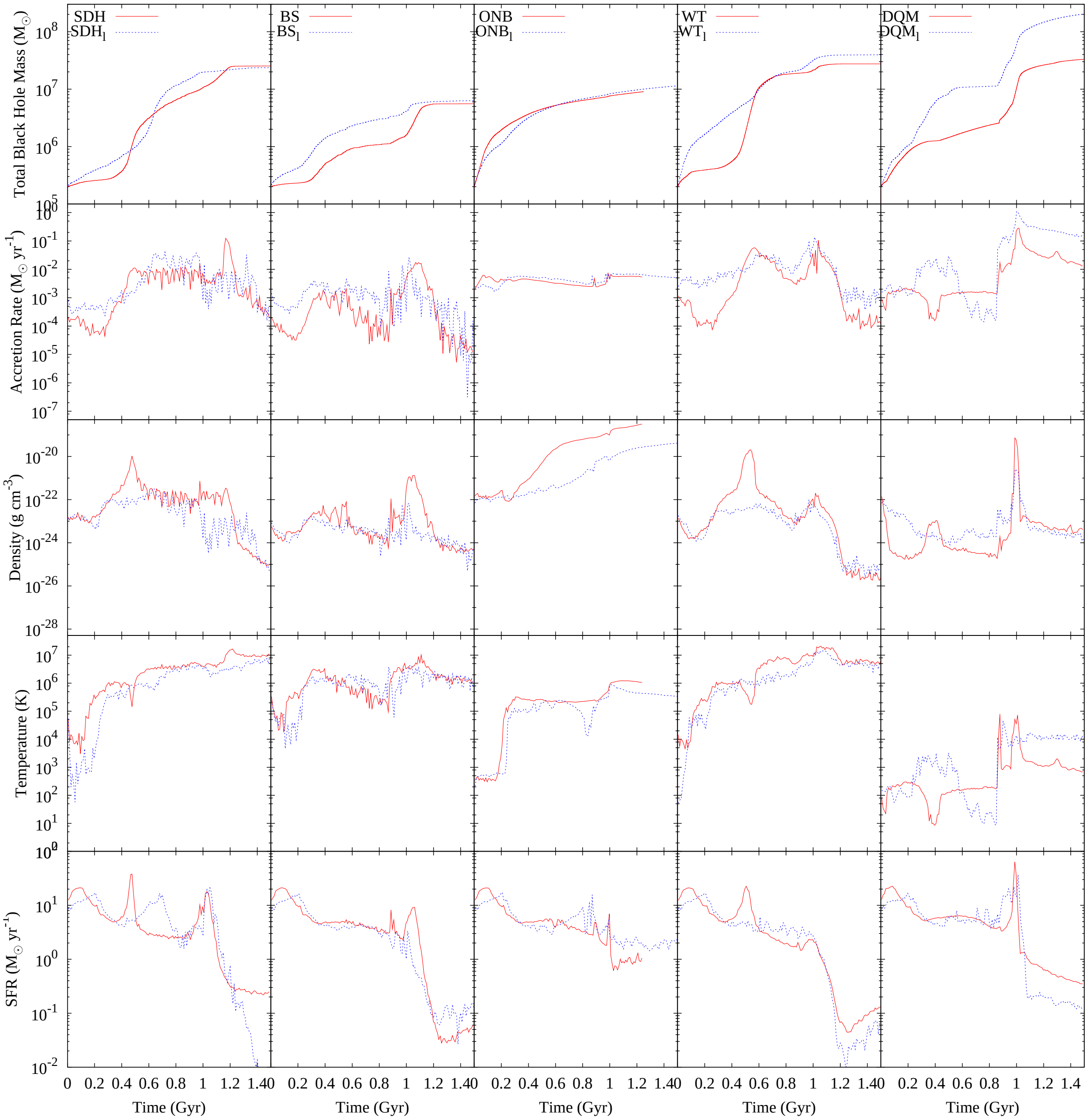

Figure B.14: Total black hole mass, accretion rates, gas density, gas temperature and global star formation rate for both resolutions of the models presented in Chapter 2. The bottom four rows are geometrically averaged over both black holes in bins of 10 Myr.